



Università degli Studi di Ferrara

DOTTORATO DI RICERCA IN "FISICA"

CICLO XXIX

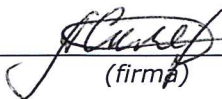
COORDINATORE Prof. Vincenzo Guidi

DEVELOPMENT OF NOVEL CYCLOTRON TARGET FOR ^{99m}Tc PRODUCTION

Settore Scientifico Disciplinare FIS/03, FIS/07, ING-IND/12, ING-IND/22

Dottorando

Dott. Hanna Skliarova



(firma)

Tutori

Prof. Giovanni Fiorentini



(firma)

Prof. Vincenzo Palmieri



(firma)

Anni 2013/2016

“All science is either physics or stamp collecting”

Ernest Rutherford

ACKNOWLEDGEMENTS

Firstly, I would like to express my sincere gratitude to my advisors Prof. Fiorentini and Prof. Palmieri for the continuous support of my Ph.D study and related research.

Besides my advisors, I would like to thank the referees of my thesis: Prof. Vaglio, Dr. Giove and Dr. Marengo, for their availability, interest to my work and valuable suggestions.

My Ph.D thesis is realized in a framework of two INFN projects: LARAMED and TECHNOSP. I would sincerely thank the projects leaders Prof. Duatti and Ing. Esposito for their help, moral, scientific and financial support.

My great thanks to the LNL INFN fellow student Sara Cisternino, who has followed me and helped me in different aspects of my Ph.D work. I would like also to thank all the colleagues of the Laboratory of Surface Treatments and Superconductivity of the LNL INFN for their availability and help, when it was required. I can't not mention the great contribution of the staff of the mechanical workshop of the LNL INFN. Any new apparatus, parts and ideas would not be able to come into practice without their help.

My sincere thanks also goes to Dr. Marengo and Dr. Cicoria, who provided me an opportunity to realize the under beam-tests of the developed target prototypes by the cyclotron of the Medical Physics Department of the Azienda Ospedaliero Universitaria Policlinico S.Orsola-Malpighi. Without their precious support, it would not be possible to carry out this research.

I would like to express my great thankfulness to Dr. Rossi-Alvarez, Dr. Bezzon, Dr. Zanon and Dr. Buso for the development of the MoO₃ reduction system, which allowed studying the method for Mo recovery. I must mention the great help of Dott.ssa Carturan in the study of the chemical aspects of Mo recovery.

I thank Dr. Rossi for the development of the software for automatic multilayer sputter deposition, I have used in my Ph.D work, and for the preliminary study of the aspects of thick film deposition.

Last but not the least, I would like to thank my closest people for supporting me spiritually throughout years of study, through writing this thesis and my life in general. This accomplishment would not have been possible without them. Thank you all.

SOMMARIO

Il ^{99m}Tc è un radionuclide estremamente importante, utilizzato in più dell'80% degli esami diagnostici. Generalmente, il ^{99m}Tc viene estratto da generatori portatili contenenti il ^{99}Mo (quest'ultimo proveniente dai reattori a fissione che utilizzano ^{235}U altamente arricchito). Il 95% di tutta la produzione mondiale del radionuclide ^{99}Mo è attualmente supportato da cinque impianti nucleari, alcuni dei quali hanno raggiunto più di 50 anni di attività. E sono pertanto esposti a frequenti e improvvise interruzioni che causano periodici cali nella produzione del ^{99}Mo .

Presso i Laboratori Nazionali di Legnaro dell'Istituto Nazionale di Fisica Nucleare (LNL-INFN) si è scelta la strategia basata su acceleratore, come alternativa alla via standard per avere una soluzione di riserva in caso di una nuova crisi del ^{99m}Tc .

Tra le varie possibilità studiate, la migliore, e più promettente, è la produzione diretta del ^{99m}Tc attraverso l'irraggiamento, con fascio di protoni, di target di ^{100}Mo arricchito. Un'ulteriore alternativa è la produzione nel nuclide precursore ^{99}Mo nella stessa cornice di irraggiamento. Riguardo la produzione indiretta del ^{99}Mo , il principale svantaggio è l'attività specifica piuttosto bassa se paragonata alla fissione nucleare nei reattori. Pertanto, la produzione del ^{99m}Tc a partire dalla reazione $^{100}\text{Mo}(p,2n)^{99m}\text{Tc}$, è stata sviluppata e valutata presso LNL-INFN; tuttavia alcune questioni devono ancora essere risolte.

Il problema chiave in esame è il design e la costruzione di un target idoneo per la produzione del radionuclide e il recupero del costoso isotopo ^{100}Mo dopo la produzione del radiofarmaco a base di ^{99m}Tc . Infatti, solo una tecnologia consolidata e a circuito chiuso può rendere competitiva la via basata sull'acceleratore con la produzione standard basata sul reattore nucleare.

Per massimizzare la resa della reazione nucleare, la produzione dovrebbe essere effettuata alle massime correnti protoniche. Questo significa che il target dovrebbe fornire un'elevata efficienza di dissipazione del calore. Un sistema di target solido standard si suppone essere costituito dal materiale target depositato su un backing plate, raffreddato con liquidi. Per massimizzare la dissipazione del calore, il target dovrebbe essere costruito con un materiale avente la massima conducibilità termica, e dovrebbe essere usato un metodo che fornisca un buon contatto termo-meccanico tra il materiale target in sé e il backing plate.

Al fine di consentire la massima velocità di produzione di ^{99m}Tc attraverso il ciclotrone, la tecnica di deposizione metallica deve garantire:

- buona conducibilità termica del Mo;

- spessore uniforme e controllato dello strato di Mo;
- elevata densità del Mo (bulk-like);
- basso livello di ossidazione del Mo;
- buon contatto termo-meccanico con il backing plate.

Le più comuni tecniche di deposizione per produrre il target di Mo, che includono la sinterizzazione, l'elettrodeposizione, laser melting, laminazione, ecc., non sono in grado di soddisfare i suddetti requisiti.

Il gruppo dell'LNL-INFN ha proposto di usare il magnetron sputtering come tecnica base per depositare il ^{100}Mo direttamente su un backing plate. Una delle principali sfide tecnologiche di questa tesi è stata quella di sviluppare un metodo per depositare film ultra spessi (centinaia di micrometri) di metalli refrattari (Nb e Mo) con la tecnica magnetron sputtering. I film depositati con il metodo proposto sono risultati densi (>98% della densità bulk) e aderenti al backing plate ad alta conducibilità termica.

Il comportamento termico del sistema (100 μm di spessore di Mo depositato su un backing di rame) è stato testato sotto fascio a 15.6 MeV e 60 μA . Il film di Mo spesso 100 μm depositato con la tecnica magnetron sputtering sul backing di rame ha mostrato un'eccellente stabilità termomeccanica (nessuna delaminazione o rottura) sotto un fascio di protoni di circa 1 kW/cm^2 di densità di potenza.

Il rame è lontano dall'essere un materiale ideale per il backing plate, poiché si dissolve nella soluzione reattiva di H_2O_2 nella quale il materiale target è normalmente disciolto dopo l'irraggiamento e prima della separazione chimica, utilizzando un modulo $^{100}\text{Mo}/^{99\text{m}}\text{Tc}$. Questi svantaggi costringono ad usare moduli di separazione aggiuntivi per ottenere il prodotto finale puro, ma questi sono incompatibili con la necessità di abbreviare e automatizzare le procedure.

Il concetto proposto in questa tesi include un sottile strato di materiale ceramico chimicamente inerte, per evitare impurità di radioisotopi. A questo scopo, sono stati proposti i materiali ceramici ad alta conducibilità termica, come parte del target plate. Per minimizzare l'energia persa sulla parte ceramica, è stato minimizzato il suo spessore. Inoltre, per mantenere una rigidità meccanica del sistema, e minimizzare i costi del target, i substrati ceramici sono stati brasati in vuoto a un backing plate di rame. Per realizzare questo prototipo, è stata studiata la brasatura in vuoto dei materiali ceramici con i metalli con diversi filler brasanti.

Sono stati usati filler a base di rame in forma pastosa “home-made” per la preparazione del prototipo di target. Al fine di migliorare il contatto brasato, la parte ceramica è stata metallizzata con un sottile strato di Ti depositato con la tecnica magnetron sputtering.

I prototipi di target sviluppati sono stati preparati depositando, mediante magnetron sputtering, 100µm di Mo su dischi ceramici che sono stati brasati al supporto metallico ad alta conducibilità termica (rame).

I prototipi di target prodotti hanno mostrato buona stabilità termomeccanica sotto la massima potenza di fascio di protoni del ciclotrone GE PETtrace (60 µA, 15.6 MeV, densità di potenza di circa 1 kW/cm²). Sono stati realizzati test brevi (1 minuto) e test lunghi, più vicini alle condizioni di irraggiamento per la produzione.

Per diminuire i costi per la produzione di ^{99m}Tc con il metodo basato su ciclotrone, è stato sviluppato un sistema per recuperare in forma metallica, il costoso ¹⁰⁰Mo dagli scarti del modulo di separazione. In questo modo, il metodo proposto permette il recupero del MoO₃ con un'efficienza del 94% partendo dallo scarto, arricchito di Mo, del modulo. La seguente riduzione dell'ossido di molibdeno, in un sistema chiuso in sovrappressione di idrogeno (senza flusso di idrogeno), fornisce più del 95% di Mo metallico. Lo stesso metodo di recupero può essere applicato per minimizzare le perdite del costoso ¹⁰⁰Mo durante la deposizione via magnetron sputtering.

ABSTRACT

^{99m}Tc is extremely important in nuclear medicine as it is being used in over 80% of all diagnostic examinations. ^{99m}Tc is eluted usually from portable generators containing ^{99}Mo (This one is produced in fission reactors from highly enriched ^{235}U). About 95% of all ^{99}Mo radionuclide world production is currently covered by five nuclear power plants, some of them having achieved more than 50 years operation. Therefore, they are exposed to frequent unscheduled shutdown, which usually course periodical shrinkage in capacity of ^{99}Mo production.

At the Legnaro National Laboratories of the Istituto Nazionale di Fisica Nucleare (LNL-INFN) the accelerator-based strategy was chosen as an alternative to standard path in order to have a backup solution in a case of new ^{99m}Tc crisis.

Among different possibilities that have been investigated, the best as well as most promising one, is the direct ^{99m}Tc production through proton beam irradiation of ^{100}Mo -enriched targets. Another possible route is the ^{99}Mo precursor nuclide production through the same irradiation framework. About the indirect ^{99}Mo production, the main drawback is the quite low specific activities if compared with nuclear fission reactors. Thus, cyclotron-based production of ^{99m}Tc starting from ^{100}Mo by $^{100}\text{Mo}(p,2n)^{99m}\text{Tc}$ reaction has been developed and evaluated at the LNL-INFN; however some issues must be resolved.

The key issue under consideration is the design and construction of a suitable radionuclide production target and the recovery of the expensive ^{100}Mo isotopic material after production of ^{99m}Tc radiopharmaceutical. Indeed, only well-established closed-loop technology for ^{100}Mo recovery can make the accelerator-based route competitive with the reactor-based standard.

In order to maximize the nuclear reaction yield the production should be performed at maximum proton currents. This means that the target system should provide high efficiency of heat dissipation. The basic solid target system supposed to be the target material deposited on a baking plate, liquid cooled. In order to maximize the heat dissipation the target should be constructed of materials with maximum thermal conductivity, including both target material itself and target backing plate, by a method providing good thermo-mechanical contact between them.

In order to allow the maximum cyclotron production rate of ^{99m}Tc , the metallic deposition technique must guarantee:

- good thermal conductivity of Mo;

- uniform and controlled thickness of Mo layer;
- high density of Mo (bulk-like);
- low level of Mo oxidation;
- good thermomechanical contact to the backing plate.

The common techniques for Mo target production, including sintering, electrodeposition laser melting, lamination, etc. are not able to satisfy those requests.

LNL-INFN group have proposed to use magnetron sputtering as basic technique for deposition of ^{100}Mo directly onto a backing plate. One of the main technological challenges of this thesis was to develop a method to deposit ultra-thick film (hundreds of microns) of refractory metal (Nb and Mo) by magnetron sputtering. The films deposited by the proposed method were dense (>98% of bulk density) and adherent to high thermal conductivity backing plate.

The thermal contact behaviour of the system (100 μm thick Mo deposited onto copper backing) was tested under 15.6MeV and 60 μA proton beam. The 100 μm thick Mo film deposited by magnetron sputtering onto copper backing showed excellent thermomechanical stability (no delamination or cracking) under the proton beam of heat power density of about 1kW/cm².

Copper is far from being an ideal material for the backing plate, since it dissolves in H₂O₂, reactive media, in which target material is normally dissolved after irradiation and before the chemical separation using a $^{100}\text{Mo}/^{99\text{m}}\text{Tc}$ -module. These drawbacks force to use further separation modules in order to obtain the purity of the final product, intolerable with the necessity to shorten and automatize the procedures.

The concept proposed in this thesis comprise a thin layer of chemically inert ceramic material, avoiding radioisotope impurities. For this purpose, ceramic materials with high thermal conductivity were proposed to be a part of target plate. In order to minimize the energy losses on the ceramic part, its thickness was minimized. Moreover, in order to keep mechanical rigidity of the system, and minimize the cost of such target, the ceramics substrates were brazed in vacuum to a copper target backing plate. In order to realize such prototypes, the vacuum brazing of ceramics to metal with different brazing fillers was studied.

Copper-based active brazing alloy fillers in a form of homemade paste were used for the target prototype preparation. In order to improve the brazed contact a preliminary Ti metallization of the ceramic part using magnetron sputtering was realized.

The proposed advanced target prototypes were prepared by deposition of 100 μm thick Mo by magnetron sputtering on ceramic discs, which were brazed to high thermal conductivity metallic holder (copper).

The produced solid target prototypes showed good thermomechanical stability under the maximum power of proton beam of GE PETtrace cyclotron (60 μA , 15.6MeV, heat power density of about 1kW/cm²). Both short (1 min) and long test, the second closer to the production irradiation conditions (30 min), were realized.

In order to decrease the costs of cyclotron-based method for production of ^{99m}Tc, a method to recover expensive ¹⁰⁰Mo from separation module waste in metallic form, was developed. Thus, the proposed method allowed a MoO₃ recovery efficiency of 94% starting from the module Mo-rich waste. The following reduction of molybdenum oxide, in a closed system in overpressure of hydrogen (without hydrogen flow), provided >95% of Mo metallic. The same recovery method can be applied to minimize the losses of expensive ¹⁰⁰Mo during magnetron sputter deposition.

CONTENTS

1 INTRODUCTION.....	1
1.1 Unique role of ^{99m}Tc in nuclear medicine.....	1
1.2 Standard ^{99m}Tc production method.....	2
1.2.1 $^{99}\text{Mo}/^{99m}\text{Tc}$ generator	2
1.2.2 Current supply issues of nuclear reactor-based ^{99}Mo precursor.....	4
2 STATE OF ART.....	7
2.1 Reactor-based ^{99}Mo production.....	7
2.2 Production of ^{99m}Tc by cyclotron.....	8
2.2.1 Cyclotron accelerator	8
2.2.2 Cyclotron-based ^{99m}Tc production	9
2.2.2.1 Parent ^{99}Mo production	9
2.2.2.2 Direct ^{99m}Tc production	10
2.3 Preliminary study of $^{99}\text{Mo}/^{99m}\text{Tc}$ production at LNL INFN	10
2.3.1 $^{100}\text{Mo}(\text{p},\text{pn})^{99}\text{Mo}$	11
2.3.2 $^{100}\text{Mo}(\text{p},2\text{n})^{99m}\text{Tc}$	14
2.4 Techniques for ^{100}Mo cyclotron target preparation	16
2.5 Cyclotron solid target design.	24
2.5.1 Low current cyclotron solid target.....	25
2.5.2 High current cyclotron solid target.....	28
2.5.3 Alternative target configurations.....	30
2.5.4 Heat exchange in solid cyclotron target.....	32
2.6 Proposal of an Advanced target preparation	34
2.6.1 Target deposition requirements	35
2.6.2 Magnetron sputtering as a solution	35
2.6.3 Backing plate inertness.....	36

2.6.4 Sapphire and DLC as a solution	37
2.6.5 Evaluation of other opportunities	38
2.6.5.1 Advanced materials for high thermal conductivity backing plate	38
2.6.5.2 Advanced cooling with liquid metals and its difficulties	38
2.6.6 $^{99}\text{Mo}/^{99\text{m}}\text{Tc}$ generator vs cyclotron produced $^{99\text{m}}\text{Tc}$	39

3 FUNDAMENTAL ASPECTS OF THE TECHNOLOGICAL PROCESSES..... 41

3.1 Magnetron sputtering	41
3.1.1 What is sputtering?	41
3.1.1.1 Simple sputtering configuration.....	41
3.1.1.2 Sputtering sources	42
3.1.2 Control of stress during vapour deposition	44
3.1.2.1 What is stress?.....	44
3.1.2.2 Stress in thin films.....	46
3.1.2.3 Stress evolution during film growth	50
3.1.2.4 Parameters influencing stress.....	51
3.1.2.5 Methods to reduce stress	55
3.1.2.6 Methods to measure stress.....	56
3.1.3 Protective coatings engineering	58
3.1.3.1 Diffusion barriers	58
3.1.3.2 Methods to obtain amorphous films by sputtering.....	58
3.1.3.3 Sputtering recipes of a packed structure	59
3.2 Vacuum brazing	60
3.2.1 Fundamentals of brazing	60
3.2.1.1 Filler-metal characteristics.....	61
3.2.1.2 Base-material characteristics	63
3.2.2 Metal-ceramics brazing	64
3.2.2.1 Molybdenum-manganese/nickel plating method	65
3.2.2.2 Thin-film method.....	65
3.2.2.3 Active filler-metal brazing	66
3.2.3 Pre-brazing considerations.....	66
3.2.3.1 Surface preparation.....	66

3.2.3.2 Filler metal selection	67
3.2.3.3 Joint design and clearance.....	68
3.2.3.4 Heating methods	70
3.2.3.5 Post-brazing treatments and inspection	73
4 EXPERIMENTAL SETUP.....	75
4.1 Analytical techniques used.....	75
4.1.1 Diffractometric analysis of films and powders.....	75
4.1.1.1 Basic principles.....	75
4.1.1.2 XRD-data treatment.....	76
4.1.1.3 Short description of the XRD-device	79
4.1.1.4 The XRD-method used	79
4.1.2 SEM.....	80
4.1.2.1 Principles of operation	80
4.1.2.2 The SEM devise used in current study.	82
4.1.3 EDX analysis	82
4.1.4 Contact profilometry.....	82
4.2 Substrates preparation for sputtering and brazing.....	83
4.2.1.1 Copper substrates.....	83
4.2.1.2 Aluminium substrates.....	85
4.2.1.3 Ceramic substrates.....	86
4.3 The vacuum system for deposition and brazing	87
4.4 Film sputtering.....	89
4.4.1.1 Substrate holders for sputter deposition	91
4.4.1.2 Magnetron sputtering source.....	93
4.4.1.3 Cathode power supplies: control and automation.....	94
4.4.2 Materials used	96
4.4.2.1 Sputtering targets quality.....	96
4.4.2.2 Sputtering gas quality	96
4.5 Corrosion tests for protective films.....	96
4.5.1 The acid test	96

4.5.2 The liquid gallium test	97
4.6 Vacuum brazing	98
4.6.1 The vacuum system	98
4.6.2 Furnace used for vacuum brazing	98
4.6.2.1 The inductive furnace	98
4.6.2.2 Resistive furnaces	100
4.6.3 Preliminary ceramics materials treatment.....	103
4.6.3.1 Titanium coating deposition	103
4.6.4 Brazing fillers preparation	103
4.6.4.1 Powders mixing	104
4.6.4.2 Paste-creating agents.....	105
4.7 Cyclotron irradiation tests.....	106
4.7.1 GE PETtrace Cyclotron.....	106
4.7.1.1 The vacuum system	107
4.7.1.2 The ion source	108
4.7.1.3 The magnet	108
4.7.1.4 The RF-source.....	108
4.7.1.5 Beam extraction	108
4.7.1.6 Beam control system.....	108
4.7.1.7 Cyclotron control.....	109
4.7.2 The solid target station design and constrictions	110
4.7.2.1 Design	110
4.7.2.2 Cooling systems	111
4.7.2.3 The target	111
4.7.3 Gamma spectroscopy	113
4.8 Reduction system for Mo target material recovery	114
4.8.1 Short description of process chemistry	114
4.8.2 Equipment	116
4.8.2.1 The vacuum system	117
4.8.2.2 The oven.....	118
4.8.2.3 The reactor.....	118
4.8.2.4 Automatized control.....	118
4.8.2.5 Operation conditions	119

5 EXPERIMENTAL RESULTS.....	121
5.1 Study of non-conventional target cooling: liquid metal cooling.....	121
5.1.1 Protective coatings against LME for equipment protection.....	121
5.1.1.1 R&D methodology	121
5.1.1.2 Main results.....	122
5.1.2 Liquid metal cooling circuit engineering, or "why not LM cooling?"	127
5.1.2.1 Cooling system design and complications	127
5.1.2.2 Safety	131
5.2 Target prototype preparation	133
5.2.1 PVD for Mo target material deposition.....	133
5.2.1.1 Nb thick film deposition.....	133
5.2.1.2 Nb thick film deposition onto ceramics substrates	141
5.2.1.3 Mo optimal sputtering pressure	142
5.2.1.4 Stress-free Mo deposition.....	143
5.2.1.5 Estimation of stress in Mo sputtered films	151
5.2.2 Novel backing plate	155
5.2.2.1 Study of vacuum brazing for ceramics	155
5.2.2.2 Study of synthetic diamonds vacuum brazing.....	165
5.3 Irradiation tests by cyclotron	173
5.3.1 Mo sputtered target material	173
5.3.2 Advanced backing	175
5.3.2.1 Sapphire	175
5.3.2.2 CVD Diamond	178
5.3.2.3 Sapphire brazed to metal.....	180
5.3.2.4 CVD diamond brazed to metal	183
5.4 Development of recovery procedure for Mo powders	184
5.4.1 MoO ₃ from permolybdate	184
5.4.1.1 Literature approach and problems.....	184
5.4.1.2 Alternative method	186
5.4.2 MoO ₃ recovery from sputtering of Mo	187
5.4.3 Mo recovery from MoO ₃ by reduction.....	188
5.4.3.1 Reduction of commercial MoO ₃	190

5.4.3.2 Reduction of recovered MoO₃..... 192

6 CONCLUSIONS 195

6.1 Main achievements 195

6.1.1 Ultra-thick films by magnetron sputtering..... 195

6.1.2 Working target prototypes 195

6.1.3 Molybdenum recovery..... 196

References.....197

LIST OF TABLES

Table 2.1 Isotopic purity of ^{100}Mo -enriched (99.05% level) from ISOFLEX Isotopes..	13
Table 2.2 Efficient ^{100}Mo target thickness for ^{99}Mo production	13
Table 2.3 Nb and Tc isotopes expected to be produced by $^{100}\text{Mo}(p,x)$ reactions	13
Table 2.4 State of art: cyclotron targets for production of ^{99m}Tc (preparation and irradiation).....	18
Table 3.1 Metal-filler base materials for brazing	62
Table 3.2 Common types of brazed joints	68
Table 3.3 Brazing joints clearances for different filler metals group and process.....	70
Table 4.1 XRD beam optics configuration	80
Table 4.2 Thermal features of substrate materials.....	87
Table 4.3 Different substrate-holders.....	91
Table 4.4 Powders quality	104
Table 4.5 Heating parameters for reduction control	118
Table 5.1 Influence of pressure and negative bias on Nb protective film sputtering	122
Table 5.2 Niobium oxide and multilayer protective coatings.....	124
Table 5.3 Ga-In-Sn alloy, Ga and water comparison	127
Table 5.4 Products of ^{71}Ga neutron irradiation ($E < 20\text{MeV}$).....	128
Table 5.5 Products of ^{69}Ga neutron irradiation ($E < 20\text{MeV}$).....	129
Table 5.6 Products of ^{113}I neutron irradiation ($E < 20\text{MeV}$).....	130
Table 5.7 Products of ^{115}I neutron irradiation ($E < 20\text{MeV}$).....	131
Table 5.8 Nb thick film deposition parameters.....	134
Table 5.9 Nb thick film deposition parameters.....	135
Table 5.10 Nb thick film deposition parameters	136
Table 5.11 XRD analysis of Nb sputtered thick films with and without program	137
Table 5.12 Comparison of multilayer deposition of Nb at different temperature	138
Table 5.13 Efficiency of multilayer deposition of Nb sputtering at different temperature	140
Table 5.14 Multilayer sputtering of Nb on thick sapphire.....	141
Table 5.15 Multilayer sputtering of Mo onto different substrates	144
Table 5.16 Multilayer sputtering of Mo onto different substrates	147

Table 5.17 Multilayer sputtering of Mo onto different substrates.....	149
Table 5.18 Properties of Mo and substrate materials.....	152
Table 5.19 Stress estimation in 125 μ m Mo sputtered films.....	154
Table 5.20 Comparison of current result with literature	155
Table 5.21 Thermal expansion coefficients of brazed elements.....	155
Table 5.22 Content of brazing fillers.....	156
Table 5.23 Brazing alumina to metal experiments	156
Table 5.24 Brazing alumina to metal experiments	157
Table 5.25 Content of brazing fillers for aluminum 6082	161
Table 5.26 Brazing discs sapphire to copper for target prototype	164
Table 5.27 Content of fillers used for synthetic diamond brazing.....	165
Table 5.28 Experiments on brazing synthetic diamond powders to metal	166
Table 5.29 Thermal conductivity measurement.	171
Table 5.30 Brazing CVD diamond discs to copper for target prototype.....	173
Table 5.31 Gamma spectrum analysis of proton-irradiated Mo sputtered sapphire.....	177
Table 5.32 Decay curve data of irradiated diamond obtained with dose-calibrator.	179
Table 5.33 Tests of novel target prototype: ceramics-metal composite baseplate.	182
Table 5.34 MoO ₃ reduction experiments.....	189
Table 5.35 Analysis of R-1 MoO ₃ reduction product.	190
Table 5.36 Analysis of R-2 MoO ₃ reduction product.	190
Table 5.37 Analysis of R-3.1 MoO ₃ reduction product.....	191
Table 5.38 Analysis of R-3.2 MoO ₃ reduction product.....	191
Table 5.39 Analysis of R-4 MoO ₃ reduction product.	192
Table 5.40 Analysis of R-5 MoO ₃ reduction product.	192

LIST OF FIGURES

Figure 1.1: (a) Schematic representation and (b) cutaway view of commercial $^{99}\text{Mo}/^{99\text{m}}\text{Tc}$ generator.....	2
Figure 1.2: ^{99}Mo decay chain	3
Figure 1.3: Production of ^{99}Mo from ^{235}U fission.....	3
Figure 1.4: Classical $^{99\text{m}}\text{Tc}$ production chain.....	4
Figure 2.1: Operating principle of a cyclotron.....	8
Figure 2.2: Experimental data on excitation function for $^{100}\text{Mo}(\text{p},\text{pn})^{99}\text{Mo}$	11
Figure 2.3: $^{100}\text{Mo}(\text{p},\text{pxn})^{9\text{x}}\text{Mo}$ theoretical excitation functions and experimental measurements.....	12
Figure 2.4: $^{100}\text{Mo}(\text{p},2\text{pxn})^{9\text{x}}\text{Nb}$ theoretical excitation functions and experimental measurements.....	12
Figure 2.5: Experimental data on excitation function for $^{100}\text{Mo}(\text{p},2\text{n})^{99\text{m}+\text{g}}\text{Tc}$	14
Figure 2.6: Theoretical excitation function for $^{100}\text{Mo}(\text{p},\text{xn})^{\text{x}}\text{Tc}$	15
Figure 2.7: An internal target used for production of ^{211}At	24
Figure 2.8: Multipurpose internal slanted solid target with extremely low angle (Nuclear Physics Institute AS CR, v.v.i.,Řež)	25
Figure 2.9: A typical low current solid powder target.	25
Figure 2.10: Nirta® Solid Compact irradiation Target of IBA.....	26
Figure 2.11: Cross-section of Nirta® target.	26
Figure 2.12: ALCEO PTS irradiation module and Metal solid target system (COMECER).....	27
Figure 2.13: PETtrace solid target of GE.....	27
Figure 2.14: Foil target holder for production of ^{66}Ga from ^{66}Zn foil in CS-15 cyclotron.....	28
Figure 2.15: TR19 target of Advanced Cyclotron Systems Inc.....	28
Figure 2.16: IBA high current solid target.....	29
Figure 2.17: Modification of IBA solid target baseplate with metallic foam.....	29
Figure 2.18: Design of a solid target system (a) with 4π water-cooling of the target capsule (b).....	30
Figure 2.19: Universal encapsulated solid cyclotron target of TRIUMF.....	31
Figure 2.20: Encapsulated target for production ^{82}Sr and ^{68}Ge at ARRONAX.....	31
Figure 2.21: Internal rotating target holder: water-cooled spherical copper cap, should be covered by a target layer (Nuclear Physics Institute AS CR, Řež)	32

Figure 2.22: Heat exchange in solid cyclotron target.....	34
Figure 3.1: Schematic representation of simple sputtering system.	42
Figure 3.2: Planar magnetron sputtering.....	43
Figure 3.3: (a) Interatomic potential function vs interatomic distance. (b) Applied force vs atomic displacement.	44
Figure 3.4: Deformation and fracture in stressed films.....	46
Figure 3.5: Schematic representation of thermal (extrinsic) and intrinsic stress contributions.	47
Figure 3.6: Explanation of tensile (a) and compressive (b) residual stress in thin film.....	47
Figure 3.7: Thornton's Structural Zone Model.....	49
Figure 3.8: Force-per-width curve (proportional to curvature) measured as a function of time/effective thickness during vapor deposition [48].....	51
Figure 3.9: Schematic representation of the stress vs thickness curves of high melting (Type I) and low melting (Type II) materials.	52
Figure 3.10: General stress-pressure dependency in sputtered thin films.....	53
Figure 3.11: (a) Stress-pressure relation in MS Mo films, (b) Dependency of the critical pressure for the compression-to-tension stress transition, and the critical pressure for loss of reflectance, on the coating material atomic mass	54
Figure 3.12: Typical brazing temperature ranges for various filler metals.....	62
Figure 3.13: Moly-manganese (left) and thin film (right) metallization processes.....	65
Figure 3.14: Active filler-metal brazing process.	66
Figure 3.15: Tensile strength versus joint clearance.....	69
Figure 3.16: Different brazing methods: a) torch brazing, b) resistive brazing.	70
Figure 3.17: Different brazing methods: a) inductive brazing, b) dip brazing of Al in molten flux.....	71
Figure 3.18: Industrial scale resistive vacuum brazing furnace.	72
Figure 3.19: Typical braze cycle for furnace brazing.	73
Figure 4.1: Constructive (a) and destructive (b) interference of X-rays interacting with atomic planes.....	75
Figure 4.2: Example of XRD spectrums of crystalline and amorphous structures	78
Figure 4.3: X'Pert Philips PW3040/60 diffractometer.	78
Figure 4.4: X'Pert Philips XRD device assembled for θ - 2θ Gonio configuration.....	79
Figure 4.5: Zero-background silicon sample holder for low quantity of powders.	80

Figure 4.6: a) Basic components of SEM; b) XL-30 Philips SEM with QUANTAX EDS of Brucker	81
Figure 4.7: a) Dektak 8 profiler of Veeco; b) internal view of the system.	83
Figure 4.8: Different copper substrates for sputtering deposition.	84
Figure 4.9: Different copper substrates for vacuum brazing.....	84
Figure 4.10: Aluminum substrate for vacuum brazing with Ti coated sapphire sample.....	85
Figure 4.11: Sapphire substrates for vacuum brazing with Ti coated sapphire sample.....	86
Figure 4.12: Substrates: square quartz (a) sapphire (b), CVD synthetic diamond (c), Si wafer (d).	87
Figure 4.13: Vacuum system: a) top view, b) PLC control system, c) full system.....	88
Figure 4.14: MaxiGauge™ pressure control box.	88
Figure 4.15: MKS multi gas controller 647C.....	89
Figure 4.16: a) Chamber #4 assembled for top-down MS deposition without heating, b) chamber #2 assembled for down-top MS deposition on a heated substrate.	90
Figure 4.17: Metallic flakes from magnetron shield on sputtering target in “down-top” configuration.....	90
Figure 4.18: IR heated substrate holder.	92
Figure 4.19: IR lamp power supply: a) automatic control, b) manual control.....	92
Figure 4.20: Different ways to fix substrates for thick film deposition.	93
Figure 4.21: The schematic representation of UBM.....	93
Figure 4.22: The UBM used in the deposition experiments: (a) drawing, (b) photo....	94
Figure 4.23: DC power-supplies used for magnetron sputtering.	94
Figure 4.24: NIUSB-6009 connections.....	95
Figure 4.25: Interface of USB6009 mdx-1.5K LabVIEW program.	95
Figure 4.26: Principal scheme of acid diffusion barrier test.....	97
Figure 4.27: Evaluation of results of acid diffusion barrier test.....	97
Figure 4.28: Evaluation of results of liquid gallium test: resistance and corrosion.	98
Figure 4.29: Installation of inductive vacuum brazing furnace.....	99
Figure 4.30: Inductive brazing furnace: a) samples positioning, b) graphite chamber closed, c) pyrometer temperature control.	99
Figure 4.31: Vacuum chamber with IR lamp heated brazing furnace assembled.	100
Figure 4.32: D40mm IR lamp driven vacuum brazing furnace.....	101

Figure 4.33: D76mm IR lamp driven vacuum brazing furnace design.....	101
Figure 4.34: D76mm IR lamp driven vacuum brazing furnace.	102
Figure 4.35: Sapphire substrates with Ti coating deposited.....	103
Figure 4.36: TURBULA® shaker mixer for powders.....	104
Figure 4.37: Application of just prepared brazant paste on copper and aluminum samples.....	105
Figure 4.38: GE PETtrace cyclotron of S. Orsola-Malpighi Hospital, Bologna.....	106
Figure 4.39: GE PETtrace cyclotrons system.....	107
Figure 4.40: The PETtrace service system interface.....	109
Figure 4.41: Solid target station.	110
Figure 4.42: Automatic target dismounting procedure.....	111
Figure 4.43: 4-pin clamping target system.....	112
Figure 4.44: Liquid nitrogen cooled HPGe of “St. Orsola-Malpighi” Hospital, Bologna.	112
Figure 4.45: Gamma-BRONTOLO software interface.....	113
Figure 4.46: Reduction system scheme.	114
Figure 4.47: Reduction system scheme.	115
Figure 4.48: Nitrogen gas line.....	116
Figure 4.49: Quartz crucible placed inside tungsten reduction cell.	117
Figure 4.50: Compressed air flange cooling.....	117
Figure 4.51: Automatic program interface.....	119
Figure 5.1: High resolution SEM of Nb-1 coating: a) FIB SEM of cross-section using electron beam; b) FIB SEM of cross-section using ion beam; c) SEM of the film surface.....	123
Figure 5.2: SEM of amorphous Nb ₂ O ₅ : a) top view; b) FIB-SEM of cross-section.	123
Figure 5.3: FIB-SEM of the cross-sections of sputtered Nb-Nb ₂ O ₅ multilayers: a) thin layers (M-1); b) thick layers (M-2); c) with thermal oxidation (M-3).....	124
Figure 5.4: XRD spectrums of Ta-Zr alloy films.....	125
Figure 5.5: SEM of the cross-sections of sputtered Ta-Zr alloy films.....	126
Figure 5.6: Stress vs sputtering pressure.....	134
Figure 5.7: 200µm self-sustaining Nb film deposited at 25 ⁰ C (TNb-15).	136
Figure 5.8: XRD patterns of TNb-15 and TNb-16 deposited at 25 ⁰ C with and without program.....	137
Figure 5.9: 200µm self-sustaining Nb-15 film deposited with program at r.t.....	138

Figure 5.10: 250 μ m Nb film deposited at 450 $^{\circ}$ C with program (Nb-19).....	139
Figure 5.11: XRD patterns of 110-peak of TNb-15, TNb-16 and TNb-17 films on copper.....	140
Figure 5.12: Nb films sputtered at 25 $^{\circ}$ C on Cu TNb-15 (a, b) and sapphire TNb-22 (c, d) substrates.....	141
Figure 5.13: 85 μ m Nb sputtered on sapphire at 400 $^{\circ}$ C.....	142
Figure 5.14: Stress in Mo sputtered vs sputtering pressure.....	143
Figure 5.15: 5 μ m Mo sputtered at 500 $^{\circ}$ C on sapphire (a) and silicon wafer (b).....	143
Figure 5.16: SEM of cross-section of 5 μ m Mo sputtered at 500 $^{\circ}$ C on silicon wafer...	144
Figure 5.17: Thick molybdenum films on sapphire (a) and copper coins (b).....	144
Figure 5.18: 110 μ m Mo sputtered on Cu: SEM-EDS of cross-section.....	145
Figure 5.19: SEM of cross-section 110 μ m Mo on Cu: grain size.....	146
Figure 5.20: 90 μ m molybdenum films on sapphire (a) and copper (b) discs.....	146
Figure 5.21: SEM of cross-section 90 μ m Mo on Cu.	147
Figure 5.22: Mask for deposition onto multiple substrates.	148
Figure 5.23: Mo-4 and Mo-5 110 μ m thick Mo sputtered by multilayer approach at 500 $^{\circ}$ C.....	148
Figure 5.24: Mo-6 and Mo-7 110 μ m thick Mo sputtered onto sapphire to be brazed to Cu.....	149
Figure 5.25: Mask for deposition onto multiple substrates.	150
Figure 5.26: Self-sustaining 125 μ m Mo film delaminated from CVD synthetic diamond.....	150
Figure 5.27: Mo-8 125 μ m Mo sputtered onto copper D32 for cyclotron test.....	151
Figure 5.28: Dektak 8 profiler estimation of curvature radius.....	152
Figure 5.29: Mo properties vs temperature.	153
Figure 5.30: Thermal expansion coefficient of Si wafer (a) and CVD diamond (b) vs temperature.....	154
Figure 5.31: Brazing thermal cycle Alu-10, Alu-14 with CuSnTi ABA paste.....	158
Figure 5.32: SEM (a) and EDS (b) analysis of cross section of Alu-10 brazed sample.....	159
Figure 5.33: Sapphire 10 \times 10 \times 1mm brazing to Cu by CuSil ABA: (a) before, (b) after.....	159
Figure 5.34: Brazing thermal cycle for brazing with CuSil ABA paste.	160
Figure 5.35: Thermal cycle for brazing sapphire to Al 6082.	161

Figure 5.36: Brazing sapphire to Al 6082: (a) before and (b) after thermal cycling..	162
Figure 5.37: Brazing 0.5mm thick sapphire to Al 6082: (a) before and (b) after thermal cycling.....	162
Figure 5.38: S-1. Brazing D19 sapphire to copper: (a) before and (b) after thermal cycling.....	163
Figure 5.39: S-2. Brazing D25 sapphire to copper: (a) before and (b) after thermal cycling.....	163
Figure 5.40: S-3, S-4, S-5. Brazed D13 sapphires with Mo film sputtered to copper.	164
Figure 5.41: SEM of Ti coated diamond powders brazing by NiCuSil-3 Dp-2 (a) and CuSil Dp-6 (b)	166
Figure 5.42: SEM of Ti coated diamond powders brazing with TiCuSil: a) Dp-3, b) Dp-4.	167
Figure 5.43: SEM of Ti coated diamond powders brazing with CuSil ABA: a) Dp-5, b) Dp-6.	167
Figure 5.44: SEM (a) and EDS (b) analysis of Ti coated diamond powders brazing with CuSnTi.	168
Figure 5.45: Thermal cycle for preparing diamond-metal composite material.....	169
Figure 5.46: SEM (a) and EDS (b) analysis of Cu-Ag- diamond composite cross-section.....	169
Figure 5.47: Experimental set-up for measurement of relative thermal conductivity	170
Figure 5.48: SEM (a) and EDS (b) analysis of CuAgDia composite cross-section.....	171
Figure 5.49: Thermal cycle for brazing diamond plate to copper with CuSil ABA paste.	172
Figure 5.50: D-1(a) and D-2(b) diamond discs brazed to copper plate with CuSil ABA paste.....	173
Figure 5.51: Cyclotron irradiation test of 110 μ m Mo-4 sputtered onto copper.....	174
Figure 5.52: 125 μ m Mo-8 samples sputtered onto copper \varnothing 32 after cyclotron irradiation test at 60 μ A.	174
Figure 5.53: Mo-5 sputtered on sapphire after cyclotron irradiation test in 4-pin target-holder.	175
Figure 5.54: Dissolution test of irradiated Mo sputtered onto sapphire backing.	176
Figure 5.55: Gamma spectrum of proton irradiated natMo sputtered on sapphire...	176

Figure 5.56: CVD synthetic diamond irradiation test in 4-pin clamping target-holder.....	178
Figure 5.57: Gamma spectrum of proton irradiated CVD synthetic diamond disc.	178
Figure 5.58: Gamma spectrum of proton irradiated CVD synthetic diamond disc.	180
Figure 5.59: Cyclotron irradiation test of S-1 sapphire-based prototype at 40 μ A.....	180
Figure 5.60: Cyclotron irradiation test of S-3 sapphire-based prototype.	181
Figure 5.61: Cyclotron irradiation test of S-4 sapphire-based prototype at 60 μ A.....	181
Figure 5.62: Cyclotron irradiation test of S-5 sapphire-based prototype at 60 μ A.....	182
Figure 5.63: Cyclotron irradiation test of D-1 synthetic diamond-based prototype..	183
Figure 5.64: 30min cyclotron irradiation test of D-2 C synthetic diamond-based prototype at 60 μ A.....	183
Figure 5.65: MoO ₃ recovery as regeneration of spent catalyst.....	185
Figure 5.66: Modifications of color with pH change in MoO ₃ recovery.....	186
Figure 5.67: Substrate-holder with mask and six D13 substrates sputtered by Mo. .	188
Figure 5.68: MoO ₃ reduction thermal cycle.....	189
Figure 5.69: EDS-map analysis of R-5 MoO ₃ reduction product.....	193

LIST OF ABBREVIATIONS AND ACRONYMS

PVD - Physical Vapor Deposition

MS - Magnetron sputtering

VW –Volmer-Webber grow

SZM – Structural Zone Model

CTE - Coefficient of Thermal Expansion

SH – Substrate holder

UBM – Unbalanced magnetron

EDX, EDS - Energy-dispersive X-ray spectroscopy

XRD – X-ray diffraction

SEM-Scanning Electron Microscope, Scanning Electron Microscopy

DECODING OF SAMPLE/EXPERIMENT NAMES

<i>Sample name</i>	<i>Description of experiments</i>	<i>Chapter</i>
Nb-#	Thin Nb coatings for protection against LME	5.1.1.2.1
Nb ₂ O ₅ -#	Thin Nb ₂ O ₅ coatings for protection against LME	5.1.1.2.2
M-#	Thin Nb/ Nb ₂ O ₅ multilayer coatings for protection against LME	5.1.1.2.2
TNb-#	Thick Nb film sputtering as preliminary study for Mo	5.2.1.1
Mo-#	Thick Mo film sputtering for cyclotron target prototype	5.2.1.4
Alu-#	Alumina brazing as preliminary study for sapphire to copper brazing	5.2.2.1.1
S-#	Brazing sapphire to copper for cyclotron target prototype preparation	5.2.2.1.4
Dp-#	Brazing diamond powders as preliminary study for diamond plate to copper brazing	5.2.2.2.1
D-#	Brazing CVD synthetic diamond plate to copper for cyclotron target prototype preparation	5.2.2.2.3
MoO ₃ -#	MoO ₃ recovery starting from Mo-rich waste from ¹⁰⁰ Mo/ ^{99m} Tc separation module	5.4.1
R-#	Hydrogen batch-reactor reduction of MoO ₃ to metallic Mo	5.4.3.7

1 INTRODUCTION

1.1 Unique role of ^{99m}Tc in nuclear medicine

^{99m}Tc is an extremely important radionuclide, used almost in all types' traditional diagnostic examinations. Each year, roughly, 30 million procedures are carried out with ^{99m}Tc radiopharmaceuticals, and this figure is projected to grow at a rate of about 15% per year. ^{99m}Tc is usually extracted from portable generators containing ^{99}Mo , coming from fission reactors that use highly enriched uranium Weapon-Grade (i.e. ^{235}U enrichment level $>80\%$). Once chemically separated among the ^{235}U fission products, and further purified, it is loaded in alumina column of portable generators that are sent to hospitals. It decays into ^{99m}Tc , which is eluted from generators and then labelled to a compound product to get a radiopharmaceutical that can be administered to patients.

^{99m}Tc is the close to ideal radioisotope for "conventional" nuclear medicine. It offers many advantages with respect to many other radionuclides, due to its very good physical and chemical characteristics. Among other aspects, the emitted gamma radiation has the appropriate energy (neither too low nor too high) to provide a good image whilst keeping low radiation dose to the patient (also because Tc is a nearly pure gamma emitter: 89%). Its almost 6-hours half-life is appropriate (neither too long nor too short) to be used for a medical diagnostic procedures providing a good image quality. It is long enough to allow labelling for a number of molecules and short enough to allow the patient to leave the hospital shortly after the examination. The delivery of the radionuclide to hospitals in a form of $^{99}\text{Mo}/^{99m}\text{Tc}$ generator is very comfortable from the point of view of logistics.

Owing to its multiple oxidation states, ^{99m}Tc has a versatile chemistry, making it possible to produce a variety of complexes with specific desired characteristics, which is a major advantage of ^{99m}Tc for radiopharmaceutical development. There are hundreds of ^{99m}Tc complexes useful for diagnostic procedures, among which over thirty are used in clinical studies. The most frequent diagnostic nuclear medicine procedures in the world are:

- cardiac imaging (12 million/year; mainly ^{99m}Tc , some with ^{201}Tl)
- bone scintigraphy, including tumor metastases (10 million/year; mainly ^{99m}Tc)
- lung investigation (5 million/year; mainly ^{99m}Tc)

- thyroid (5 million/year; ^{99m}Tc , or $^{123/131}\text{I}$)
- kidney function analysis (^{99m}Tc)
- tumor staging (PET, ^{18}F -FDG)

It is difficult to overevaluate the role on ^{99m}Tc in nuclear medicine as soon as it is used for over 80% of all procedures.

1.2 Standard ^{99m}Tc production method

1.2.1 $^{99}\text{Mo}/^{99m}\text{Tc}$ generator

^{99m}Tc is commonly available in a generator form. A $^{99}\text{Mo}/^{99m}\text{Tc}$ generator (see Figure 1.1) is a device used to recover and concentrate technetium from ^{99}Mo . A conventional generator consists of an alumina (Al_2O_3) column having about the size of a short length pencil, associated tubing, valves and filters for extracting technetium, and lead shielding for radiation protection.

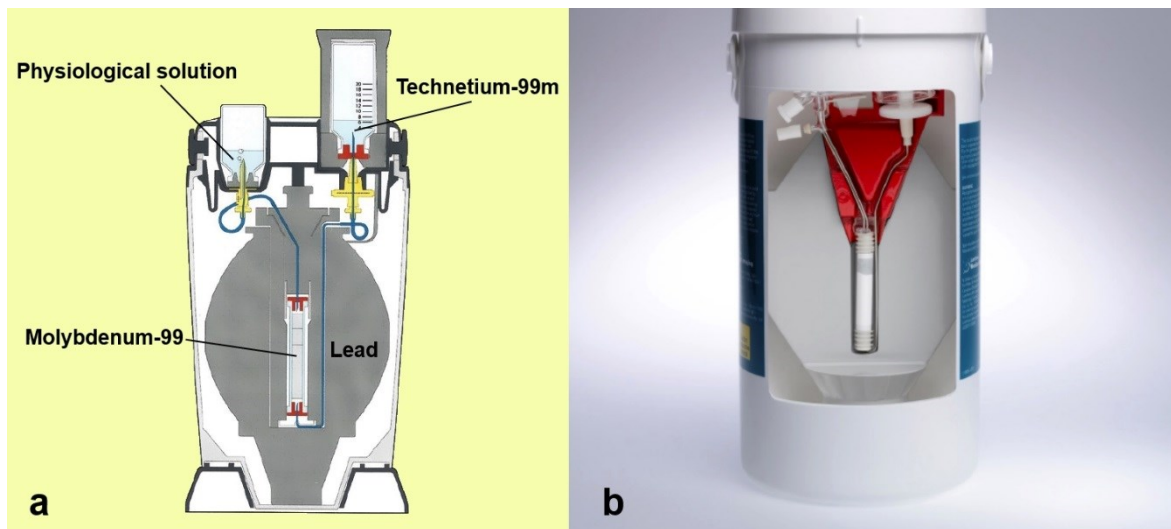


Figure 1.1: (a) Schematic representation and (b) cutaway view of commercial $^{99}\text{Mo}/^{99m}\text{Tc}$ generator

The column is loaded with ^{99}Mo at the generator manufacturing facility before being shipped to a hospital, radiopharmacy or clinic. The ^{99}Mo in the column decays to technetium with about a 66 hours half-life. About 88.6% of the ^{99}Mo decays to ^{99m}Tc ; the remainder decays to ^{99g}Tc (see Figure 1.2). Technetium is eluted (extracted) by passing a saline solution through the column.

^{99}Mo and $^{99\text{m}}\text{Tc}$ are in transient equilibrium because the half-life of ^{99}Mo is about 10 times longer than $^{99\text{m}}\text{Tc}$, therefore in the generator, after 24 h, the daughter activity basically achieves an equilibrium with the parent one. $^{99\text{m}}\text{Tc}$ can be eluted from the generator to obtain patient dose quantities as often as every 6 hours. The useful life of a generator is between three and five times the half-life of ^{99}Mo (i.e. 8–14 days).

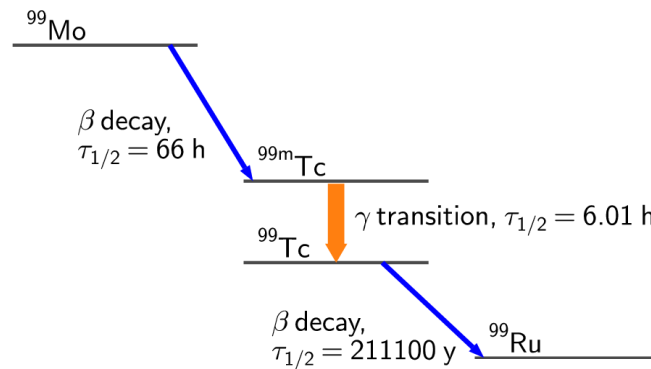


Figure 1.2: ^{99}Mo decay chain

Daily extraction of $^{99\text{m}}\text{Tc}$ under pertechnetate [$^{99\text{m}}\text{Tc}$] TcO_4^- chemical form from generators allows to use it directly or to label other molecules to obtain different radiopharmaceuticals. Indeed, $^{99\text{m}}\text{Tc}$ -pertechnetate is used for thyroid imaging, but most applications involve incorporating the $^{99\text{m}}\text{Tc}$ in selected carriers with commercially available kits to yield specific $^{99\text{m}}\text{Tc}$ radiopharmaceuticals suitable for SPECT imaging of major medical conditions, such as heart and lung function and cancer.

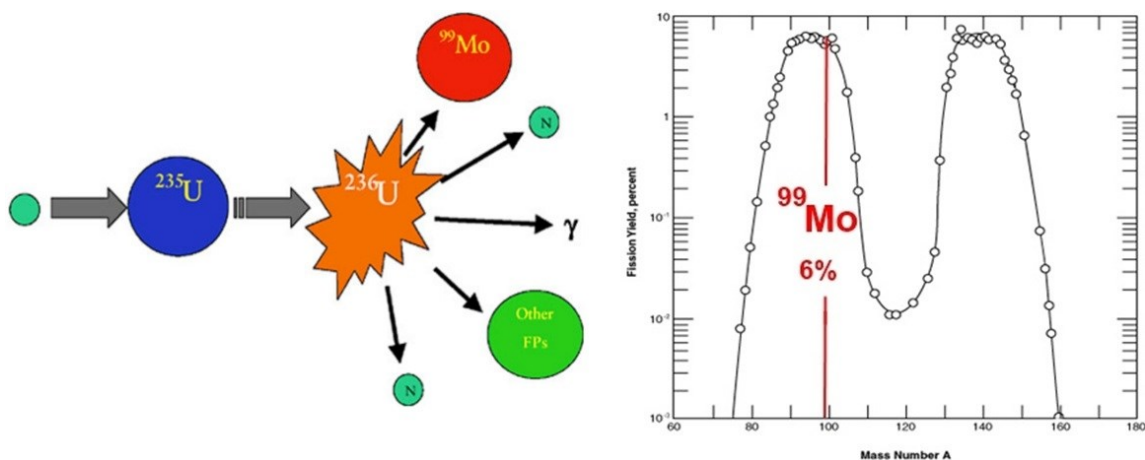


Figure 1.3: Production of ^{99}Mo from ^{235}U fission

1.2.2 Current supply issues of nuclear reactor-based ^{99}Mo precursor.

Nuclear fission is a process during which the nucleus of an atom is split into two or more fragments, fission products, and other particles as byproducts (Figure 1.3).

The enriched uranium is a mixture of uranium isotopes, which differs from natural uranium to a higher content of the ^{235}U isotope (concentration higher than 20%), obtained through the isotope separation process. In natural uranium the percentage of this isotope is, by weight, about 0.711%, while most of the material is composed almost entirely of ^{238}U .

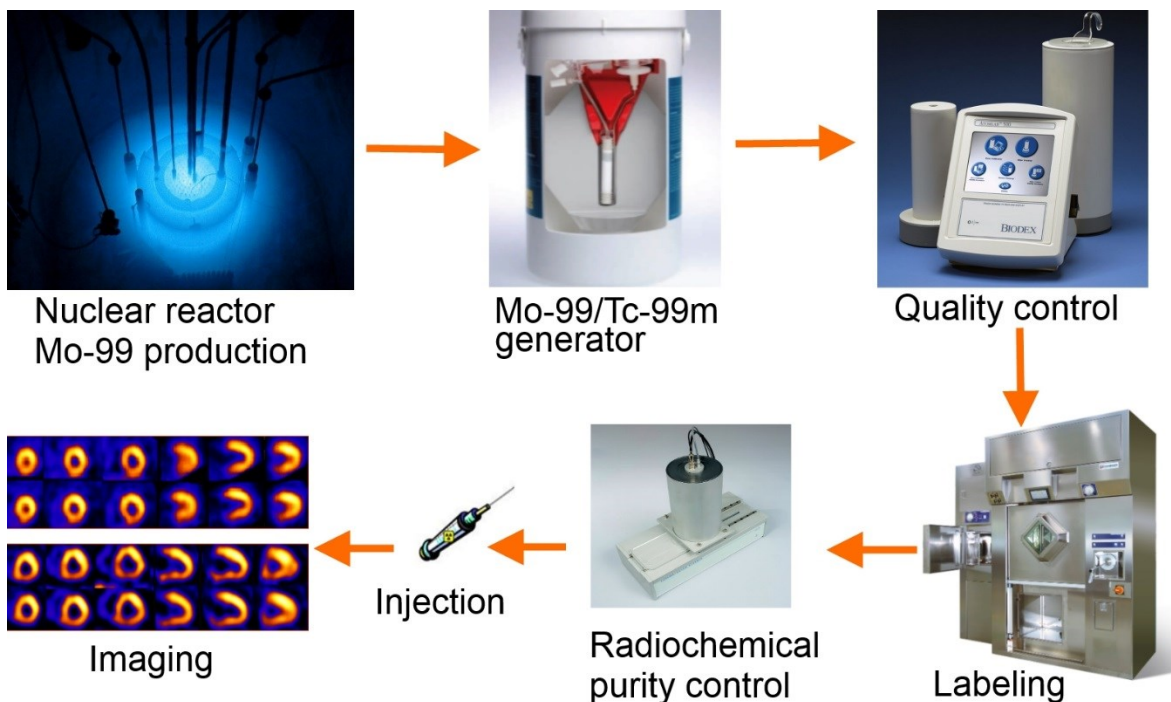


Figure 1.4: Classical $^{99\text{m}}\text{Tc}$ production chain

For many years, ^{99}Mo and its decay product $^{99\text{m}}\text{Tc}$ have been supplied to the medical community through irradiation of highly enriched uranium alloy targets in reactors and processing of the irradiated targets in dedicated processing facilities (Figure 1.3, Figure 1.4). This has been a mature and effective supply process, which has been capable of supplying the world market needs and coping with the growth in that market for more than 30 years. The reliability of the industry has allowed widespread use of $^{99\text{m}}\text{Tc}$ as a diagnostic imaging agent and around 30 million procedures performed each year. Demographic and medical trends suggest that, at least in the near future, global demand for $^{99\text{m}}\text{Tc}$ will grow at an average annual rate of 3–8% as these diagnostic imaging procedures expand to new markets, like Asia for example.

Up to now, the supply has relied mainly on reactors, which are over 40 years old, like the NRU in Chalk River, Ontario (Canada), and the HFR in Petten (The Netherlands). Planned and unplanned shutdowns of some of these reactors have resulted in several recent $^{99}\text{Mo}/^{99\text{m}}\text{Tc}$ supply shortages. These interruptions prompted international organizations and several government agencies to step up efforts to find out solutions to supply possible future shortages. In order to avoid future $^{99\text{m}}\text{Tc}$ crisis the alternative strategies for production of $^{99\text{m}}\text{Tc}$ both reactor-based and accelerator-based are intensively developed.

2 STATE OF ART

A global shortage of ^{99}Mo exposed vulnerabilities in the supply chain of medical radioisotopes, therefore, individual countries and companies have been exploring various options for a future supply of medical radioisotopes.

2.1 Reactor-based ^{99}Mo production

Nowadays, the main efforts by the international community are directed toward substituting Highly Enriched Uranium (HEU) targets with Low Enriched Uranium (LEU) ones, but the process of production of ^{99}Mo or $^{99\text{m}}\text{Tc}$ is becoming much more complicated from economic and technological point of view. The main methods for ^{99}Mo production with LEU reactors [1, 2] contain:

- **Fission production of ^{99}Mo from LEU.** The standard chemical processing is basically modified in order to separate ^{239}Pu , ^{240}Pu , ^{241}Pu , ^{242}Pu , impurities coming from ^{238}U . The OPAL (Open Pool Australian Lightwater) reactor at the Australian Nuclear Science and Technology Organization was built to operate with LEU targets. The other operators have all made commitments to convert over the next few years. However, in reality the process is not as fast as planned.
- **Neutron activation production of ^{99}Mo .** Production through neutron activation of ^{98}Mo -enriched targets, referred to as $(n,\gamma)^{99}\text{Mo}$ production. The approach provides low-specific-activity ^{99}Mo , with specific activity ranging from 7.4 to 130 GBq/g (0.2 to 3.5 Ci/g), from reactors that have thermal neutron flux values of $5 \cdot 10^{13}$ to $1 \cdot 10^{15}$ neutrons $\cdot \text{cm}^{-2} \cdot \text{s}^{-1}$ [2].
- **Power reactor production of ^{99}Mo .** The method considers neutron irradiation of ^{98}Mo -enriched MoO_3 in a power reactor pressure tube. ^{99}Mo produced in power reactors has a higher specific activity, than the one produced in research reactors, but much lower than fission-produced ^{99}Mo . The separation methods are not so user-friendly.

2.2 Production of ^{99m}Tc by cyclotron

Since after the State Referendums in 90th all nuclear plants on the territory of Italy were closed, the cyclotron-based approaches to solve problem of ^{99m}Tc crisis are in the focus in Italy. Indeed, cyclotron-based production of ^{99m}Tc starting from ^{100}Mo by $^{100}\text{Mo}(p,2n)^{99m}\text{Tc}$ reaction has been developed and evaluated at the Istituto Nazionale di Fisica Nucleare – Legnaro National Laboratory (LNL-INFN); however, a number of issues still must be resolved.

2.2.1 Cyclotron accelerator

The principle of acceleration used in all accelerators is the fact that a charged particle has its energy changed when exposed to an electric field. The idea behind Lawrence cyclotron is to bend the path of the particle in a linac (linear accelerator) into a circle and, therefore, to repeatedly use the same electrode system to accelerate the particles. The cyclotron utilizes this fact to produce particles of reasonably high energy in a relatively confined space.

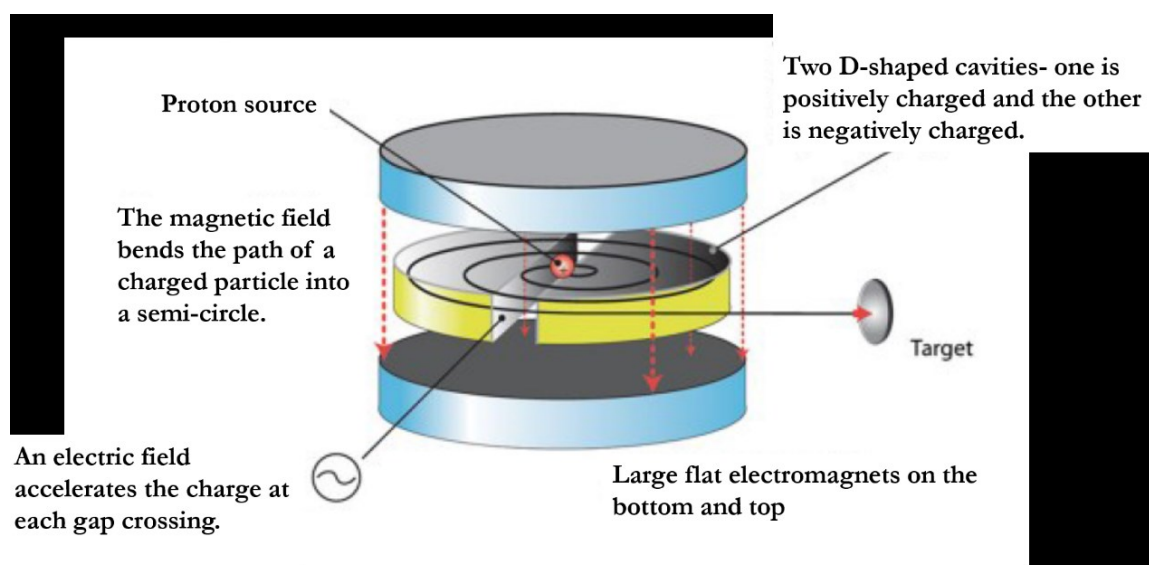


Figure 2.1: Operating principle of a cyclotron

The Figure 2.1 shows the operating principle of a cyclotron. The acceleration chamber of the cyclotron is placed between the poles of homogenous magnetic field. The cyclotron magnetic field causes particles to travel in circular orbits. Ions are produced by the ion source in the center of the machine and are accelerated out from the center by a high frequency electric field through two hollow electrodes, called “dees”. The particles are accelerated when they pass from one dee to the next through a gap between the dees. Since the rotational

frequency of the particles remains constant, as the energy of the particles increases, the diameter of the orbit increases until the particle can be extracted from the outer edge of the machine.

The main components of a cyclotron include:

- An ion source to produce particles to be accelerated
- A vacuum system both to increase the mean free path of the particle and provide an electrical insulation
- A radiofrequency system to accelerate the particle
- A magnet to keep the particles on a circular path
- One or more extractors to guide the ions towards the targets
- Some targets being the reaction sites
- Cooling system to remove heat

2.2.2 Cyclotron-based ^{99m}Tc production

Several accelerator-based reactions were investigated [2, 3] for the production of ^{99m}Tc , directly or indirectly, via production of ^{99}Mo :

2.2.2.1 Parent ^{99}Mo production

- $^{100}\text{Mo}(\text{p},\text{pn})^{99}\text{Mo}$: The process resulted sufficient ^{99}Mo yields [3, 4]. The main drawback is however the final chemical form: ^{99}Mo cannot indeed be separated from the bulk ^{100}Mo target material, thus leading to a much lower specific activity radionuclide than the standard (obtained by ^{235}U -based nuclear reactors) one.
- $^{100}\text{Mo}(\gamma,\text{n})^{99}\text{Mo}$: The photons are produced by an electron accelerator that accelerates a high intensity electron beam of around 35–50 MeV which then bombards a high “Z” material such as tungsten, called a converter. Deceleration within the converter produces a beam of photons called bremsstrahlung radiation. The resulting ^{99}Mo specific activity following such production route is very low, because the target and product are of the same element and will not be acceptable for $^{99}\text{Mo}/^{99m}\text{Tc}$ generator for this reason[2, 5].
- $^{98}\text{Mo}(\text{n},\gamma)^{99}\text{Mo}$: Neutrons are produced using either the spallation reactions on heavy target systems or the relatively low energy beams driven by high intensity accelerators on light targets. The radiative capture reaction (n,γ) on ^{98}Mo -enriched targets can provide ^{99}Mo production with a good purity level. But the resulting ^{99}Mo

specific activities, both at saturation and after the first 24 hours irradiation, are too low to consider a massive production using such a system [6, 7].

- $^{100}\text{Mo}(n,2n)^{99}\text{Mo}$: High-energy neutrons for this reaction are provided by energetic deuterons (SPIRAL2) bombarding a $^{\text{nat}}\text{C}$ foil target [8]. The method allows multiple target irradiation, when each target has 4 cm thickness. This method has a sense for irradiation of big quantities of precursor.

2.2.2.2 Direct $^{99\text{m}}\text{Tc}$ production

- $^{98}\text{Mo}(d,n)^{99\text{m}}\text{Tc}$: The production considers 10-20MeV deuteron bombardment of ^{98}Mo target [9]. This reaction is currently not competitive in respect to other routes mainly because of low deuteron beam current accelerators.
- $^{98}\text{Mo}(p,\gamma)^{99\text{m}}\text{Tc}$: As soon as the cross-section of the reaction is very low, it provides a low contribution to the $^{99\text{m}}\text{Tc}$ direct production compared with the other direct reaction channels.
- $^{100}\text{Mo}(p,2n)^{99\text{m}}\text{Tc}$: The most promising accelerator-based route for direct $^{99\text{m}}\text{Tc}$ is directly production [3, 5, 10]. The method is useful only for a local production because $^{99\text{m}}\text{Tc}$ is a short-lived radioisotope.

2.3 Preliminary study of $^{99}\text{Mo}/^{99\text{m}}\text{Tc}$ production at LNL INFN

The Legnaro National Laboratories of the Istituto Nazionale di Fisica Nucleare – is among the research groups involved in the research efforts aimed at the alternative and more flexible $^{99\text{m}}\text{Tc}$ production routes, based upon the use of accelerators.

Indeed, two main alternative routes have indeed been investigated [3], based upon:

- ^{99}Mo production by accelerator-driven neutron sources;
- $^{99}\text{Mo}/^{99\text{m}}\text{Tc}$ accelerator-driven direct production.

The overview about the main nuclear reaction routes investigated was already given in Chapter 2.2.2. The reactions based on neutron beams can provide higher ^{99}Mo purity, with negligible contamination of other nuclides. However, in the case of the $^{98}\text{Mo}(n,\gamma)^{99}\text{Mo}$ reaction, the production yield is too low even in optimal conditions (if 90% of the neutron flux is slowed down to the ^{98}Mo resonance energy interval 1-100 eV). Due to the fact that precursor and product are the same element, the specific activity of the final product is low (the specific activity of around 5.4mCi/g and 7.5mCi/g could be achieved at saturation conditions (19.25 days) by neutron facility driven by 100 μA proton accelerator beam at 40

MeV and 70MeV correspondingly starting from fully enriched ^{98}Mo [11]. For comparison, irradiation under high flux of neutrons from nuclear reactor under secular equilibrium conditions provides specific activities of order of 1-2Ci/g. This makes the neutron-based accelerator route not competitive and not applicable for a massive production.

That is why only the proton-induced reactions on ^{100}Mo were taken into account and particular attention was paid to the evaluation of contaminant isotopes:

- $^{100}\text{Mo}(p,pn)^{99}\text{Mo}$
- $^{100}\text{Mo}(p,2n)^{99m}\text{Tc}$

2.3.1 $^{100}\text{Mo}(p,pn)^{99}\text{Mo}$

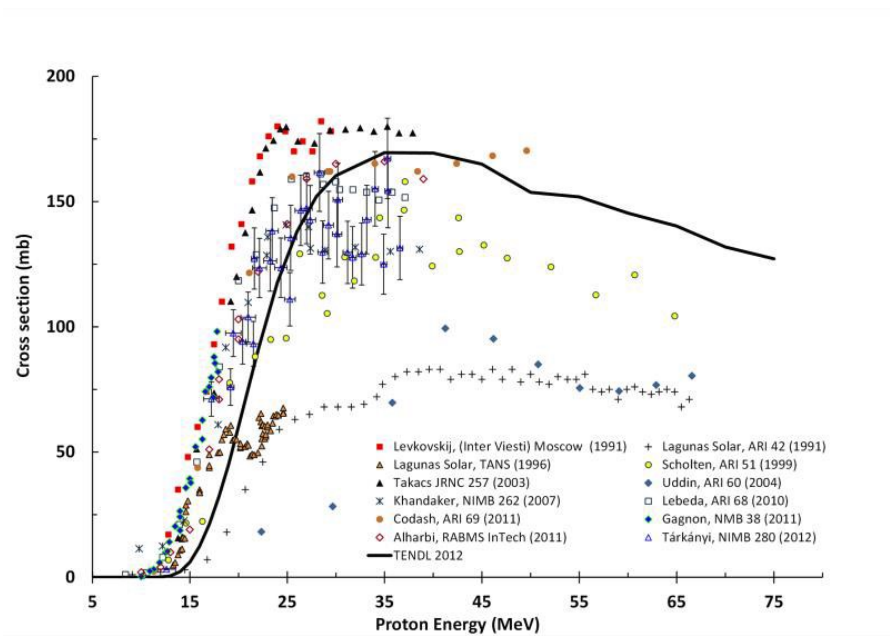
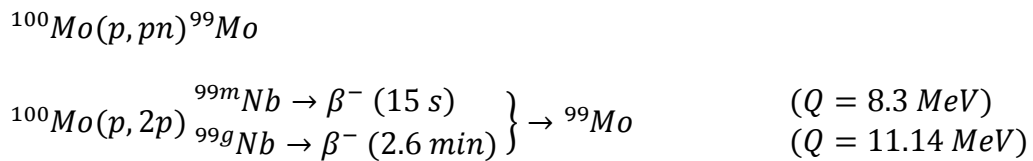


Figure 2.2: Experimental data on excitation function for $^{100}\text{Mo}(p,pn)^{99}\text{Mo}$

^{99}Mo production, by means of proton beam hitting ^{100}Mo -enriched thick targets, occurs through two reaction channels:



The Figure 2.2 shows the $^{100}\text{Mo}(p,pn)^{99}\text{Mo}$ experimental excitation functions measured in the last two decades. The results are consistent up to 25MeV, while at higher proton energies an uncertainty band up to 100 mb appears.

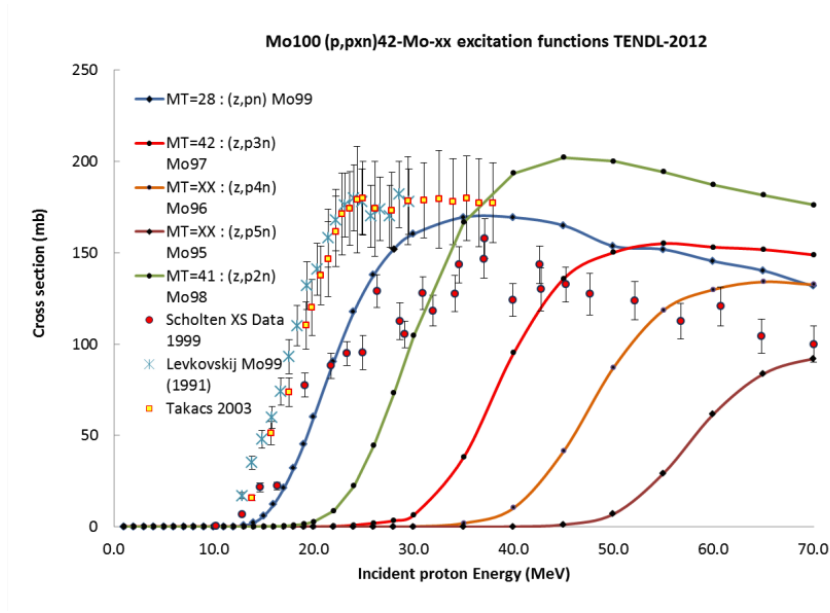


Figure 2.3: $^{100}\text{Mo}(p,pxn)^{9x}\text{Mo}$ theoretical excitation functions and experimental measurements.

Even considering 100% of ^{100}Mo -enriched samples, additional reaction routes for the production of different Tc, Mo, and Nb isotopes are anyway opened starting from proton energies of 10–15 MeV. The Figures 2.3 and 2.4 show the theoretical excitation functions with some experimental cross-section measurements performed of such reaction routes up to the (p,p5n) and (p,2p4n) levels.

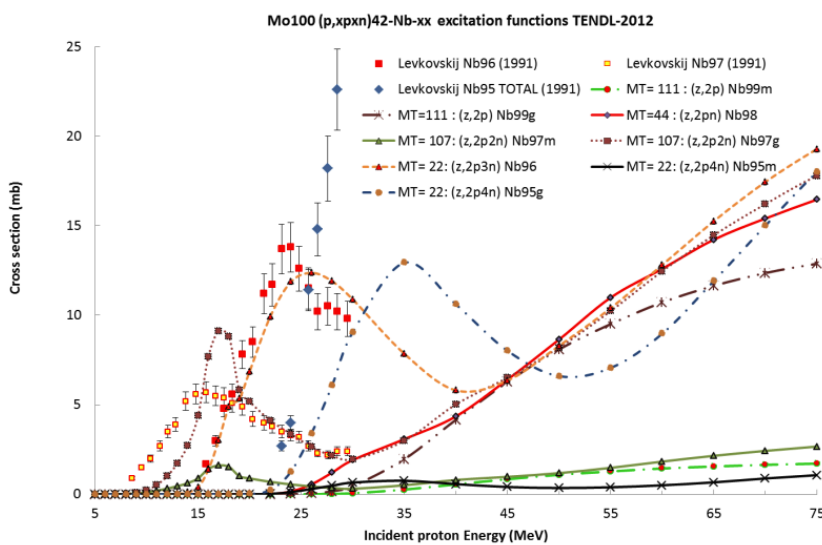


Figure 2.4: $^{100}\text{Mo}(p,2pxn)^{9x}\text{Nb}$ theoretical excitation functions and experimental measurements.

Table 2.1 Isotopic purity of ^{100}Mo -enriched (99.05% level) from ISOFLEX Isotopes

<i>Mo isotope</i>	^{100}Mo	^{98}Mo	^{97}Mo	^{96}Mo	^{95}Mo	^{94}Mo	^{92}Mo
Abundance, %	99.05	0.54	0.07	0.11	0.10	0.05	0.08

The final product can contain either contaminants coming from the target itself related to abundance level lower than 100% (see Table 2.1), or ^{9x}Tc radionuclidic contaminants coming to the product, due to alternative reaction routes[3] (see Table 2.3).

Table 2.2 Efficient ^{100}Mo target thickness for ^{99}Mo production

<i>Proton energy</i>	<i>15MeV</i>	<i>20MeV</i>	<i>25MeV</i>	<i>40MeV</i>	<i>70MeV</i>
Optimized target thickness, mm	0.14	0.46	0.66	1.825	5.93
Max. useful target thickness, mm	0.33	0.63	1.00	2.47	6.74

The specific activities expected are order of tenths lower than the ones provided by the current Mo/Tc generators ($\sim 10^4$ Ci/g). Indeed the highest in-target specific activity for the ^{99}Mo accelerator-based production is estimated to be about 386 mCi/g (for optimized thickness of 1.82mm), corresponding to 24h irradiation at 40 MeV, 500 μA proton beam[3].

Table 2.3 Nb and Tc isotopes expected to be produced by $^{100}\text{Mo}(\text{p},\text{x})$ reactions

Reaction	Product	Decay	$t_{1/2}$	Daughter
p, α 2n	^{95}Nb	β^-	34.99 d	^{95}Mo (stable)
p, α n	^{96}Nb	β^-	23.35 h	^{96}Mo (stable)
p, α	^{97}Nb	β^-	72.1 m	^{97}Mo (stable)
p,2pn	^{98}Nb	β^-	2.9 s	^{98}Mo (stable)
p,2p	^{99}Nb	β^-	15 s	^{99}Mo
	^{99m}Nb	β^-	2.6 m	^{99}Mo (96.2%) ^{99g}Nb (3.8%)
p,6n	^{95m}Tc	IT	61 d	^{95}Mo (96.1%) (stable)
		IT		^{95g}Tc (3.9%)
p,5n	^{95g}Tc	EC	20 h	^{95}Mo (stable)
		EC		^{96}Mo (2.0%) (stable)
p,5n	^{96m}Tc	IT	51.5 m	^{96g}Tc (98.0%)
		EC		^{96}Mo (stable)
p,4n	^{97g}Tc	EC	$4.2 \cdot 10^6$ y	^{97}Mo (stable)
		IT		^{97m}Tc
p,4n	^{97m}Tc	IT	91 d	^{97g}Tc (96.1%)
		EC		^{97}Mo (3.9%) (stable)
p,3n	^{98}Tc	β^-	$4.2 \cdot 10^6$ y	^{98}Ru (stable)
p,2n	^{99m}Tc	IT	6.01 h	^{99g}Tc (99.9963%)
		β^-		^{99}Ru (0.0037%) (stable)
p,2n	^{99g}Tc	β^-	$2.1 \cdot 10^5$ y	^{99}Ru (stable)
		β^-		^{100}Ru (99.9982%) (stable)
p,n	^{100}Tc	β^-	15.46 s	^{100}Ru (99.9982%) (stable)
		EC		^{100}Mo (0.0018%) (stable)

The integral yields, using 40 MeV, 500 μ A proton beams, was estimated to be about 65 mCi/ μ Ah during the initial irradiation stages (24 h). The estimated integral yield extrapolated in nearly saturated condition was reported to be about 290 mCi/ μ A[3].

The optimal target configuration depends on the beam energy (see Table 2.2).

2.3.2 $^{100}\text{Mo}(p,2n)^{99\text{m}}\text{Tc}$

Feasibility of cyclotron production of $^{99\text{m}}\text{Tc}$ via the $^{100}\text{Mo}(p,2n)^{99\text{m}}\text{Tc}$ reaction was demonstrated in the early seventies [12]. The excitation function, shown in the Figure 2.5, has been repeatedly measured over the past 20 years by different groups. In a wide energy range, from 5 up to 70 MeV, there is a single peak, centered around 15 MeV. The peak value, measured was estimated as 200 mb – 300 mb, and the lower value is considered more correct. At proton energies higher than 30MeV the cross section quickly drops down to about 15-20 mb.

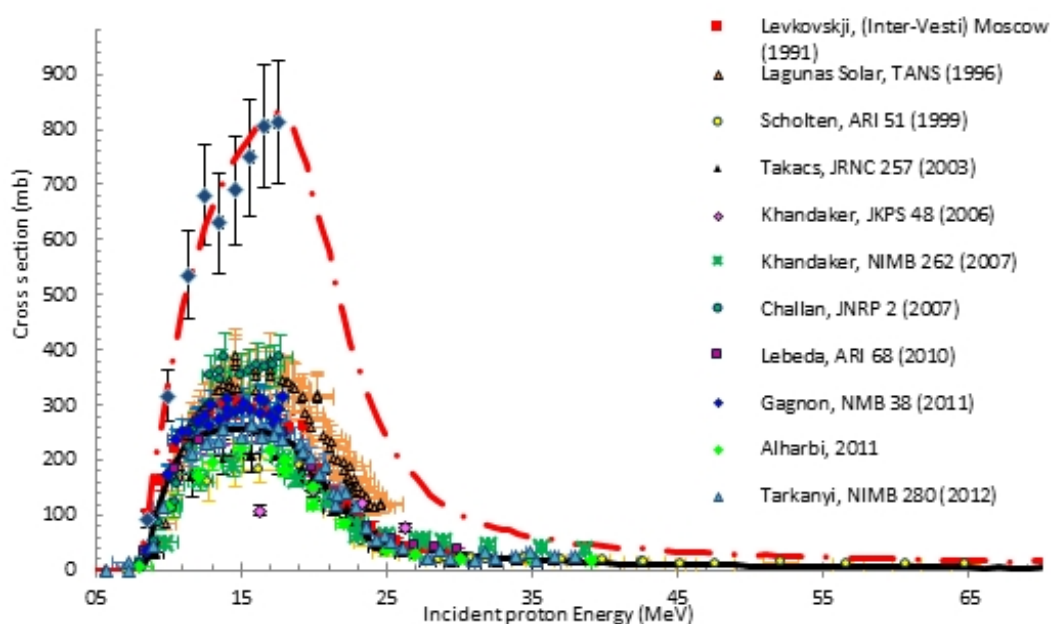


Figure 2.5: Experimental data on excitation function for $^{100}\text{Mo}(p,2n)^{99\text{m}}\text{Tc}$

In the case of the direct $^{99\text{m}}\text{Tc}$ production, particular attention should be paid to the radiochemical extraction and purification and to the optimal irradiation conditions in order to reduce the in-target production of other $^{9\text{x}}\text{Tc}$ contaminant isotopes, which cannot be separated from $^{99\text{m}}\text{Tc}$ by using chemical procedures.

Radionuclide contaminants with long half-lives such as ^{99g}Tc , ^{98}Tc and ^{97g}Tc can have a direct impact on the activity of the final product specification. Other isotopes with short half-life such as ^{100}Tc may affect the isotopic purity (IP) and the radionuclide (RNP) purity of the final product.

From the Figure 2.6 can be noticed that at energies lower than 25MeV only ^{98}Tc , ^{99g}Tc , and ^{97g}Tc will be produced by bombardment of ^{100}Mo -fully enriched targets. This allowed to estimate the optimal irradiation conditions for the direct production of ^{99m}Tc as a short irradiation times (to avoid decay of ^{99m}Tc) with <25 MeV proton energy beam.

$^{100}\text{Mo}(p,2n)^{99m}\text{Tc}$ reaction offers potential opportunities to get interesting amounts of ^{99m}Tc using high current (500 μA) cyclotrons with output energies about 20-25 MeV. In particular it was shown that, if the irradiation times do not exceed the 3 hours with 15 and 20MeV and 500 μA proton beam the IP and RNP, some hours after the end of bombardment (EOB), are close to those relative to product by ^{99m}Tc generator. The specific activity in EOB, using described conditions, is similar to that derivable from generator i.e. of about 10^6 Ci/g [3]. The integral yield after 3h proton bombardment with 500 μA , 20MeV is of about 28mCi/ μAh starting from ^{100}Mo .

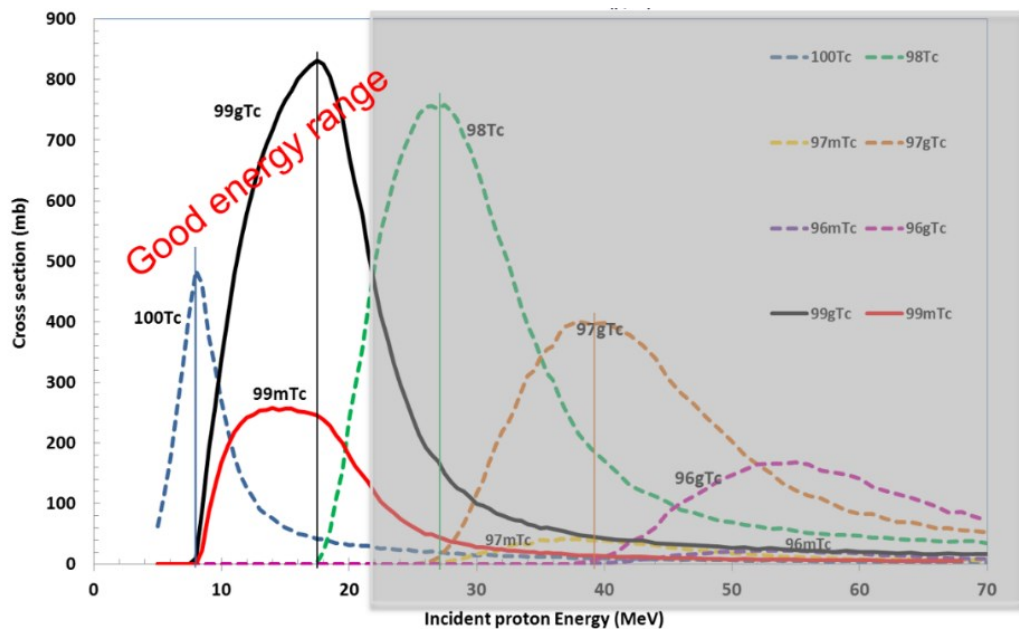


Figure 2.6: Theoretical excitation function for $^{100}\text{Mo}(p,xn)^x\text{Tc}$

The amount of ^{99g}Tc (pure β -emitter) produced by the same $^{100}\text{Mo}(p,2n)$ reaction is expected to be in excess of a factor 3 than ^{99m}Tc according to the only theoretical excitation function, as can be observed from the Figure 2.6.

The nuclides ratio $R = N^{99gTc}/N^{99mTc} > 4$ is reducing the effectiveness of Tc-based scans. Therefore, ^{100}Mo samples need to be irradiated for short times, i.e. no longer than half-life ($T_{\text{irr}} \leq 6 \text{ h}$) so that the N^{99gTc}/N^{99mTc} ratio in the final product may be considered still acceptable, compared to product provided by the current Mo/Tc generators.

2.4 Techniques for ^{100}Mo cyclotron target preparation

The $^{100}\text{Mo}(p,2n)^{99m}\text{Tc}$ reaction is considered one of the most perspective routes of direct ^{99m}Tc production through cyclotron accelerators. The preferred proton energy window for the reaction providing maximum production with minimum impurities is 10-22MeV. The effective thickness of the enriched ^{100}Mo target material is of a range of hundreds of microns. Target systems for a number of different cyclotrons have been developed and tested. Irradiation tests of enriched and natural Mo-metallic, oxide and carbide on different backing materials were realized [5, 10].

There are two critical requirements for the target to be applied for radiopharmaceutical production: the high level of heat dissipation, to apply maximum cyclotron current to reach maximum production yield; and the inertness of the baseplate in the target dissolution conditions to provide chemical and radiochemical purity of the product.

Although oxide [5, 10, 13-15] carbide [5, 10] and even solution [5, 10] targets were studied, still metallic Mo solid targets are considered the most perspective, as soon as only metallic Mo targets are able to provide high production yield of ^{99m}Tc . This is due to high level of heat dissipation associated with good thermal conductivity of metal. Even traces of oxygen are drastically reducing the thermal conductivity of target material.

Both approaches: preliminary Mo pellet preparation followed by subsequent bonding to backing plate and direct deposition of Mo onto backing, are used.

^{100}Mo is commercially available in a form of metallic powders, so transformation of refractory metal powders into dense and not porous pellet or foil is proposed by different research groups by different methods, including pressing, sintering and rolling.

The targets produced by only hydraulic pressing of powders [5, 10, 16-18] can sustain only to low cyclotron currents, as soon as the target density is much lower than of bulk material. The sintering of Mo powder [10, 19, 20] in reducing or inert atmosphere [5, 10, 16-18] followed by press bonding [5, 10, 16-18] or vacuum brazing [10, 19, 20] was used to construct the Mo targets sustaining currents of the order of hundred μA .

For the cross-section measurements press rolling from powders or from Mo beads produced by e-beam powder melting [5, 10, 21] or also re-melting of Mo powders followed by press-roller reshaping is considered standard procedure. Unfortunately, for production this approach did not give a success since it is very difficult to provide a good thermal contact between foils, foils and backing during irradiation.

Direct deposition of Mo target material onto backing plate can eliminate the 2nd step of bonding of the pellet to backing plate. The easiest approach, direct melting of Mo powders onto backing plate [22] is not able to provide uniformity of Mo layer.

Electroplating of metals from aqueous solutions is a well-known industrial process. However, refractory metals, as Mo, are not deposited easily by standard electrodeposition methods because of their high affinity to oxygen. However, electroplating from particular alkaline [23] or acetate [24] solutions was described. It is worth to mention that such deposits showed thickness not exceeding 20 μ m and high level of oxidation. Besides that, the process of electrodeposition from aqueous solution is very inefficient (<2%). The Co-deposition of molybdenum with zinc [25] was reported to be much more efficient. The electrodeposition from ionic liquids or molten salts [10, 26, 27] is providing better Mo layer quality, but require expensive equipment and more difficult protocol. Electrophoretic deposition from mixture of Mo powders and molybdate with additives, followed by subsequent sintering at high temperature was reported to provide efficient Mo thickness and resistance to 300 μ A [28] [5]. Following improvement of the process by sintering in inert atmosphere [10] provided targets resistant to 500 μ A. The main disadvantage of all electrochemical deposition methods is the impossibility to avoid the impurities coming from electrolyte bath.

The described in literature PVD direct Mo deposition methods include thermal spray[29], cathodic arc [10], argon [30] and xenon [31] FIB sputtering. No information of the tests under the cyclotron beam is available for arc-and FIB-sputtered Mo targets. Even if no thickness of FIB-sputtered Mo coatings higher than micron was reported, the method still seems very interesting, because it allows extremely low target material amounts, very low losses of expensive enriched material during deposition and high purity of target material. Our group has proposed instead the magnetron sputtering as a method for direct Mo deposition [5].

There is a number of materials used as a backing plate for ^{99m}Tc production target. Among them the most popular are copper [5] [10, 29, 32], aluminum [5, 10, 16-18, 21], tantalum [5, 10, 16-18, 22, 28] GLIDCOP[10, 19, 20], platinum [5, 10, 23].

Table 2.4 State of art: cyclotron targets for production of ^{99m}Tc (preparation and irradiation).

Country	Institution	Cyclotron type	Target-holder system	Irradiation conditions	Target material
Saudi Arabia	King Faisal Specialist Hospital and Research Center (KFSH&RC)	CS-30 Cyclotron, external beam, 15-23 MeV	Cooled by both water and helium channels, the beam perpendicular to target. Size = GE PETtrace	1 μ A 10 min in 2013; 15 μ A already burnt	^{nat} Mo, oxide, ¹⁰⁰ Mo
Canada	University of Alberta	TR24 ACSI 500uA, 24MeV, external beam line	-	-	Mo metallic
		TR19, external beam line	Rectangular inclined	100 μ A	Mo metallic
		TR24 ACSI 500uA, 24MeV, external beam line	TR24 standard, rectangular inclined	150 μ A-500 μ A	Mo metallic
		TR19, external beam line	Rectangular inclined	20-30 μ A	Mo metallic
		TR19/9 ACSI, external beam line	30° to beam	15.5/18MeV up to 95 μ A max 71 μ A average on target 360 min	Mo metallic
	TRIUMF	ACSI TR19	Patented ACSI TR19 target station: both inclined to beam with micro channels and perpendicular to beam	80-300 μ A 16-30MeV 0.5-8h; 10.8kW, 0.6kW/cm ² , 300 μ A 18MeV elliptical beam spot 10x20 mm 10 degrees to beam. (<500° C on plate)	Mo metallic oxidation-reduction-Mo metallic refined
		ACSI TR24/TR30	TR30 target	24MeV. 500 μ A, 2.1kW, 1.2kW/cm ²	Mo metallic
		GE PETTRACE	GE PETTRACE	16.5MeV 130 μ A, 5.6 kW, 0.3kW/cm ²	¹⁰⁰ Mo metallic powders
				-	-
	Advanced Cyclotron System Inc.	TR-19 ACSI	Inclined	15-52 μ A 1,5-3h 15,5-17MeV	¹⁰⁰ Mo powders
	Isopor-Isotopos Para Diagnostico E Terapeutica S.A.	Low energy cyclotron	-	-	¹⁰⁰ Mo metallic or oxide

Backing material	Process of deposition	Problems	Sources	Reference
Cu, Al	Hydraulically pressing ^{nat} Mo, ¹⁰⁰ Mo oxides powder into the circular cavity target plates, heating (450 - 400 °C)	Only low current test is ok. ^{nat} Mo burns.	Report IAEA 2013, 2015	[5, 10]
Ta, W, glassy carbon, quartz, Al ₂ O ₃	1600°C sintering in reducing atmosphere, 600°C press bonding to backing	Not tested	Report IAEA 2013	[5]
Al ₂ O ₃	1600°C sintering in reducing atmosphere, 600°C press bonding to backing	No information about tests	Report IAEA 2015	[10]
Al	Foils made of powders rolled, annealed, hot pressed to backing	Backing is not inert as claimed	Report IAEA 2015	[10]
Al	Hydraulically pressed to backing	Backing is not inert as claimed	Paper 2012 Gagnon et all	[16]
Al, Ag, Pt, Au, Ta, Ti, V, Ni, Zn, Zr, Nb, Ru, Rh, Pd, Ir	Foils, pressing to backing, melting on Ta backing, 1600°C sintering in reducing atmosphere, 400-500°C press bonding to backing of Ta, Cu, preliminary oxidized Al in H ₂ O ₂ and HNO ₃	Backing is not inert as claimed. But no clear data on Al pre-oxidized	Patent WO2012139220 A1 Gagnon 2012 = Patent US 2014/0029710 A1 Wilson 2014	[16-18]
Ta, other transition metals are described, but not claimed	Electrophoretic deposition from mixture of refined Mo powders 10µm + molybdate+binder onto Ta backing, sintering 1200-1900°C 38h in inert atmosphere	85% density, also Ta backing is not inert as claimed	Patent US 2013/0301769 A1 Schaffer 2013, IAEA 2015, IAEA 2013	[5, 10, 28]
Ta		Ta backing is not inert as claimed	IAEA 2015	[10]
GLIDCOP 30mm D 1.3 mm thick, brazed to 20mm 0.7 mm thick Mo	Mo sintered at 1300-2100°C disc 18.5-19.5 mm diameter 0.6 mm thick, placed in GLIDCOP baseplate and brazed in vacuum, H ₂ /Ar at 500-1000°C by Ag-Cu-P	No chemical inertness	Patent WO2015161385 A1 Zeisler 2015 = paper Schaffer, report IAEA 2015	[10] [19, 20]
-	Electrochemical deposition up to 20µm Mo from aqueous solution 10M acetate	Deposition very inefficient <2 %	Morley... 2015 Electrochemistry communications	[24]
Ta	Direct melting onto backing	No data on thickness and resistance of Mo. Non uniform thickness.	WTTC 2012 abstract of the conference talk Zyuzin	[22]
	3 layer sandwich: substrate 40-1500µm/ ¹⁰⁰ Mo layer 25-500µm/ 2nd hard core layer(Al, Ag, Cu) 25-500µm/1st hard core layer (Nb, Pt, Ta, Ag, Havar)	Strange and not clear target concept	Patent WO 2011002323 A2 2010 R.R. Johnson	[33]

Country	Institution	Cyclotron type	Target-holder system	Irradiation conditions	Target material
Japan	Fukui Medical University, Matsuoka, Fukui, Japan	-	Vertical beam	-	-
	Japan Atomic Energy Agency, Ibaraki	Nuclear reactor	-	-	MoO ₃ pellet for radioactive Mo solution by (n,gamma) reaction + dissolution in ultrasonic, 6M NaOH
	MIC NIRS	-	Horizontal beam	-	3-5 mm layered MoO ₃ (¹⁰⁰ Mo oxide)
		-	Vertical beam	-	Powder ¹⁰⁰ Mo as purchased, without solidification
Armenia		Cyclotron C18	NITRA commercial solid target system	-	Pellet from powder (Mo, MoO ₃) + silver powder compound
	A. I Alikhanyan National Science Laboratory	Cyclotron C18	Target is fixed by pneumatic clamps; (work in progress--> cryogenic cooling to use 100 µA)	18 MeV; proton current 30 µA	Tablet of ^{nat} Mo
India	Variable Energy Cyclotron Centre (VECC), Kolkata	Low power cyclotron	Circular target	8-18MeV 10-50nA 5 min	^{nat} Mo foils 25µm
				1-6h 1-3uA 8-18MeV	^{nat} Mo powders
Italy	JRC-Ispra	Scanditronix MC40 K=38	Al cylindrical screw-type target station devoted to stack foil irradiation	100nA 1h 8-21MeV	¹⁰⁰ Mo powders in foils
	LNL INFN	GE PETTRACE	First prototype of TEMA solid target	70µA, 16MeV, 30 min	^{nat} Mo bulk
Iran	RRDL, NSTRI, ...	Cyclone-30	Inclined target	160µA 25MeV 1000µA-h	^{nat} Mo
Poland	RC POLATOM	GE PETtrace 870	2.5/5.7 µA for ¹⁰⁰ Mo target	-	^{nat} Mo
					^{nat} Mo powders
	-	-	-	-	-

Backing material	Process of deposition	Problems	Sources	Reference
Target vessel for in situ preparation (Alumina)	-	The production of ^{89}Zr by $^{89}\text{Y}(p,n)$ was investigated; not tested for Tc	Report IAEA 2013	[5]
Irradiation container	Plasma sintering method + Oxidation process	Low thermal conductivity material	Patent US 2013/0136221 A1, Nishikata	[13]
Target vessel for irradiation and dissolution	Preparation of 3-5 mm thick ^{100}Mo oxide layer: $^{100}\text{Mo} + \text{H}_2\text{O}_2 + \text{N}_2$ flow in a target vessel	Enriched powder; lower ^{99m}Tc yield/higher contaminants	Japan presentation, IAEA 2015	[10]
SiC target vessel	-	-		[10]
-	-	Under investigation	IAEA 2013, A.E. Avetisyan, paper 2015 Avertisyan Int. J. Eng. Sci.	[5, 14]
Solid state target disk: Nb or Ti	Compression method + tablet surface burning method using focused laser beam to increase mechanical strength + additional treatment to provide adhesion with the backing	No irradiation test	IAEA 2015	[10]
Cu spacers	Stack of 4-7 25 μm foils with Cu foil monitor	Very low currents	IAEA 2013, IAEA 2015	[5, 10]
-	980MPa pressed powders	Very low currents	IAEA 2013, IAEA 2015	[5, 10]
Al degraders, target holder of Al	Stacked foils technique alternating Al and enriched Mo and Ti foils. Mo foils prepared by electron-beam melting in nitrogen, slow cooling, lamination with pack-rolling technique	Low currents	Manenti... 2014 Appl radiat. Isotopes. IAEA 2013 Salvini	[5, 21]
Cu	Magnetron sputtering of ^{nat}Mo	For the moment work only with ^{nat}Mo	IAEA 2013	[5]
Cu	Thermal spray 130 μm Mo	Not inert backing	DARU 2011 Jililian	[29]
Pt	Electrodeposition from aqueous solutions	Only oxide is deposited	IAEA 2013	[5]
-	Pressing, sintering pellet, preliminary H_2 treatment 166°C. 50-78 percent density After H_2 treatment was improved	A lot of oxide-low thermal conductivity	IAEA 2013, IAEA 2015	[5, 10]
-	Electrodeposition from molten salts $\text{LiCl-NaCl-KCl-MoCl}_3$ 600°C on Ni plate in argon gave low oxidation	No data on thickness and quality	IAEA 2015	[10]

Development of novel cyclotron target for Tc-99m production

Country	Institution	Cyclotron type	Target-holder system	Irradiation conditions	Target material
Poland	RC POLATOM	-	-	-	-
	Institute of metallurgy and Mat. Sci.	-	-	-	Mo-Zn alloy
USA		-	-	-	-
	Washington University	CS-15	-	10-15 MeV 3,4,5μA	¹⁰⁰ Mo ₂ C
	Massachusetts Institute of Technology	-	-	-	-
Syria	-	-	Inclined elliptical IBA blank copper target	-	MoO ₂
				-	natMoO ₃ oxide
				100μA 3h	natMo powders
-	Mallinckrodt Lic	-	-	-	¹⁰⁰ Mo metallic, MoO ₃ or their combination
Germany	GSI	-	-	-	¹⁰⁰ Mo, ⁹² Mo, ⁹⁸ Mo
	Sektion Physik Universitat Munchen	-	-	-	¹⁰⁰ Mo, ⁹⁸ Mo
UK	Daresbury Laboratory	-	-	-	¹⁰⁰ Mo
Romania	Institute of physical chemistry	-	-	-	0.01mm quite dense, adherent.

Backing material	Process of deposition	Problems	Sources	Reference
-	Mechanical reshaping: melting, remelting, rolling, annealing in vacuum. Different thickness 0.25-600 μ m. H ₂ treatment before remelting. Heating in an envelope of stainless still	Lamination technological difficulties	Stolarz 2015 J Raioanal. Nucl. Chem.	[34]
-	Mo-Zn alloys co-electrodeposited from citrate solutions	not pure Mo	Kazimerczak 2013 ELECTROCHIMI CA Acta	[25]
Pt	Electroplating from alkaline solutions	Mixture of oxide and metal. Not pure metal	US Patent 1,885,700 1932 Fink	[23]
Pt	¹⁰⁰ Mo ₂ C synthesized from ¹⁰⁰ MoO ₃ using 3 steps thermal carburization method; pressed on Pt target holder (5000 psi for 30 sec)	Low beam current and irradiation time	IAEA 2013, IAEA 2015	[5, 10]
-	Electrodeposition: Pre-electrolysis + Electrodeposition of Mo. K ₃ MoCl ₆ (source of soluble Mo) and KCl (principal constituent of the supporting electrolyte) -> thickness 0.5 mm, columnar structure, but presence of protrusion on the surface.	Technique appears to be no limitation on the thickness of the deposited metal, but the process is complicated and contaminants are present.	Georges J. Kipouros et al., 1988	[26]
Cu	Electroplating from aqueous solution.	Very thin layer, poor adherence, oxidation	IAEA 2013, IAEA 2015	[5, 10]
Cu	Pressing, sintering 750°C 50 μ m MoO ₃	Not inert backing	IAEA 2013	[5]
Cu	Pressing Mo powders	Not inert backing	IAEA 2015	[10]
-	Target obtained from commercial supplier(probably material)	No data on irradiation	Patent WO 20141384 A1 Barbosa 2014	[15]
C or Cu	FIB sputtering with Ar+ Sletten-Type apparatus. 0.1/0.14 μ m films also self-sustaining	small thickness reported	Folger 1982 Conf. contribution	[30]
Cu backing or self-sustaining	High vacuum sputter deposition with 10keV Xe+ gun. 100-400nm thick films/foils	100-400nm thick films/foils	Maier 1993 Nucl. Instr. and meth	[32]
-	Rolling from powders. Thickness is about 0.5 and 10 μ m thick	About 0.5 and 10 μ m thick	Morrall 1008 Nucl. Instr. Meth.	[31]
Metal	Electrodeposition from molten salts NaCl-KCl-NaF K ₂ MoO ₄ 1123K on Ni plate in argon gave low oxidation	Difficult preparation. Expensive equipment	Ene 2006 J. Optoelectronic	[27]

In $^{100}\text{Mo}(p, n)^{99\text{m}}\text{Tc}$ production standard target processing procedure includes dissolution of Mo and Tc mixture in hot concentrated H_2O_2 . Transition, post transition and refractory metals are not perfectly inert at such conditions. Speaking about radiopharmaceutical production even very low amount of impurities is becoming critical.

The idea to use really inert baseplate was presented by the group of University of Alberta during on IAEA meeting of 2013[5] and 2015[10] devoted to accelerator-based production of $^{99\text{m}}\text{Tc}$, including such materials as glassy carbon, quartz and aluminum oxide. At the same meetings Japanese proposed use of inert vessel (aluminum oxide[5], SiC[10]) for direct irradiation of Mo powders by vertical cyclotron beam.

The Table 2.4 presents comparative summary on the studies realized in different countries of the world on targetry and target preparation for production of $^{99\text{m}}\text{Tc}$ by cyclotron, revealing also the main weak points of each approach.

2.5 Cyclotron solid target design.

Cyclotron targets are designed to accommodate the material being irradiated. The design of the target varies if target material is gas, liquid or solid. Besides that, solid targets can be as placed inside (internal) or outside (external) the cyclotron, that is also influencing the target design. The last way to classify the targets is linked to their position towards the beam: perpendicular or slanted (placed under a small in respect to the beam direction), stable or rotating.

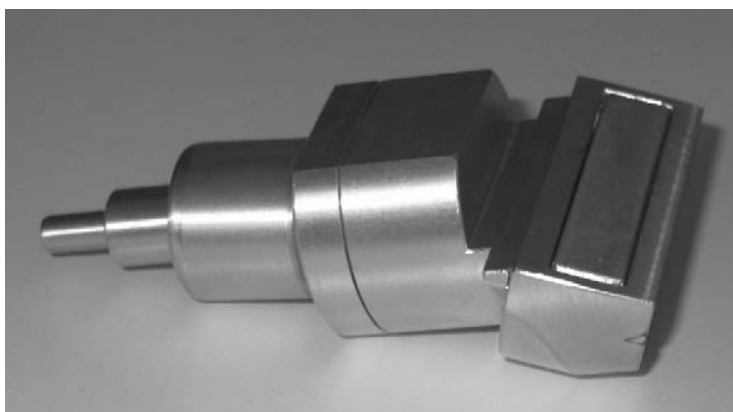


Figure 2.7: An internal target used for production of ^{211}At .

Internal targets were the first targets to be used in cyclotrons. The real advantage of these targets is that the target can be built to match maximally the beam curvature and, by this

way, distribute the power of the beam over the maximum area and increase the amount of beam current that may be applied to the target. This type of targets was used for the production of non-volatile solid radioisotopes such as ^{123}I , ^{124}I , ^{201}Tl , ^{67}Ga , ^{211}At and ^{111}In . The Figure 2.7 [35] and Figure 2.8 [36] present low angle slanted internal solid targets.

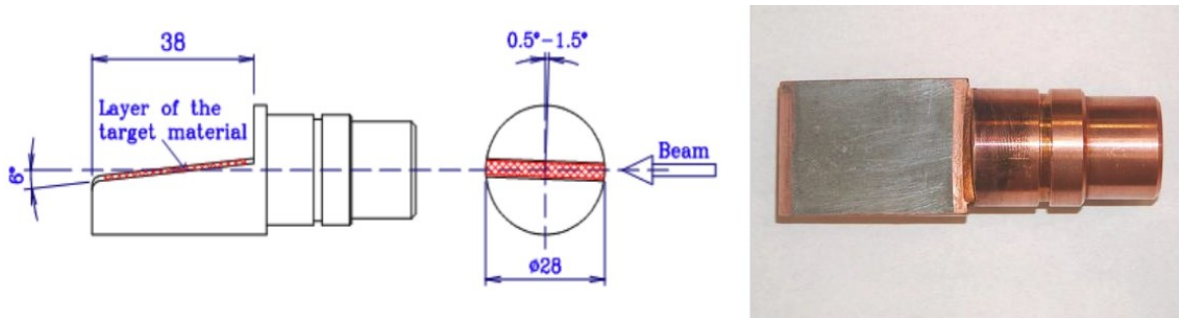


Figure 2.8: Multipurpose internal slanted solid target with extremely low angle (Nuclear Physics Institute AS CR, v.v.i.,Řež)

Internal target stations are available almost solely on older, medium-energy cyclotrons. Modern medical cyclotrons usually support the use of external targets, allowing opportunity to switch fast from one target to another.

2.5.1 Low current cyclotron solid target

The solid target material can be deposited onto backing plate or placed inside the target in the form of a foil or a powder. A typical low current solid target for powders is shown in the Figure 2.9.

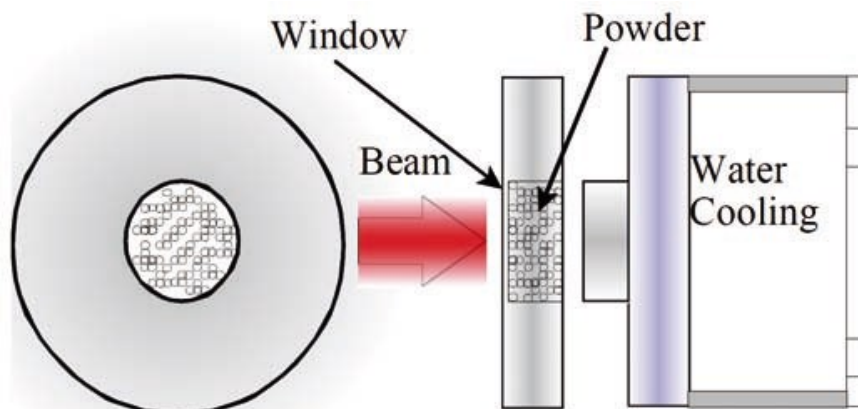


Figure 2.9: A typical low current solid powder target.

In low current solid targets, the beam is usually hitting the target with perpendicular alignment. This type of targets is commonly used in small medical-type cyclotrons up to 19MeV for production of ^{123}I , ^{124}I , ^{64}Cu , ^{89}Zr with currents not exceeding $100\mu\text{A}$ (in reality the currents up to $50\text{-}60\mu\text{A}$ are used).

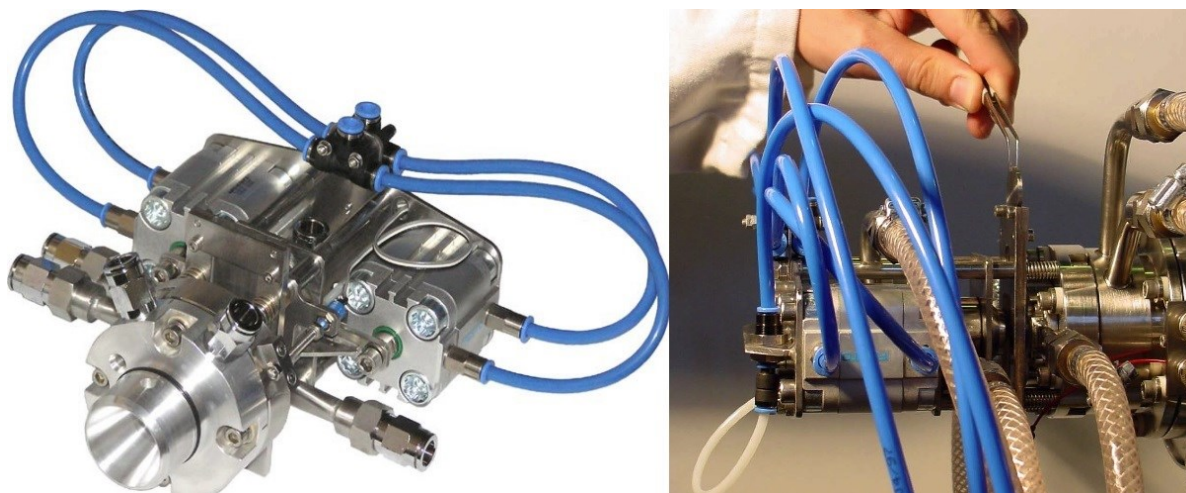


Figure 2.10: Nirta® Solid Compact irradiation Target of IBA.

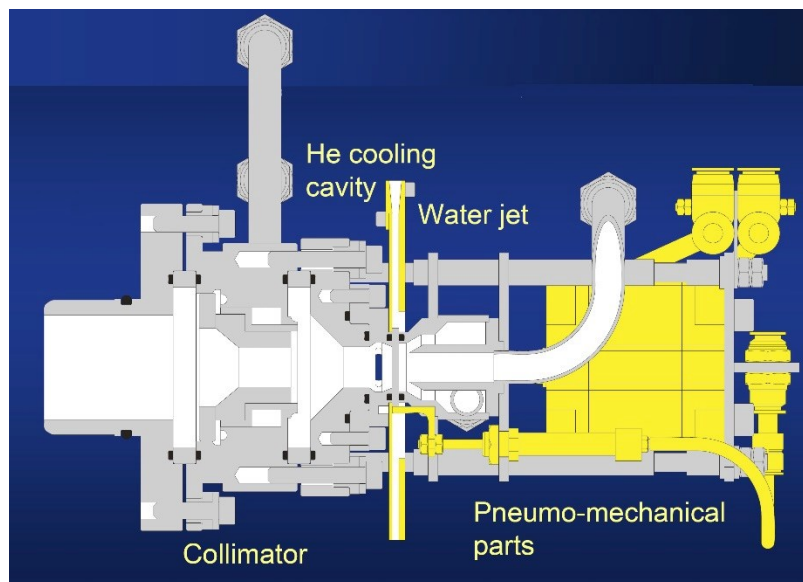


Figure 2.11: Cross-section of Nirta® target.

The Figures 2.10 and 2.12 show typical commercially available cyclotron solid target stations Nirta® of IBA Radiopharma Solutions and ALCEO of Comecer. Low current solid targets can use both cooling in front of the target with He gas and cooling with water from the back side (see Figures 2.11) in order to increase the heat dissipation level. Otherwise,

only water-cooling from the backside is used, like in PETtrace system of General Electrics (GE) shown in the Figure 2.13.

Water can as directly flow touching the backing plate (as in Nitra[®], PETtrace and ALCEO targets), or can be contained inside a small chamber, brought in contact with target backing plate with a pneumatic piston system (as Tema Sinergie target, that will be described in details later).

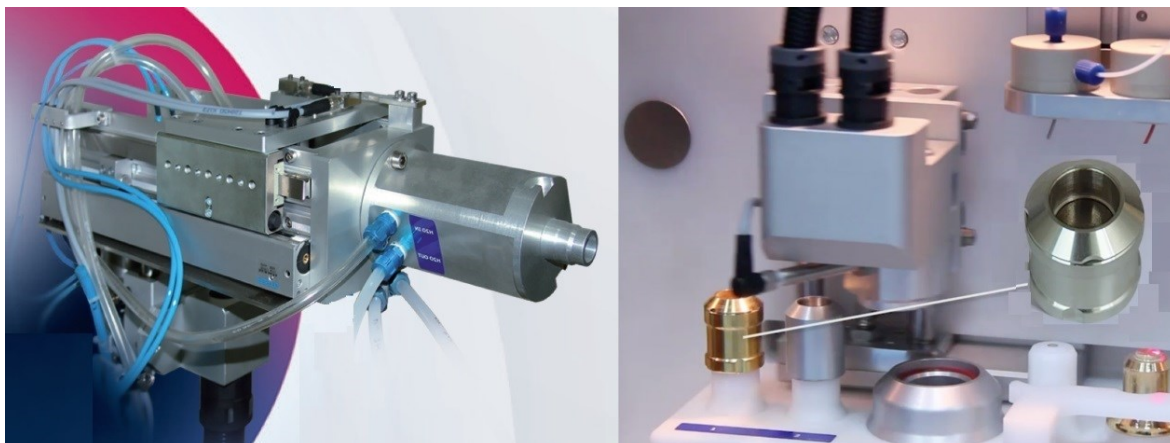


Figure 2.12: ALCEO PTS irradiation module and Metal solid target system (COMECER).

The target backing plate could be as simple metallic disk like in Nitra[®], PETtrace or Tema targets, or more complicated shape, like ALCEO, being in the same time a target shuttle for automatic displacement with pneumatic system.

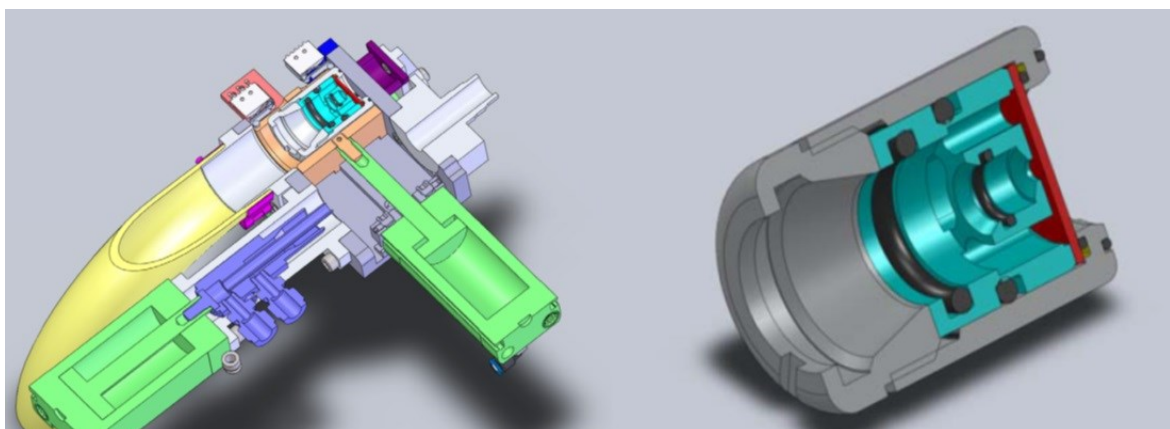


Figure 2.13: PETtrace solid target of GE.

Processing of foil target material is much easier. However, this configuration allows to use only very low currents on the target. An example of foil target used for production of ⁶⁶Ga

from ^{66}Zn foil in CS-15 cyclotron of Washington University Medical School [37] is presented in the Figure 2.14.

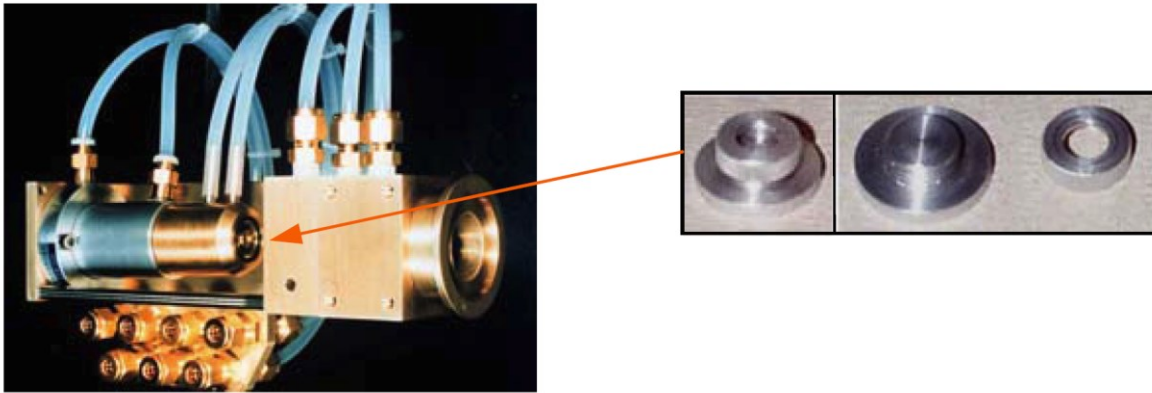


Figure 2.14: Foil target holder for production of ^{66}Ga from ^{66}Zn foil in CS-15 cyclotron.

2.5.2 High current cyclotron solid target

The use of inclined baseplate in respect to the proton beam direction allows to increase the heat exchange area several times and correspondingly increase the total power levels dissipated from the target. Thus, such type of targets allows to reach proton beam currents up to $300\mu\text{A}$.

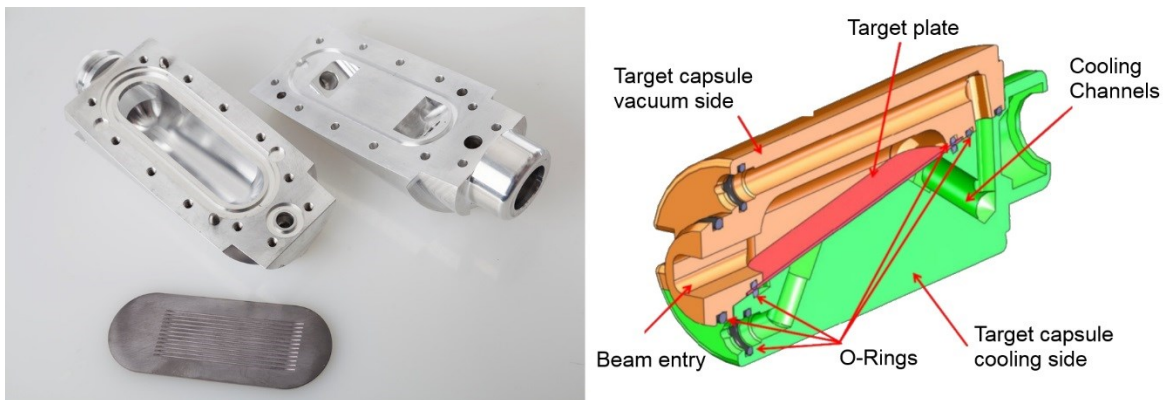


Figure 2.15: TR19 target of Advanced Cyclotron Systems Inc.

The inclining angles of the target can vary from very low (used for internal target configuration only) up to $10\text{-}15^\circ$ more common for external slanted solid targets.

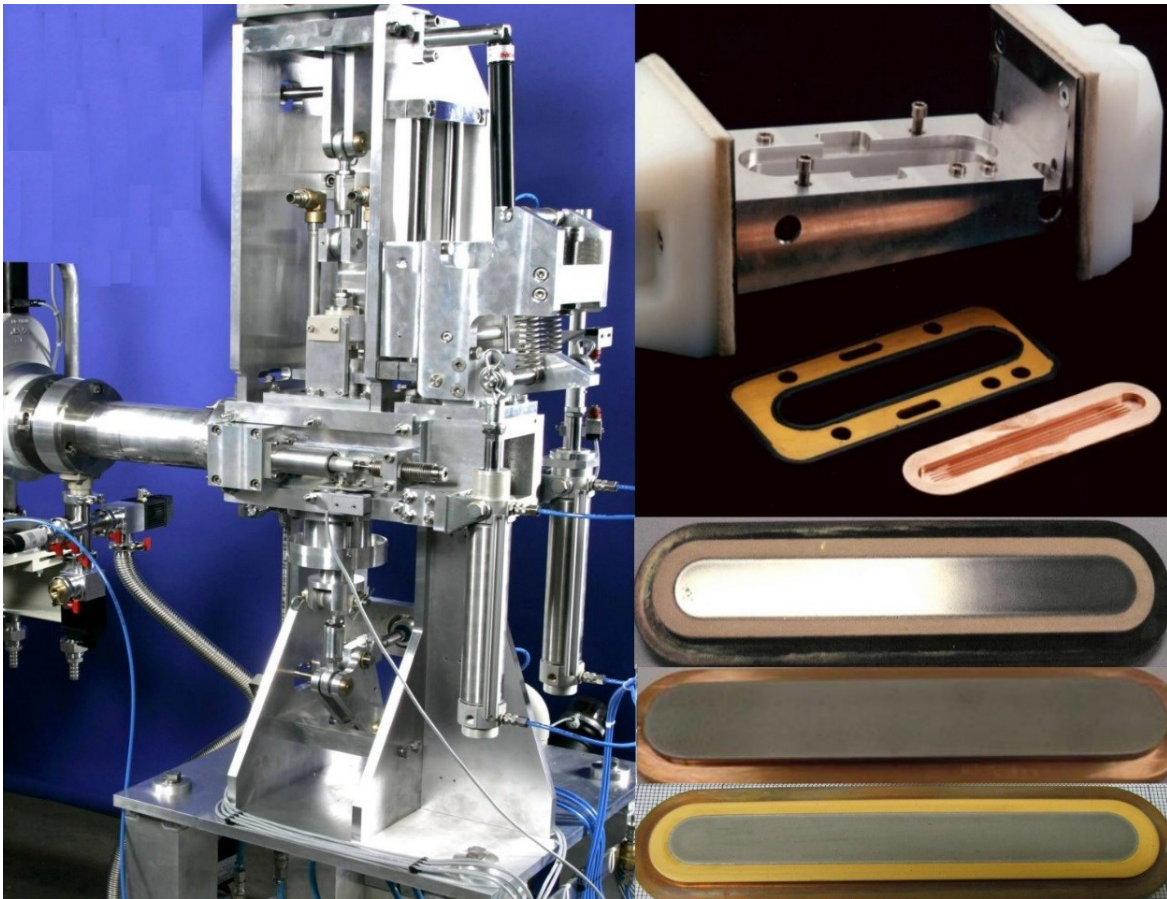


Figure 2.16: IBA high current solid target.

Of course, direct water-cooling from the back is preferable for maximum heat dissipation as shown on the Figure 2.13 of TR19 solid target of Advanced Cyclotrons Inc. The use of upgraded baseplate, like the one containing micro fins (Figure 2.13, 2.14) or brazed to a metallic foam (Figure 2.15), as it was proposed by Korean group [38], is suggested.

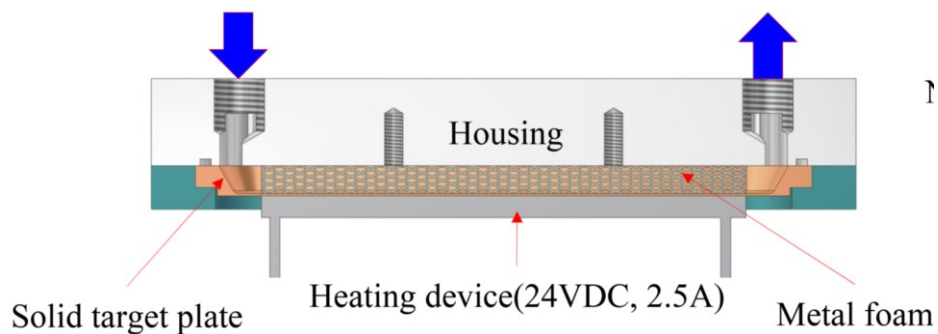


Figure 2.17: Modification of IBA solid target baseplate with metallic foam.

2.5.3 Alternative target configurations

One of the approaches to use higher beam currents onto powder materials, low thermal conductivity and/or low melting point, or non-metallic materials is encapsulation of the target material inside suitable metal. Such capsule can be placed directly inside the cooling chamber providing the so called 4π water-cooling (see Figure 2.18) [36]. This approach is used, for example, for aggressive metallic Rb (providing Liquid Metal Embrittlement) and RbCl targets for ^{82}Sr production and for metallic Ga target for ^{68}Ge production. A universal encapsulated target proposed by Applied Technology Group at TRIUMF is shown in the Figure 2.19 [39].

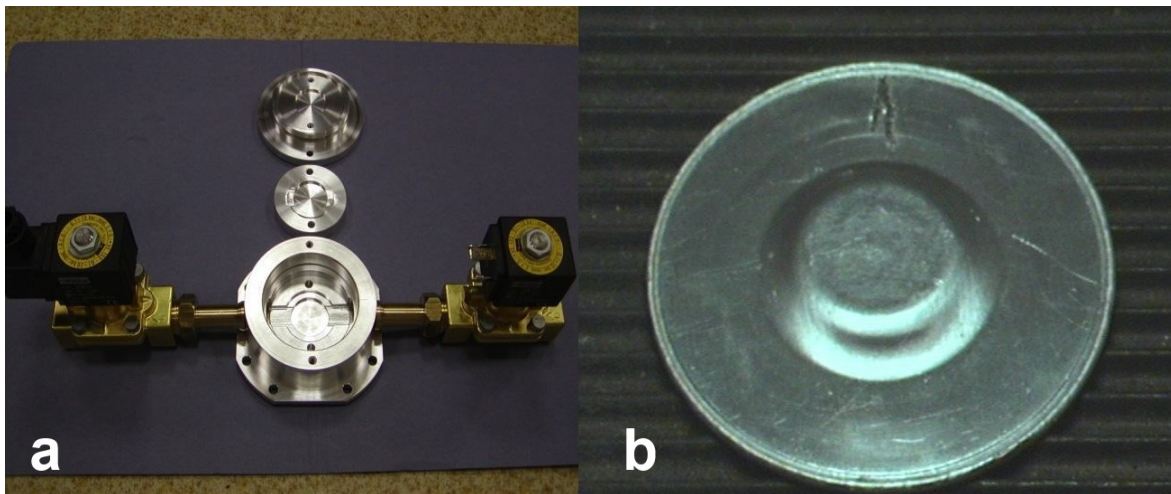


Figure 2.18: Design of a solid target system (a) with 4π water-cooling of the target capsule (b).

The use of a batch of encapsulated targets at high-energy cyclotron allows to get more than $100\mu\text{A}$ currents even on low thermal conductivity materials like RbCl. In ARRONAX in order to optimize the irradiations and to use also the low energy beam region, after several RbCl targets encapsulated in stainless steel for ^{82}Sr production, also a target of Ga encapsulated in Nb for production of ^{68}Ge is placed (see Figure 2.20).

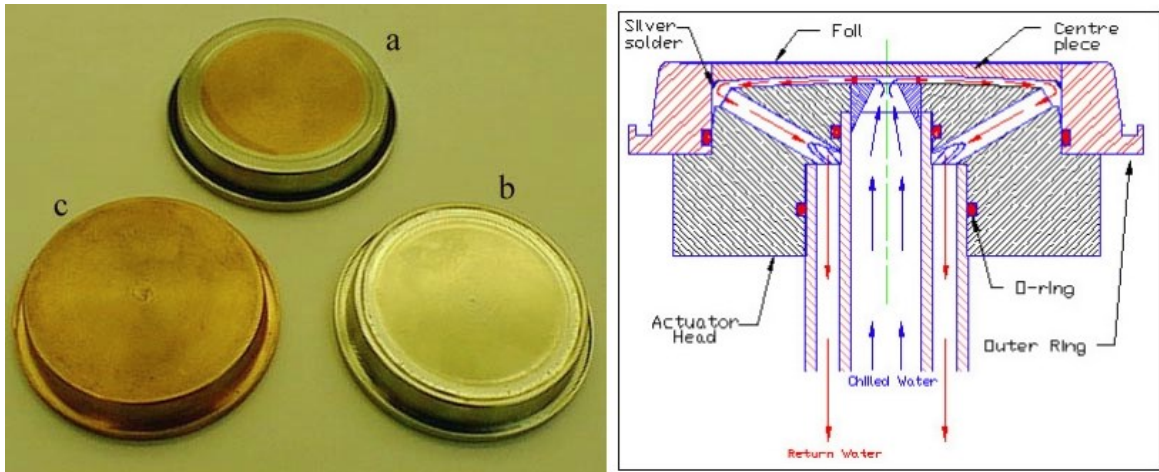


Figure 2.19: Universal encapsulated solid cyclotron target of TRIUMF.

Previously described targets are stable. Another way to maximize the beam current is rotating the target during irradiation. A combination of rotation with the irradiation angles $< 90^\circ$ is shown in the Figure 2.21. The targets holder represents revolving spherical cap, on which the target layer material should be electroplated. Similar effects can be obtained by irradiating external stable targets with sweeping the beam over larger area of the target surface with a magnet.

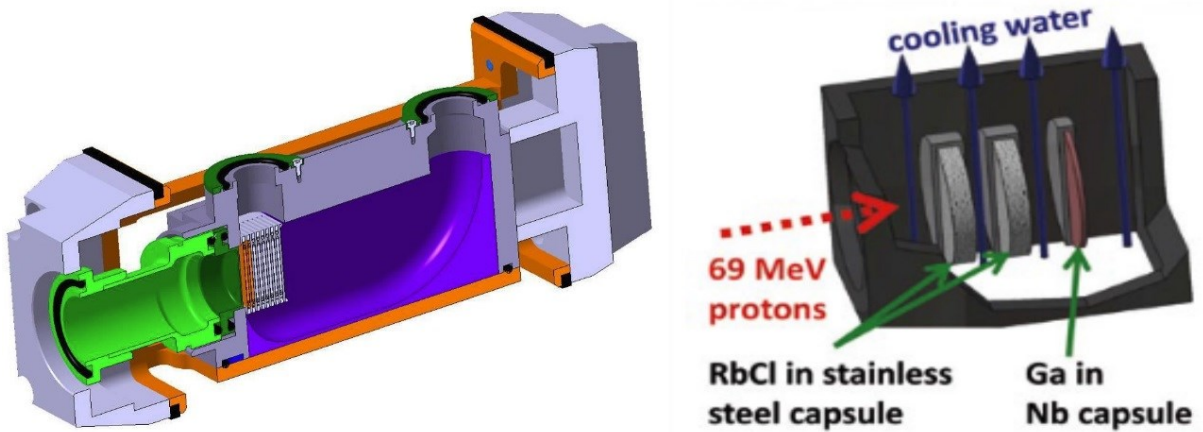


Figure 2.20: Encapsulated target for production ^{82}Sr and ^{68}Ge at ARRONAX.

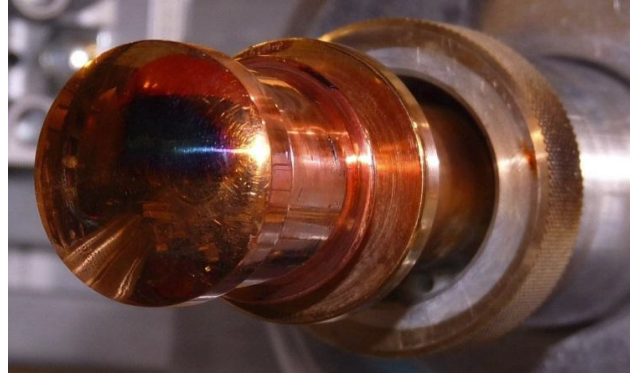


Figure 2.21: Internal rotating target holder: water-cooled spherical copper cap, should be covered by a target layer (Nuclear Physics Institute AS CR, Řež)

2.5.4 Heat exchange in solid cyclotron target

For all target types, the key performance parameter is the ability to effectively remove the heat deposited during the particle bombardment. The total power deposited onto target is given by the beam voltage multiplied by the beam intensity:

$$Q_{total}(W) = \frac{E(MeV)}{z \cdot e} \times I(\mu A) \quad (2.1)$$

Where $E(MeV)$ is beam energy, $I(\mu A)$ is beam current or beam intensity, z is charged state of accelerated particle and e is the elementary charge. For example, at 30MeV and 100 μA of proton beam, the total power deposited is 3 kW.

The distribution of this power into target depth is corresponding to the stopping power. In nuclear physics, charged particles moving through matter interact with the electrons of atoms in the material. The interaction excites or ionizes the atoms, which leads to an energy loss as given by the Bethe formula (2.2). The Bethe formula describes the energy loss per distance travelled of charged particles passing through matter. This is also the resultant stopping power of the material.

The proton enters the target with an initial kinetic energy. After undergoing Coulombic interactions and radiation losses (bremsstrahlung), the kinetic energy of the proton is reduced after travelling a distance x along its path. Stopping power is defined as incremental energy lost (dE) per unit distance travelled (dx), or $(-dE/dx)$. As the proton decelerates the stopping power increases further back into the target, reaches a peak, and drops off to zero.

$$\frac{-dE}{dx} = \frac{4\pi z^2 e^4 N Z}{m_0 v^2 A} \ln \left(\frac{2m_0 v^2}{I} \right) \quad (2.2),$$

where

z is the particle atomic number (amu);

Z is the absorber atomic number (amu);

e is the electronic charge (esu);

m_0 is the rest mass of the electron (MeV);

A is the atomic mass number of the absorber (amu);

V is the particle velocity (cm/s);

N is Avogadro's number;

I is the ionization potential of the absorber (eV).

The assumption is made in the above approximation that the particle is massive in comparison with the electron. This assumption leads to a maximum energy transfer of $2m_0V^2$. Therefore; the above expression can be reduced to the following formula:

$$\frac{-dE}{dx} = \frac{144z^2Z}{AE} \ln\left(\frac{2195E}{I}\right) \quad (2.3),$$

where

z is the particle atomic number (amu);

Z is the absorber atomic number (amu);

A is the atomic mass number of the absorber (amu);

E is the energy (MeV);

I is the ionization potential of the absorber (eV).

The stopping power and ranges may also be obtained from the SRIM computer code.

The total heat transfer in a target system consists of radiative, conductive and convective (see Figure 2.22).

1) Radiative heat transfer from the front part of the target

$$O_{rad} = \sigma \cdot A \cdot (T_1^4 - T_2^4) \quad (2.4)$$

In this formula, σ is the Stefan-Boltzmann constant; A is cross-sectional area (cm²); T_1 and T_2 are temperatures of the source and the sink, correspondingly. Radiative heat transfer is becoming significant only at temperatures >500°C.

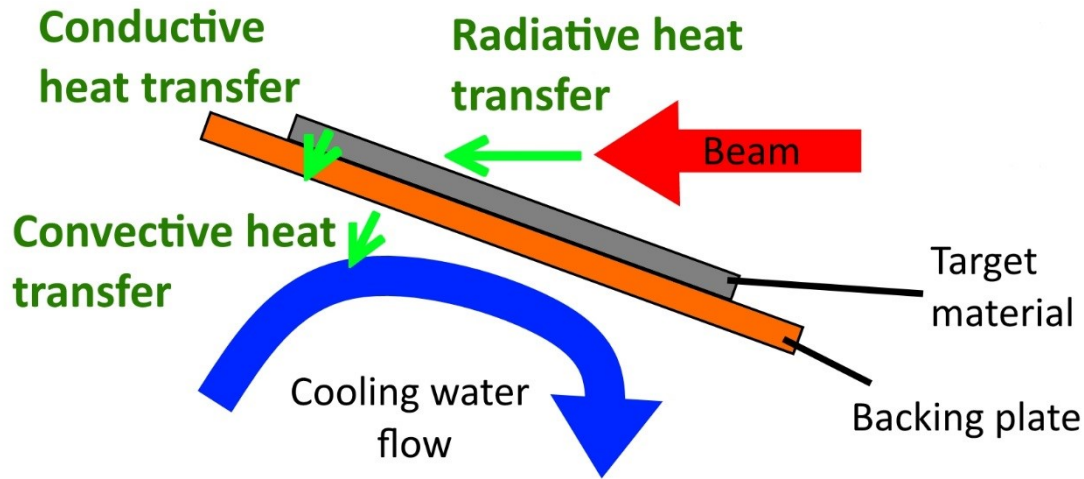


Figure 2.22: Heat exchange in solid cyclotron target.

- 2) Conductive heat transfer through target material, and target backing plate material

$$O_{cond} = \frac{-k \cdot A \cdot (T_1 - T_2)}{x} \quad (2.5),$$

where, k is the thermal conductivity coefficient ($\text{W} \cdot \text{m}^{-1} \cdot \text{K}^{-1}$), A is cross-sectional area (cm^2); x is distance (cm); T_1 and T_2 are temperatures of hotter and colder part correspondingly.

- 3) Convective heat transfer to water in the water cooling chamber

$$O_{conv} = -h_c \cdot A \cdot (T_1 - T_2) \quad (2.6)$$

In the latter formula, h_c is the heat transfer coefficient in convection method ($\text{W} \cdot \text{m}^{-2} \cdot \text{K}^{-1}$), A is cross-sectional area (cm^2); T_1 and T_2 are temperatures of hotter and colder part correspondingly.

In the case, when front cooling with He gas is present, also convective heat transfer to gas should be taken into account.

Each of these three aspects can be improved in order to maximize the heat exchange efficiency and, by that way, to grow the radionuclide production yield.

2.6 Proposal of an Advanced target preparation

The feasibility of direct production of $^{99\text{m}}\text{Tc}$ by cyclotron starting from ^{100}Mo was widely demonstrated in theoretical and experimental studies. However, these studies have not covered such an issue as the development of the target capable to produce sufficient amounts of $^{99\text{m}}\text{Tc}$ for the clinical use. In order to maximize nuclear reaction yield high proton currents

should be involved. This means that target system should be able to remove the hitting heat power with high efficiency.

2.6.1 Target deposition requirements

The basic system supposed to be target material deposited on baking plate, cooled by cooling liquid. As already described in the previous chapter, all cyclotron solid targets for radiopharmaceuticals production have this approach. Taking into account that the main ways of heat transfer are conduction and convection (radiation is not considered, because the target temperature should not exceed 500°C) the target cooling efficiency can be lost (decreased) on target material itself, target backing material and cooling chamber.

The first point of efficiency loss is target itself. The poor thermal conductivity of molybdenum oxide limits a lot the amount of beam current that can be applied to target. Thus, only metallic Mo targets will be considered to the high power irradiations needed for the large-scale production of ^{99m}Tc .

The main requirements to metallic Mo target for efficient cyclotron production of Tc must follow:

- high heat dissipation level (good thermal conductivity);
- uniform and controlled thickness;
- high density (bulk-like);
- low level of oxidation.

The denser and the thinner is the target material, the better is the thermal exchange. Furthermore, targets must also be sufficiently durable to allow for transport post-irradiation and the post irradiation process. The bulk sintering of the isotope powders indeed results in a massive target that will not support high power density fluxes because of its intrinsic porosity between grain boundaries.

2.6.2 Magnetron sputtering as a solution

The LARAMED group of the INFN – LNL proposed to use magnetron sputtering as the basic technique for deposition of ^{100}Mo onto a backing plate. Magnetron sputtering is a very flexible technique, allowing to change a lot the properties of the deposited film by changing the sputtering parameters. Sputtering is able to provide both high density of target material and good adherence of the target material to a backing plate. In addition, deposition by sputtering allows to control the thickness of the target.

Among PVD techniques, Magnetron Sputtering is a well-known technique for deposition of thin metallic films. However, it is not used for thick film deposition because of tensile or compressive stress always present in the films. One of the main technological challenges of this thesis is to develop a method to deposit dense stress free films of refractory metal (Mo) of hundreds of microns thick. Therefore, we propose the application of this technique to the direct deposition of a thick target to a baseplate. This approach would have a further advantage to simplify the often under-evaluated problem of the thermal contact between target and target backing plate.

2.6.3 Backing plate inertness

After the production of ^{99m}Tc via the $^{100}\text{Mo}(p,2n)^{99m}\text{Tc}$ reaction, a separation procedure should be applied to separate ^{99m}Tc from bulk ^{100}Mo and isolate the radionuclide of interest under a suitable chemical form.

Because of easier *in vivo* application, medical radionuclides are usually supplied in aqueous solutions. The radionuclides for medical applications, similar to any other pharmaceutical products, must fulfill the quality standards, which are declared in European Pharmacopeia. Specifically, such characteristics as high radionuclidic and chemical purity are considered mandatory. These requirements can be fulfilled by developing efficient separation procedures, which yield the radionuclide in an ultrapure form, within a relatively short time to prevent excessive loss of radioactivity through its natural decay. For these reasons the procedures must be automatic and they should be performed as brief as possible.

Various physicochemical separation methods have been proposed since different target materials (e.g. Mo metal, MoO_3 , etc.) were used as a precursor for ^{99m}Tc production by different groups. The most common approach for target processing is target dissolution in concentrated H_2O_2 at elevated temperature and after use of one of the next methods to separate ^{99m}Tc from ^{100}Mo is used:

- Method of Chattopadhyay(tetrabutylammonium bromide-TBAB extraction)[40];
- ABEC (biphasic aqueous extraction chromatography)[41];
- Solvent extraction MEK (methylethylketone) and column chromatography[42];

Since concentrated hydrogen peroxide at elevated temperatures is a corrosive media, the choice of backing plate material should be taken from the point of view of chemical inertness in such conditions, in order to minimize possible impurities in a final product.

The most common material used as backing plate is copper because of its good thermal conductivity (390 W/(m K)) and relatively low cost.

However, copper is highly activated under the proton beam during irradiation producing a huge amount of long-lived radionuclides and it dissolves in H₂O₂. These drawbacks mean further separation modules in order to obtain the purity of the final product, intolerable with the necessity to shorten and automatize the procedures.

Gold could be used as backing plate but its thermal conductivity is lower than copper and it is very expensive.

Therefore, the choice of better material mainly depends on the strategy followed for the chemical dissolution of Mo irradiated sample as well and on the technique for the molybdenum deposition on the support material.

Thereby, in addition to Mo deposition technique requirements, the set of requirements to a backing plate of the target should be taken into account:

- high thermal conductivity;
- machinability;
- mechanical strength;
- chemical inertness;
- minimizing activation products;
- reasonable cost.

2.6.4 Sapphire and DLC as a solution

Our proposal is to use a thin layer of ceramic material that is inert chemically and under the beam, avoiding radioisotope impurities. Further, both the target itself and the target holder must have the capability of being irradiated at high beam current, and so, the peculiarity to dissipate as much as possible the power heat level.

For this reason sapphire, as ceramic material with highest thermal conductivity (60 Wm⁻¹K⁻¹), and synthetic diamond (CVD), material with extremely high thermal conductivity (up to 2000 Wm⁻¹K⁻¹), are proposed to be a part of the target plate. In order to minimize the losses on ceramic part, its thickness is minimized. Moreover, in order to keep mechanical rigidity of the system, and minimize the cost of such target, the ceramics substrates should be brazed to metallic target holder part (copper or aluminum).

The proposal of the advanced target preparation consists in a ~100 µm thick of ¹⁰⁰Mo deposited by magnetron sputtering on sapphire or DLC, brazed to high thermal conductivity metallic holder.

The choice of magnetron sputtering as deposition technique is providing an opportunity to prepare uniform, dense and adherent films also on ceramic substrates.

It should be mentioned that the main drawback of such substrates is brittleness. Thus, the MS deposition technique should resolve the problem of residual stress of film deposited, because high residual stress can cause plastic deformation (buckling or bending) of the films, cracking in the deposit or the substrate, or cracking at the substrate-deposit interface. Therefore, stress must be avoided in order to respect the requirements for Mo target for cyclotron production of ^{99m}Tc.

2.6.5 Evaluation of other opportunities

2.6.5.1 Advanced materials for high thermal conductivity backing plate

An alternative way to use extremely high thermal conductivity level of synthetic diamonds avoiding unlimited costs for target production is to use, rather than normal copper, silver or aluminum, diamond-metal composites based on the same metals. For example, diamond-copper composites can provide the thermal conductivities 3-4 times higher than copper.

One of the tasks of this PhD thesis is to evaluate the idea to use diamond-metal composite backing plate for solid cyclotron target and the preparation methods for this type of composites and if is worthwhile to prepare them in laboratory or to buy from industrial producers.

2.6.5.2 Advanced cooling with liquid metals and its difficulties

Another idea of heat exchange improvement, never used for radiopharmaceutical production target, but enough known to solve the problem of heat removal from narrow irradiation area in the nuclear reactors, is liquid metal cooling. The difficulty lays in the fact that the liquid metal alloys are normally chemically aggressive, and all the metals with high thermal conductivity suffer from the liquid metal embrittlement.

Liquid Metal Embrittlement (LME) or Liquid Metal Cracking (LMC) is the loss of ductility in normally ductile metals when stressed under contact with liquid metal. The general rules for the possible occurrence of liquid metal embrittlement are:

- Low mutual solubility between the liquid and solid metals.
- Absence of intermetallic compound formation between the solid-liquid couple.

There is a specific combination of liquid metals and stressed metals or alloys that can lead to catastrophic intergranular cracking. For example, carbon steels and stainless steels are susceptible to liquid metal embrittlement by zinc and lithium; aluminum and aluminum alloys are susceptible to liquid metal embrittlement by mercury, gallium and zinc; copper and copper alloys are susceptible to liquid metal cracking by mercury and lithium. Cracking is frequently observed to be a single intergranular crack that propagates rapidly, at a rate of 25 cm/s. When stresses are present, embrittlement is manifested by extremely fast rates of crack propagation.

The mechanism of liquid metal cracking is clearly not electrochemical in nature. It is most probably an adsorption-induced cracking. The liquid metal atoms when adsorbed on a susceptible metal or alloy reduce the metal bond strength within the grain boundary regions of the susceptible metal. Under tensile stress, crack initiates and propagates rapidly along the grain boundaries.

The liquid metal cooling strictly requires the use of highly resistive to LME materials in a contact with liquid metals. Metals resisting to LME are usually refractories, like Nb, Zr, Ta, Pt, that have enough low thermal conductivity in respect to copper and aluminium, usually used as cyclotron target backing plate. The method to overcome this problem is to use protective layer of refractory metal of micron level onto high thermal conductivity backing plate. In a detailed way, chemical and microstructural requirements and methods to create such protective coatings will be described in the further chapters of the thesis.

2.6.6 $^{99}\text{Mo}/^{99\text{m}}\text{Tc}$ generator vs cyclotron produced $^{99\text{m}}\text{Tc}$.

The standard diagnostic procedure generator-based $^{99\text{m}}\text{Tc}$ requires the activity of about 30mCi and cost to a hospital of about 15€/dose, or 500 €/Ci.

It is not difficult to imagine the cost of cyclotron produced ^{99}Tc . The activity of $^{99\text{m}}\text{Tc}$ at the end of bombardment that can be produced by 2h irradiation with 100 μA proton beam at 16MeV (common for small medical cyclotrons) incident energy onto “thick target” (of about 0.4 mm) is 72.5 GBq (about 2 Ci) [5].

The mass of ^{100}Mo needed for disc-like target preparation with 10mm diameter and 0.4mm thickness (0.0314 cm³ volume) is about 0.33 g. The cost of ^{100}Mo enriched (>99%) varies depending on total amount and starts from 800€/g. Thus, each target cost is about 265€. The

cyclotron produced ^{99m}Tc activity cost is about 133€/Ci, or 4.4€/dose. These calculations are made taking into account only ^{100}Mo material cost, the target preparation, backing plate and other expenses will increase the cost of about 2 times.

Since one target for low energy medical cyclotron irradiation cost of about 265€ (only ^{100}Mo material), the accelerator-based ^{99m}Tc production rout will be economically reasonable *only in a case* when an efficient way to recover expensive precursor ^{100}Mo material will be developed. Thus, the study of Mo recovery procedures starting from permolybdates solution coming as a “waste” from the separation module up to production of metallic Mo is also one of the tasks of this thesis.

3 FUNDAMENTAL ASPECTS OF THE TECHNOLOGICAL PROCESSES

3.1 Magnetron sputtering

The following chapter presents an overview of magnetron sputtering technique with particular focus on origin, evaluation and modification of intrinsic stresses in sputtered thin films.

3.1.1 What is sputtering?

Sputtering and evaporation of solid materials are fundamental physical processes currently used in the physical vapor deposition (PVD) of thin films. As far as known to be a very flexible method, that allows to adjust the properties of a desirable coating changing the deposition parameters and configurations, sputtering was chosen as Mo deposition technique in current investigation.

Sputtering is performed by means of plasma, which generates charged particles that can be accelerated towards a surface of the target by electric field. While the target is bombarded by the energetic particles of plasma, the atoms are ejected from a solid target material. These atoms can endure collisions with atoms or ions of plasma gas and after scattering can either return back to the target or reach the substrate, creating a thin film.

3.1.1.1 Simple sputtering configuration

The principle of sputter deposition is shown in the Figure 3.1, which is a schematic representation of a typical system for DC sputtering. Inside a vacuum chamber, two electrodes are placed in parallel, where on the cathode is placed the material to be deposited (target). The cathode is connected to an ordinary DC power supply, and typically, a voltage of -400..-500 V is applied. In front of the target there is the substrate, which may be floating, grounded or biased. An inert process gas, usually argon, is introduced and serves as the medium, in which an electrical discharge is initiated and maintained. The formation of plasma will typically only happen in the gas pressure range 0.1-10 Pa.

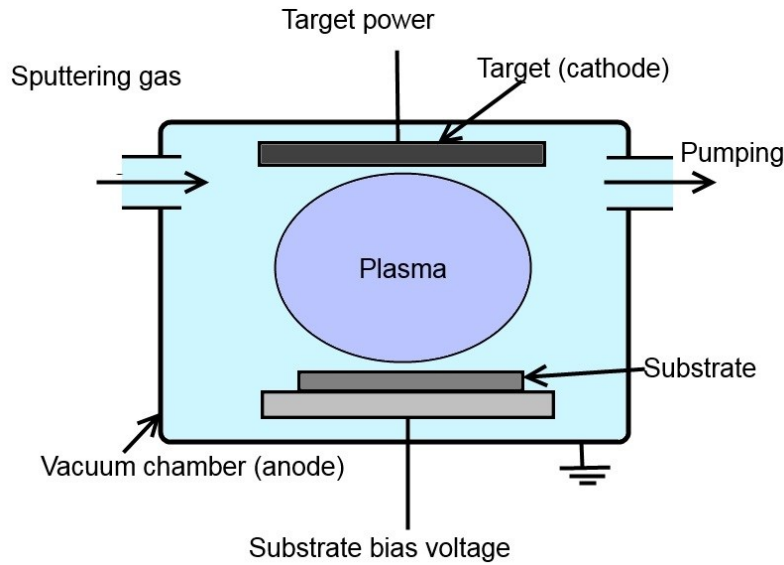


Figure 3.1: Schematic representation of simple sputtering system.

In simple terminology, a plasma is defined as a partially ionized gas (equal amounts of electrons and ions, in addition to neutral atoms and molecules) that exhibits collective behavior in the presence of an electromagnetic field. Imposed by the electric field between the electrodes Ar^+ -ions are accelerated at high energies towards the target material, causing, upon impact, the emission of mainly neutral target atoms by momentum transfer. The sputtered atoms are condensing into a thin film when reaching the substrate.

3.1.1.2 Sputtering sources

Two main types of plasma sources are the most used: diode and magnetron. **Diode** is simply an anode and a cathode inside a vacuum system (see Figure 3.1). Under the right conditions, with adequate voltage across the electrodes and the appropriate gas pressure, the gas will breakdown into a plasma discharge. Diode plasma is uniform and electrons can reach the substrate causing heating of the substrate. Diode process is characterized by low efficiency, low deposition rate and low adhesion of the film to the substrate.

A **magnetron** uses a static magnetic field (permanent magnets) in a suitable configuration behind the cathode (target). In planar magnetron source the magnetic field is located parallel to the cathode surface (see Figure 3.2). The Lorentz force, acting on secondary electrons emitted from the cathode due to ion bombardment, is given by

$$F = m \frac{dv}{dt} = q(E + v \times B), \quad (3.1),$$

where m , q and v are the electron mass, charge and velocity, respectively. E and B are the electric and magnetic fields respectively.

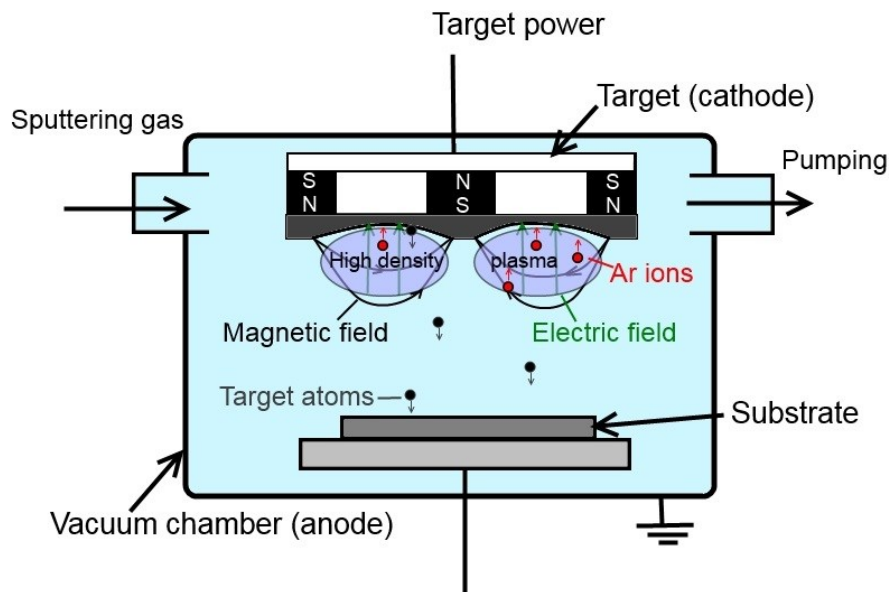


Figure 3.2: Planar magnetron sputtering

Electrons of plasma are constrained to move in a direction perpendicular to both the electric field (normal to the surface) and the magnetic field (Figure 3.2). This is known as an $E \times B$ drift. This drift causes electrons to move parallel to the cathode surface in a direction 90 degrees away from the magnetic field. If the magnetic field is set up correctly, this $E \times B$ drift can be arranged to close on itself, forming a current loop of drifting secondary electrons (racetrack).

When electrons are “trapped”, their lifetime in the plasma is prolonged, resulting in more collisions with the gas atoms before the electrons are lost to the chamber walls. This contributes to an intensified ionization of the working gas, meaning that more atoms are ejected from the target during the sputtering process. The ionization is most effective just above the racetrack, due to the high concentration of secondary electrons. This effect is seen in practice, due to the creation of an erosion profile along the racetrack on the target. One of the drawbacks with magnetron sputtering is that only 20-30% of the target material is utilized, due to the uneven erosion.

Generally, the deposition rate in sputter-systems is proportional to the DC power dissipated in the target. Magnetron sputtering is a method to increase the deposition rate, due to an increased ion density in the plasma. Thanks to higher ion density, the plasma in magnetron

sputtering can be sustained at lower pressures. This, again, means that the sputtered atoms lose less energy, due to gas atoms collisions, when they are transported through the plasma.

3.1.2 Control of stress during vapour deposition

3.1.2.1 What is stress?

Stress σ is the force per unit area that is acting on a surface of a solid, more commonly expressed in Pascals (Pa) or Nm^{-2} . A piece of solid is under stress when its atoms are displaced from their equilibrium positions by the force. The displacement is governed by the interatomic potential (Figure 3.3a). It is well known that the internal force F is a derivative of potential Φ ($F = -\partial\Phi/\partial r$) between two atoms. Thus, when external force is applied it has the opposite sig: $F_{ex} = +\partial\Phi/\partial r$ (see Figure 3.3b).

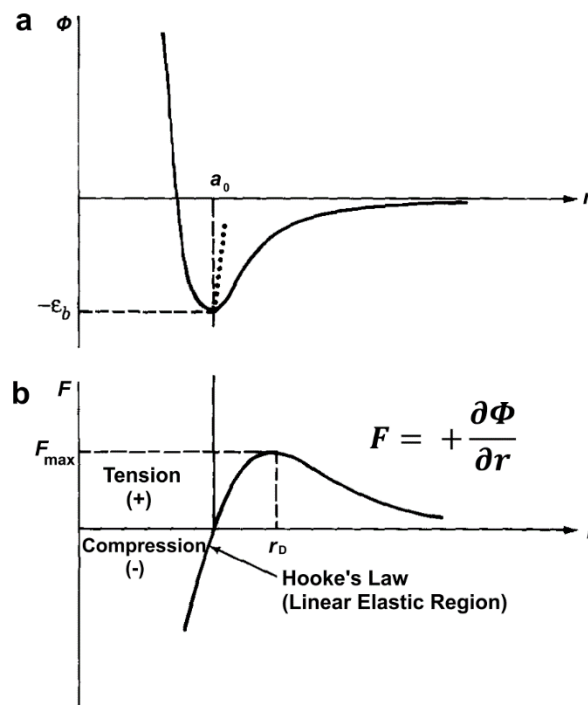


Figure 3.3: (a) Interatomic potential function vs interatomic distance. (b) Applied force vs atomic displacement.

An external tensile force tends to lengthen the solid and in turn to increase the interatomic distance. Based on the sign convention, a force that increases the interatomic distance is positive, and hence the tensile force (or stress) is positive. An external compressive force (or stress) which tends to shorten the solid is negative.

In the Figure 3.3 F_{max} represents the maximum force that corresponds to the dissociative distance r_D . F_{max} is maximum tensile force needed to pull the solid piece until baking or theoretical strength of the solid. At the equilibrium position a_0 , the external force is equal to zero, and the potential corresponds to the minimum potential energy ε_b between the atoms. At a small displacement from a_0 in whatever direction, the force is linearly proportional to the displacement. It corresponds to elastic behavior of solids under stress and is described by Hooke's law. Within the elastic region, the displacement disappears if the force is removed. Over the elastic limit, permanent deformations in a solid occur.

Stresses can be the result of externally applied forces. In this case, after the load is removed, the stresses are expected to vanish. On the other hand, thin films are stressed even without the application of externally imposed forces and are characterized by an internal or residual stress. Residual stress can be compressive or tensile. By convention, stress in first case will be expressed with a minus sign and in second case, with a positive sign.

When subjected to a stress, any free body literally is pushed (or pulled) out of shape. Strain ε is the measure of this deformation of the material. It is therefore defined in terms of the partial derivatives of the displacement. Strain is a dimensionless variable. In static equilibrium, the strain is caused by stress, so the principal coordinate system is the same for stress and strain [58].

If the stress is supposed to be uniaxial, the stress is proportional to strain with the coefficient E , called Young's Modulus:

$$\sigma = E \cdot \varepsilon \quad (3.2)$$

The elastic modulus or Young's Modulus E tells how much a material is elongated under a given load. It has units of force per unit of area, just like stress and pressure. It may also be thought as the stiffness or material resistance to elastic deformation. The higher the material elastic modulus, the lesser the deformation for a given stress, and thus the stiffer it is. For example, an incompressible material would have an infinite Young's modulus, while a "soft" material would deform considerably for a given amount of stress, so its modulus of elasticity would be quite low.

Under uniaxial tensile stress, the solid piece expands in the direction of the stress, and contracts in directions perpendicular to the stress. In this situation, there are two strains, one axial and one transverse. The ratio of the transverse to the axial strains, or the proportionality between the contraction and the elongation, is the Poisson ratio ν . This ratio is dimensionless, and has a value between 0.2 and 0.5 for most materials. The volume of the element has

changed because of the strain. The volume expansion is proportional to $(1 - 2\nu)$, which means that materials with $\nu = 0.5$ does not change their volume under uniaxial stress and are called incompressible.

3.1.2.2 Stress in thin films

High residual stresses can cause plastic deformation (buckling or bending), cracking in the deposit or the substrate, or cracking at the substrate–deposit interface, poor adhesion to substrate, becoming serious practical problems (see Figure 3.4).

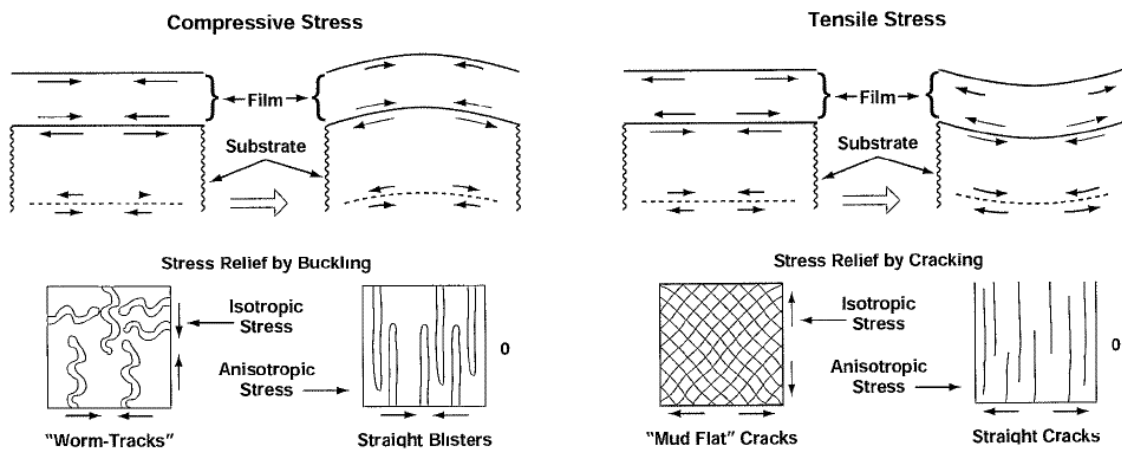


Figure 3.4: Deformation and fracture in stressed films.

In particular, for the purpose of this thesis it is mandatory to avoid stressed films because poor adhesion between Mo films and backing plate can drastically increase the thermal resistance of the contact, decreasing the heat exchange efficiency. Reduction of stress is mandatory when hundred micron thick films are to be deposited.

Stress in thin films is a combination of two components: extrinsic, such as stresses arising from a mismatch in thermal expansion coefficients, and intrinsic, such as stresses arising from coherent epitaxial deposition (see Figure 3.5,[43]). Differential thermal contraction stresses are an unavoidable consequence of processing at elevated temperature and can become quite large because coating and substrate often have very different thermal expansion characteristics. Such stresses are easily calculated in process models. Of course, the deposition process itself may introduce residual stresses related to deposition method.

The *extrinsic stress* is imposed by unintended external factors (such as temperature gradients, for example). The extrinsic stress in thin film mainly comes from the adhesion to its substrate. Stress can be introduced in thin film, due to the difference of thermal expansion

coefficients of film and substrate, due to lattice misfit with the substrate, or due to chemical reaction with the substrate (formation of intermetallic compounds). Extrinsic stress is commonly uniform through the depth.

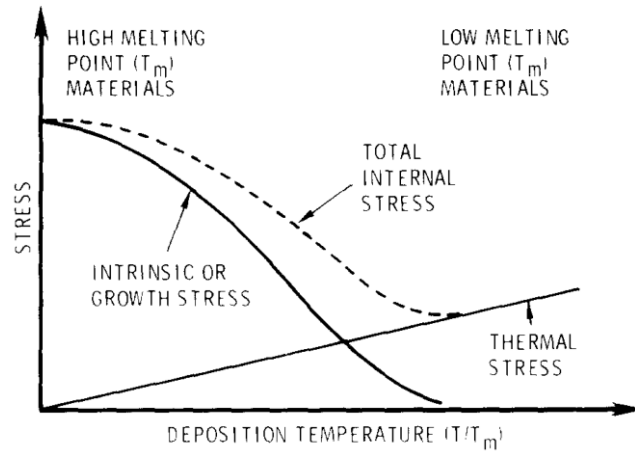


Figure 3.5: Schematic representation of thermal (extrinsic) and intrinsic stress contributions.

Thermal-mismatch stress is the more common source of extrinsic stress and is well understood. It specially arises in structures with inhomogeneous thermal expansion coefficients, subjected to uniform temperature change. The Figure 3.6 is called to explain the causes and effects of thermal-mismatch stress in thin films.

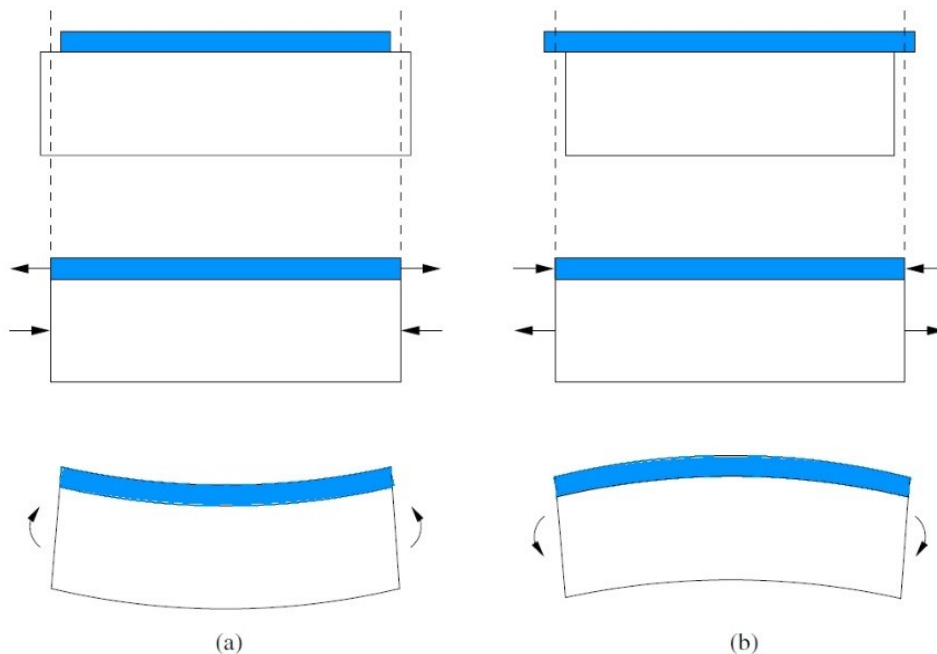


Figure 3.6: Explanation of tensile (a) and compressive (b) residual stress in thin film.

When a thin film is deposited on a thick substrate at elevated temperature, and subsequently cooled and operated at ambient temperature, the difference between the thermal expansion coefficients of the film and substrate creates stress and strain. If after deposition the growing film initially shrinks relative to the substrate the case shown in the Figure 3.5a occurs. If the thermal expansion coefficient of the substrate is lower than that of the film, the film is constrained during deposition and stretches after, while the substrate accordingly contracts. If the structure is free to move, it will elastically bend to counteract the unbalanced moments. Thus, films containing internal tensile stresses bend the substrate concave upward (Figure 3.5a). Similarly, compressive stresses lead their origin from films that tend to initially expand relative to the substrate and bend the substrate convex outward (Figure 3.5b).

The extrinsic stress can be evaluated knowing the thermal expansion coefficients of the thin film and substrate materials. The thermal expansion coefficient of a material is defined as

$$\alpha = \frac{d\varepsilon}{dT} \quad (3.3)$$

Assuming that the thermal expansion coefficients are temperature independent, the strain caused by thermal expansion is

$$\varepsilon(T) = \varepsilon(T_0) + \alpha_s \cdot \Delta T \quad (3.4),$$

where the first part of the equation is assumed to be negligible and the last part is the strain caused by thermal expansion.

As the substrate is very thick compared to the film, is possible to assume that the substrate contracts to the size it would have attained in absence of the film:

$$\varepsilon_s = -\alpha_s \cdot \Delta T \quad (3.5),$$

where α_s is the coefficient of thermal expansion of the substrate, and the minus means the compression of the film. The film reaches the same strain, due to the fact that it is attached to the substrate:

$$\varepsilon_{f,attached} = -\alpha_s \cdot \Delta T \quad (3.6)$$

If the film was unattached (free), however, its strain would be

$$\varepsilon_{f,free} = -\alpha_f \cdot \Delta T \quad (3.6)$$

Then the thermal mismatch strain is:

$$\varepsilon_{f,mismatch} = \varepsilon_{f,attached} - \varepsilon_{f,free} = (\alpha_f - \alpha_s) \cdot \Delta T \quad (3.7)$$

Due to the Equations 3.2 and 3.7 the thermal mismatch stress in a case of biaxial system can be presented:

$$\sigma_{f,mismatch} = \frac{E}{1-\nu_s} (\alpha_f - \alpha_s) \cdot \Delta T \quad (3.8)$$

The *intrinsic stress* reflects the internal structure of a material during its deposition. Its understanding is less evident than the one of the thermal stress. In most cases, intrinsic stress is non-uniform through the depth and is therefore responsible of stress gradient. The intrinsic stresses in thin film are similar to internal stresses in bulk material, formed during cold working. In a case of cold working, the stresses result from the strain, which is associated with different lattice defects created by deformation. The density of defects that are “frozen” in a film during deposition is orders of magnitude higher than that produced by cold working of bulk material [44]. Dislocations and grain boundaries are the most common defects in thin films.

The microstructure and thus the intrinsic stresses in vacuum deposited films depends drastically on deposition conditions, including deposition rate, deposition temperature, pressure in the deposition chamber, incorporation of impurities during growth, grain structure, fabrication process defects, etc.

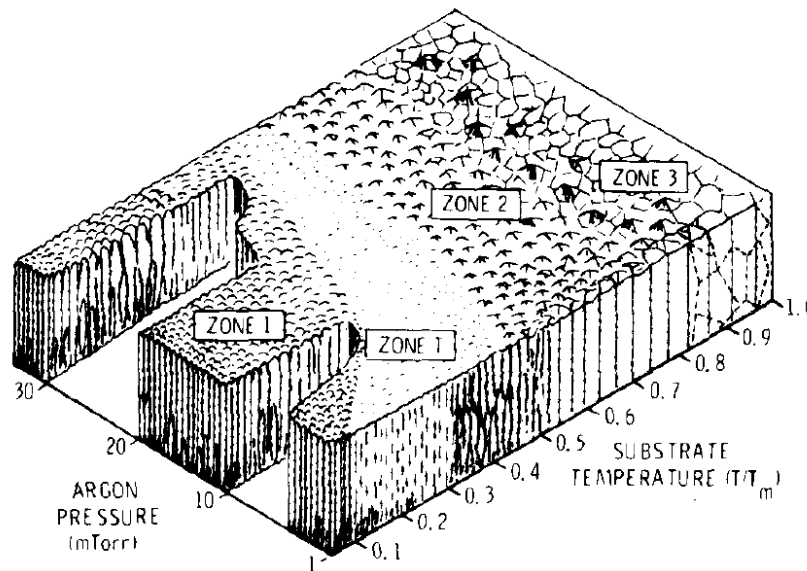


Figure 3.7: Thornton's Structural Zone Model

The growth of vacuum-deposited coatings involves atoms (arriving in a distribution that depends, through self-shadowing, on atom arrival directions and coating surface roughness) and their diffusing over the surface until they become trapped in low energy lattice sites and

are incorporated into the growing coating [44]. Finally, the deposited atoms can change again their positions in the coating by recrystallization. The occurrence of recrystallization is guided by deposition pressure homologues temperature:

$$T_h = \frac{T}{T_m} \quad (3.9),$$

where T is the temperature during vacuum deposition and T_m is melting point of material deposited. The Figure 3.7 present the famous Thornton's Structure Zone Model (SZM), relation of recrystallization on pressure and temperature of deposition [45].

Zone 1 represents the situation at elevated pressure and low temperature, when atoms arriving to the substrate in randomized directions (causing shadowing) due to numerous collisions with gas atoms. The structure is columnar with high distance between the grain boundaries. It is corresponding to high tensile stresses.

Zone T is more evident for lower deposition pressures. Such coatings are formed when the flux of atoms arriving is mainly normal to the surface. Zone T can be associated to large intrinsic stresses.

Zone 2 dense structure consists of big columnar grains with small distance between grain boundaries.

Zone 3 is a bulk-like material. Such coating is usually created at elevated temperatures. Recrystallization limits the intrinsic stresses both in Zone 2 and in Zone 3 coating.

3.1.2.3 Stress evolution during film growth

Most polycrystalline films grow via a Volmer-Weber (VW) mode, where the growth process is divided into three stages of evolution: discrete island nucleation and growth, coalescence and percolation of the island network, and planar film growth. Each of these regions has a distinct stress profile, with the stress often going through a compressive, tensile, compressive evolution during the respective phases (see Figure 3.8).

First crystallites of critical size nucleate on the surface of the substrate as isolated islands. During this phase compressive stress is generated, associated with high pressure due to surface tension [46] decreasing the lattice parameter in respect to normal bulk materials. As the islands grow in diameter, they impinge to form a network of islands, eventually coalescing into a continuous polycrystalline film. As two islands impinge and form a grain boundary at their intersection, part of the free surface of each island is eliminated, resulting in a significant energy reduction. According to Hoffman [44] if neighboring islands are

within close proximity, they will stretch toward each other to form a grain boundary to reduce the interfacial energy at the expense of an associated strain energy. It was demonstrated that the development of tensile stress is associated with this island coalescence process, with the peak tensile stress that corresponds to completion of coalescence[47].

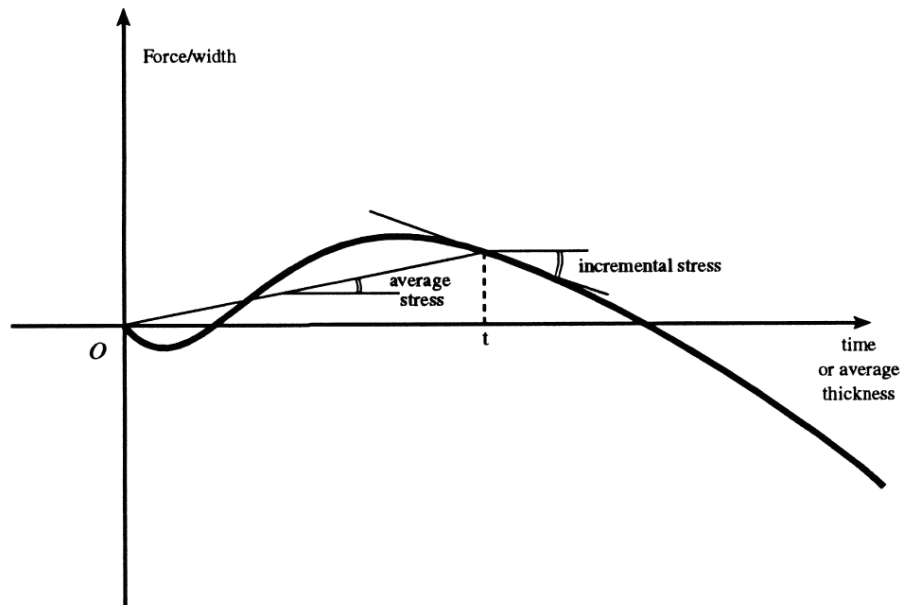


Figure 3.8: Force-per-width curve (proportional to curvature) measured as a function of time/effective thickness during vapor deposition [48].

In both high and low mobility materials the initial tensile stresses are associated with grain boundary coalescence. However, in high mobility materials, the grain boundaries are mobile during coalescence even at room temperature (low melting point materials), thus the coalescence stresses are reduced by means of boundary motion and grain boundary diffusion. Instead, in low mobility materials high tensile stresses are retained, when deposition is performed at lower temperatures, and are increasing with increase of the film thickness (post-coalescence tensile stress).

Compressive post-coalescence stress can be generated in high mobility materials or at high temperatures in low mobility materials and might be associated with incorporation of excess material either in the lattice or in grain boundaries[48, 49].

3.1.2.4 Parameters influencing stress

Stress state in deposited films is caused by mechanisms depending on the energy supplied to the growing film surface. Vacuum deposition parameters vary depending upon the type

of deposition, and in a very general case it can include deposition temperature, pressure in the deposition chamber, deposition rate, bias applied to the substrate, incorporation of impurities during growth.

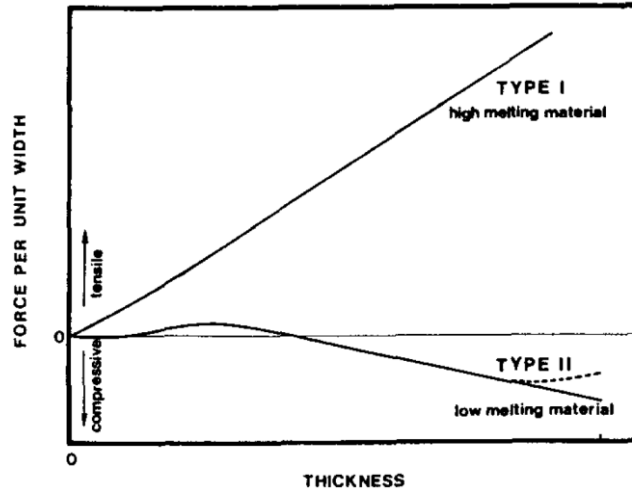


Figure 3.9: Schematic representation of the stress vs thickness curves of high melting (Type I) and low melting (Type II) materials.

In a case of *vacuum evaporation* of low melting point materials (Type II, high mobility materials), the recrystallization (recovery) is happening when deposition is realized at homologous temperatures more than 0.2-0.3, leading to stress relaxation.

In a case of high melting point materials (Type I, low mobility materials) process parameters, as substrate temperature, residual gas level and deposition rate, are becoming very important, but difficult to control. Mainly the stress in such type of evaporated coatings is tensile, not depending strongly on substrate material, increasing with thickness[43]. Compressive stress is observed mainly due to impurities[44].

The substrate temperature influences the kinetic energy of the particles already arrived to the substrate. A low temperature promotes the columnar voided microstructure that is associated with the tensile stress due to grain boundary relaxation mechanism. The size of this contribution is growing with the film thickness. It is larger for smaller grain size films. A high temperature corresponds to an increase of ad-atom mobility that leads to a bulk-like structure and minimization of grain-boundary relaxation induced stress.

As it was presented in a standard Movchan-Demchishin SZM for evaporation[50], Thornton SZM for sputtering (Figure 3.7) there is a temperature corresponding to transition from

voided microstructure of Zone 1 to dense columnar Zone 2 (Zone T). The grain-boundary relaxation induced stress depends on microstructure, as it was mentioned before. It is conversed at a “recrystallization point”, corresponding to transition from Zone 1 to Zone 2 (Zone T).

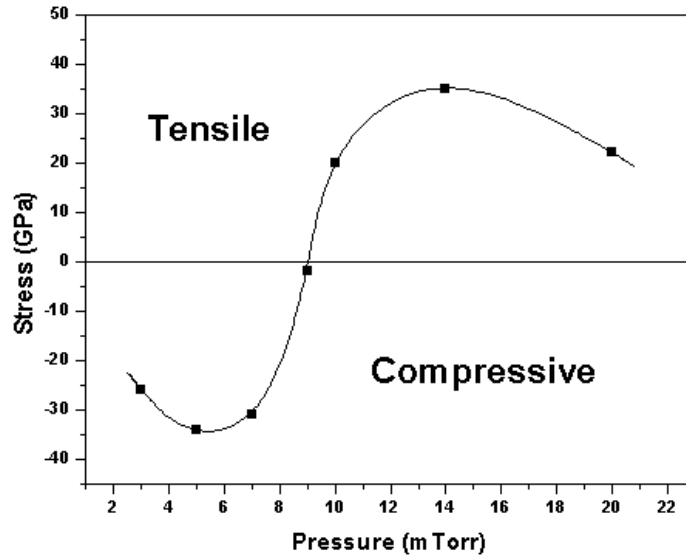


Figure 3.10: General stress-pressure dependency in sputtered thin films

For the evaporated films (Figure 3.9) this stress conversion was described by Abermann [46, 51] as Type I (high melting material or low atomic mobility), that is corresponding to Zone 1 (Zone T) microstructure and Type II (low melting point or high atomic mobility), corresponding to Zone 2 microstructure.

Magnetron sputtering (MS) technique allows controlling the kinetic energy of the particles in order to minimize stress. The main parameters influencing in very general meaning the kinetic energy of atoms deposited, and so influencing the microstructure growth, are sputtering gas pressure, sputtering gas, temperature of the holder, bias, deposition rate, incident angle of deposition, apparatus geometry, distance between the magnetron and the substrate, etc.

The influence of substrate temperature during deposition is very similar to the one described for evaporated coatings. Porous structures deposited at low temperatures yield tensile stresses, and dense films deposited at elevated temperature relax the intrinsic stress due to recrystallization [52].

The general stress-pressure dependence for MS is shown in the Figure 3.10. A gas pressure that signs the transition from tensile to compressive stress for each combination of a

sputtered material and deposition system is called critical pressure. At relatively high pressure, the frequency of the gas phase collision increases, reducing kinetic energy of sputtered atoms and reflected neutrals, bombarding the growing film, exhibiting an open porous microstructure; the interatomic attractive forces produce tensile stress. At low pressure, the arriving atoms have high kinetic energy and the resulting film has a dense microstructure, perceiving compressive stress.

The relation of stress in 200 nm thick Mo films, deposited with Ar plasma by planar DC MS cathode at 7 cm distance from the substrate is presented in the Figure 3.11a. The σ_{11} and σ_{22} are stresses in the plane of the specimen surface in two perpendicular (x - and y -axes) directions[53].

The critical pressure, which separates the compression and tension deposition conditions for different material can be observed from the Figure 3.11b. There the critical pressure for the onset of loss in coating reflectance increases with the atomic mass of the coating material and corresponds approximately to the stress transition pressure [44, 54].

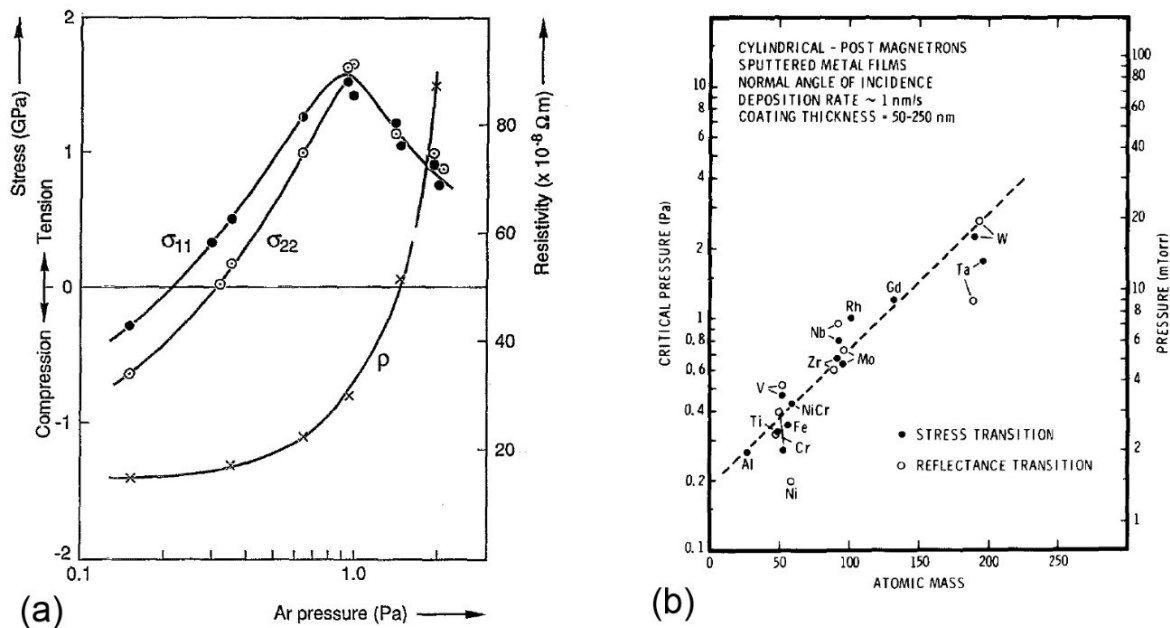


Figure 3.11: (a) Stress-pressure relation in MS Mo films, (b) Dependency of the critical pressure for the compression-to-tension stress transition, and the critical pressure for loss of reflectance, on the coating material atomic mass

The influence of the distance target-substrate is very similar to the effect of sputtering pressure in terms of kinetic energy of particles. When increasing the distance (at the same

pressure), the deposited material atoms suffer more collisions with gas atoms, thus decreasing the energy of atoms deposited.

The influence of the angle of incidence is seen to be strikingly similar to that of the pressure. Compression stresses are seen at near normal incidence. However, above a critical angle that depends on the atomic mass of the coating materials, the coatings are in tension. Continuous rotation of the substrates tends to produce tensile stresses [44].

Compressive stresses were found in coatings deposited in a presence of gas ion bombardment (deposited by bias sputtering) [55, 56]. Biasing is the application of a usually negative voltage to the substrate such that surface bombardment by gas positive ions occurs on the substrate as well as on the target cathode. This causes re-sputtering of the depositing layer or at least an increase in surface energy[57]. These effects also control film growth, improve step coverage profile, and can eliminate some commonly observed defects. Increasing bias voltages will lead to an effect similar to that of reduction of process gas pressure that is increasing the ad-atom mobility, resulting in better films in terms of microstructure[58].

3.1.2.5 Methods to reduce stress

The control of stress in physical vapor deposited films is extremely important because of its close relationship to material technological properties, adhesion strength to the substrate, and the limit of film thickness without cracking, buckling or delamination.

During heating or cooling, very high stresses are induced in the coating when the thermal-expansion coefficients of the films and the substrate vary significantly from each other. Besides optimal choice of deposition pressure, sputtering system geometry, substrate temperature, and several additional methods can be applied to decrease the stress levels.

Some of the methods to reduce the mismatch of thermal expansion coefficients include use of chemically compatible interlayers having intermediate expansion coefficients. These methods to enhance adhesion have been successful in some material systems; however, in very large thermal-mismatched systems, cracking or de-bonding of the coating can still occur. The other opportunity used to decrease the stress levels in ceramics materials, is to insert metallic layer at the beginning of ceramics layer deposition and then continue again with thick layer of ceramics [59].

Karabacak et al. 2005 [60, 61] have reported significant reduction of stress values in sputter deposited tungsten films on Si surfaces by means of nanostructured layer by high working

gas pressures that acts as a compliant layer under the subsequently deposited continuous film grown under low gas pressure. In this way, they have obtained adhesion improvement and higher critical thickness. Besides that, the stress of multilayer film decreases as the total thickness increases. The work of Alagoz et al. [62] is using the same density modulation method for Ru deposition by DC magnetron sputtering at different pressures. The use of different controlled negative bias was proposed for multilayer stress control in CrN films by Daniel et al [63].

Therefore, in the multilayer film deposition, every time a new layer is started, new, isolated crystals are nucleated on the previous layer (re-nucleation); in this case, there is a small stress associated with the beginning of each layer, as there is for deposition on a fresh substrate. It is therefore quite possible to have re-nucleation of each layer in the fabrication of the multilayers. By tailoring the precise thickness of the individual layers, it is possible to produce multilayered films with minimal stress [48].

3.1.2.6 Methods to measure stress

The most well-known method of stress measurements is a **substrate curvature method**. In practice, it can be realized as in situ monitoring deflection of cantilever onto which film is deposited (stress corresponding to deposition time/film thickness) by optical interferometry, laser beam reflection, change of electrical capacitance between the surfaces. Otherwise, an ex situ curvature measurement of flexible the substrate after deposition, or film itself detached from the substrate after deposition can provide the total stress in the film.

The measurement of stresses in thin films by the measurement of curvature of narrow strips usually relies on the modified Stoney formula[64]:

$$\sigma^{(f)} = \frac{d_s^2}{6 \cdot d_f} \cdot \frac{E_s}{(1-\nu_s)} \cdot \frac{1}{R} \quad (3.10),$$

where E_s is substrate Young's modulus, d_f and d_s are the film and substrate thicknesses correspondingly, R is the radius of curvature of the coated substrate, and ν_s is Poisson's ratio of the substrate. If the substrate itself is not planar, formula should be modified, using the radius of curvature of the substrate R_s :

$$\sigma^{(f)} = \frac{d_s^2}{6 \cdot d_f} \cdot \frac{E_s}{(1-\nu_s)} \cdot \left(\frac{1}{R} - \frac{1}{R_s} \right) = \frac{d_s^2}{6 \cdot d_f} \cdot \frac{E_s}{(1-\nu_s)} \cdot (K - K_s) \quad (3.11)$$

The notion curvature (K and K_s correspondingly) can be used instead of radius of curvature. Stress measured by Stoney method is an average stress since it is obtained by integrating the stress over the section or more precisely, over the thickness of the beam. If the thin film has

an intrinsic stress or stress gradient, the Stoney calculated stress would be the average stress present at the middle of the beam, at the neutral axis, taking therefore into account, the effect of the gradient.

Compressive and tensile stresses in curved substrate vanish since stress is relaxed when bending. The stress is replaced by relaxed strain expressed in this case by the curvature of the substrate. Thanks to this curvature, the stress can be measured. Without it, it would be impossible to extract the residual stress because the film would stay constrained. The curvature measurement therefore gives the residual stress the thin film would have, if it was not able to be relaxed.

Relaxation processes, such as plastic flow, creep, and micro cracking, can act to reduce coating stress. This combined with the fact that their extent may vary as a function of depth, can complicate the prediction of coating stress. Furthermore, it can often be difficult to determine the elastic properties of coatings that in reality could be different from ones of bulk material.

The stress, due to the atom displacement (strain) can be also measured by **XRD-techniques**. During a measurement the specimen is irradiated with high energy X-rays that penetrate the surface, the crystal planes diffract some of these X-rays, according to Bragg's law and a detector, which moves around the specimen to detect the angular positions where diffracted X-rays are located, records the intensity of these rays at that angular position. The location of the peaks enable the user to evaluate the stress within the component. The displacement of the peak in the spectrum is related to modification of lattice parameter in respect to bulk not stressed material. However, this method does not take into account the film morphology effects, the effect of high concentration of lattice defects and the grain boundaries.

Depth-resolved residual stress analysis was proposed by Sebastiani et al. [65-67] based on semi-destructive **focused ion beam (FIB) ring-core milling**, combined with high-resolution in situ SEM-FEG imaging of the relaxing surface and a full field strain analysis by digital image correlation (DIC).

Besides the division to extrinsic and intrinsic, residual stresses in thin films can be defined as either macro or micro stresses and both may be present in a component at any time [12]. **Macro residual stresses** vary within the body of the component over a range much larger than the grain size. **Micro residual stresses**, which result from differences within the microstructure of a material, can be divided into micro residual stresses that operate at the grain-size level and generated at the atomic level. Micro residual stresses often result from

the presence of different phases or constituents in a material. They can change sign and/or magnitude over distances comparable to the grain size of the material under analysis. Thus, XRD techniques are providing the information on micro-residual stress. Macro residual stresses are estimated by substrate curvature method.

3.1.3 Protective coatings engineering

3.1.3.1 Diffusion barriers

As it was already declared, the chemical inertness of solid cyclotron target backing plate both to dissolution media for target processing after irradiation and for aggressive liquid metal coolants (if such configuration is chosen) is absolutely required. The chemically inert materials are usually expensive and can decrease the target performance by low thermal conductivities. The combination of high thermal conductivity backing plate, covered with a chemically resistant protective layer can be a good solution.

Unfortunately, the chemical inertness of protective coating material is not guaranty of its efficiency. Thus, several additional requirements have to be followed. It is obvious, that first necessary demand for a protective coating is the uniformity in order to guarantee the same corrosion rate. Any extended defects, such as pores, pin-holes and grain boundaries are of primary significance for thin film barriers because they offer paths which can carry foreign atoms rapidly across the films thereby dominating the atomic traffic [68].

On the other hand, diffusion through the amorphous layers is very difficult due to the irregularity of the atomic structure[69]. The high corrosion resistance of amorphous alloys is explained by the absence of the typical structural defects of a crystalline state, such as dislocations, grain boundaries, second phases, precipitates and segregates[70].

Therefore, the approach in efficient diffusion barrier coatings production include, from one side, maximum packing and densifying the structure of the coatings, and, from the other side, the tendency to create the protective films with amorphous microstructures.

3.1.3.2 Methods to obtain amorphous films by sputtering

Several approaches in order to sputter amorphous metallic film have been applied in the past, such as deposition at low temperature, alloying with other elements, gas admixture, deposition at high deposition rate and use of a substrates with amorphous structure[71].

Cooling of a substrate at cryogenic temperatures during sputter deposition decreases the mobility of atoms arriving to the substrate. Whereas the heat of condensation is absorbed

without essential rise in temperature, crystalline growth is inhibited resulting in amorphous structure. Thus aluminum and aluminum-copper alloy amorphous like films have been deposited at temperatures lower 30 K using He, Ne, Ar as sputtering gases[72].

As far as the monoatomic amorphous films are not stable at room temperatures, alloying is used to increase the thermodynamic stability of a system. Thus sputtered films of niobium and manganese alloys with 40÷75 Nb content have been found amorphous by XRD investigation, whereas pure Nb and pure Mn films were crystalline[73].

Admixture of different gases, such as helium[74], hydrogen[75] and oxygen[76] in a metal has been found to decrease the degree of film crystallinity. Thus amorphous Ni, Fe, Au films were deposited by getter-sputtering using both approaches: low deposition temperature, and the incorporation of large amounts of helium gas into the film[74]. Amorphous Yb-H films with 40-55% H₂ contamination were deposited by vapor condensation in extra high vacuum[75]. Amorphous-like tungsten films were prepared by oxygen admixture during sputtering[76].

Increase of the deposition rate, maintaining cooling of a substrate, can reduce the adatom migration mobility, resulting in a less ordered structure than the one obtained by conventional deposition methods[77].

3.1.3.3 Sputtering recipes of a packed structure

There are several approaches known to be effective to achieve a compact coating structure. High temperatures are known to promote the grain growth and result in more packed structure due to the increased ad-atom mobility. At certain high temperatures of deposition, films can achieve even bulk-like microstructures.

Ion bombardment of a surface can liberate neutral and charged species from a surface, as well as change the physical, electrical, and chemical properties of a surface[78]. The momentum exchange associated with ion bombardment can cause surface rearrangement, which can have dramatic effects on the structure and properties of a growing film. The most well-known example of low-energy ion irradiation during film deposition is negative biased sputtering.

Unbalanced magnetron sputtering (UBMS) and High Power Impulse Magnetron Sputtering (HiPIMS), are well known methods used to increase the degree of plasma ionization and respectively to control the growing film microstructure.

3.2 Vacuum brazing

The following chapter presents an overview of brazing theory and other relevant concepts that support this research. Fundamentals of brazing, metal-ceramics brazing, surface treatments, joint design, heating methods are presented in this chapter.

3.2.1 Fundamentals of brazing

The term brazing comprises a group of welding processes that produce binding of materials by heating them to the brazing temperature in the presence of a filler metal having a liquidus above 450 °C (890 °F) and below the solidus of the base material. The brazing filler metal turns liquid and is distributed between the closely faying surfaces of the joint by capillary action, then creates an alloy bond with the faying surfaces. Brazed joint could be strong as, or stronger than, the base materials: this depends on the design of the joint and the filler metal.

Strong, uniform, high thermally conductive, leak-proof joints of the same or different metals can be made fast, inexpensively, and even simultaneously. Joints that are inaccessible and parts that may not be joinable by other methods often can be joined by brazing.

There are several physical principles, which are important for the brazing process.

Capillary motion is the ability of a liquid to flow in narrow spaces without the assistance. Capillary motion is the dominant physical phenomenon that ensures good brazing joints when both faying surfaces to be joined are wet by the molten filler metal. The capillary acts because of the relative attraction of the molecules of liquid to each other (surface tension) and those of the solid (adhesive forces) influence the brazing filler metal flow. The joint must be properly spaced to permit efficient capillary motion and coalescence. In actual practice, brazing filler metal flow characteristic are also influenced by dynamic considerations involving fluidity, viscosity, vapor pressure, gravity, and, especially, by the effect of any metallurgical reactions between the filler metal and the base material [79].

The ability of a liquid to maintain contact with a solid surface is called *wetting*; this is the result of intermolecular interactions between solid and liquid. Wettability describes the degree of wetting of the solid by particular liquid rather than another. The phenomena of wetting and spreading are very important for the formation of brazed joint. High wettability guarantees that liquid brazing filler metal is going to adhere to the surface of the material in the solid state and, when cooled below its solidus temperature, to make a strong bond with this material. Wetting is a function not only of the nature of the filler metal, but the degree

of interaction between materials to be joined. There is considerable evidence that in order to wet well, a molten metal must be capable of dissolving or alloying with some of the metals through which it flows [79]. Another factor that affect wetting is represented by the impurities on the surfaces to be wetted. Oxide layers inhibit wetting and spreading, as do grease dirt, and other contaminants, that prevent good contact between the brazing filler metal and the base materials.

Diffusion is the net movement of molecules or atoms from a region of high concentration (or high chemical potential) to a region of low concentration (or low chemical potential). This phenomenon occurs when a system is not in equilibrium. Base material and filler metal interact through diffusion, the atoms of the filler metal in liquid state diffuses into the base material forming diffusion-bonds. The rate of diffusion is proportional to the temperature. At brazing temperatures, the possibility of diffusion is very high. Diffusion of the filler metal into the base metal should be at a minimum for the best joint quality, and diffusion can be minimized by minimizing the heat input at brazing temperature [80].

In a properly designed brazing process, an oxide-grease-free surface guarantee wetting and spreading of the filler metal. In a suitable joint design, the molten filler metal is drawn completely through the joint area without any voids or gap, at the right temperature and time, the diffusion occurs, and the filler metal diffuse into the base material forming bond which will keep the junction.

3.2.1.1 Filler-metal characteristics

Most of the brazing filler are alloys which melt in a range of temperature and depending of the base-metal properties can react or not during the brazing process. Several metal-filler base materials are describes in the Table 3.1.

Several characteristics desirable in a filler-metal are:

- Proper fluidity at the brazing temperature to ensure flow by capillarity action and provide full alloy distribution. A high liquid surface tension, low contact angle, low viscosity are desirable for promoting filler-metal flow.
- Ability to alloy or combine with base metal to form an alloy with higher melting temperature.
- Stability to avoid anticipatory release of low-melting-point elements for filler metals at brazing temperature.

Table 3.1 Metal-filler base materials for brazing

Base material	Nickel (Ni)	Cobalt (Co)	Silver (Ag)	Gold (Au)	Aluminum (Al)	Copper (Cu)
Braze range (°C)	927-1205	1175-1245	620-980	890-1230	570-620	705-1150
Max service temperature (°C)	980	1040	370	800	150	370
Applications	Alloy steels Carbon Steels Copper Alloys Stainless Steel Nickel-Cobalt alloys	Cobalt alloys	Alloy steels Carbon steels Cast iron Copper alloys Nickel alloys Stainless steel Tool steels	Alloy steels Carbon steels Cooper alloys Nickel-cobalt alloys Stainless steels Tool steels	Aluminum alloys	Alloy steels Carbon steels Cast iron Cooper alloys Nickel alloys Stainless steels Tool steels

The ability to wet the base-metal joint surface, a low contact angle, which implies wetting, is necessary but is not a sufficient condition for flow, because viscosity of the filler metal is also important.

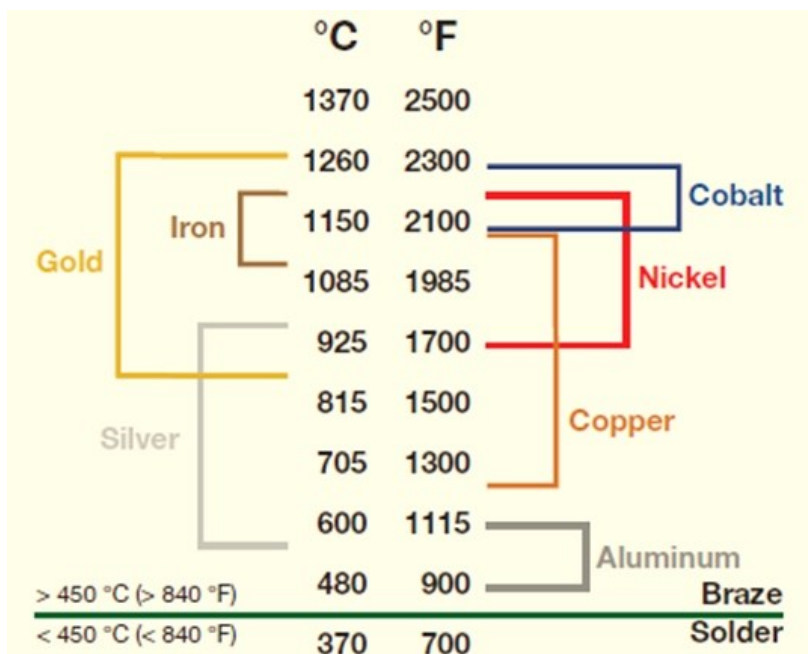


Figure 3.12: Typical brazing temperature ranges for various filler metals.

The joint strength depends on many factors as joint design, state of stress, brazing temperature, heating rate, holding time at the peak temperature, amount of filler metal used, location and method of application, and many others.

Diffusion is an essential part of the metallurgical process. The filler metal is selected able to diffuse readily and alloy with base metal.

The melting method used and working temperature in brazing process is related directly to the strength of the brazed-joint. Filler metals in which the solidus and liquidus are close together do not usually exhibit a strong tendency to separate and they are relatively fluid, the Figure 3.12 presents typical brazing temperature ranges for various filler metals.

Depending on the application, other important filler-metal properties are corrosion resistance (such as oxidation and environmental or galvanic corrosion with other part of the assembly), electrical and thermal conductivity, hardness and machinability, ductility, color match to base metal, etc.

The filler-metal must be able to form a strong and permanent bond with the base materials, but this can be difficult to achieve when oxides are present in the brazing joint. Brazing ceramics, such as alumina is the extreme case of such situation. The oxide make difficult wetting over its surface and the filler-metal does not diffuse correctly.

If the base materials not wetted by “conventional” brazing, a reactive metal (usually Titanium) is added into metal-filler, the addition of reactive metal to several braze alloy compositions results in increased reactivity and considerable improvement in wetting behavior. In ceramics brazing case, the reactive metal (titanium) act as strong “getter” of oxygen, that means joining process will depend very much on the ability of titanium in the filler to react at brazing temperature with these oxides that are present in the ceramic structure.

Since reactive metal (titanium) will react with any oxygen contamination of the process with free oxygen or water vapor in the furnace atmosphere, or with metal-oxides on the metal surfaces during heat-up, should be minimized. To avoid poisoning of reactive metal during this high-temperature joining process, it is wise to use a good vacuum brazing furnace with vacuum levels of about 10^{-5} - 10^{-6} torr. Additionally, the vacuum furnace should be very clean, with no significant contamination on the inner cold-walls of the chamber.

3.2.1.2 Base-material characteristics

The base metal has an important effect on joint strength; a high-strength base metal produces joints of greater strength than those made with softer base metals. The larger number of complex metallurgical reactions in metals can cause changes in the base-metal hardenability and residual stress, therefore the joint strength become less predictable.

The coefficient of thermal expansion (CTE) is another important parameter because the differences of CTE's of the components of brazing joint generate the residual stress that may produce distortion, depending on the joint design and can affect the strength of the joint.

Several metallurgical phenomena influence the behavior of brazed joints. Among them are alloying, carbide precipitation, stress cracking, and oxide stability.

The brazing cycle by itself can affect the properties of the base metal, if the brazing-process temperature and time are in the annealing range of a reinforced by cold working alloy, this will be annealed and the joint strength reduced.

One of the advantages of brazing process is the possibility to joint dissimilar metals or even metal and ceramics. These inorganic and non-metallic materials have very different properties from metals, normally, higher melting temperature, lower thermal expansion coefficient. The oxide on its surface avoids the wetting by most of filler metals. In this case, is needed to select the right filler metal, the right method and consider the difference of the properties between the materials in order to avoid the residual stress.

3.2.2 Metal-ceramics brazing

The often request for high technology applications is joining dissimilar materials. Metal-ceramic brazing is the only solution for fabricating high-reliability devices such as those used in high-voltage applications or requiring hermetically sealed joints.

Joining different materials is usually a complicated task. Atoms, ions, or molecules in materials of different classes are joined together in different ways, and therefore characterized by particular combinations of physico-chemical and mechanical properties. Joining dissimilar materials introduce structure discontinuities and properties mismatch. In metal to ceramic brazing, the process relies on wetting of the ceramic surface by some kind of metal, which is often hindered by the covalent nature of the ceramics. Besides that, the differences in thermal expansion coefficient result in the development of residual stresses, which can become a problem for the integrity and quality of the final piece.

Metal-to-ceramic brazing can be realized by several methods, among them the application of metallic layer onto the ceramic surfaces or brazing directly to the unmodified ceramic surface (oxide) using active brazing alloys. There are several metallization methods, the most used for joining metal to ceramic are molybdenum-manganese/nickel plating and physical vapor deposition or thin-film method[81].

3.2.2.1 Molybdenum-manganese/nickel plating method

This method is also known as moly-manganese (Mo-Mn) metallization. A coating of molybdenum and manganese particles mixed with glass additives and volatile carriers (Mo-Mn paint) is applied onto the ceramic surface to be brazed. After air-drying; the coating is heated in a wet hydrogen environment ($15^{\circ}\text{--}30^{\circ}\text{C}$ dew point) at $1450^{\circ}\text{--}1600^{\circ}\text{C}$ producing a “glassy” metallic coating $7\text{--}12\ \mu\text{m}$ thick.

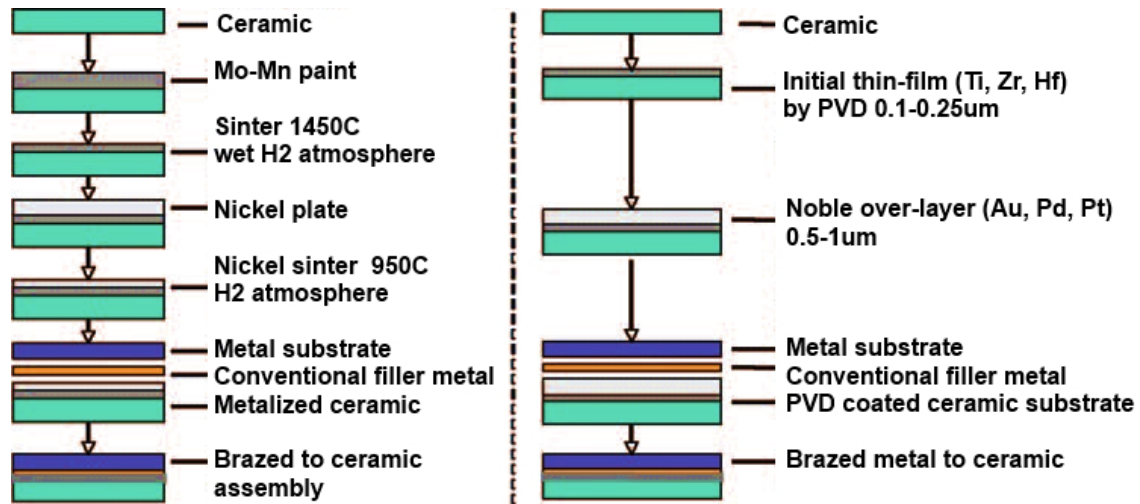


Figure 3.13: Moly-manganese (left) and thin film (right) metallization processes.

Sintered coating is after plated with a $25\text{--}75\ \mu\text{m}$ layer of nickel. The nickel plating is then sintered at $850^{\circ}\text{--}950^{\circ}\text{C}$ in a dry hydrogen atmosphere (-50°C dew point or less) producing metallic surface ready to braze using standard braze filler metals [81].

3.2.2.2 Thin-film method

One material or a combination of materials are deposited onto the non-metallic surface using a physical vapor deposition (PVD) method, such as evaporation or sputtering. The first layer deposited, often titanium, is typically $0.25\text{--}1\ \mu\text{m}$ thick. Other oxygen-getter elements such as hafnium, zirconium, chromium, niobium, etc. may be chosen instead of Ti depending on the application and service temperature.

Occasionally, an intermediate layer or layers are deposited to prevent unwanted metallurgical reactions between the initial metal layer and the braze filler metal. The top, or outer, layer is normally a noble metal such as gold, platinum, or palladium that is $0.25\text{--}1.0\ \mu\text{m}$ thick. A noble metal is chosen in order to prevent the underlying layer from oxidizing

and subsequently preventing proper brazes filler metal wetting and flow [81]. The Figure 3.13 summarizes both moly-manganese and thin-film metallization processes.

3.2.2.3 Active filler-metal brazing

Active filler metals provide good wetting of most ceramic materials. Active filler metal brazing is a metal-ceramic joining method that permits to use the standard brazing techniques when making metal-to-ceramic brazing without applying any metallization to the ceramic substrate[82]. The scheme of the process is demonstrated on the Figure 3.14. The metal and non-metal substrates are cleaned, and the active filler metal is applied between the faying surfaces of base materials. The brazing operation is usually performed in an inert or ultrahigh vacuum environment, this because excessive oxygen in the atmosphere can react with the active element in the active braze filler metal (usually Ti) and compromise joint strength and integrity [83].

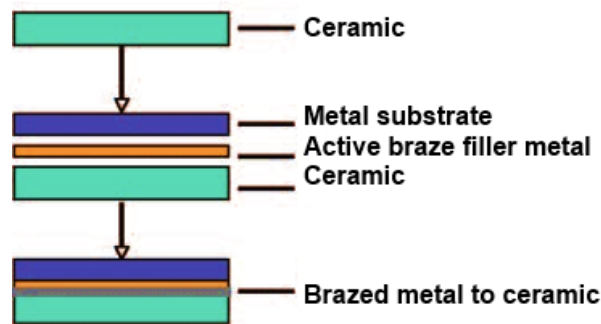


Figure 3.14: Active filler-metal brazing process.

3.2.3 Pre-brazing considerations

Many factors can deteriorate the quality of the brazing joint. Among them is the presence of oxide, grease or dirt, a wide clearance, extensive exposure to high temperature, etc. In order to avoid these factors some considerations have to be done before the process:

3.2.3.1 Surface preparation

In order to obtain uniform quality in brazing process is strongly required to have a clean and nearly oxide-free surface. All grease, oil, wax, dirt, and nearly all oxide have to be carefully removed from the base metal and filler before brazing. It is important to remember that metal surfaces are usually coated with a thin layer of oxide crystals formed by reactions with other metals or with oxygen from air. Only after penetration through the metal oxide layer, the

atoms of metal itself are starting to be involved into process and the bonding can be achieved. The main effort in surface preparation is devoted to removing those materials. Moreover, brazing is recommended to be done as soon as possible after cleaning and etching[79].

Cleaning is commonly divided into two major categories: chemical and mechanical. Chemical cleaning is the most effective, means the removing all traces of oil or grease. Those vary from simple manual immersion to complex multistage operations. Chemical methods include solvent cleaning, alkaline cleaning, vapor degreasing and acid pickling. The selection of the chemical cleaning agent depends on the nature of the contaminants, the base metal, the surface condition and the joint design. After, it is important to control that all residues of surface film are removed from the cleaned parts by adequate rinsing to prevent the formation of undesirable films on the faying surfaces.

Mechanical cleaning may be adequate, in cases, when the design permits it: the most used mechanical methods are dry and wet abrasive blast cleanings. The purpose of blasting is to remove all oxide films and to roughen the surfaces in order to increase the wettability by the filler metal.

Another technique of surface preparation is the use of solid or liquid fluxes; compounds, which prevent, dissolve or facilitate removing of oxides and other undesirable surface substances. It is a very well known method for non-vacuum brazing.

3.2.3.2 Filler metal selection

The selection of the filler metal is one of the most important of the pre-brazing considerations. The selection of an unsuitable filler metal can bring to complete failure of the process.

When selecting a braze filler metal, there are important factors to consider. They include the base metals, the brazing process, the design of the joint and method to apply the braze filler metal, the environment of the service of the joint.

The base metals to be joined. Each of the braze filler metals is designed for use with specific base metals and combinations of base metals.

The brazing process to be used. The filler metal should be selected considering the brazing method available, means that brazing system must be able to provide necessary brazing temperature.

The design of the joint and method to apply the braze filler metal. There is a limited number of ways the braze filler metal can be introduced between the base metal faying surfaces. The

filler may be pre-placed prior to heating in the joint, or manually face fed after heating. The joint design and brazing process will drive the selection of way to apply the filler metal.




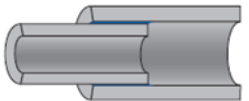

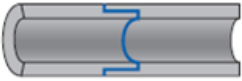

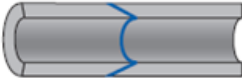
The environment of the service of the joint. The work temperature, corrosion environment, stress conditions, electrical and thermal conductivities, etc. are considerations to take into account when selecting the filler metal.

3.2.3.3 Joint design and clearance

The quality and strength of a brazing joint depends on many factors. Among them, the design of a brazed joint that requires some special considerations dictated by the nature of the joining process.

Since distribution of the molten filler-metal during brazing depends on the principle of capillary, joint clearance, joint type and bonding areas (in simplified mode giving information on capillary size) are critical factors affecting the brazing process. Both of these affect not only the strength of the completed joint but also the ease of brazing [79].

Table 3.2 Common types of brazed joints

<i>Joint type</i>	<i>Flat parts</i>	<i>Tubular parts (cutaway)</i>
Butt joint		
Lap joint		
Butt-Lap joint		
Scarf Joint		

There are, basically, only two types of brazed joints: butt and lap. All other joints are just the modifications of these two basic types.

The preparation for brazing of a *butt joint* is relatively simple, and the joint has sufficient strength for many applications. The main disadvantage is that the thinnest member dictates the maximum strength of the joint. Some advantages of the butt joint are ease of preparation and single thickness at the joint, which reduces stress concentrations.

The bonding area of a *lap joint* can be made larger than that one of a butt joint. In fact, the area of overlap can be varied so that the joint is as strong as the weaker member is, even

when a lower-strength filler metal is used or when small defects are present in the final braze. The lap joint has a double thickness at the joint, but the load is transmitted primarily as shear stress, which is desirable.

The *butt-lap* and the *scarf* joint are attempts to combine the advantage of a single thickness with maximum bonding area and strength. It requires more complicated preparation than straight lap or butt joints and cannot be applied to thin pieces.

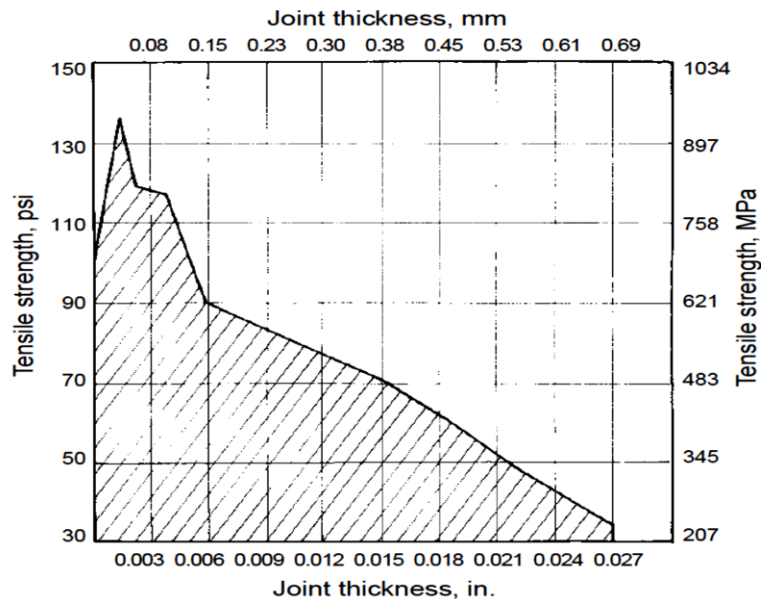


Figure 3.15: Tensile strength versus joint clearance.

The *clearance* is the distance between the faying surfaces to be joined. It is the most important design consideration to achieve a good brazed joint. The clearance affects the mechanical performance of the final piece and is strongly related to the amount of intermetallic phases present in the layers, the probability of voids creation, the tensile strength of the final piece and the capillarity action important for filler metal distribution. The relation between the tensile strength and the joint clearance is shown in the Figure 3.15 [79]. The smaller the clearance, (if there is extensive alloying or erosion) the easier, for capillarity, to distribute the filler metal throughout the joint area, and less the probability that voids or shrinkage cavities will form when the filler metal solidifies. Small clearances and correspondingly thin filler-metal films make stronger joints. The Table 3.3 shows acceptable joint clearances for various filler-metal systems [79].

Other factors influencing optimal joint gap with a specific filler metal are joint length, brazing temperature, and base-metal reactions.

In the design of a suitable joint is important to take into account that an assembly expands during heating and that the joint gap may either widen or close by the time when the filler metal starts to melt and move. Moreover, ensure that the filler metal amount is enough to absorb room-temperature tensile stresses in order to compensate for any reduction in joint gap.

Table 3.3 Brazing joints clearances for different filler metals group and process.

Brazing filler-metal system	Joint clearance, mm (in.)
Al-Si alloys(a)	0.15–0.61 (0.006–0.024)
Mg alloys	0.10–0.25 (0.004–0.010)
Cu	0.00–0.05 (0.000–0.002)
Cu-P	0.03–0.13 (0.001–0.005)
Cu-Zn	0.05–0.13 (0.002–0.005)
Ag alloys	0.05–0.13 (0.002–0.005)
Au alloys	0.03–0.13 (0.001–0.005)
Ni-P alloys	0.00–0.03 (0.000–0.001)
Ni-Cr alloys(b)	0.03–0.61 (0.001–0.024)
Pd alloys	0.03–0.10 (0.001–0.004)

(a) If joint length is less than 6 mm (0.240 in.), gap is 0.12 to 0.75 mm (0.005 to 0.030 in.). If joint length exceeds 6 mm (0.240 in.), gap is 0.25 to 0.60 mm (0.010 to 0.024 in.). (b) Many different nickel brazing filler metals are available, and joint-gap requirements may vary greatly from one filler metal to another.

3.2.3.4 Heating methods

Effective capillary requires efficient transfer of heat from the heat source into the joint. The rate of heating, thermal gradients, cooling rates, the size of individual assemblies, and the rate of production are factors influencing in the selection of the heating method.

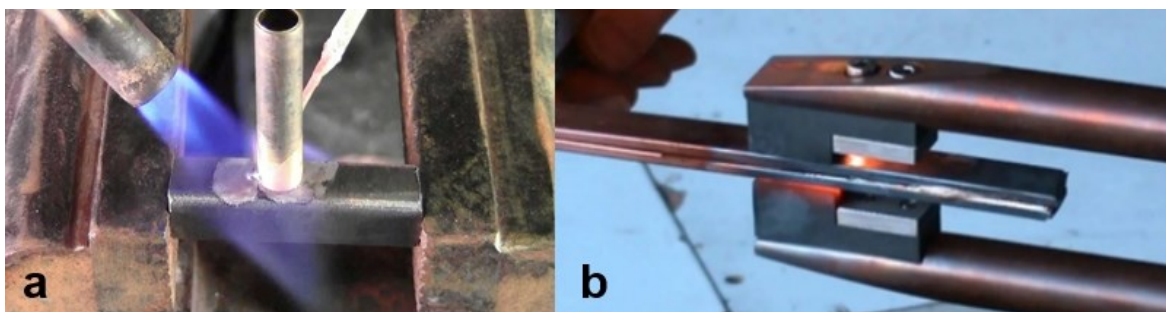


Figure 3.16: Different brazing methods: a) torch brazing, b) resistive brazing.

There are six methods commonly used for brazing process:

Torch brazing: Manual torch brazing is the most frequently used method thanks of its relatively low cost and portability. A torch is used to focus flame at the joint. Normally, a reducing flame is used to prevent oxidation. The flame is generated by the combustion of a combination of oxygen and a fuel gas. The process requires the use of special fluxes in order to avoid oxidation to remove the contaminants after process (see Figure 3.16a).

Induction brazing: The heat is generated in electrically conductive object by electromagnetic induction through the eddy currents. The parts are pre-loaded with the filler metal and placed in a high frequency AC field (from 5 to 5000 kHz). High frequency power source provides surface heating, lower frequency causes deeper heating into the workpieces. The example of inductive brazing of copper tube to brass fitting is presented in the Figure 3.17a.

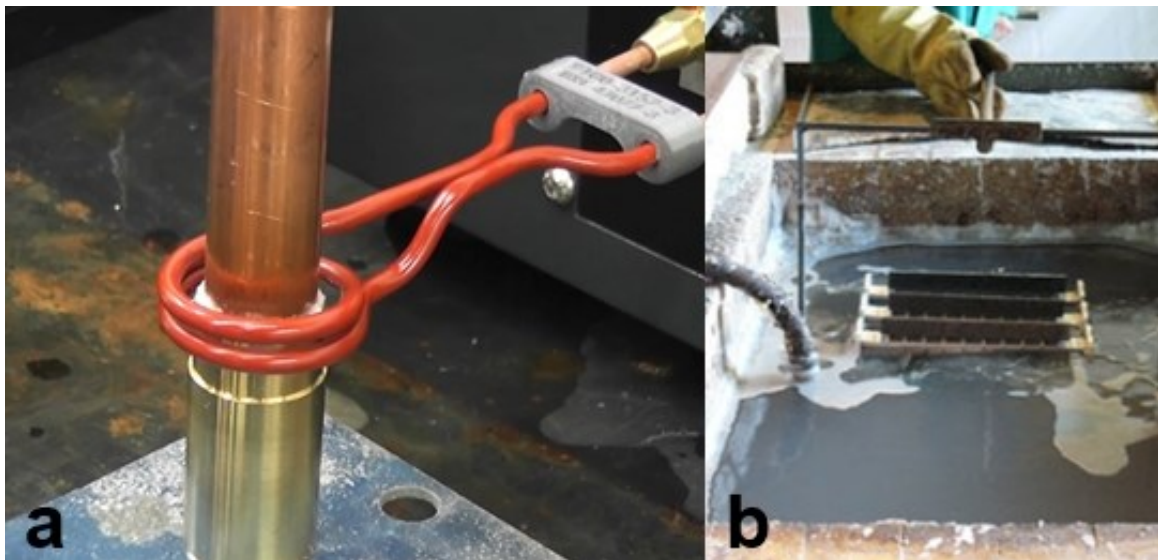


Figure 3.17: Different brazing methods: a) inductive brazing, b) dip brazing of Al in molten flux.

Resistance brazing: Resistance brazing is most applicable to relatively simple joints in metals that have high electrical conductivity. The workpiece, with filler metal preplaced, is part of an electric circuit, which means the heat to melt the filler metal is obtained by resistance to flow of electric current through the joint (Figure 3.16b)

Dip brazing: In this case, the heating of the joint is done by immersing it into the molten salt bath or molten metal bath. In case of salt bath method, filler metal is pre-loaded into the joint and the salt bath contain flux (see Figure 3.17b). The filler metal melts inside the joint when it is immersed into the hot bath. In case of molten metal bath method, the bath contains molten filler metal. The joint is supplied with the flux and dipped to the bath. Molten filler

metal fills the joint through capillary. In both cases, the joint forms during its solidification after taking it out from the bath.

Furnace brazing: In this case, the furnace is used to heat the workpieces to be joined by brazing operation. Besides combustion heating, also both induction and resistive (see Figure 3.18) heating can be used to create a furnace. In this case, a particular susceptor (chamber) is used. For inductive heating, it should be made of electrically conductive material. For resistive heating, the chamber is usually low thermal conductivity material, as alumina or quartz to minimize the heat losses. Furnace is used for a medium- to high-volume production process.

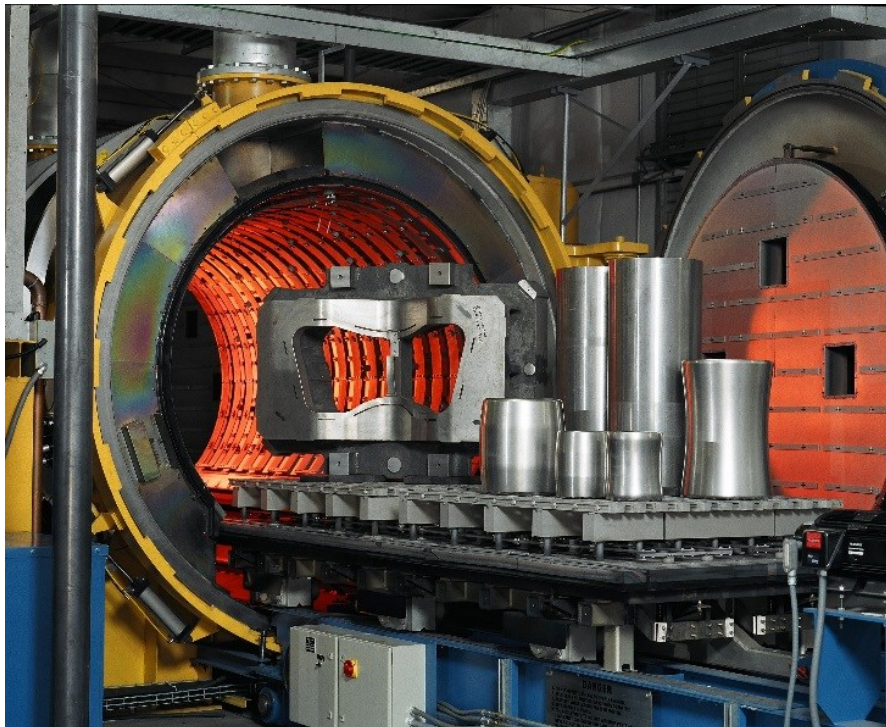


Figure 3.18: Industrial scale resistive vacuum brazing furnace.

The filler metal is preplaced between the faying surfaces before the joint is placed in the furnace. The furnace is purged with a gaseous atmosphere or evacuated from air and heated to a temperature above the liquidus of the filler metal but, less than the melting point of the base metals. The brazing joints are then cooled or quenched by appropriate methods. The thermal cycle is designed to produce of required parameters.

The Figure 3.19 shows the typical braze cycle for furnace brazing [1]. A brazing cycle consists of an initial pump down at room temperature, initial heating ramp, binder burn-off, stabilizing soak, heating ramp to brazing temperature, brazing soak and cooling down.

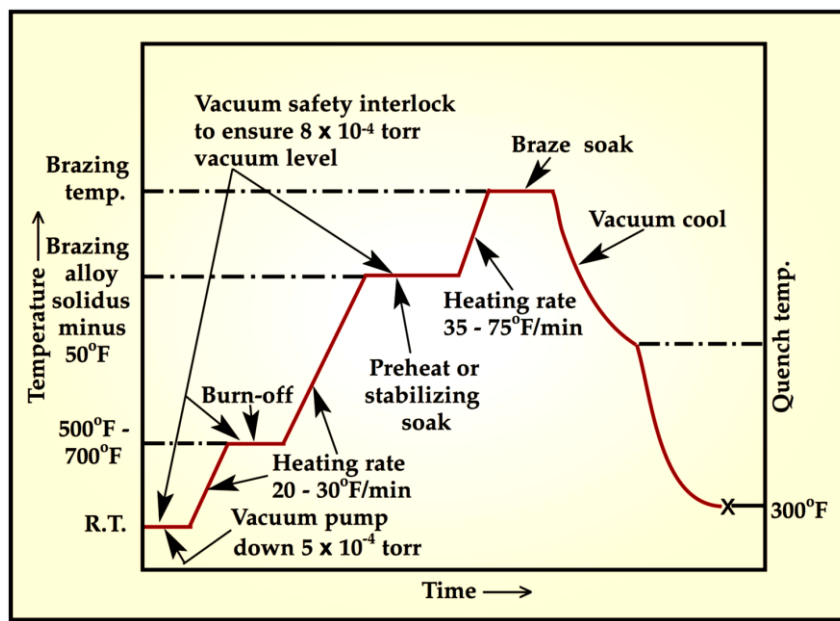


Figure 3.19: Typical braze cycle for furnace brazing.

The pump down temperature allows solvents or water in the paste or binder vehicle to outgas from the braze alloy deposit, helps to prevent voids in the braze deposit and restore the atmosphere quality which can degrade from gasses. The burn-off temperature allows the organics (not liquids) in the braze to become gaseous and to be removed through the pumping system. The preheat or stabilizing soak allows to minimize the thermal gradients incise the pieces, so all parts in the load will reach brazing temperature at approximately the same time during the next heating cycle. The braze soak allows sufficient time for the alloy to melt and flow into the joint, but at the same time minimized to decrease the heat effect on base metal and the base-metal/filler-metal interactions.

3.2.3.5 Post-brazing treatments and inspection

Joints brazed in a suitable atmosphere should be bright and clean and should require any further processing.

A quality control system should be adequate for both general and critical applications. Inspection of finished brazed assemblies includes visual inspection, leak testing and radiographic examination or test of mechanical performance.

4 EXPERIMENTAL SETUP

4.1 Analytical techniques used

4.1.1 Diffractometric analysis of films and powders

4.1.1.1 Basic principles

X-ray diffraction is one of the most useful characterization methods since it can provide a lot of information about material. X-ray diffraction can be used to find the crystalline quality and the orientation of the crystallites of a sample. It can also be used to determine the film thickness, crystallite sizes and, in some cases, the chemical composition of the sample.

The method is based on constructive and destructive interference of a collimated and ideally monochromatic X-ray beam in the atomic planes of the sample. The constructive interference will occur when the Bragg criterion is fulfilled:

$$2d\sin\theta = n\lambda \quad (4.1)$$

Here d is the lattice spacing of the crystal, λ is the wavelength of the X-rays, θ the scattering angle and n is an integer number. Thus, constructive interference will occur when the path difference for X-rays reflected in parallel atomic planes is a whole number of wavelengths.

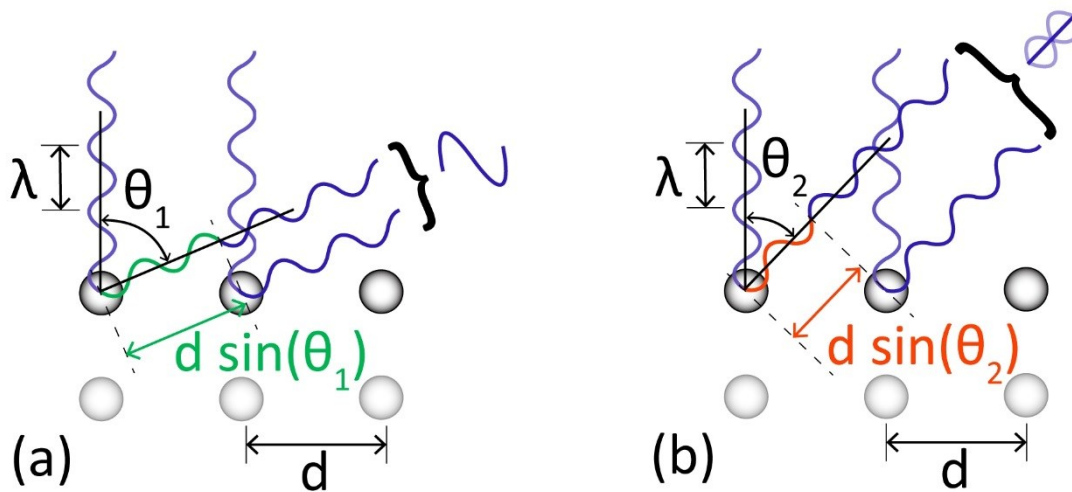


Figure 4.1: Constructive (a) and destructive (b) interference of X-rays interacting with atomic planes

Measuring the intensity of the X-rays scattered in the sample as a function of the scattering angle will give rise to peaks in the spectrum corresponding to the lattice spacing of the different atomic planes, if they fulfill the Bragg criterion.

XRD line scans are usually performed in two different geometries. In θ - 2θ -scan the incidence angle, θ , and the scattering angle, 2θ , are scanned synchronously. In this mode, scattering only takes place in the lattice planes parallel to the sample surface. By comparing the peak intensities from the different lattice planes in θ - 2θ -scans is possible to approximate the degree of preferred orientation of the grains in the film.

In the grazing incidence geometry the incidence angle is kept constant at a small angle, usually below 5 degrees, while the scattering angle is varied. The small incidence angle results the X-rays travelling a longer path through the film resulting in more scattered intensity from the film. The results cannot be used to estimate the degree of preferred orientation and it might miss peaks entirely if the film crystallites are highly aligned.

4.1.1.2 XRD-data treatment

The spacing between the planes in the atomic lattice can be evaluated by use of the Bragg law:

$$d_{hkl} = \frac{n\lambda}{2 \sin \theta}, \quad (4.2)$$

The changes in the lattice spacing in the film crystallites will be expressed as *shifts of the diffraction peak*, compared to the unstrained peak position, if the lattice expands or contracts equally everywhere in the film; or *peak broadening*, if there is a distribution of lattice spacing. In plane film stress, intrinsic or extrinsic, results in an out-of-plane expansion or contraction of the lattice, and thus *shifts of the diffraction peak* position while point defects results in local changes of the lattice parameter which together with the crystallite size results in a *peak broadening*. The out-of-plane lattice expansion, or contraction, is related to the film stress by the equation:

$$\frac{d}{d_0} = 1 - \frac{\nu \times \sigma}{Y}, \quad (4.3)$$

where d_0 is the stress free lattice parameter, ν is the Poisson ratio of the material, σ is the film stress and Y is the elastic modulus of the material.

4.1.1.2.1 Grain size calculation through Debye-Scheerer formula

Average grain size for films analysis in current study was determined from the plot $I_r = f(2\theta)$

(where I_r is the relative intensity of the diffracted X-ray and 2θ is the angle between the X-ray source, the substrate and the detector) using the Debye-Scherrer formula:

$$D = \frac{0.9\lambda}{B \cos \theta} \quad (4.4)$$

Where λ is the wavelength of the X-ray source, in the case of Cu-K $_{\alpha}$ X-ray $\lambda=1.54056\text{\AA}$ and B is a Bragg XRD peak breadth.

4.1.1.2.2 Composition analysis

The positions and corresponding intensities of the peaks on the XRD spectrum are characteristic to each type of crystalline material, thus, they can be used for material identification. X-ray diffraction procedures for phase quantification have been developed extensively for some specific materials, and the scientific literature includes many procedures for data analysis. For a number of materials, the National Institute of Standards and Technology in the USA (NIST) sells Standard Reference Materials (SRM) with known phase fractions. When quantitative phase fraction measurements are needed, checks with these standards are strongly encouraged. Even when quantifying phases in materials for which no NIST SRM samples are available, other SRM standards can help to check the reliability of the equipment and the data analysis. The main idea of quantification by XRD is to use the ratio of peak intensities, which is proportional to a ratio of weight fractions of materials. In any case, this method has many constrictions on the preparation of samples for analysis and sometimes require the data not available in database.

The most reliable approach is so-called “refinement” method (or “Rietveld refinement”) for powder diffraction patterns. The idea is to represent the experimental diffraction pattern, both peaks and background, with a multi-parameter mathematical model. The best set of these parameters is then found by an iterative procedure that minimizes the difference between calculated and measured diffraction patterns. A wide variety of parameters can be refined, including lattice parameters, crystallographic site occupancies, and sample positioning error. The crystal structure itself is not practical for a refinement calculation, and must be provided as input information for the refinement code. The variations of the peak shapes with diffraction angle, 2θ , can be used to determine structural features in the sample such as strain distributions and particle sizes.

4.1.1.2.3 Detection of crystalline and amorphous structure.

The shape of a graph can be used to provide general recognition of crystalline or amorphous structure. Thus, graphs possessed exact sharp peaks should indicate crystalline structure and,

contrariwise, absence of peaks should signify that a film has had an amorphous structure. The Figure 4.2 shows an example of two XRD spectrums corresponding to crystalline and amorphous structures.

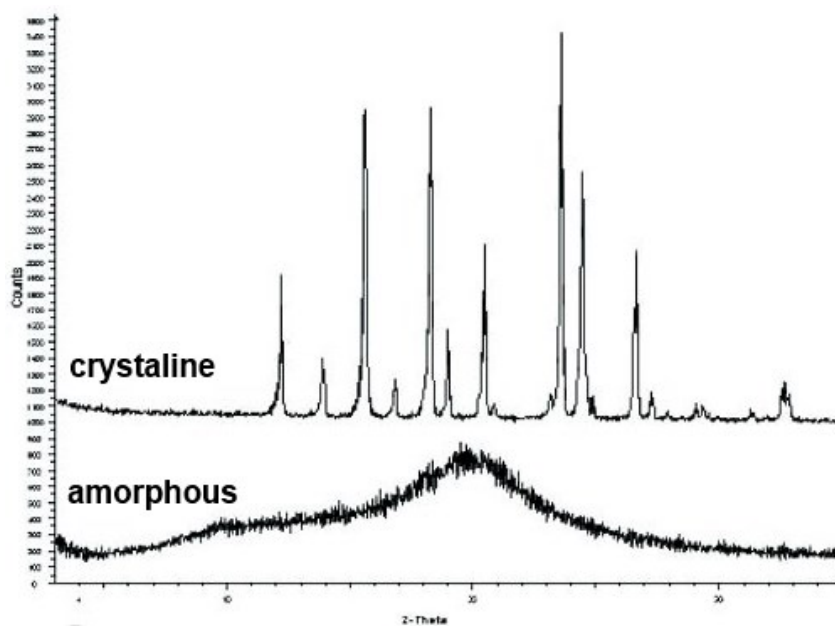


Figure 4.2: Example of XRD spectrums of crystalline and amorphous structures



Figure 4.3: X'Pert Philips PW3040/60 diffractometer.

4.1.1.3 Short description of the XRD-device

For the analysis, both films deposited by magnetron sputtering and powder materials produced during Mo recovery study, a Philips PW3040/60 diffractometer was used. The diffractometer is equipped with 1.54 Å Cu-K α X-ray. The picture of the device is presented in the Figure 4.3.

4.1.1.4 The XRD-method used

The XRD investigation was carried out by performing θ/θ scan (both X-ray gun and detector are moving synchronously for the angle θ) with 2θ from 10° to 100° (2θ is the angle between X-ray source, substrate and detector). The scans were taken at 40kV, 40mA of Cu-K α X-ray gun. The PW3071/xx Bracket sample stage was used in reflection mode.

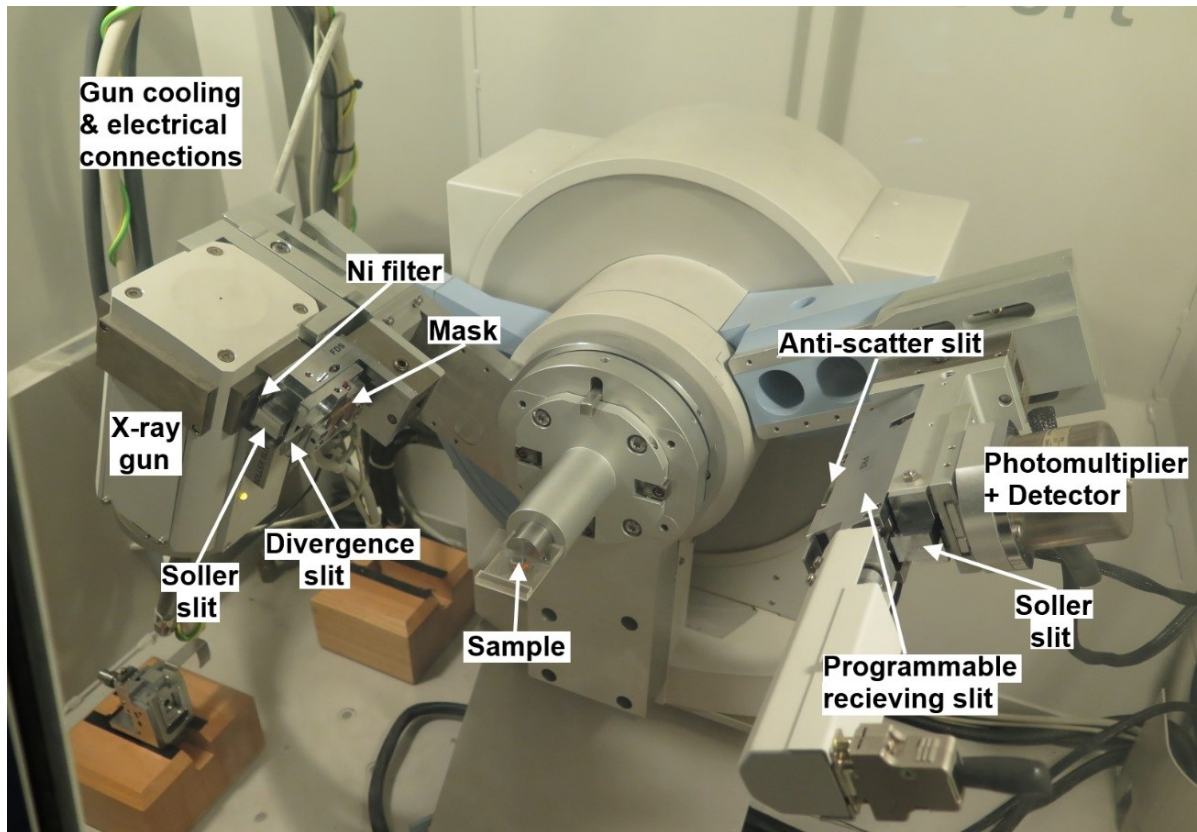


Figure 4.4: X'Pert Philips XRD device assembled for θ - 2θ Gonio configuration.

The parts of the optics are shown in the Figure 4.4. Since small size ($<20*20\text{mm}$) samples were analyzed for sputtered film measurements, the configuration described in the Table 4.1 was used.

Table 4.1 XRD beam optics configuration

Optics	Value
Incident beam optics	
Soller slit	0.04rad
Divergence slit	1/4°
Mask	10mm
Ni filter	Yes
Distance to sample	140mm
Diffracted beam optics	
Soller slit	0.04rad
Programmable receiving slit	0.1mm
Detector	Proportional detector Xe[1]

For the analysis of the powders in Mo-recovery experiments, Si zero-background sample holder was used. The powders were preliminary grinded in agate mortar. A semi-quantitative analysis with X'Pert HighScore software was applied without any additional calibration. As soon as the reliability of such quantification is not sufficient, the results were compared with other analyzing methods (EDS-analysis, calculation of mass change according to reaction equation).



Figure 4.5: Zero-background silicon sample holder for low quantity of powders.

4.1.2 SEM

4.1.2.1 Principles of operation

SEM is one of the most versatile instruments available for the examination and microstructural characterization of solid objects with high-resolution (down to nm scale) compared with a resolution of about 1 μm for a conventional optical microscope.



Figure 4.6: a) Basic components of SEM; b) XL-30 Philips SEM with QUANTAX EDS of Bruker

SEM involves scanning a sample with a fine beam of electrons and detecting the signals, which are emitted with appropriate detectors. The SEM imaging is carried out under vacuum, since electrons cannot travel through the air for the necessary distance. The basic components of the SEM are illustrated in the Figure 4.6a.

Electrons emitted by the gun (usually a tungsten filament) are accelerated towards the anode by 5-30 kV potential. They pass through a set of magnetic lenses (usually condenser and objective lenses), and then through a set of scan coils and an aperture. The electrons emitted by the specimen are detected and amplified; the signal is then used to produce an image. The image is generated simultaneously on a computer monitor with the beam rasters the surface of the sample.

When high-energy electrons impinge on the specimen, a number of signals are generated.

Secondary electrons originate in the specimen itself having an energy typically < 50 eV. They originate from within a few nm from the surface. They are, therefore, very sensitive to surface structure, and provide topographic information.

Backscattered electrons are high-energy electrons, which are scattered out of the specimen, losing only a small amount of energy. They originate from much deeper within the sample (a few μm below the surface), and interact much more strongly with the sample. They therefore provide compositional information, but give lower resolution images.

X-rays give an information about the elemental composition of the sample (EDS see below).

A system of corresponding detectors allows obtaining images.

4.1.2.2 The SEM devise used in current study.

Fei (ex Philips) Scanning Electron Microscope SEM XL-30 was used for sputtered coatings surface, cross-section analysis and for analysis of powders produced during Mo recovery. The Figure 4.6b shows the device used.

4.1.3 EDX analysis

Energy-dispersive X-ray spectroscopy (EDS, EDX) is an analytical technique used for the elemental analysis of a sample. Each element has a unique atomic structure allowing unique set of peaks on its X-ray spectrum. To stimulate the emission of characteristic X-rays from a specimen, a high-energy beam of charged particles (for example, such as electrons from electron gun of SEM) is focused into the sample being studied. At rest, an atom within the sample contains ground state (or unexcited) electrons in electron shells. The incident beam may excite an electron in an inner shell, ejecting it from the shell while creating an electron hole where the electron was. An electron from an outer, higher-energy shell then fills the hole, and the difference in energy between shells may be released in the form of an X-ray. The number and energy of the X-rays emitted from a specimen can be measured by an energy-dispersive spectrometer. The energy of the X-rays is characteristic of the difference in energy between the two shells, and of the atomic structure of the element. This allows measuring the elemental composition of the sample.

During current study, the QUANTAX energy-dispersive X-ray spectrometer of BRUCKER was used for sputtered films analysis, for analysis of brazed joints with alumina and synthetic diamonds and for recovered MoO₃ and reduced Mo powders analysis. It should be mentioned that the inaccuracy of the quantitative elemental analysis by EDX method is not less than 5%.

4.1.4 Contact profilometry

The stylus profilers rely on a small-diameter stylus moving along a surface in a horizontal direction being pressed to the analyzed sample surface with particular force to keep the contact. As the stylus encounters the surface features, such as a deposited film and irregularities, it changes the vertical position.

The stylus is mounted on an arm, coupled to a linear variable differential transformer (LVDT). The output voltage changes from plus to minus as a function of core displacement, corresponding to the mechanical changes that occur whenever the stylus moves up and down

over the features on the surface. The varying DC signal is then converted and stored to represent the surface profile of the sample.

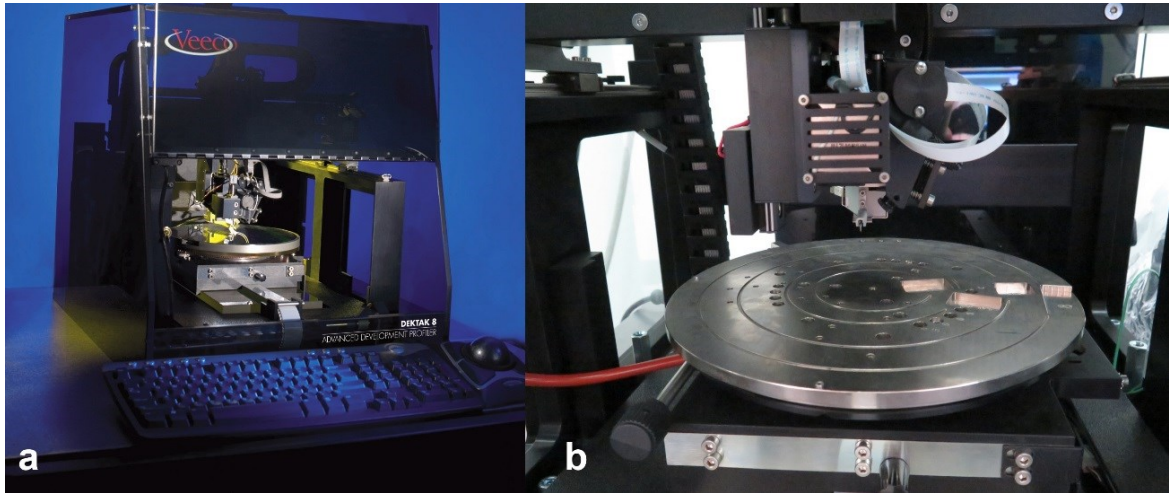


Figure 4.7: a) Dektak 8 profiler of Veeco; b) internal view of the system.

The Dektak 8 of Veeco is a system that accurately measures a surface texture below submicro-inch and film thickness up to 262 μm (see Figure 4.7a).

The Dektak 8 characterizes film thickness, roughness, stress and defects on samples up to 200mm in length. The sample stage is showed in the Figure 4.7b. The system is working with low-force tip technology. The tip is shown in the upper part of the Figure 4.7b. The Dektak 8 profiler was used for following applications: sputtered film thickness determination and estimation of stress in thick sputtered films.

4.2 Substrates preparation for sputtering and brazing

4.2.1.1 Copper substrates

Copper substrates of different dimensions were used for sputtering deposition. Copper discs with a diameter of 13 mm and 0.5 mm thickness (Figure 4.8b) and 32 mm diameter 0.5mm thickness (Figure 4.8c) were cut in LNL mechanical workshop by electro erosion. Instead, copper discs of 32mm diameter and 1 mm thickness (Figure 4.8a) were prepared by mechanical cutting.

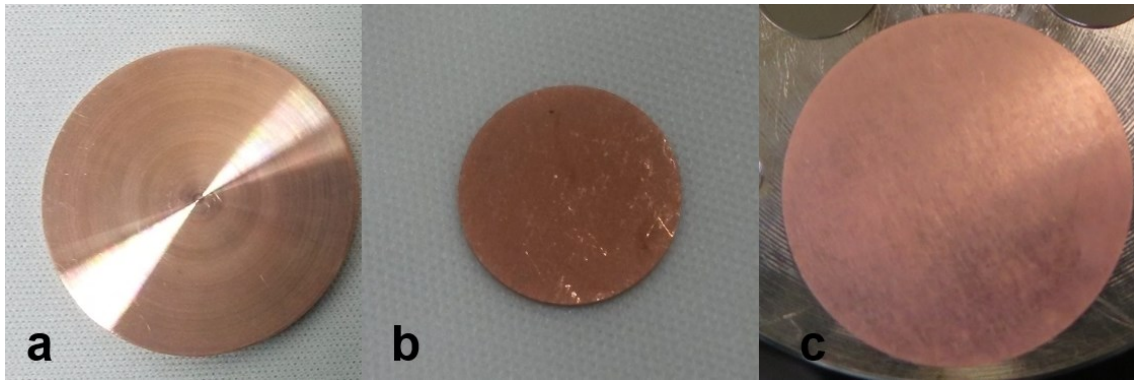


Figure 4.8: Different copper substrates for sputtering deposition.

Copper substrates for brazing were discs of 32mm diameter and 1.5 mm thickness with a cylindrical recess of 0.5 mm depth and diameter corresponding to the size of sapphire/synthetic diamond to be brazed plus the radial clearance (Figure 4.9). These substrates were prepared by mechanical cutting.

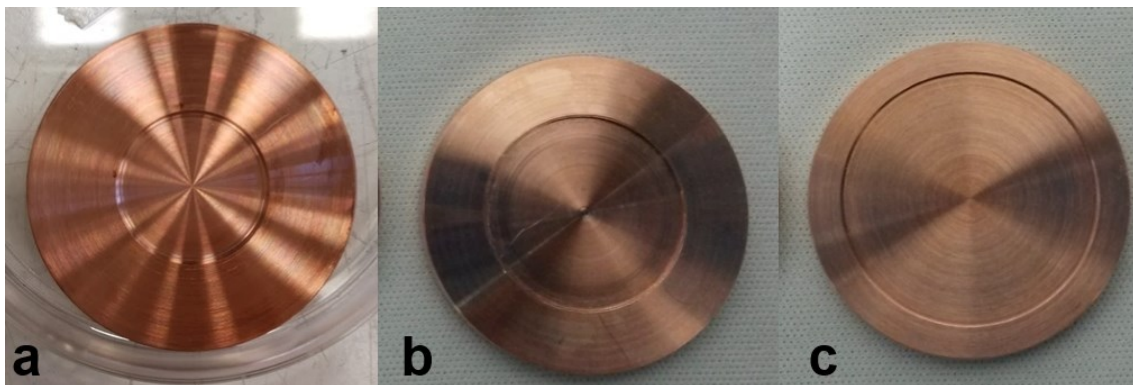


Figure 4.9: Different copper substrates for vacuum brazing.

The following copper substrate preparation included the next steps:

- 1) NGP soap ultrasound washing for 20 min
- 2) Ultrasound washing with water for 20 min
- 3) Chemical etching with SUBU at $72\pm 4^\circ\text{C}$ in order to remove surface oxides
- 4) Passivation in 20g/l sulfamic acid
- 5) Ultrasound washing with water for 20 min
- 6) Rinsing with ethanol
- 7) Drying with nitrogen

SUBU solution contains:

- 5 g/l sulfamic acid (H_2NHSO_3);
- 1 g/l ammonium citrate ($(\text{NH}_4)_2\text{C}_6\text{H}_6\text{O}_7$);
- 50 ml/l butanol (n-BuOH);
- 50ml/l hydrogen peroxide (H_2O_2);
- 1l of deionized water.

The time of etching was chosen in respect to the state of copper substrate. For example, mechanically cut copper samples required shorter etching, than produced by electro erosion. The etching rate of copper with SUBU solution was of the order of $1.5\mu\text{m}/\text{min}$.

4.2.1.2 Aluminium substrates

Aluminum 6082 was mechanically cut to produce simple square cut pieces and discs of 32mm diameter and 1.5 mm thickness with a cylindrical recess of 0.5 mm depth and 19.5 mm diameter (Figure 4.10).

The aluminum substrate preparation was done without chemical etching and included the next steps:

- 1) Mechanical treatment with abrasive paper;
- 2) NGP soap ultrasound washing for 20 min;
- 3) Ultrasound washing with water 20 min;
- 4) Rinsing with ethanol;
- 5) Drying with nitrogen.

The steps were realized directly before the brazing procedure. Mechanical treatment with abrasive paper served to minimize the aluminium oxide layer limiting the wettability by molten metal during brazing.

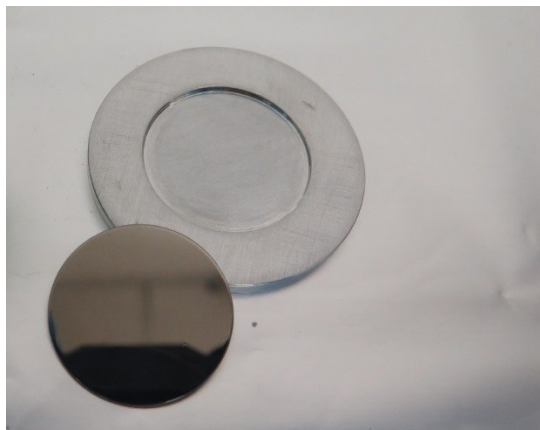


Figure 4.10: Aluminum substrate for vacuum brazing with Ti coated sapphire sample.

4.2.1.3 Ceramic substrates

The non-metallic substrates used included quartz, sapphire, synthetic diamond, and silicon wafer.

Quartz pieces 9x9x1 mm were purchased from Helios Italquartz. The quartz pieces were mainly used for sputtering deposition rate estimation by measuring the thickness of the film deposited by contact profiler.

Silicon wafers of 50.8 mm diameter 250-300 μ m thickness of semiconductor quality of (100) orientation were purchased from SILTRONIX. The silicon wafers were cracked into 4-quarter parts for deposition of Mo.

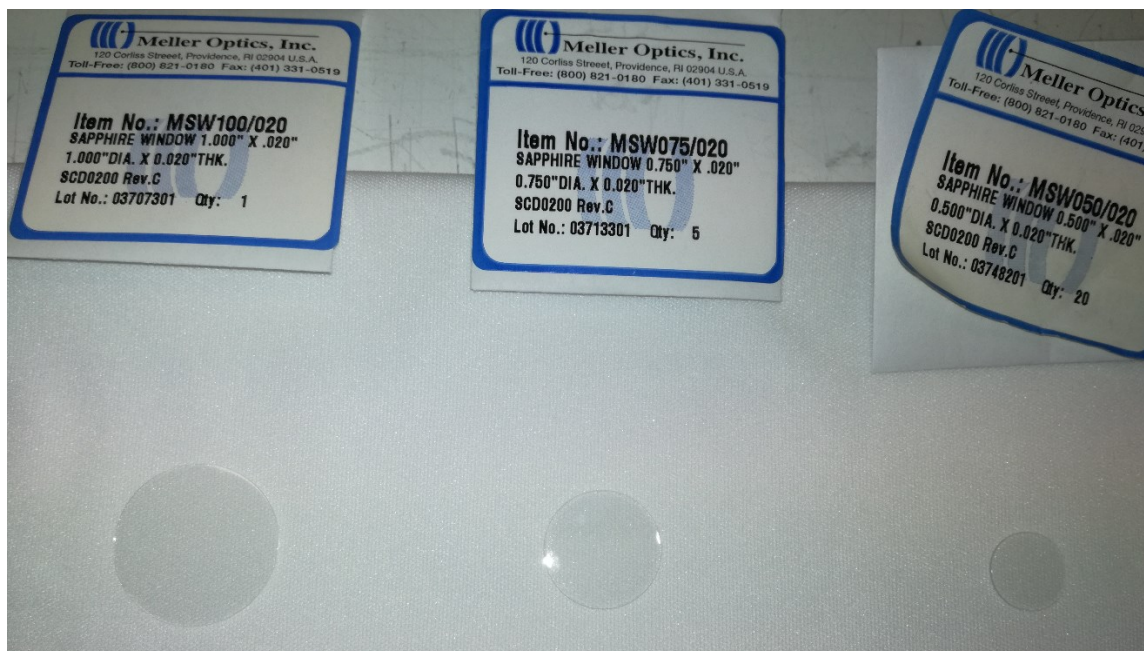


Figure 4.11: Sapphire substrates for vacuum brazing with Ti coated sapphire sample.

Sapphire pieces 10 x 10 x 1 mm and sapphire coins with diameter of 12.7 mm, 19.05 mm, 25.4 mm and thickness of 0.5 mm were purchased from Meller Optics, Inc. (Figure 4.11). The sapphire discs were made of IR grade sapphire, with C-axis orientation.

CVD Synthetic diamond substrates of 13.5 mm diameter and 0.3 mm thickness of thermal grade with thermal conductivity 1500 W/(m·K) were purchased from II-VI Advanced materials (Figure 4.12).

Alumina (Al_2O_3) discs of 28 mm diameter and 5mm thickness were used as substrates for preliminary study of vacuum brazing.

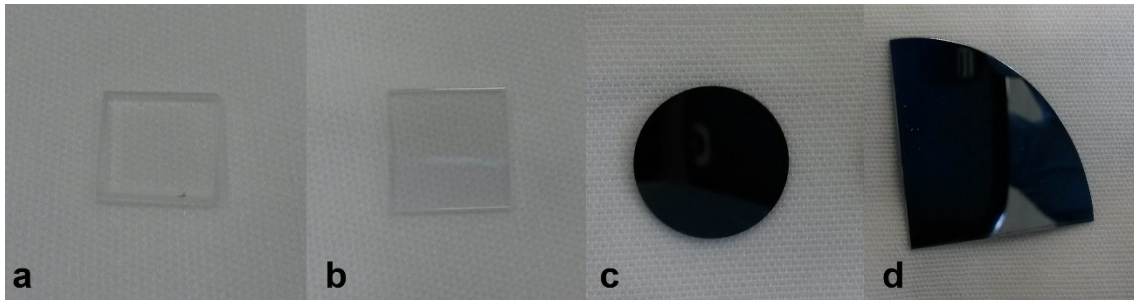


Figure 4.12: Substrates: square quartz (a) sapphire (b), CVD synthetic diamond (c), Si wafer (d).

The same pre-treatment procedure was used for all non-metallic substrates described above. The ceramic substrate preparation was done without chemical etching and included the next steps:

- 1) Rodaclean[®] soap ultrasound washing for 20 min;
- 2) Ultrasound washing with deionized water for 20 min;
- 3) Rinsing with ethanol;
- 4) Drying with nitrogen flux.

SANDVIK MBG 660TI diamond powders coated with Ti of 170/200 mesh were used for preliminary study of vacuum brazing. The diamond powders did not require preliminary treatment before the brazing experiment.

In the Table 4.2 the thermal features of the materials used as a substrates are presented.

Table 4.2 Thermal features of substrate materials

<i>Material</i>	<i>Thermal expansion coefficient</i>	<i>Thermal conductivity</i>	<i>Melting temperature</i>
Quartz	$0.6 \cdot 10^{-6}/K$	8 W/(m K)	~1000°C
Sapphire	$6.1 \cdot 10^{-6}/K$	40 W/(m K)	2030°C
Copper	$16.6 \cdot 10^{-6}/K$	390 W/(m K)	1084°C
Synthetic diamond	$1 \cdot 10^{-6}/K$	1500 W/(m K)	-
Silicon wafer	$2.6 \cdot 10^{-6}/K$	148 W/(m K)	1414°C
Alumina	$8.1 \cdot 10^{-6}/K$	30 W/(m K)	2072°C

4.3 The vacuum system for deposition and brazing

The sputtering system consisted of four vacuum chambers connected through the central zone and separated by pneumatic gates in order to be able to carry on processes in different chambers in series (Figure 4.13).

The central zone was connected to general pumping system including Pfeiffer turbo molecular pump of 360 l/min (with Pfeiffer DCU display and operating unit) and Varian Tri Scroll Pump 210 l/min as a primary pump. The base vacuum pressure of about 1×10^{-5} mbar was reached without additional backing before each experiment. The entire system was controlled by a LabVIEW programmed PLC human-machine interface (see Figure 4.13b).

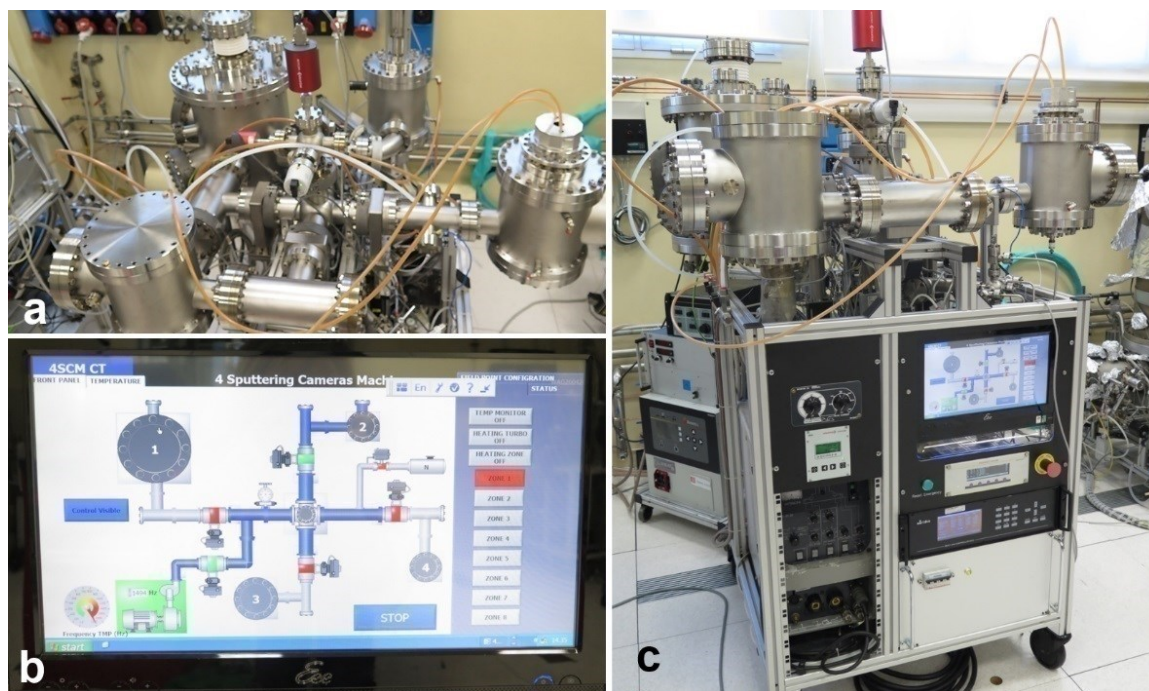


Figure 4.13: Vacuum system: a) top view, b) PLC control system, c) full system.

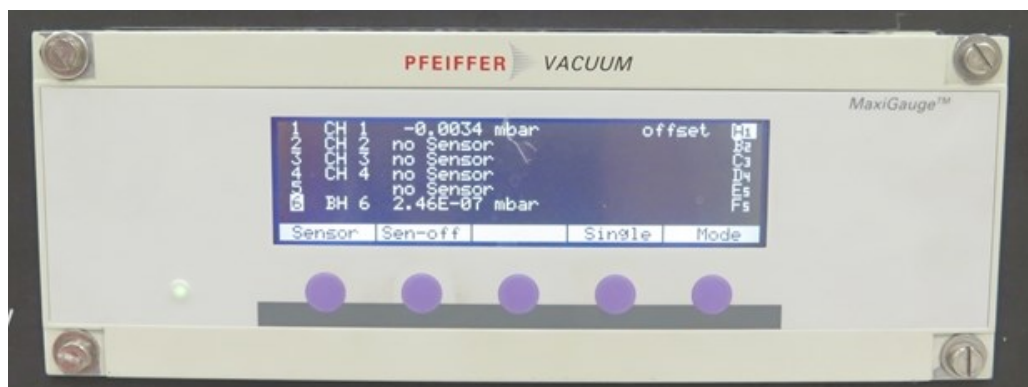


Figure 4.14: MaxiGauge™ pressure control box.

The base vacuum pressure was controlled with full-range Bayard-Alpert (BA) vacuum-meter. The pressure during MS deposition was controlled with capacitance vacuum-meter,

since it was not sensitive to plasma as BA. The vacuum-meters are connected to Pfeiffer MaxiGauge™ control box (Figure 4.17). The MKS multi gas mass-flow controllers powered by MKS 647C four-channel power supply/readout system (Figure 4.19) was used for gas flow control during the deposition process.



Figure 4.15: MKS multi gas controller 647C.

The picture of the top view of the four chambers (Figure 4.13a) can be presented by the PLC scheme (Figure 4.13b). The chamber number 1 was the biggest, and it allowed, with use of appropriate flange, co-deposition with two 2” planar magnetron sources simultaneously. The chambers number 2 and 4 were used for sputter deposition with 2” magnetron sources. The chamber number 3 was used for vacuum brazing.

4.4 Film sputtering

Sputter deposition was carried out in cylindrical, stainless steel vacuum chambers of 25 cm in diameter and 25 cm in length (Figure 4.16). An external wall of the chamber was hollow to allow a water-cooling for the personnel safety aspect during deposition at elevated temperature. The base pressure before the deposition was about $1 \cdot 10^{-5}$ mbar.

Both deposition configurations: “top-down” and “down-top”, were used. The “down-top” deposition configuration with magnetron source placed from downside of the cylindrical chamber and substrate holder with substrates from the top of the chamber (Figure 4.16b) was used mainly for thick film deposition in order to minimize film delamination probability caused by metallic dust particles. The reverse “top-down” configuration (Figure 4.16a) was used only for fast small-thickness films deposition.

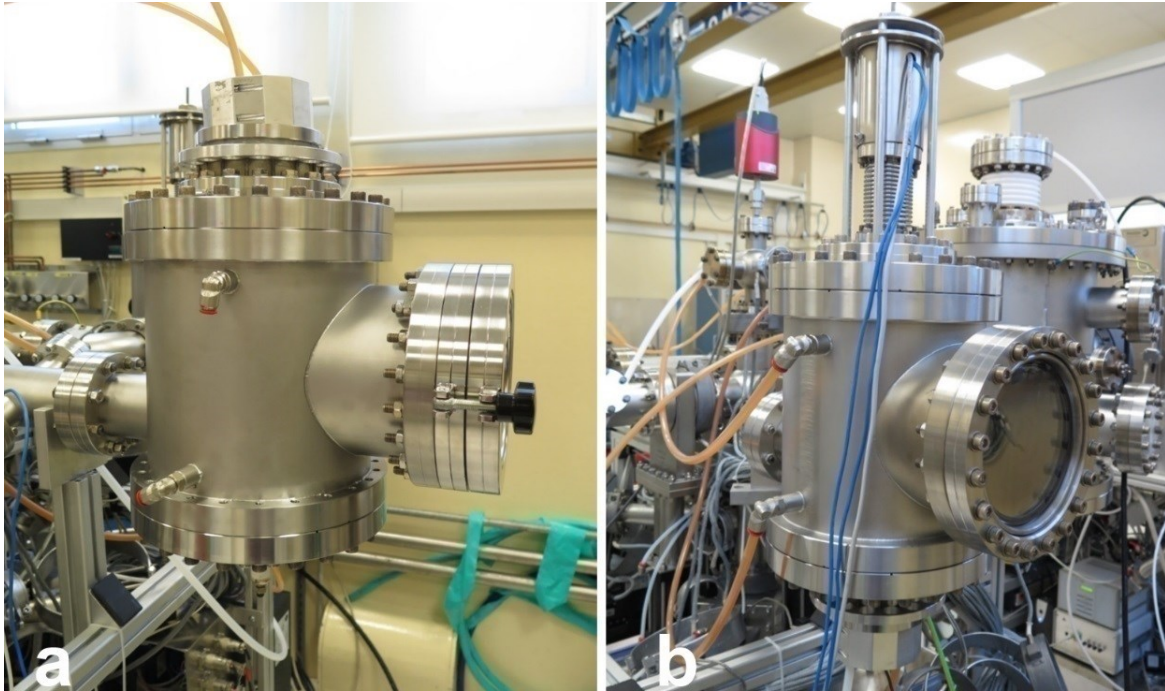


Figure 4.16: a) Chamber #4 assembled for top-down MS deposition without heating, b) chamber #2 assembled for down-top MS deposition on a heated substrate.

The critical point in thick film deposition is the absolute cleanliness of the whole sputtering system. A small particle of dust left on the substrate or flakes (coming from the delamination of film from the sputtering chamber), if deposited on the substrate, can work as a nucleation of protrusions growing on the deposited film and amplified by the film thickness. Otherwise, appearing on the sputtering source in DC mode, dust particles (see Figure 4.17) can course the shortcut or plasma instability, provoking new imperfections in the deposited film. For that reason, the substrate holder, the magnetron shields, the sputtering chamber and the sample surfaces must be absolutely clean and free of whatever (also metallic) type of dust.

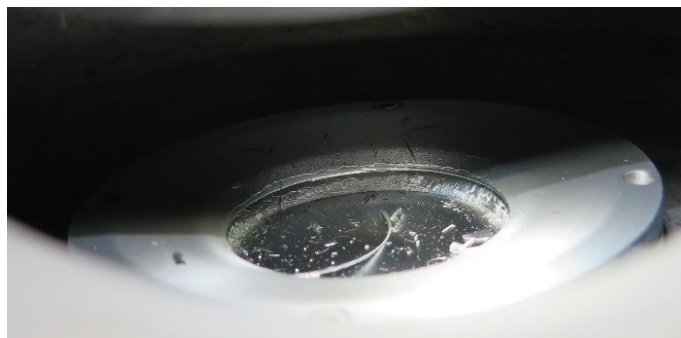


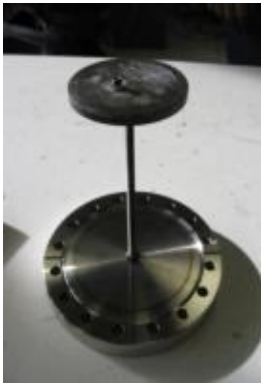



Figure 4.17: Metallic flakes from magnetron shield on sputtering target in “down-top” configuration.

4.4.1.1 Substrate holders for sputter deposition

Deposition was carried out on different planar substrate holders with the possibility to heat up or cool down the substrate and even change the distance to the magnetron cathode. The Table 4.3 presents main substrate holders (SH) and their features. The distance between magnetron and substrate was kept in a range 4.5-6 cm.

For deposition of Ti films on ceramic substrates before brazing, the SH without cooling/heating was used. Instead, for thick film deposition, the SH allowing either water cooling or heating were prepared. Thus, the drawing and photograph of the substrate holder heated by IR 450W lamp of Helios Italquarz are shown of the Figure 4.18. The sample holder had a SS shield to concentrate the heat around the plate. The temperature was controlled by the K-type thermocouple inserted in SH plate. This particular substrate holder allowed to adjust the distance between substrate and magnetron changing the height of SH.

Table 4.3 Different substrate-holders

Grounded	Water-cooled	Heated	Heated
			
No temp-re control No heating No cooling No bias No plasma etching	Cooling by water Stationary temperature No bias No plasma etching	Heating Temp-re control No bias No plasma etching Stationary geometry	Heating Temp-re control No bias No plasma etching Adjustable SH height

Two systems were used to control the IR lamp and correspondingly the temperature of the substrate holder: an automatic custom-made infrared lamp backing control system (see Figure 4.19a) and a manual tension regulator (see Figure 4.19b). The temperature control module (Figure 4.19a) was based on a commercial temperature control device and a power controller device. Both IR lamp power supplies were used with a transformer connected in series in order to avoid “coupling” of the current in the lamp filament with the sputtering plasma during deposition.

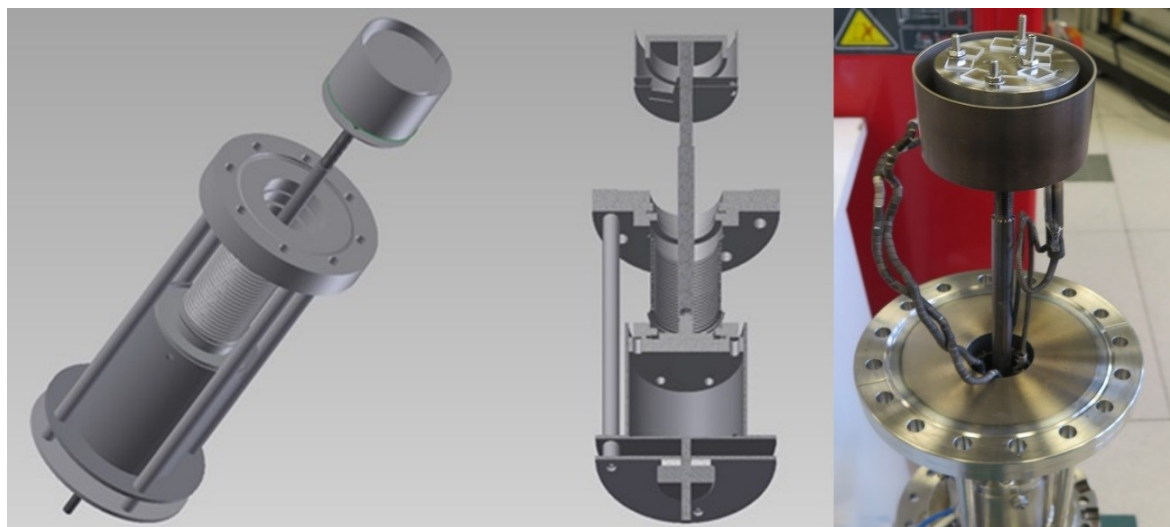


Figure 4.18: IR heated substrate holder.

For the thick film depositions, substrates were always fixed on the substrate holder by means of screws and covering masks of different size and shape in respect to the number and size of the substrates. The examples of fixing masks are presented in the Figure 4.20.

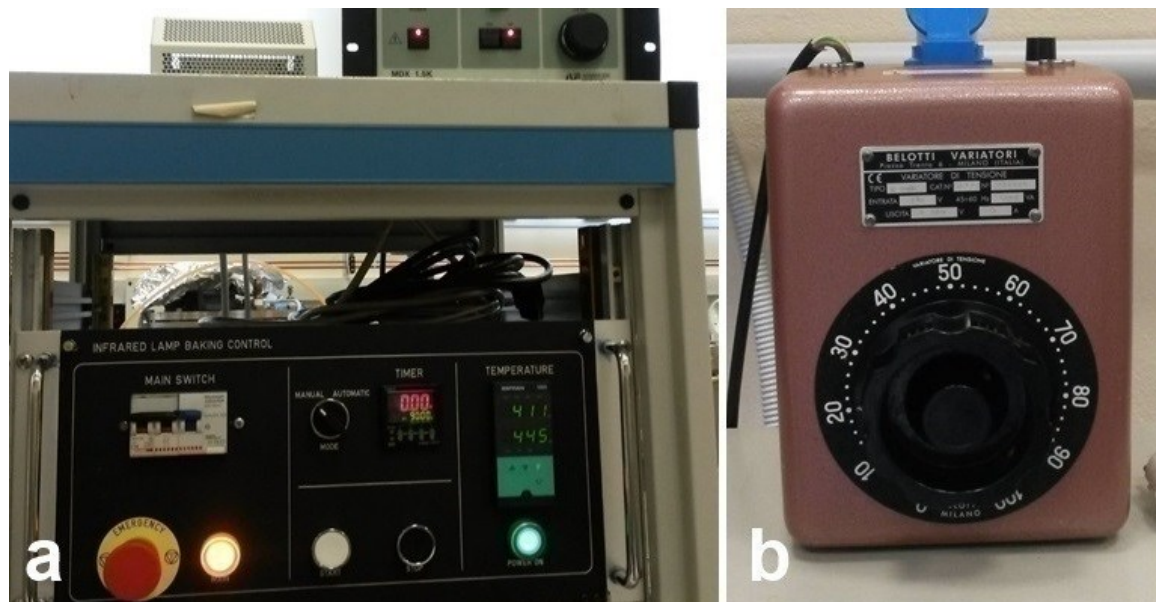


Figure 4.19: IR lamp power supply: a) automatic control, b) manual control.

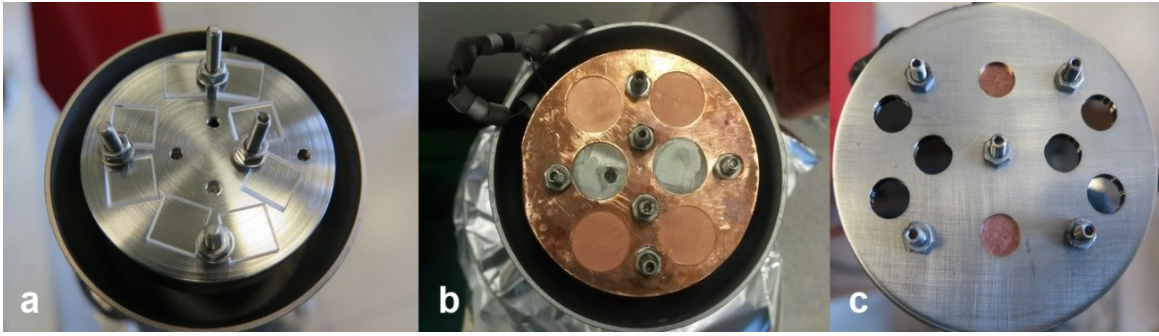


Figure 4.20: Different ways to fix substrates for thick film deposition.

4.4.1.2 Magnetron sputtering source

The deposition was carried out with the 2 inches in diameter planar unbalanced magnetron cathode source of the II type (Figure 4.22) with low level of unbalancement in the Window and Savvides classification [84]. In the II type UBM (unbalanced magnetron) the outer ring of magnets is strengthened in respect to the central pole. Not all the field lines are closed between the central and outer poles in the magnetron: some are directed towards the substrate. Consequently, the plasma is not strongly confined to the target region, but is also allowed to flow out in the substrate direction. The scheme is presented in the Figure 4.21. UBM is characterized by higher ion and electron flux than conventional magnetron.

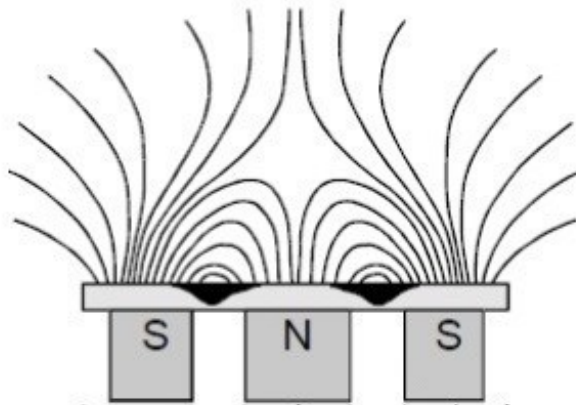


Figure 4.21: The schematic representation of UBM.

The magnetron design is shown in the Figure 4.22, representing the 3D drawing and a photo of the magnetron sputtering source used in the deposition experiments. The magnetron is water-cooled, but the magnets are placed in the center of a copper cooled chamber and are not in a contact with cooling water. Magnetron has DN100CF flange to be connected to the vacuum chamber. The powering connection is protected for the safety reason by grounded

shield. The magnetron source can be used to sputter from disc targets of 2-inch (5.08 cm) diameter and of 1÷5 mm thickness.

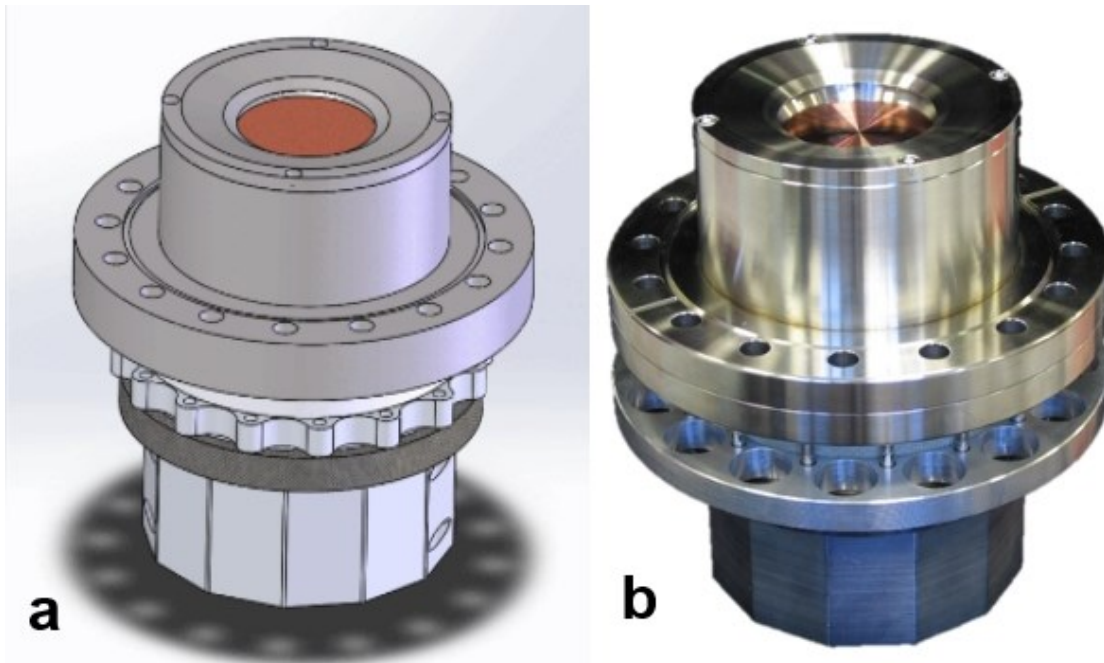


Figure 4.22: The UBM used in the deposition experiments: (a) drawing, (b) photo.

4.4.1.3 Cathode power supplies: control and automation

The MDX Pinnacle™ 20 kW (Figure 4.23a) and MDX 1.5 kW (Figure 4.23b) magnetron drives from Advanced Energy were used to carry out the sputtering experiments.



Figure 4.23: DC power-supplies used for magnetron sputtering.

In order to control the pulsing mode of the MDX 1.5kW power supply to provide the multilayer deposition an automatic control system was designed by Dr. A. Rossi.

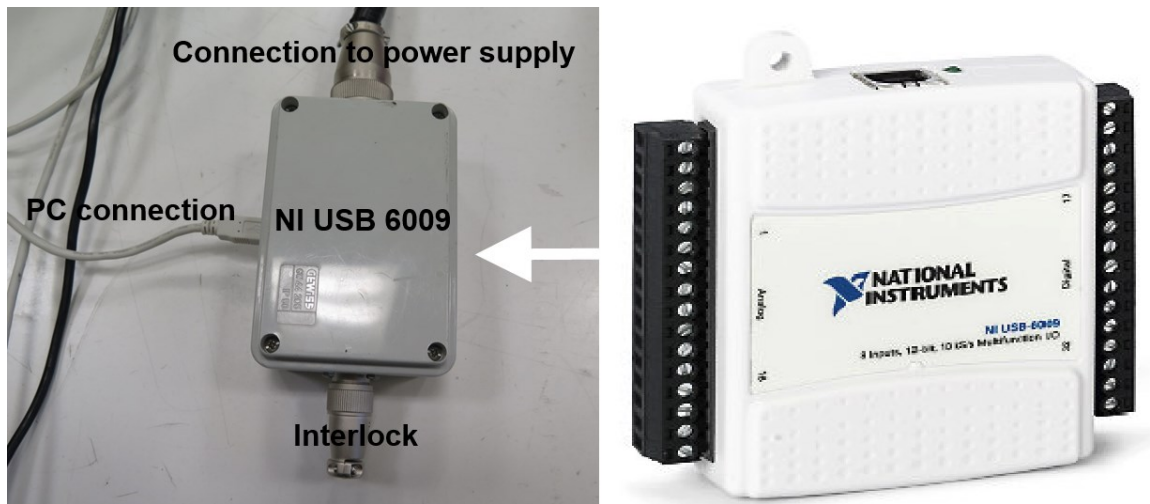


Figure 4.24: NIUSB-6009 connections.

The MDX power supply (Figure 4.23b) was connected to National Instruments device NIUSB-6009 (commercially available) by a cable (see Figure 4.24). The NIUSB-6009 device was connected to the PC by USB connection in order to control the power supply by the LabVIEW® USB6009 mdx-1.5K program. In the Figure 4.24 the connections from power supply to PC are shown. The interface of the automatic control program is presented in the Figure 4.25.

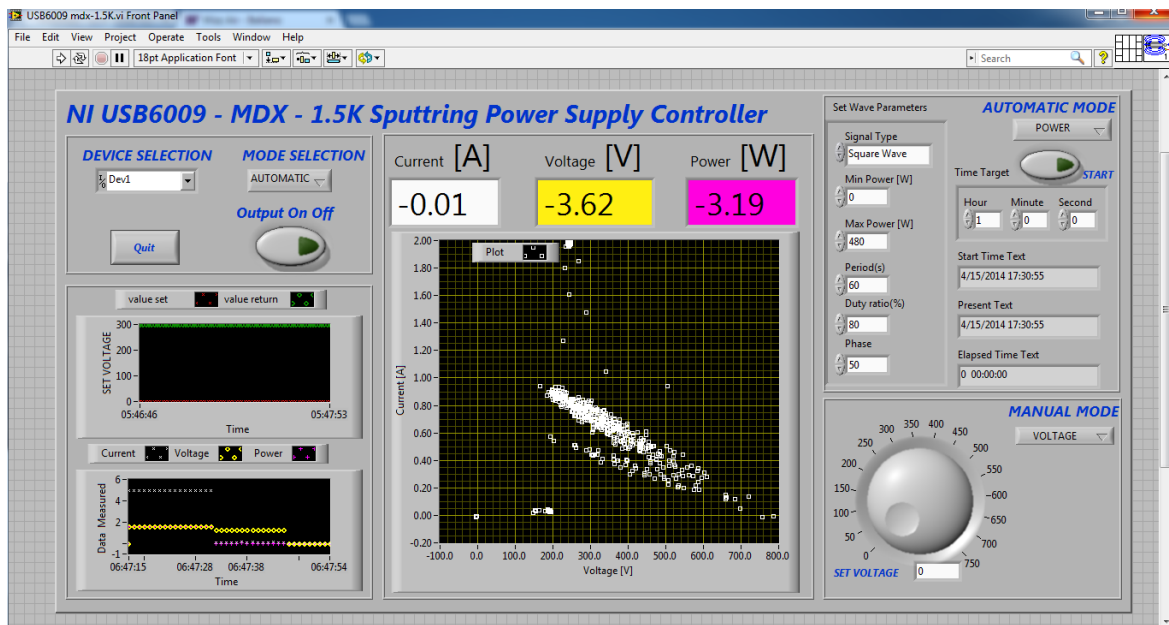


Figure 4.25: Interface of USB6009 mdx-1.5K LabVIEW program.

The program allowed to control the power supply in voltage, current or power both in manual and in automatic way. The automatic control allowed to change the duration of the pulse (the

thickness of monolayer) and the duration of the stop after deposition of each layer. Besides the already described multilayer deposition this approach can be useful to sputter from low thermal conductivity (like sintered Mo powders) sputtering targets, optimizing the target cooling.

4.4.2 Materials used

4.4.2.1 Sputtering targets quality

A high grade bulk Nb for superconducting cavities (99.99% purity, RRR=250) was used for as a sputtering target.

Mo (99.99% purity), Zr (99.99% purity), Ta (99.99% purity), Al (99.99% purity) and Ti (99.99% purity) commercial targets were used for deposition of films for different aspects of the work presented here. All the elements were used in natural form without enrichment.

4.4.2.2 Sputtering gas quality

Argon (99.99% purity) was used as sputtering gas for films deposition. Oxygen (99.99% purity) was used as sputtering gas for reactive sputtering of Nb₂O₅ protective coating deposition. The flow of the gases was controlled by the mass-flow controller (0-100 sccm) described before.

4.5 Corrosion tests for protective films

Two fast and easy tests of protective films efficiency as diffusion barriers were used in the current study. They used the diffusion of protons of hydrochloric acid solution and Gallium atoms through the inert protective film. Aluminum sputtered quartz samples were used as the substrates for protective coating deposition. Unlike aluminum, with its extreme susceptibility for both acid corrosion and liquid gallium corrosion, refractory metals like Tantalum, Zirconium, and Niobium are chemically inert. Thus the corrosion in the system aluminum covered with the inert coating can identify poor barrier properties of the protective coating (for more details see [85-87]).

4.5.1 The acid test

The proton diffusion test was carried out by immersing the samples into 10% hydrochloric acid at 30° C during 10 min. The hydrogen bubbles appeared on the surface of the coating

revealed both macro porosity owing to macro particles generation during sputtering process, micro-voids and grain-boundaries depending on the coating microstructure. The scheme of the test is shown on Figure 4.26.

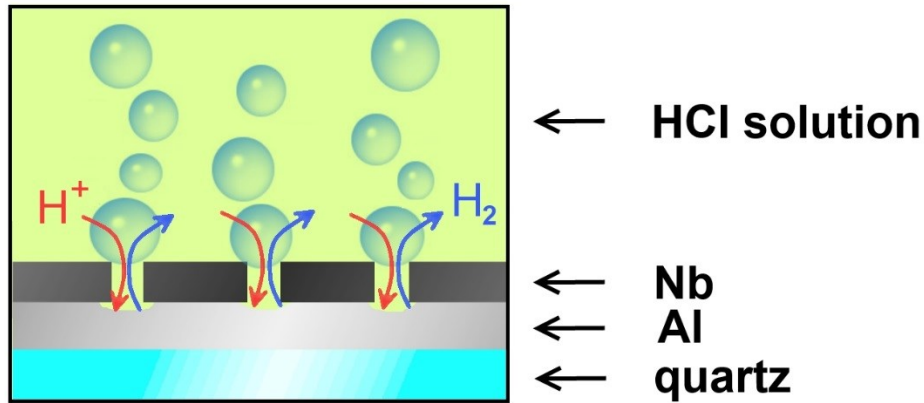


Figure 4.26: Principal scheme of acid diffusion barrier test.

The results were evaluated due to the number of hydrogen bubbles appeared on the surface of the coating. The acid test results were evaluated numerically in a scale from “1” to “5”, where “1” meant the smallest amount of hydrogen bubbles and appropriately the best barrier quality of a coating (see Figure 4.27).

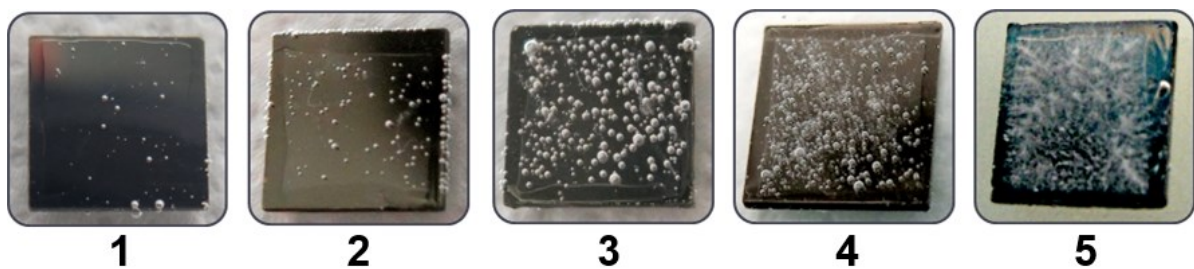


Figure 4.27: Evaluation of results of acid diffusion barrier test.

4.5.2 The liquid gallium test

The liquid gallium diffusion test was carried out by heating aluminated quartz samples coated by investigated protective coatings with liquid gallium droplets during 40 hours at 200 °C. The Figure 4.31 shows the result of interaction of the aluminated samples covered with protective layer with Ga. In the case of diffusion of gallium atoms through the film, they interacted with aluminum under-layer to form a liquid alloy (see Figure 4.28).

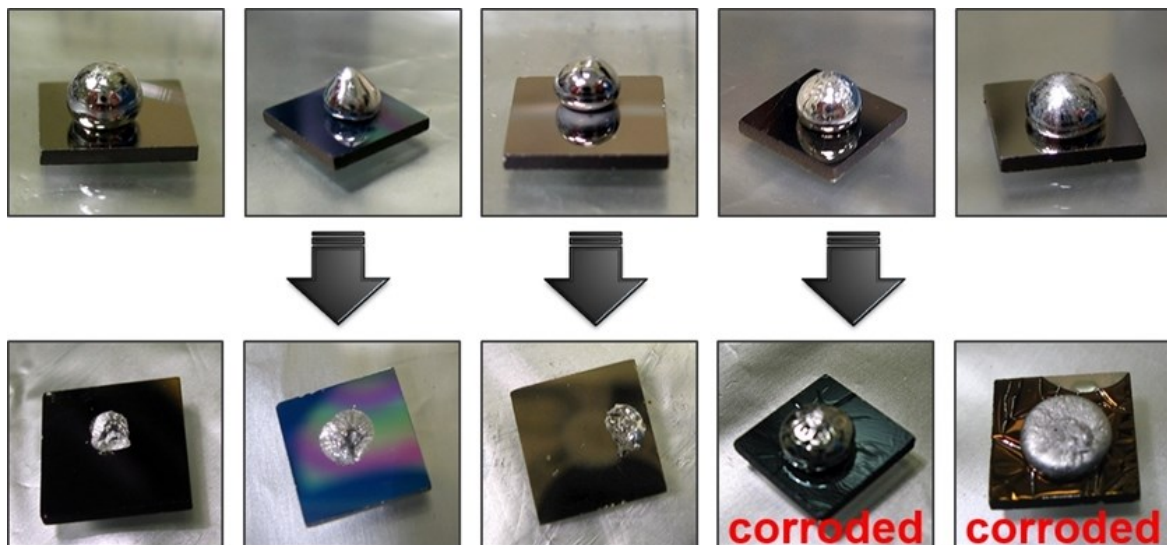


Figure 4.28: Evaluation of results of liquid gallium test: resistance and corrosion.

4.6 Vacuum brazing

4.6.1 The vacuum system

Two of four chambers of 4-chamber vacuum system described in Chapter 4.3 were used in order to set-up inductive and resistive vacuum furnaces.

4.6.2 Furnace used for vacuum brazing

4.6.2.1 The inductive furnace

A small inductive furnace (8 cm diameter 10 cm height) was constructed directly inside the vacuum chamber of 25 cm in diameter and 25 cm in length. The approach of this furnace was to heat up by induction a graphite susceptor, a kind of “hot chamber”, where the processed pieces were placed. The high purity HIP sintered graphite of Tokai Carbon was used to machine the susceptor (Figure 4.30b). The inductor was fitted to the shape of the graphite susceptor (Figure 4.29). The graphite “hot chamber” is thermally insulated from SS vacuum chamber by alumina. External wall of SS vacuum chamber was water-cooled for the safety reasons.

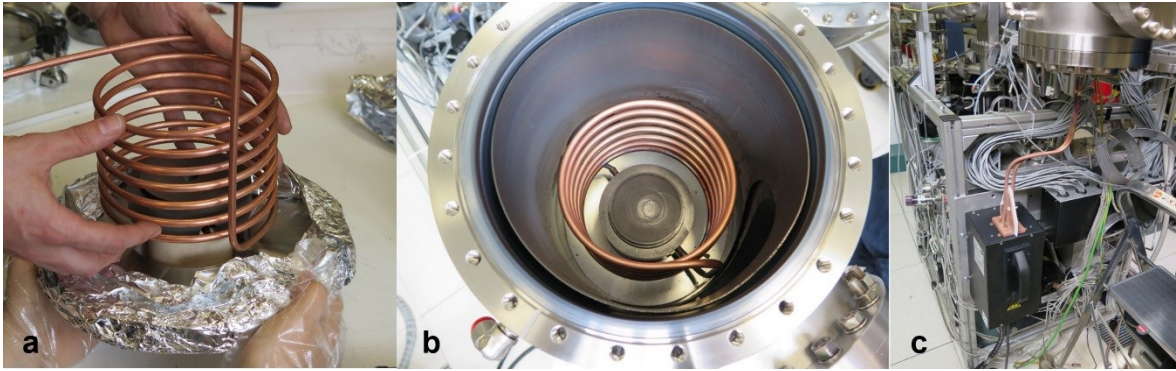


Figure 4.29: Installation of inductive vacuum brazing furnace.

The inductor was powered by 10kW Ambrell EkoHeat power supply. The power supply and the inductor were connected to the general water-cooling circuit of the laboratory (5kW total).



Figure 4.30: Inductive brazing furnace: a) samples positioning, b) graphite chamber closed, c) pyrometer temperature control.

The heating control was realized due to changes of the set power of the inductor power supply. The temperature inside graphite “hot chamber” was controlled by a pyrometer (Figure 4.30c) with PYROSOFT Spot 2.6.1.0 software.

Some tests were performed for diamond powders-SS brazing with the designed induction furnace. However, unfortunately, this installation was not able to provide acceptable heating ($5^{\circ}\text{C}/\text{min}$) and cooling ($3^{\circ}\text{C}/\text{min}$) rates, allowing to minimize the stresses in metal-ceramic brazing joint and avoid cracking ceramics pieces of bigger size. The reason was the overloading of the chiller system available in the laboratory. In a case of change of the chiller to more powerful ($\sim 20\text{kW}$) or use of additional to existing (5kW) chiller, another one for inductor Ambrell EkoHeat power supply, designed inductive brazing furnace can be used without problem.

Taking into account the described limitation of the chiller, all following brazing experiments were realized by means of IR lamp based resistive furnace.

4.6.2.2 Resistive furnaces

Small mobile resistive furnaces were constructed in order to be directly placed inside the vacuum chamber of 25 cm in diameter and 25 cm in length (see Figure 4.31). The external wall of the SS vacuum chamber was water-cooled for safety reasons. The vacuum chamber is shown in the Figure 4.31. The DN100CF flange with assembled furnace and all electrical connections was placed downside the vacuum chamber.

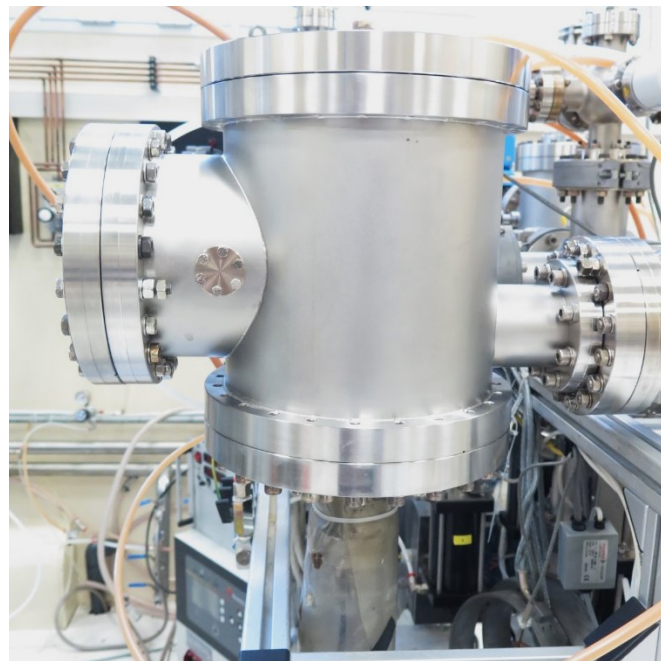


Figure 4.31: Vacuum chamber with IR lamp heated brazing furnace assembled.

4.6.2.2.1 IR heating system

Instead of usual resistive elements, the 450W IR lamps of Helios Italquarz were used as a heating source in the furnace. The temperature was controlled by the K-type thermocouple placed inside the furnace.

The automatic custom-made infrared lamp backing control system (see Figure 4.16a) was used to control the IR lamp reading the temperature from the thermocouple placed inside the furnace box. The temperature control module (Figure 4.16a) is based on a commercial temperature controller GEFTRAN 1600 and a power controller device. This system allowed

to set up the heating temperature and also the heating and cooling velocities, since that aspect was extremely important for successful ceramics brazing.



Figure 4.32: D40mm IR lamp driven vacuum brazing furnace.

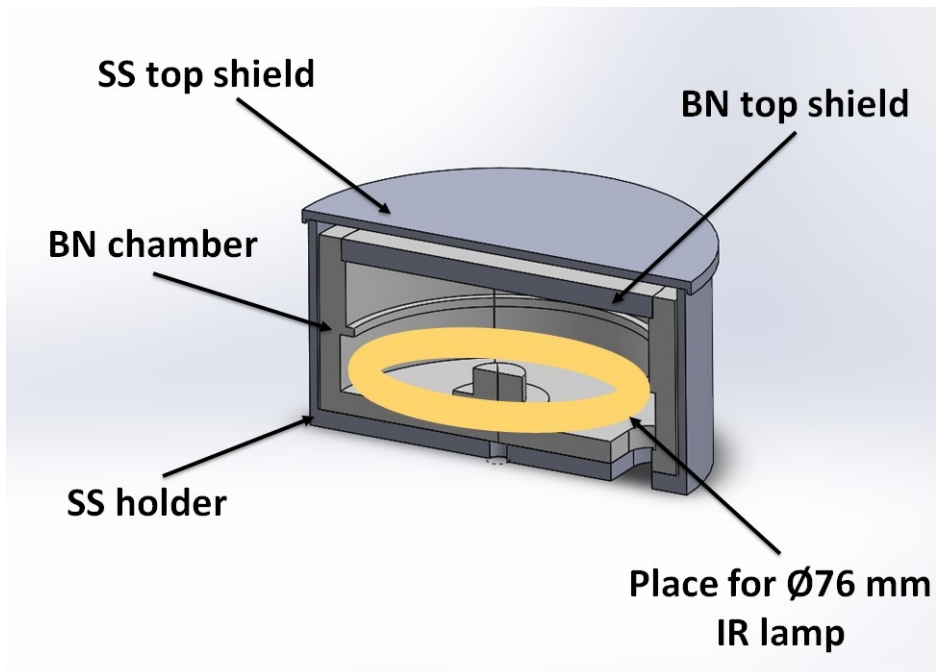


Figure 4.33: D76mm IR lamp driven vacuum brazing furnace design.

4.6.2.2.2 *Small vacuum oven design*

The most important aspect in a small furnace design was to make the appropriate thermal insulation in order to provide successful heating up to required temperature. A double insulation of ceramics and SS was chosen. Sintered boron nitride (BN) was used to realize ceramic part of insulation thanks to its high machinability in respect to commonly used alumina. In reality, a small furnace presents a kind of double box of BN and SS attached to DN100CF flange (see Figures 4.32, 4.34).

At first the furnace presented on Figure 4.32 with an internal cylindrical space $\varnothing 35\text{mm} \times 5\text{mm}$ (with the possibility to increase the height of the chamber) was realized starting from a sintered BN bar of 50 mm diameter to hold the 40mm diameter 450W IR lamp.

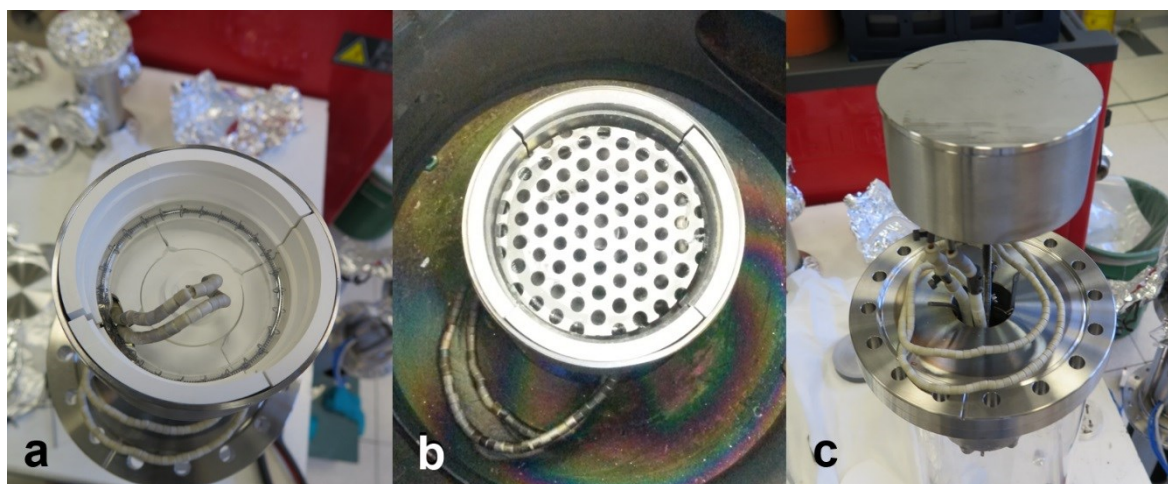


Figure 4.34: D76mm IR lamp driven vacuum brazing furnace.

After, in order to allow brazing of bigger samples, a new furnace based on the 76mm diameter IR lamp as a heating source was designed (Figure 4.33) and realized (Figure 4.34). The BN shield, in this case, was realized in 6 pieces machined from the same 50mm diameter BN bar. The internal space in furnace was $\varnothing 76\text{mm} \times 10\text{mm}$. The external shield was made of SS. The SS grid was used to hold the samples during brazing. The temperature was controlled by the K-type thermocouple attached to the grid.

The small furnaces arrived to the maximum temperature of 1050°C .

4.6.3 Preliminary ceramics materials treatment

The chemical pre-treatment of sapphire and synthetic diamond are described in Chapter 4.2.1.3. In order to provide a good thermal and mechanical contact during brazing ceramic substrate it is necessary to create a metallization layer with a good adherence.

4.6.3.1 Titanium coating deposition

Titanium metallization is the most known approach in ceramic brazing to improve the contact in a joint. Titanium onto sapphire and synthetic diamond substrates was deposited by DC magnetron sputtering. The substrates were not heated up or cooled down during deposition. The substrates were attached to the SH just by appropriate silver-glu in order to avoid using camps and to cover all the substrate uniformly by titanium (see Figure 4.35).

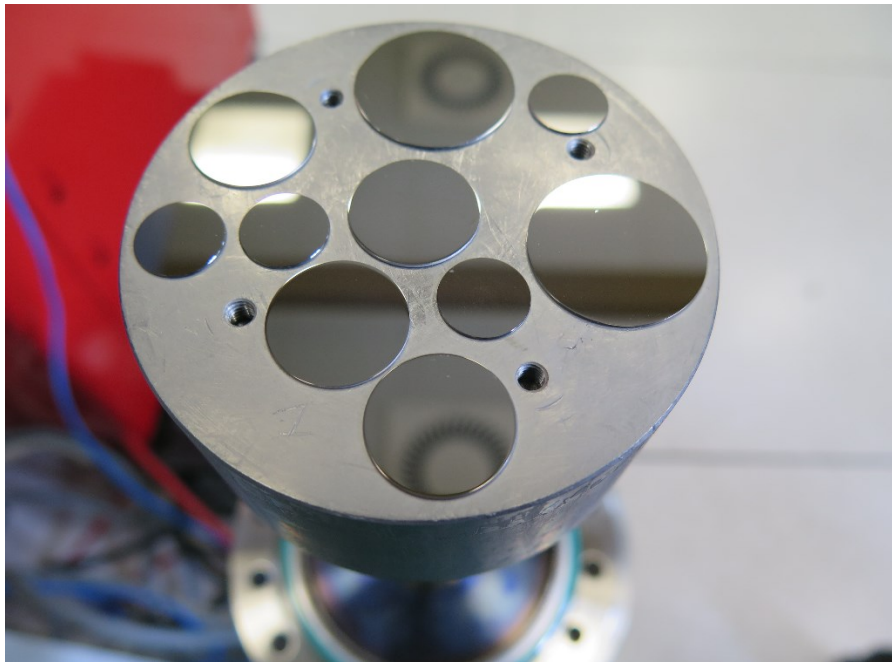


Figure 4.35: Sapphire substrates with Ti coating deposited.

1-2 μm titanium layers were deposited by MS at 0.5A DC current, $8.8 \cdot 10^{-3}$ mbar Ar pressure at 6 cm target-substrate distance during 20 min. The appropriate sputtering pressure was chosen in order to minimize the intrinsic stress in the film and avoid titanium film peeling.

4.6.4 Brazing fillers preparation

After a number of brazing tests with commercially available brazants, I realized that the most flexible approach is to use “in place” produced brazing pastes appropriate for each particular

brazing process starting from commercially available metallic powders. Thus, the powders listed in the Table 4.4 were used for brazant paste preparation.

Table 4.4 Powders quality

<i>Metal</i>	<i>Purity</i>	<i>Mesh</i>	<i>Manufacturer</i>
Copper	99%	-200	Aldrich®
Tin	99%	-100	AlfaAesar®
Titanium	99%	-325	AlfaAesar®
Silver	99%	-325	AlfaAesar®
Nickel	99.8%	-325	AlfaAesar®
Aluminium	99.97%	-325	AlfaAesar®
Silicon	99.999%	-100+325	AlfaAesar®

The utilization of “homemade” pastes allowed also to decrease a lot the costs of the brazant.

4.6.4.1 Powders mixing

A TURBULA® T2F shaker was used to mix the powders for brazing filler preparation. The TURBULA® T2F is a 3-dimensional shaker mixer for fast and homogeneous mixing of powder substances of different particle sizes, whether or not in combination with liquids. The TURBULA works with the Schatz geometry theory and achieves optimum mixing results.



Figure 4.36: TURBULA® shaker mixer for powders.

The mixing basket can hold any form of container. Polyethylene containers of 30ml and 200ml were used for powders mixing in current work without adding liquids. The containers

were fastened in place by twisted rubber rings (see Figure 4.36). The basket movement is driven by elastic drive belts an energetic drive gear. Frequency converter can vary the speed of the movement.

4.6.4.2 Paste-creating agents

The main task of the paste-creating agent is to provide a uniform mixing of the powder components and appropriate viscosity to make the paste attaching to the substrates being brazed. The paste-creating agent is an organic compound or mixture, which is decomposed at temperatures lower than the brazing temperature and leaves minimum traces after the decomposition.

Glycerol 99+% of Jansen Chimica was used as candidate for paste-creating agent. Unfortunately, it did not provide enough viscosity to the prepared pastes and thus complicated the utilization of the paste.

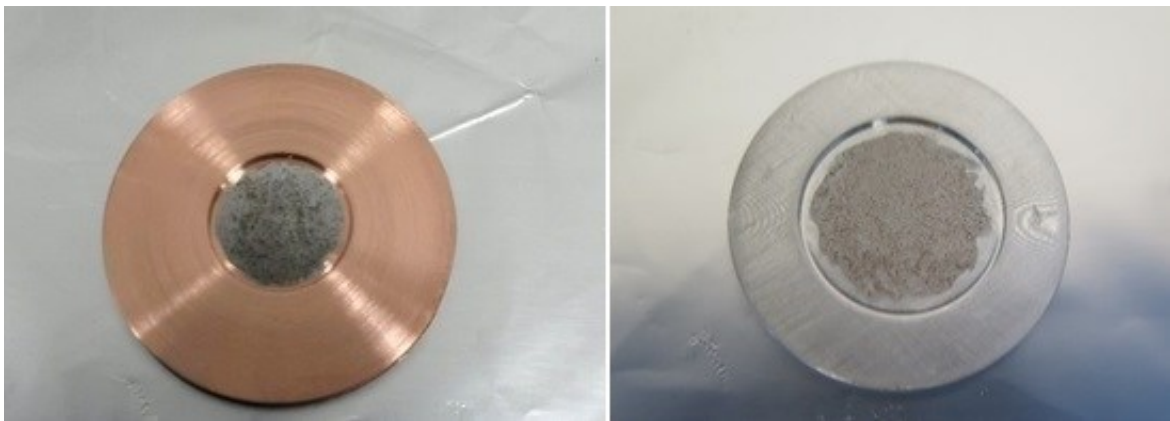


Figure 4.37: Application of just prepared brazant paste on copper and aluminum samples.

Liquid COCCOINA[®] glue presents partially hydrolyzed under heating potato starch solution (dextrins). It appeared to be the most safe, convenient and cheap paste-creating agent. It had sufficient viscosity to provide easy application on the substrates, and it was decomposed completely at elevated temperatures. The Figure 4.37 shows application of just-prepared brazing filler pastes on copper and aluminum substrates.

4.7 Cyclotron irradiation tests

4.7.1 GE PETtrace Cyclotron

Under beam tests of the produced target prototypes were realized with the PETtrace 800S cyclotron of General Electric Medical Systems at the Medical Physics unit of the Bologna University Hospital "S. Orsola-Malpighi" (Figure 4.38).



Figure 4.38: GE PETtrace cyclotron of S. Orsola-Malpighi Hospital, Bologna.

The PETtrace 800S is based on a 16.5 MeV proton accelerator with an 8.4 MeV deuteron option. The PETtrace is an isochronous cyclotron that works at fixed energy, able to accelerate negative hydrogen ions (H^-) up to 16.5 MeV, with a maximum of beam intensity of 100 μA (in reality the current depends on the source and tuning of the magnets). The PETtrace 800S is self-shielded. The beam of accelerated particles can be directed on one of the six output ports available. The cyclotron is equipped with five kinds of targets for the production of the main radionuclides of interest for PET (^{11}C , ^{13}N , ^{15}O , $^{18}F^-$, $^{18}F_2$), and is able to operate in a dual beam, i.e. it can simultaneously irradiate two targets.

The PETtrace main components include magnets, an RF-source, an ion source, a beam extraction system, a beam control system, a cyclotron vacuum system, targets, the Master System for operator control, electronics and power supplies, a cooling water system, and a power distribution system (see Figure 4.39).

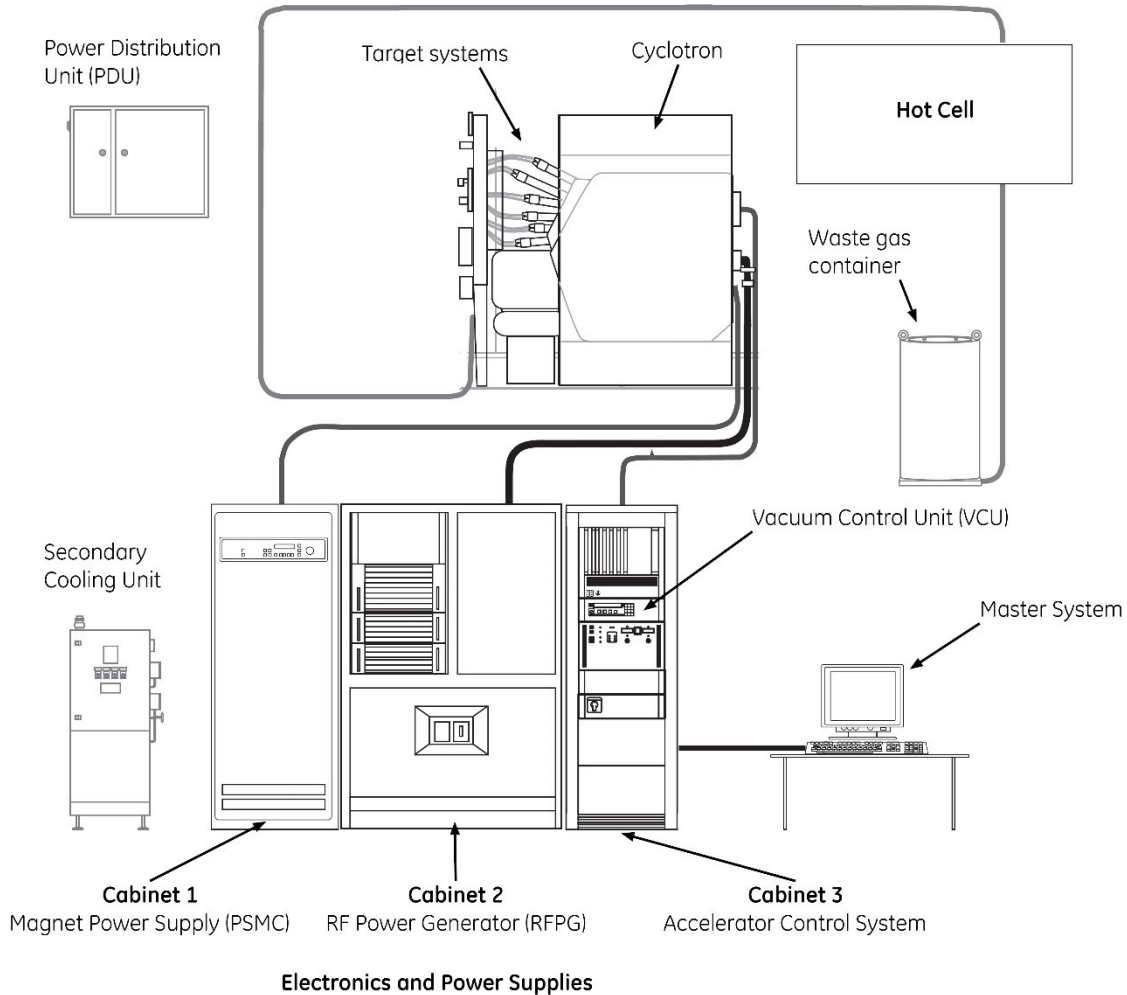


Figure 4.39: GE PETtrace cyclotrons system.

4.7.1.1 The vacuum system

The PETtrace 800 vacuum system consists of high vacuum oil diffusion pump and mechanical roughing pump. To measure the wide range of pressure inside the vacuum chamber two pressure gauges are installed: the Pirani, capable of measuring pressures from 1 bar to 10^3 mbar and the Penning pressure gauge for the measurement of high vacuum ($<10^3$ mbar). A dedicated vacuum system controller performs pressure monitoring, vacuum pump sequencing and system operation. The normal operation vacuum level before irradiation is $2\div 5 \cdot 10^{-7}$ mbar.

4.7.1.2 The ion source

The PETtrace accelerates negative ions (either protons or deuterons depending on desired isotope) generated in located in the center of the cyclotron cold-cathode Penning Ion Gauge source. The electrical discharge produced by a huge electric tension applied between the anode (side surface of the cylinder), connected to the ground, and two cathodes (bases of the cylinder), to which a negative voltage generated by the PSARC (Power Supply Ion Source) is applied. The plasma is confined inside the chamber for the presence of the magnetic field. The ions come out from the chamber when a positive voltage is applied to the dee, which is located close to the slit of the source.

4.7.1.3 The magnet

A hollow inductor coil induces the magnetic field. The coil is made of hollow-core copper conductors that are fiberglass insulated and casted in epoxy. The magnet is cooled with deionized water. Hardware interlocks continuously monitor the cooling water flow. The magnet is oriented vertically and powered with PSMC power supply (see Figure 4.39). An average magnetic field is of around 1.8 Tesla.

4.7.1.4 The RF-source

The RF system consists of two resonators and a RF Power Generator (RFPG) applying an RF power to the two resonators within the vacuum chamber. The RF cavities are designed as four dees: two powered by RFPG and placed at angle 75° , the other two are grounded. Acceleration voltages are about 35kV with the RF frequency set by crystal oscillators at 27.2MHz for protons and 27.8MHz for deuterons. The resonators operation is automatically regulated by the cyclotron control system.

4.7.1.5 Beam extraction

Extraction is achieved by carbon extraction foils (two carousels with six carbon foils each), which strip the electrons off the accelerated ions, thus reversing the polarity of the charge, and altering the direction of the orbit. By careful positioning of the extraction foils, the beam can be steered onto a particular target.

4.7.1.6 Beam control system

The beam current is continuously monitored and regulated by the beam diagnostic system. One part of the diagnostic system provides a remotely actuated internal beam probe to aid in

adjusting and tuning the beam. Another part continuously monitor the extraction foil carousel, collimators and targets to allow fully automated start-up, tuning and operation.

4.7.1.7 Cyclotron control

The PETtrace 800 control system is equipped with an accelerator control unit, a chemistry control unit and PC workstation. The control units carry out all the automated closed-loop and logical control tasks, while the workstation is used for operator inputs and database handling.

The Master System controls the Accelerator Control Unit and the Chemistry Control Unit via a local area network. It continuously displays status information for the accelerator, the targets and the radiochemistry system. The Master System software contains functions to: start up and control tracer production, edit production parameters, handle targets and radiochemistry system before and after production (Maintenance), print available reports, make screen dumps and display help texts.

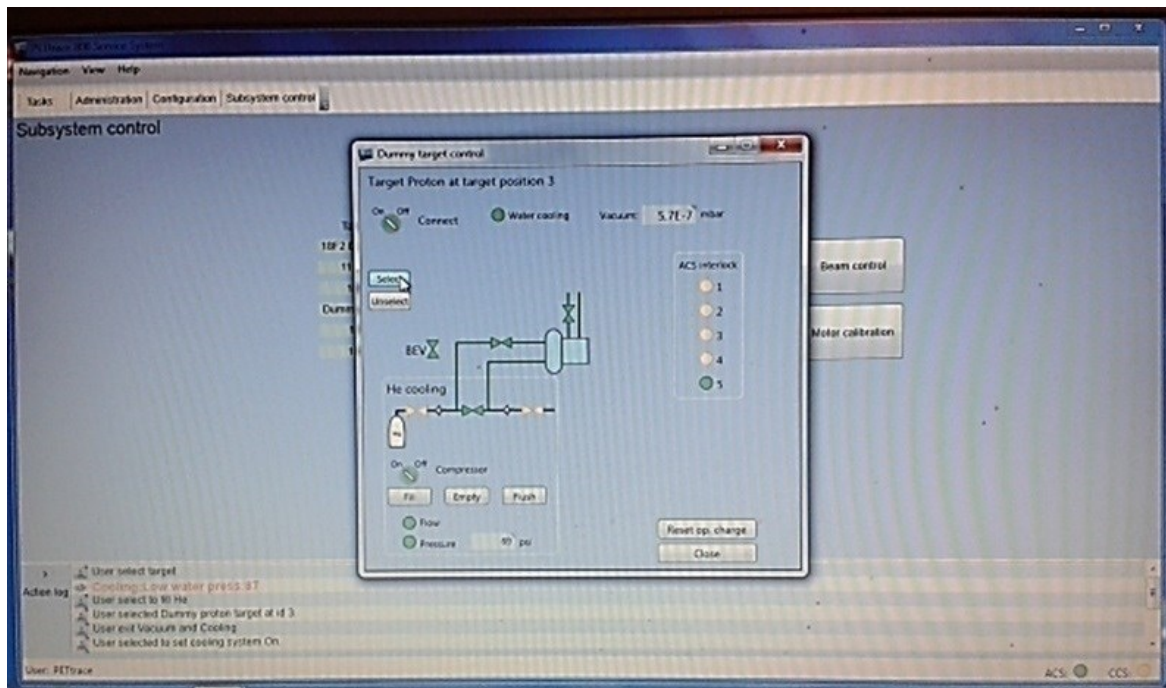


Figure 4.40: The PETtrace service system interface.

In described irradiation tests, the Master System was used only for a long time irradiation test. In all other cases, the PETtrace 800 Service System (PSS) software was used to control the cyclotron parameters. The program interface is shown in the Figure 4.40, particularly, the target control window is opened.

PETtrace 800 Service System (PSS) is a software running on a service laptop. It provides the manual control of the accelerator, the different targets and the radiochemistry subsystems. The PSS is intended for setting and monitoring different parameters, troubleshooting, configuration, and for user administration.

4.7.2 The solid target station design and constrictions

Six fixed target ports are located along the front side of the cyclotron vacuum chamber. The solid target station of the Bologna University Hospital “S. Orsola-Malpighi” cyclotron is not a commercially available unit. It was built as the first prototype of the solid target station that at present is produced by the TEMA Synergy with a bit modified dimensions.

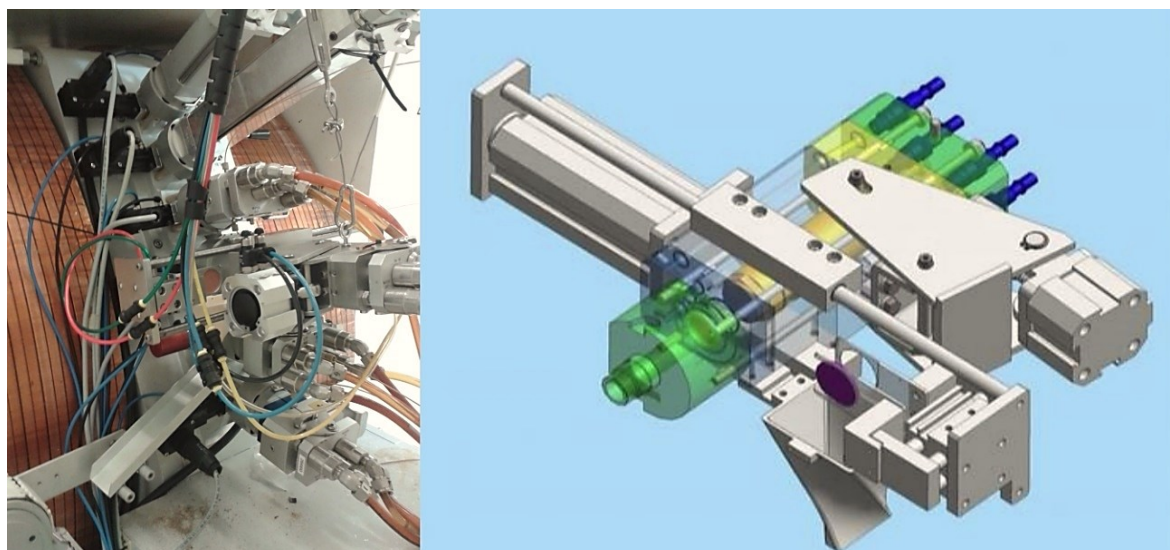


Figure 4.41: Solid target station.

4.7.2.1 Design

The target “coin” is placed inside the target station. Aluminium water cooling chamber (yellow on the 3D drawing in the Figure 4.41) is pressed to the back of the target “coin” (violet on the 3D drawing in the Figure 4.41) by ~3 bar air pneumatic piston. The target station requires manual placing of the target “coin” before irradiation and allows automatic receiving of the target after irradiation outside the cyclotron bunker. The automatic dismounting procedure is shown in the Figure 4.42.

4.7.2.2 Cooling systems

Double cooling is used to increase the current allowed on the target: a water-cooling form the back (yellow on the 3D drawing in the Figure 4.41) and a helium gas cooling from the front side (green on the 3D drawing in the Figure 4.41) of the target “coin” (violet on the 3D drawing in the Figure 4.41).

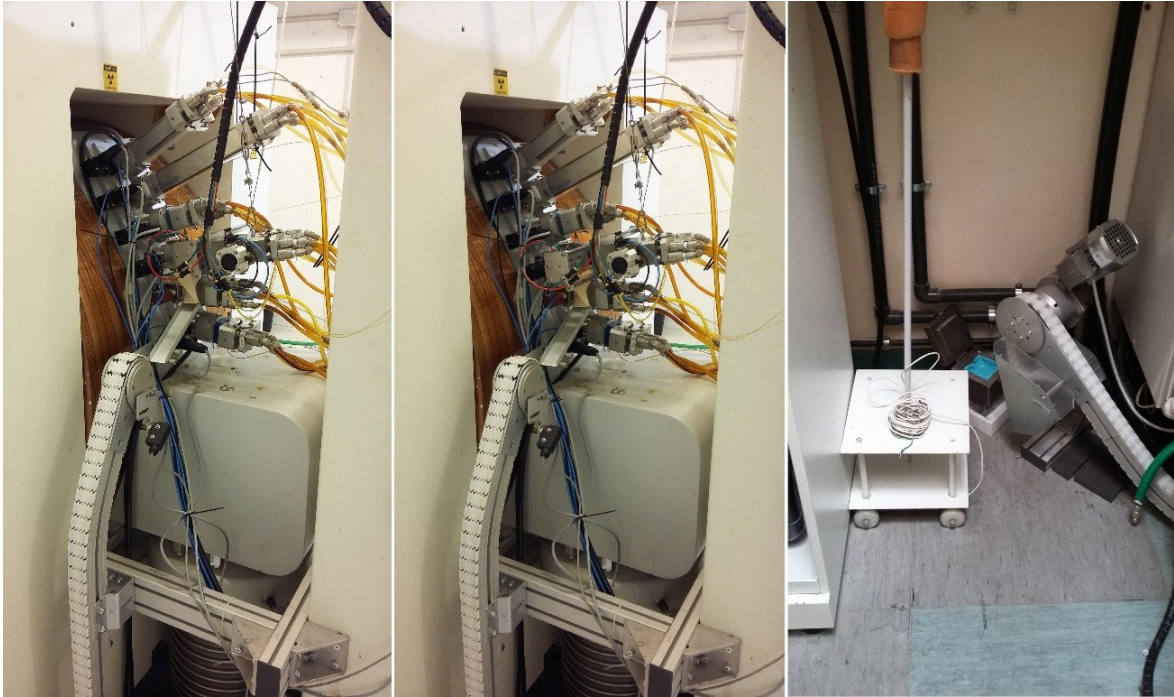


Figure 4.42: Automatic target dismantling procedure.

4.7.2.3 The target

The target dimensions are constricted by the design of the target station. The target “coin” should be a disk of 32 mm diameter and maximum 2 mm thickness.

4.7.2.3.1 Integer target disc

Integer target “coin” provides in current solid target system maximum heat exchange performance that is limited by the thermal conductivities of target material and target backing plate material and the contact between them.

The most standard method of producing such type of targets is electrodeposition of metallic target material onto target backing plate. The standard cyclotron current for production using electrodeposited target is up to 25 μ A.

4.7.2.3.2 The 4-pin clamping system

In order to house irradiated target material in a form of foils a 4-pin target holder was designed (Figure 4.43). The same system was used to house 13mm diameter discs of sapphire and synthetic diamond for test proving chemical inertness. The external dimensions of the target holder were 32mm diameter and 2 mm thickness in assembled state.

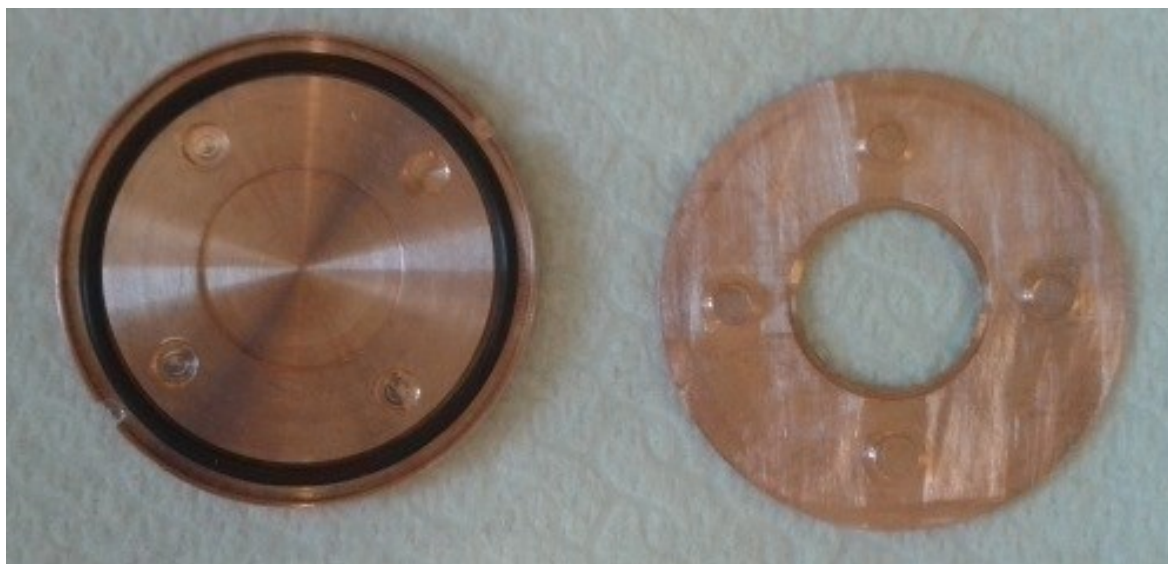


Figure 4.43: 4-pin clamping target system.



Figure 4.44: Liquid nitrogen cooled HPGe of "St. Orsola-Malpighi" Hospital, Bologna.

This system provided efficient helium gas cooling from the front side through the hole in the clamping system, but absolutely did not guaranty good thermal contact with copper from the back and, correspondingly, the cooling of aluminium chamber by water flow was not effective.

4.7.3 Gamma spectroscopy

A gamma spectroscopy analysis was used after the cyclotron irradiations in order to prove a chemical inertness of ceramic materials used in the target prototype construction (sapphire, CVD synthetic diamond).

The liquid nitrogen cooled high purity germanium coaxial detector “St. Orsola-Malpighi” Hospital, Bologna was used (Figure 4.44). The Laboratory HPGe Spectrometer with shield was used for measuring the specific gamma radiation of the radionuclides. It employs precision gamma-spectrometry methods in its operation. The spectrometer also features a low level of instrumental background and a low threshold for radionuclide detection.

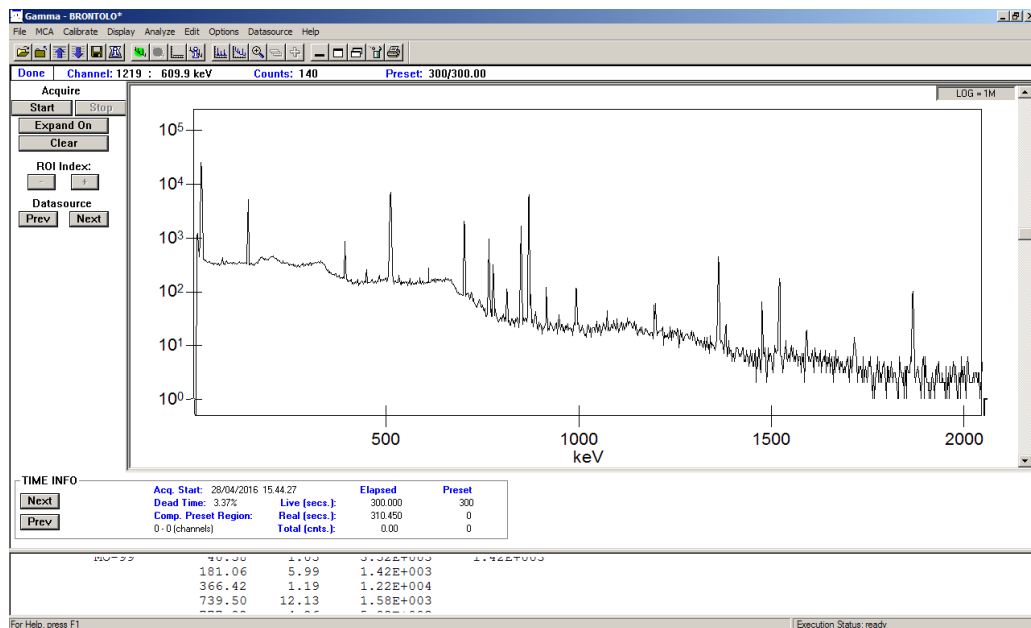


Figure 4.45: Gamma-BRONTOLO software interface

Appropriate software allowed collecting the spectrums, performing calibrations and comparing the results with the databases, determination specific activities. The software interface is presented in the Figure 4.45.

4.8 Reduction system for Mo target material recovery

The reduction apparatus was created in LNL INFN by C. Rossi-Alvarez, P. Buso, A. Zanon, and P. Bezzon as part of the TechnOsp experiment.

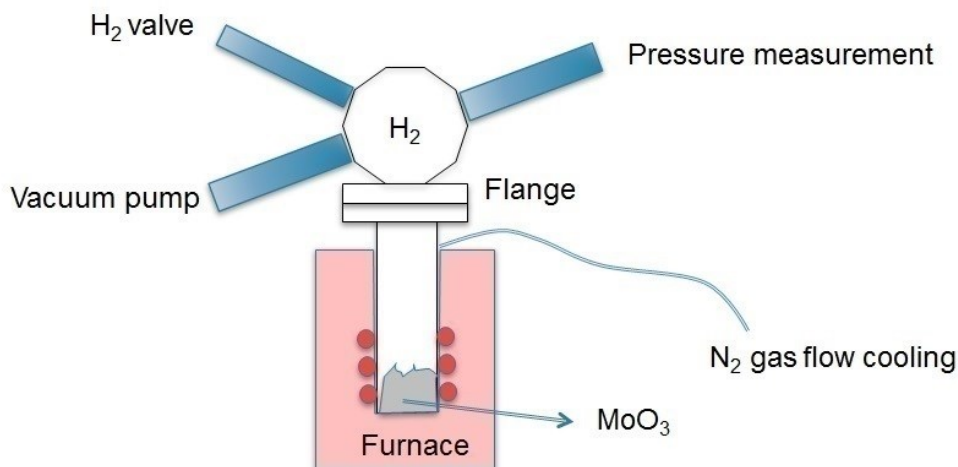


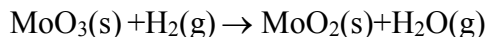
Figure 4.46: Reduction system scheme.

The system was composed of (Figure 4.46):

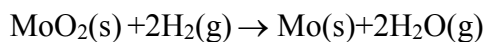
- Furnace
- Tungsten reduction cell filled with hydrogen
- Vacuum pump
- Liquid nitrogen Dewar
- Process data acquisition system

4.8.1 Short description of process chemistry

The reduction of molybdenum (VI) oxide is realized in two steps:



$$\text{Log } K_{(4)} = 4469.7/T + 1.27$$



$$\text{Log } K_{(5)} = -4363.9/T + 2.87$$

The first step of the conversion (4.5) is exothermic and thermodynamically favorable at 550-600°C [88, 89]. The exothermic reaction can cause local overheating and MoO₃ volatilization. This aspect is limiting the velocity of heating. Instead, the second step (4.6)

is endothermic, and relatively high temperature and H_2/H_2O ratio greater than two is required to provide the hydrogen reduction of MoO_2 . According to the literature, the temperature for second stage the reduction stage varied from $930^\circ C$ to $1000^\circ C$ depending on the Mo powder size. The lower was the reduction temperature, the smaller was the reduced Mo powder size. However, at a lower reduction temperature, a longer reduction time was required for complete transformation [89]. Detailed description of the kinetics of the second step can be found in work of Kim et.al.[90].

The procedure for reduction under H_2 gas flow, and the 3-step conversion starting from ammonium molybdate was described by Gupta [91] for non-enriched isotopes and by Gagnon et.al. for enriched elements recovery[16]. Here the reduction from MoO_3 to MoO_2 was considered to be realized at $500-750^\circ C$, keeping the heating rate at $2^\circ C/min$, and further reduction to metallic Mo at $750-1100^\circ C$ with heating rate $5^\circ C/min$ and reduction time of 1h at maximum temperature. The overall Mo recovery of 87% was reported [16].

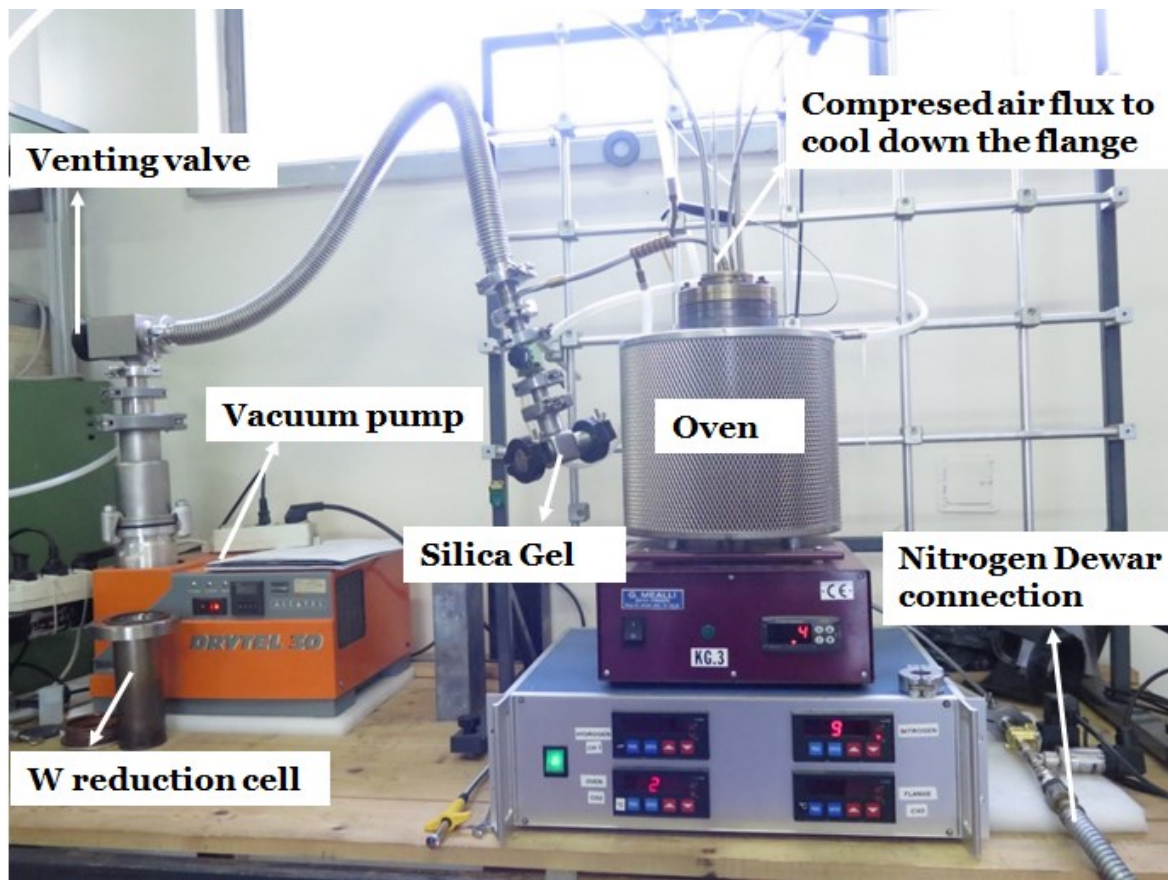


Figure 4.47: Reduction system scheme.

4.8.2 Equipment

In place of the industrial MoO_3 reduction procedures (see above), the recovery method presented in current work was not using constant hydrogen flow (that was complicated from the safety point of view in the framework of the LNL INFN laboratories). Instead, in order to shift the equilibrium in the reaction (4.6) in the direction of products, two techniques were used: carrying out the experiment in an overpressure of hydrogen; condensing and capturing the water released during reduction by an appropriate amount of silica gel. The reduction capability of the system depends on the maximum amount of hydrogen that can be inserted without safety problems, providing the overpressure even when the reduction reaction was complete and the amount of dried silica gel possible to handle.

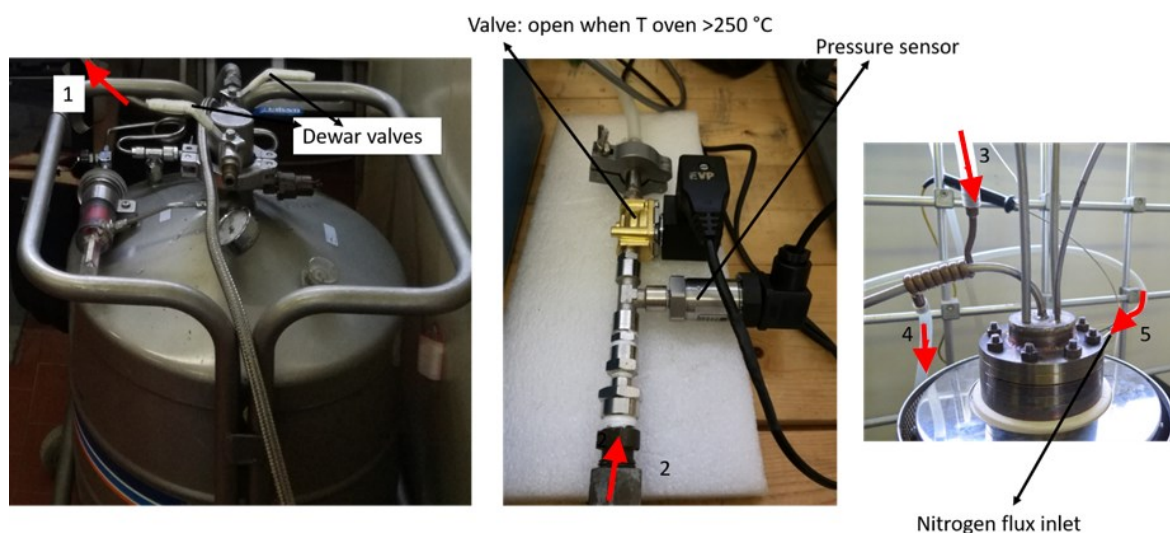


Figure 4.48: Nitrogen gas line.

The full reduction system is presented in the Figure 4.47. During reduction experiments MoO_3 was placed in a quartz crucible inside a tungsten reduction reactor (Figure 4.49). The system was pumped down to remove oxygen, and then hydrogen in overpressure was inserted by the gas valve.

The resistive furnace was used to heat up the reduction cell. Nitrogen gas released from LN_2 Dewar was used, first, for cooling down the tube to condensate the produced during reaction water, and after by flowing around the tungsten reduction cell's external wall (see Figure 4.48). The Nitrogen flux valve was opened automatically when the oven temperature was above $250\text{ }^\circ\text{C}$. Silica gel (of about 10 g) was placed in a box inside the vacuum system for capturing produced water

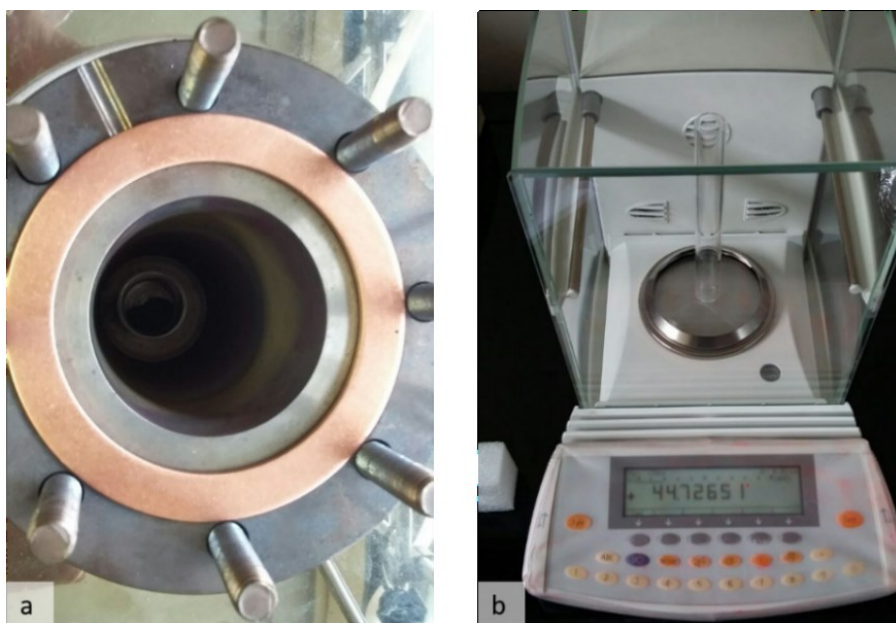


Figure 4.49: Quartz crucible placed inside tungsten reduction cell.

Compressed air was used to cool down the flange that closes the reduction cell from the top (see Figure 4.50).



Figure 4.50: Compressed air flange cooling

4.8.2.1 The vacuum system

The Alcatel Drytel 30 oil-free pumping system was used for preliminary evacuation of the reduction cell. The Drytel 30 can operate from atmosphere to 1×10^{-6} torr, with a maximum pumping speed of 16 cfm ($\sim 27 \text{ m}^3/\text{h}$) in the high vacuum range.

The Alcatel Drytel 30 multi-stage high vacuum pumping system is composed of a 7.5 l/s turbo drag pump and a 1 m³/h diaphragm pump. The turbo drag pump is very robust and can be opened to atmosphere at full speed without damages to the pump (this is not possible with a turbo molecular high vacuum pump). The diaphragm pump carries the main load of pumping from the atmosphere down to 10 torr. The Alcatel MDP-5010 turbo drag has a high compression ratio of nearly 1×10^{-9} and produces excellent high vacuum flow rates.

4.8.2.2 The oven

A 1400W resistive melting furnace of Giuseppe Mealli S.r.l., Firenze was used as a heating source for the reduction process. It is equipped with Kanthal resistors to ensure high temperatures and long duration. The thermal insulation is made of ceramic fiber in order to achieve a rapid heating in combination with a low power consumption. The maximum temperature the oven can achieve is 1150°C.

4.8.2.3 The reactor

The reduction reactor is the vessel with hydrogen atmosphere that should be heated up by the oven. The reactor was realized in tungsten-copper composite material allowing to combine high melting temperature of tungsten with good machinability of copper. A flow of nitrogen gas was passing around the external walls of the reduction cell in order to minimize its oxidation at elevated temperatures.

4.8.2.4 Automatized control

The main parameters controlled during the process include:

- Temperature of the oven (0-1100 °C);
- Temperature of the flange (0-500 °C);
- Hydrogen pressure (0-8000 mbar absolute);
- Nitrogen pressure (2-2000 mbar absolute).

Table 4.5 Heating parameters for reduction control

<i>Step</i>	<i>Temperature range (°C)</i>	<i>Programmed temperature rate (°C/min)</i>
1	r.t. – 350	5
2	350 – 750	2
3	750 – 950	5
4	950	Constant for X h
5	950 – r.t	Natural convection cooling

The program **MoO3_H_Control**, used to control the reduction system, was written in Java language (see Figure 4.51). It allows to set up the multistep heating process, described by the **Riduzione_PID.txt** file. The heating parameters are shown in Table 4.5.

In the step four, the temperature was kept constant for X hours, depending on the starting amount of MoO₃. The heating parameters can be modified, directly by the user during the process, through the GUI interface.

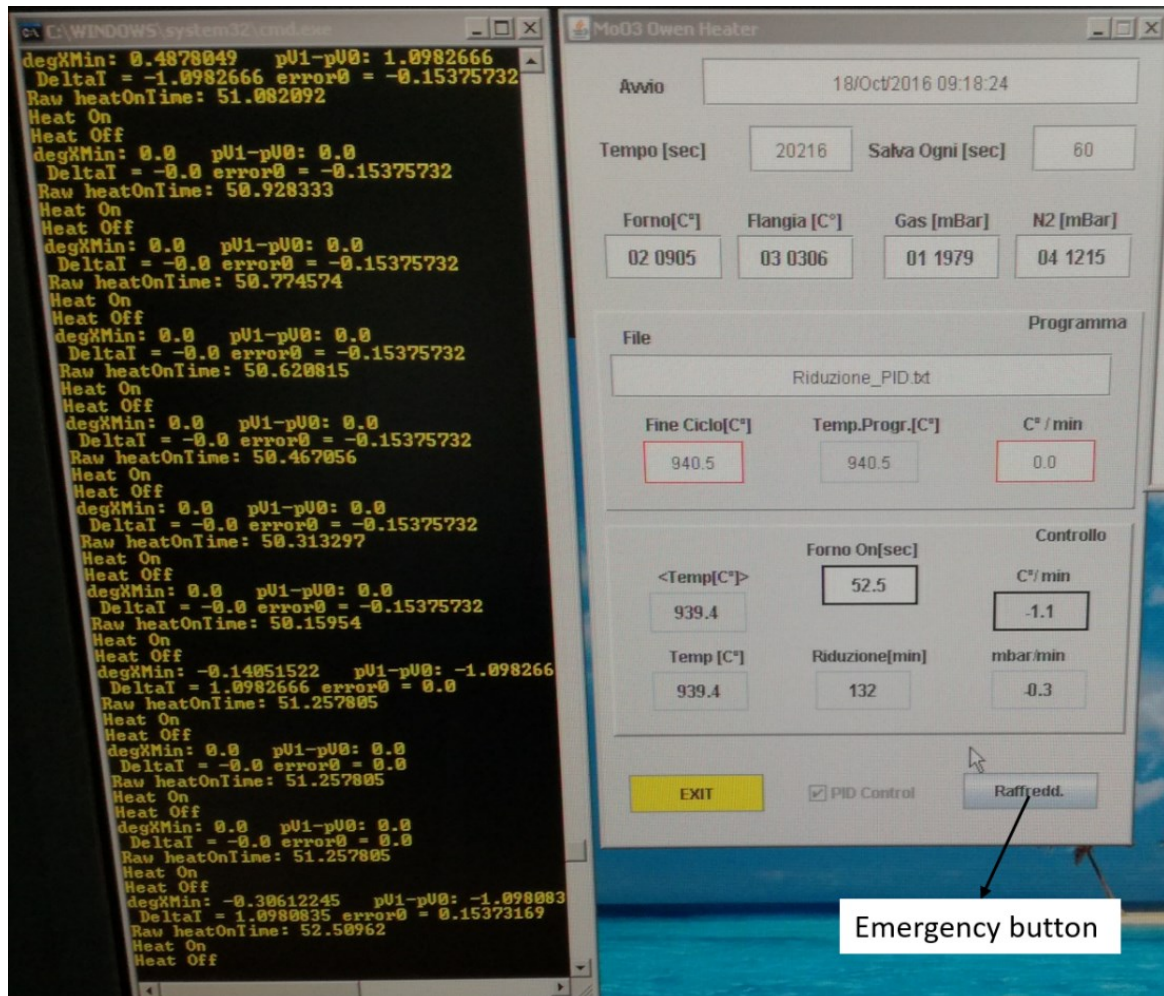


Figure 4.51: Automatic program interface.

In a case of emergency, the button **Raffreddamento** allowed interruption of the process (see Figure 4.51). If the flange temperature raises more than 350 °C, the program interrupts the process and the cooling get started.

4.8.2.5 Operation conditions

The checklist for the reduction procedure with the described system included:

1. Turning on the oven and the data acquisition system
2. Connecting the liquid nitrogen Dewar (Figure 4.48)
3. Connecting the hydrogen gas tank to the valve
4. Placing a new Cu gasket (Figure 4.49a)
5. Inserting the crucible with MoO₃ powder and closing the flange (Figure 4.49b)
6. Inserting the silica gel container (Figure 4.47)
7. Closing the venting valve (Figure 4.47)
8. Pumping up to 0-1 mbar
9. Keeping vacuum for some hours
10. Closing the valve on the vacuum pump
11. Controlling if the vacuum was stable for about 20-30 min
12. Rinsing the cell with hundreds mbar of H₂
13. Pumping until 0-1 mbar
14. Closing the valve on the vacuum pump
15. Loading 2500 mbar of H₂ (for 2.7 gr of MoO₃) from the H₂ tank
16. Disconnecting the tank from the system
17. Opening compressive air flux to cool down the flange (Figure 4.50)
18. Running the program **MoO3_H_Control** (Figure 4.51)
 - a. Selecting the folder to save the log-file of the process.
 - b. Starting the reduction with **START** button and choosing the file with the thermal cycle (**Riduzione_PID.txt**).

The maximum amount of MoO₃ powder that can be reduced in the reduction cell using 2500mbar H₂ (270 mg) is 2.7 g (18mmol). In this case, the amount of H₂ used for reduction is 108mg. When the process is finished a H₂ final pressure of 1500 mbar is obtained, maintaining the requirement of overpressure.

5 EXPERIMENTAL RESULTS

5.1 Study of non-conventional target cooling: liquid metal cooling

Metals have a thermal conductivity several orders-of-magnitude greater than water and organic liquids. Liquid (molten) metals have a viscosity comparable to that of water. High electrical conductivity and chemical stability of liquid metals makes it possible to flow them by MHD pumps without any moving parts. These features make liquid metals excellent candidates for high-performance cooling in many demanding applications, especially where heat must be removed at high heat flux. In contrast to conventional coolant such as water, the comparably high thermal conductivity of liquid metals makes it possible to acquire high-flux heat with low thermal resistance and at relatively low flow velocities.

Liquid metals for small applications are preferably room-temperature melting alloys of gallium. Many room-temperature-melting alloys of gallium, whether ordinary or eutectic, are non-toxic, stable in air, and they wet well many materials.

5.1.1 Protective coatings against LME for equipment protection

The most critical technological aspect of liquid metal use is Liquid Metal Embrittlement (LME). As soon as liquid metal corrosion is defined mainly by the diffusion of atoms of liquid metal inside the sensitive material, diffusion barriers to protect sensitive to LME metallic materials were studied.

5.1.1.1 R&D methodology

The system liquid gallium – aluminum was chosen as a testing system. Ga can represent aggressive liquid metal coolant and aluminum – material sensitive to LME. The diffusion barriers to protect aluminum from liquid gallium induced corrosion were deposited by magnetron sputtering technique.

Chemically resistant to liquid gallium materials, as Nb, Nb₂O₅, Nb-Ta, Nb-Zr, Ta-Zr were chosen as candidates for diffusion barriers.

5.1.1.2 Main results

The complete results on the study of diffusion barrier films based on refractory metals can be found in the published peer-reviewed papers [85-87]. In this thesis only the short extract is presented.

5.1.1.2.1 Nb diffusion barriers

The study of protective coating for LME was started from Nb coatings, as soon as niobium is inert to liquid gallium induced corrosion. The main approaches in protective coatings search were forwarded to 1) densification and packaging of the microstructure and 2) obtaining amorphous microstructure without prolonged grain-boundaries through the protective layer.

Table 5.1 Influence of pressure and negative bias on Nb protective film sputtering

<i>Sample Number</i>	<i>Nb-1</i>	<i>Nb-2</i>	<i>Nb-3</i>	<i>Nb-6</i>	<i>Nb-8</i>	<i>Nb-11</i>	<i>Nb-14</i>
Bias, V	grounded	-80V	grounded	-80V	grounded	grounded	grounded
Temperature, °C	floating	floating	floating	floating	500	25	-50
Ar pressure, mbar	$3 \cdot 10^{-2}$	$3 \cdot 10^{-2}$	$3 \cdot 10^{-3}$	$3 \cdot 10^{-3}$	$7 \cdot 10^{-3}$	$3 \cdot 10^{-2}$	$3 \cdot 10^{-2}$
Deposition rate, nm/sec	0.4	0.4	0.8	0.7	0.8	0.7	0.7
Crystallite size (XRD), Å	110	120	170	190	230	80	80
Cubic lattice parameter, Å	3.334	3.316	3.325	3.318	3.302	3.322	3.336
Liquid Ga corrosion	corroded	corroded	resists	resists	resist	resist	resist
Liquid Ga wettability	low	high	low	high	low	low	low
Acid test	5	3	5	1	4	3	5

As it can be seen from the Table 5.1 with main deposition parameters and results for Nb protective layer deposition, only the first approach appeared to be successful. Dense microstructures were obtained while deposited at $3 \cdot 10^{-3}$ mbar Ar pressure and at negative bias applied to the substrate.

Deposition at elevated temperature was less efficient for diffusion barrier creation, than negative bias, as soon as the grain boundaries of such coatings were also wider, that allowed faster diffusion.

According to liquid gallium and acid tests, the best condition for pure Nb corrosion protection coating were the following: -80 V bias and $3 \cdot 10^{-3}$ mbar argon pressure thanks to higher “packing” of the grains.

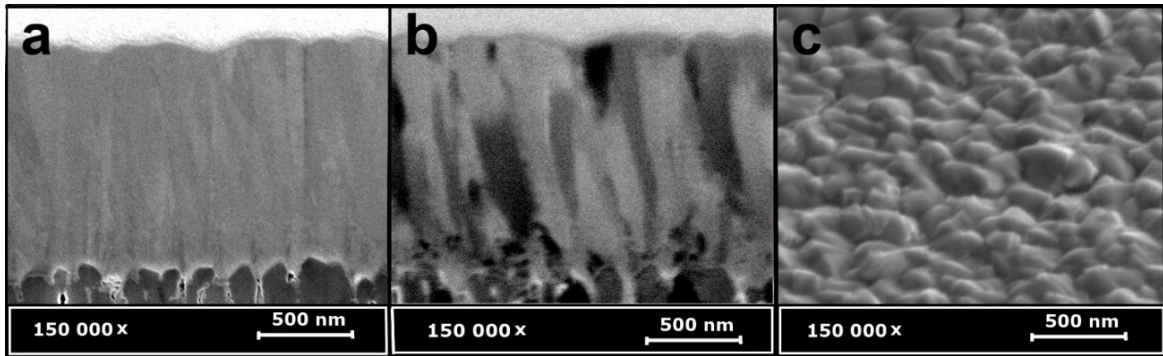


Figure 5.1: High resolution SEM of Nb-1 coating: a) FIB SEM of cross-section using electron beam; b) FIB SEM of cross-section using ion beam; c) SEM of the film surface.

The trial to obtain amorphous coatings of Nb at $<0^{\circ}\text{C}$ was realized. The coatings deposited at low temperature had a very low grain-size $\sim 60 \text{ \AA}$ but were not properly amorphous (Table 5.1). Even if the niobium coatings obtained at low temperature resisted to liquid gallium they showed quite low resistivity to the acid solution, since they were porous, that is not acceptable for the diffusion barrier.

In any case, pure Nb coatings were always crystalline with columnar microstructure (see Figure 5.1) that is not beneficial for the diffusion barrier efficiency, instead niobium oxide, obtained by reactive sputtering in stoichiometric conditions had dense amorphous microstructure (see Figure 5.2).

5.1.1.2.2 Nb_2O_5 and $\text{Nb}/\text{Nb}_2\text{O}_5$ multilayer films

Stoichiometric niobium oxide coatings showed superior resistance both to the liquid gallium corrosion and to acid corrosion in respect to pure niobium films. Besides that, niobium oxide coatings showed to resist to liquid gallium, and showed also low wettability.

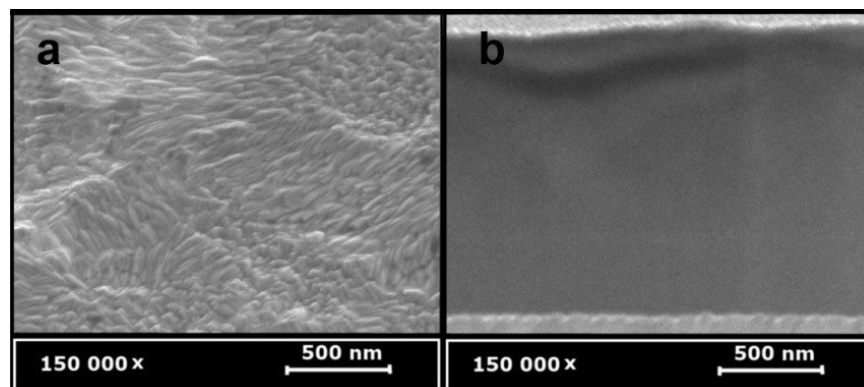


Figure 5.2: SEM of amorphous Nb_2O_5 -5: a) top view; b) FIB-SEM of cross-section.

Oxides coatings are known to be brittle [92] and this property can hinder the use of pure Niobium under conditions of mechanical stress. Multilayer structure is known to be a way to improve toughness of ceramics thin films inserting layers with higher plasticity (metallic)[93].

Table 5.2 Niobium oxide and multilayer protective coatings

Sample Number	<i>Nb₂O₅-5</i>	<i>M-1</i>	<i>M-2</i>	<i>M-3</i>
Method	Floating, grounded	Fine layers	Thick layers	Thermal oxidation
Ar flux, sccm	3	3	3	3
O ₂ flux, sccm	7	0/7	0/7	0/100
Work pressure, mbar	1·10 ⁻²	3·10 ⁻³ /1·10 ⁻²	3·10 ⁻³ /1·10 ⁻²	3·10 ⁻³ /0.2205
Number of double-layers	-	30	6	6
Expected Niobium layer thickness, nm	-	30	220	220
Expected oxide layer thickness, nm	-	3	25	-
Measured double-layer thickness, nm	-	70	320	220-280
Thickness, μm	1.5	2.5	2.5	1.9
Crystallite size (XRD), nm	-	5	16	18
Average grain size (SEM), nm	amorphous	amorphous	40	70
Cubic lattice parameter, Å	-	3.362	3.317	3.318
Liquid Ga corrosion	resisted	resisted	corroded	corroded
Acid test (1 ÷ 5)	1	1	2	2

The multilayer architecture was shown to influence on mechanical stability of multilayer [59, 94, 95]. Thus, multilayer samples with different periodicity were prepared by fixing at 3sccm the argon flux and periodically switching the oxygen flux from 0sccm to 7sccm.

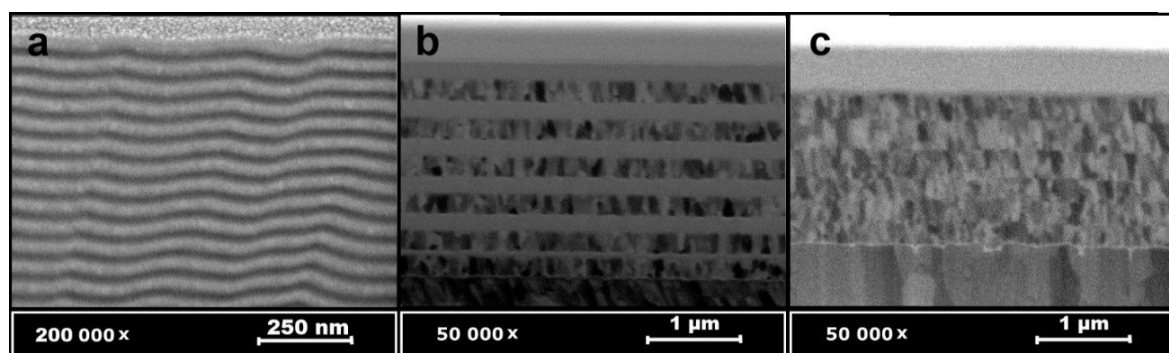


Figure 5.3: FIB-SEM of the cross-sections of sputtered Nb-Nb₂O₅ multilayers: a) thin layers (M-1); b) thick layers (M-2); c) with thermal oxidation (M-3).

The deposition parameters are resumed in the Table 5.2. Two very different architectures were investigated, preparing coatings made by 30 thin layers (M-1) and by 6 thick layer (M-2). The coating with thick layers was prepared also by thermal oxidation of niobium layer in a maximum oxygen flux allowed by the system immediately after each layer deposition (M-3). The multilayers microstructures are presented in the Figure 5.3.

The presence of amorphous niobium oxide interlayers in all multilayer coatings have provided them higher efficiency than pure niobium coatings in the acid test. However the multilayer coatings with 6 thick layers M-2 and M-3 degraded and were corroded during the liquid gallium test. Probably the reason is different CTEs on niobium and niobium oxide. Micro cracks were supposed to appear during heating to 200 °C, and allowed liquid gallium penetration. The thin layer multilayer coating M-1 showed high diffusion barrier efficiency, comparable to one of niobium oxide and resisted to heating/cooling cycles in the liquid gallium test. It can be attributed to the presence of a higher number of interfaces preventing the movement of dislocations as these results in plastic deformation in materials and stop the propagation of micro-cracks responsible for fractures in niobium oxide layer. Therefore, thin-layered niobium-niobium oxide multilayer coating was considered to be a promising candidate for protective coating against LME.

5.1.1.2.3 Search for metallic amorphous alloy system: Ta-Zr

In order to find metallic amorphous diffusion barrier for LME three binary alloy systems Nb-Ta, Nb-Zr and Ta-Zr, their microstructure and diffusion barrier efficiency were investigated.

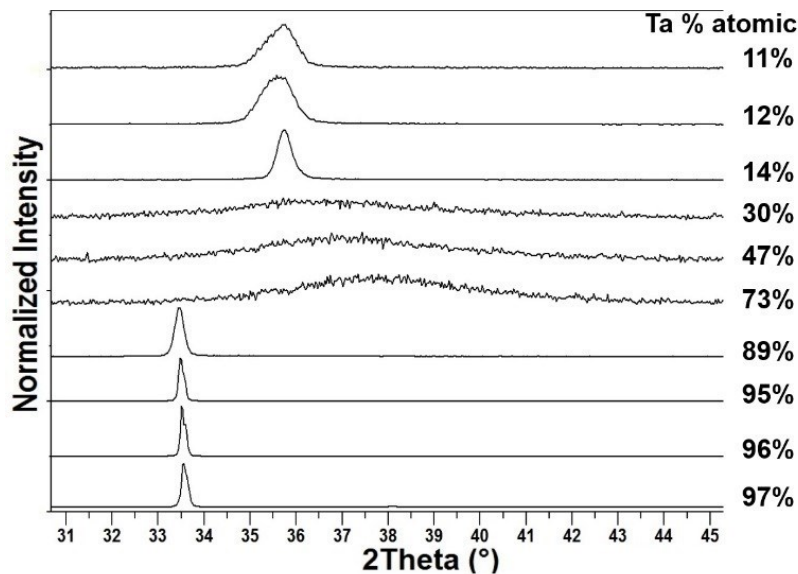


Figure 5.4: XRD spectrums of Ta-Zr alloy films.

Co-sputtered Nb-Zr and Nb-Ta alloy coatings were found to be crystalline. Performed tests showed that the diffusion barrier efficiency of Nb-Zr and Nb-Ta decreased with the increase of Nb content. All Nb-Zr and Nb-Ta film appeared to be crystalline. Ta-Zr alloys, instead, showed to have higher amorphous phase forming ability during magnetron co-sputtering than Nb-Zr and Nb-Ta alloys. Dense amorphous Ta-Zr alloy coatings were obtained by co-sputtering in a range of composition with 30-73% at. Ta (see Figure 5.4 and Figure 5.5). Since amorphous Ta-Zr coatings showed high diffusion barrier efficiency according to both tests (gallium penetration and acid test), they can be suggested for protection from liquid metal corrosion.

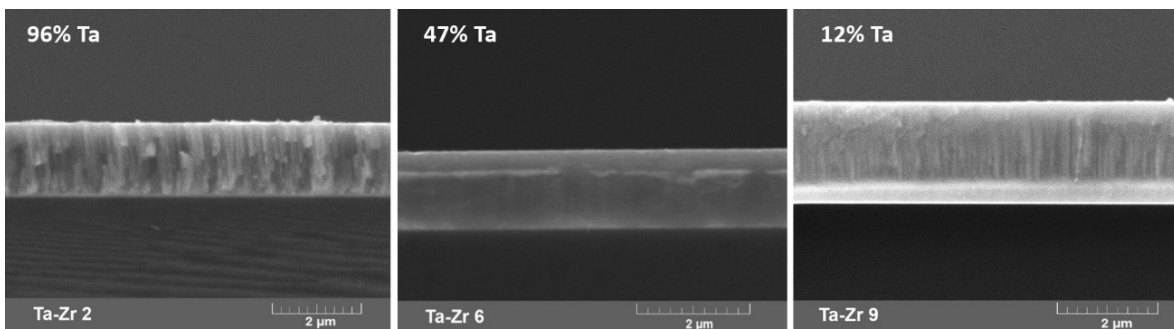


Figure 5.5: SEM of the cross-sections of sputtered Ta-Zr alloy films.

Ta-Zr alloys, instead, showed to have higher amorphous phase forming ability during magnetron co-sputtering than Nb-Zr and Nb-Ta alloys. Dense amorphous Ta-Zr alloy coatings were obtained by co-sputtering in a range of composition with 30-73% at. Ta (see Figure 5.4 and Figure 5.5). Since amorphous Ta-Zr coatings showed high diffusion barrier efficiency according to both tests (gallium penetration and acid test), they can be suggested for protection from liquid metal corrosion.

Therefore, a set of refractory metal-based protective layers were developed to protect the parts of the target system from LME in a case, if liquid metal cooling will be chosen as the main approach for high power cyclotron target heat dissipation. They include amorphous niobium oxide deposited by reactive magnetron sputtering, thin-layered multilayer of niobium-niobium oxide prepared by combination of magnetron sputtering and reactive magnetron sputtering, and, finally, a Ta-Zr (1:1) amorphous binary alloy system produced by magnetron sputtering.

5.1.2 Liquid metal cooling circuit engineering, or "why not LM cooling?"

Selecting any target cooling liquid is a multidimensional optimization task, far from trivial. Boundary conditions and constraints are different for each case and need dedicated individual assessment.

The selection criteria for the coolant should include:

- acceptable corrosion and mechanical degradation of structural and containment material and lifetime of equipment;
- high stability of the liquid media (limited chemical reactions with secondary coolants and air);
- moderate power requirement to circulate the coolant;
- high heat transfer coefficient and small size of heat exchanger;
- controllable chemical and radioactive hazards;
- simple and reliable safety measures systems;
- acceptable costs.

Table 5.3 Ga-In-Sn alloy, Ga and water comparison

<i>Property</i>	<i>Water</i>	<i>Gallium</i>	<i>Ga-In-Sn</i>
Density [kg/m ³]	1000	6090	6440
Specific heat [J/kgK]	4182	400	365
Thermal conductivity [W/mK]	0.6	33.5	16.5
Boiling point at 10 bar [°C]	180	2200	>1300
Viscosity [Kg/ms]	0.001003	0.002	0.0024
Chemical reactivity	Corroding Fe- based parts	LME	LME

The most common cooling liquid is water, of course. Among the liquid metal cooling materials, gallium and Ga-In-Sn alloy system were taken into consideration. Most relevant to cooling issues, the materials' properties of gallium are superior to water for thermal conductivity and the boiling point, whereas water features significantly higher specific heat (Table 5.3). At the first sight, gallium appears very favorable as coolant; especially for compact heat exchangers because higher heat fluxes and temperatures are accessible.

5.1.2.1 Cooling system design and complications

The easiest, from a technological point of view, is the use of liquid at r.t. metallic systems, like Hg or Ga-based alloys. They can be directly pumped by magneto-dynamic pump and do not need preliminary melting in order to be flowed in the cooled circuit. Instead, high

meting point systems like LBE (lead-bismuth eutectic) require more complicated in management and more costly equipment.

Gallium is characterized by existence of a large temperature range in the liquid state in comparison with the other metal coolants, thus Ga-based alloys can be considered the most interesting among liquid metals for high power cyclotron target cooling.

Table 5.4 Products of ^{71}Ga neutron irradiation ($E < 20\text{MeV}$)

<i>Reaction Products</i>	<i>T_{1/2}</i>	<i>Decay mode</i>	<i>Decay product</i>	<i>Stable /radioactive</i>
$^{72}\text{Ga}+\gamma$	14.1h	β^-	^{72}Ge	stable
$^{68}\text{Cu}+\alpha$	30.9 sec	β^-	^{68}Zn	stable
$^{71}\text{Ga}+\text{n}$				stable
$^{71}\text{Zn}+\text{p}$	2.45 min	β^-	^{71}Ga	stable
$^{67}\text{Cu}+\text{n}+\alpha$	61.83 h	β^-	^{67}Zn	stable
$^{70}\text{Zn}+\text{d}$				stable
$^{64}\text{Co}+2\alpha$	0.3 sec	β^-	^{64}Ni	stable
$^{70}\text{Zn}+\text{n}+\text{p}$				stable
$^{67}\text{Ni}+\text{p}+\alpha$	21 sec	β^-	^{67}Cu	radioactive
$^{69}\text{Zn}+\text{t}$	56.4 min	β^-	^{69}Ga	stable
$^{70}\text{Ga}+2\text{n}$	12.14 min	β^-	^{70}Ge	stable
$^{69}\text{Cu}+^3\text{He}$	2.85 min	β^-	^{69}Zn	radioactive
$^{66}\text{Ni}+\text{d}+\alpha$	54.6 h	β^-	^{66}Cu	radioactive
$^{63}\text{Co}+\text{n}+2\alpha$	27.4 sec	β^-	^{63}Cu	stable
$^{70}\text{Cu}+2\text{p}$	44.5 sec	β^-	^{70}Zn	stable
$^{66}\text{Ni}+\text{n}+\text{p}+\alpha$	54.6 h	β^-	^{66}Cu	radioactive
$^{65}\text{Ni}+\text{t}+\alpha$	2.57 h	β^-	^{65}Cu	stable
$^{66}\text{Cu}+2\text{n}+\alpha$	5.12 min	β^-	^{66}Zn	stable
$^{69}\text{Zn}+\text{n}+\text{d}$	56.4 min	β^-	^{69}Ga	stable
$^{68}\text{Zn}+\text{n}+\text{t}$				stable
$^{60}\text{Mn}+3\alpha$	0.28 sec	β^-	^{60}Fe	radioactive
$^{69}\text{Cu}+\text{p}+\text{d}$	2.85 min	β^-	^{69}Zn	radioactive
$^{69}\text{Ga}+3\text{n}$				stable
$^{69}\text{Zn}+2\text{n}+\text{p}$	56.4 min	β^-	^{69}Ga	stable
$^{63}\text{Fe}+\text{p}+2\alpha$	6.1 sec	β^-	^{63}Co	radioactive
$^{68}\text{Cu}+\text{p}+\text{t}$	30.9 sec	β^-	^{68}Zn	stable
$^{69}\text{Cu}+\text{n}+2\text{p}$	2.85 min	β^-	^{69}Zn	radioactive
$^{68}\text{Cu}+\text{n}+^3\text{He}$	30.9 sec	β^-	^{68}Zn	stable
$^{65}\text{Co}+^3\text{He}+\alpha$	1.16 sec	β^-	^{65}Ni	radioactive

However, not only physical properties of the liquid metal alloy should be taken into account, but also of the products of neutron activation, created inside the liquid metal. Thus, for example, the use of Ga in a coolant can lead to radioactive ^{72}Ga , whose decay product ^{72}Ge

($T_m=1229$ K) can be deposited on the surface of cooling tubes. Such deposits not only present a source of elevated radioactivity, but can also block the cooling loop.

Table 5.5 Products of ^{69}Ga neutron irradiation ($E<20\text{MeV}$)

<i>Reaction Products</i>	<i>$T_{1/2}$</i>	<i>Decay mode</i>	<i>Decay product</i>	<i>Stable /radioactive</i>
$^{70}\text{Ga}+\gamma$	21.1 min	β^-	^{70}Ge	stable
$^{66}\text{Cu}+\alpha$	5.12 min	β^-	^{66}Zn	stable
$^{69}\text{Ga}+\text{n}$				stable
$^{69}\text{Zn}+\text{p}$	56.4 min	β^-	^{69}Ga	stable
$^{68}\text{Zn}+\text{d}$				stable
$^{65}\text{Cu}+\text{n}+\alpha$				stable
$^{62}\text{Co}+2\alpha$	1.54 min	β^-	^{62}Ni	stable
$^{65}\text{Ni}+\text{p}+\alpha$	2.57 h	β^-	^{65}Cu	stable
$^{68}\text{Zn}+\text{n}+\text{p}$				stable
$^{67}\text{Zn}+\text{t}$				stable
$^{67}\text{Cu}+^3\text{He}$	61.83 h	β^-	^{67}Zn	stable
$^{64}\text{Ni}+\text{d}+\alpha$				stable
$^{68}\text{Cu}+2\text{p}$	30.9 sec	β^-	^{68}Zn	stable
$^{68}\text{Ga}+2\text{n}$	67.7 min	EC β^+	^{68}Zn	stable
$^{61}\text{Co}+\text{n}+2\alpha$	1.65 h	β^-	^{61}Ni	stable
$^{64}\text{Ni}+\text{n}+\text{p}+\alpha$				stable
$^{58}\text{Mn}+3\alpha$	3.0 sec	β^-	^{58}Fe	stable
$^{63}\text{Ni}+\text{t}+\alpha$	101.2 y	β^-	^{63}Cu	stable
$^{67}\text{Cu}+\text{p}+\text{d}$	61.83 h	β^-	^{67}Zn	stable
$^{64}\text{Cu}+2\text{n}+\alpha$	12.70 h	β^- , β^+	^{64}Ni	stable
$^{61}\text{Fe}+\text{p}+2\alpha$	5.98 min	β^-	^{61}Co	radioactive
$^{67}\text{Zn}+\text{n}+\text{d}$				stable
$^{66}\text{Zn}+\text{n}+\text{t}$				stable
$^{67}\text{Cu}+\text{n}+2\text{p}$	61.83 h	β^-	^{67}Zn	stable
$^{63}\text{Co}+^3\text{He}+\alpha$	27.4 sec	β^-	^{63}Cu	stable
$^{67}\text{Zn}+2\text{n}+\text{p}$				stable
$^{66}\text{Cu}+\text{p}+\text{t}$	5.12 min	β^-	^{66}Zn	stable
$^{66}\text{Ni}+\text{p}+^3\text{He}$	54.6 h	β^-	^{66}Cu	radioactive
$^{60}\text{Fe}+\text{d}+2\alpha$	2.62E+6 yrs	β^-	^{60}Co	radioactive
$^{66}\text{Cu}+\text{n}+^3\text{He}$	5.12 min	β^-	^{66}Zn	stable
$^{64}\text{Co}+2\text{p}+\alpha$	0.3 sec	β^-	^{64}Ni	stable
$^{67}\text{Ga}+3\text{n}$	3.26 days	EC	^{67}Zn	stable
$^{57}\text{Mn}+\text{n}+3\alpha$	85.4 sec	β^-	^{57}Fe	stable
$^{63}\text{Ni}+\text{n}+\text{d}+\alpha$	101.2 yrs	β^-	^{63}Cu	stable
$^{67}\text{Ni}+3\text{p}$	21 sec	β^-	^{67}Cu	radioactive
$^{62}\text{Ni}+\text{n}+\text{t}+\alpha$				stable

Table 5.6 Products of ^{113}I neutron irradiation ($E < 20\text{MeV}$)

<i>Reaction Products</i>	<i>T_{1/2}</i>	<i>Decay mode</i>	<i>Decay product</i>	<i>Stable /radioactive</i>
$^{114}\text{In}+\gamma$	71.9 sec	β^-	^{114}Sn	stable
$^{110}\text{Ag}+\alpha$	24.56 sec	β^-	^{114}Sn	stable
$^{113}\text{Cd}+\text{p}$				stable
$^{106}\text{Rh}+2\alpha$	30.07 sec	β^-	^{106}Pd	stable
$^{113}\text{In}+\text{n}$				stable
$^{109}\text{Ag}+\text{n}+\alpha$				stable
$^{109}\text{Pd}+\text{p}+\alpha$	13.70 h	β^-	^{109}Ag	stable
$^{112}\text{Cd}+\text{d}$				stable
$^{102}\text{Tc}+3\alpha$	5.28 sec	β^-	^{102}Ru	stable
$^{112}\text{Cd}+\text{n}+\text{p}$				stable
$^{105}\text{Rh}+\text{n}+2\alpha$	35.36 h	β^-	^{105}Pd	stable
$^{111}\text{Cd}+\text{t}$				stable
$^{108}\text{Pd}+\text{d}+\alpha$				stable
$^{98}\text{Nb}+4\alpha$	2.86 sec	β^-	^{98}Mo	stable
$^{105}\text{Ru}+\text{p}+2\alpha$	4.44 h	β^-	^{105}Rh	stable
$^{111}\text{Ag}+^3\text{He}$	7.15 days	β^-	^{111}Cd	stable
$^{112}\text{Ag}+2\text{p}$	3.13 h	β^-	^{112}Cd	stable
$^{112}\text{In}+2\text{n}$	14.88 min	EC	^{112}Cd	stable
$^{108}\text{Pd}+\text{n}+\text{p}+\alpha$				stable
$^{107}\text{Pd}+\text{t}+\alpha$	6.5E+6 yrs	β^-	^{107}Ag	stable
$^{101}\text{Tc}+\text{n}+3\alpha$	14.22 min	β^-	^{101}Ru	stable
$^{94}\text{Y}+5\alpha$	18.7 min	β^-	^{94}Zr	stable
$^{104}\text{Ru}+\text{d}+2\alpha$				stable
$^{107}\text{Rh}+^3\text{He}+\alpha$	21.7 min	β^-	^{107}Pd	stable
$^{108}\text{Ag}+2\text{n}+\alpha$	2.38 min	β^-	^{108}Cd	stable
$^{101}\text{Mo}+\text{p}+3\alpha$	14.6 min	β^-	^{101}Tc	radioactive
$^{111}\text{Cd}+\text{n}+\text{d}$				stable
$^{108}\text{Rh}+2\text{p}+\alpha$	16.8 sec	β^-	^{108}Pd	stable
$^{104}\text{Ru}+\text{n}+\text{p}+2\alpha$				stable
$^{97}\text{Nb}+\text{n}+4\alpha$	16.8 sec	β^-	^{97}Mo	stable
$^{111}\text{Ag}+\text{p}+\text{d}$	7.45 days	β^-	^{111}Cd	stable
$^{103}\text{Ru}+\text{t}+2\alpha$	39.25 days	β^-	^{103}Rh	stable
$^{110}\text{Cd}+\text{n}+\text{t}$				stable
$^{110}\text{Pd}+\text{p}+^3\text{He}$				stable
$^{104}\text{Rh}+2\text{n}+2\alpha$	42.3 sec	β^-	^{104}Pd	stable
$^{97}\text{Zr}+\text{p}+4\alpha$	16.75 h	β^-	^{97}Nb	radioactive
$^{111}\text{Cd}+2\text{n}+\text{p}$				stable
$^{100}\text{Mo}+\text{d}+3\alpha$				stable
$^{111}\text{Ag}+\text{n}+2\text{p}$	7.45 days	β^-	^{111}Cd	stable
$^{110}\text{Ag}+\text{p}+\text{t}$	24.56 sec	β^-	^{114}Sn	stable
$^{103}\text{Tc}+^3\text{He}+2\alpha$	54.2 sec	β^-	^{103}Ru	radioactive
$^{90}\text{Rb}+6\alpha$	158 sec	β^-	^{90}Sr	radioactive
$^{107}\text{Pd}+\text{n}+\text{d}+\alpha$	6.5E+6 yrs	β^-	^{107}Ag	stable
$^{106}\text{Pd}+\text{n}+\text{t}+\alpha$				stable

$^{110}\text{Ag}+n+^3\text{He}$	24.56 sec	β^-	^{114}Sn	stable
$^{111}\text{In}+3n$	2.8 days	EC	^{111}Cd	stable
$^{111}\text{Pd}+3p$	23.4 min	β^-	^{111}Ag	radioactive
$^{93}\text{Y}+n+5\alpha$	10.18 h	β^-	^{93}Zr	stable
$^{107}\text{Rh}+p+d+\alpha$	21.7 min	β^-	^{107}Pd	stable
$^{99}\text{Mo}+t+3\alpha$	68.98 h	β^-	^{99}Tc	radioactive
$^{100}\text{Mo}+n+p+3\alpha$				stable
$^{104}\text{Tc}+2p+2\alpha$	18.3 min	β^-	^{104}Ru	stable
$^{96}\text{Zr}+d+4\alpha$				stable
$^{100}\text{Tc}+2n+3\alpha$	15.46 sec	β^-	^{100}Ru	stable
$^{107}\text{Pd}+2n+p+\alpha$	6.5E+6 yrs	β^-	^{107}Ag	stable
$^{107}\text{Rh}+n+2p+\alpha$	21.7 min	β^-	^{107}Pd	stable
$^{107}\text{Ag}+3n+\alpha$				stable
$^{106}\text{Rh}+p+t+\alpha$	30.07 sec	β^-	^{106}Pd	stable
$^{106}\text{Ru}+p+^3\text{He}+\alpha$	371.8 days	β^-	^{106}Rh	radioactive
$^{102}\text{Ru}+n+t+2\alpha$				stable

5.1.2.2 Safety

The most critical aspect for using liquid metal as a coolant is safety. Even if such safety problem, as corrosion by liquid metal, can be solved, the problem of activation of the material and transmutation under irradiation is also extremely important.

5.1.2.2.1 Production of long-lived radioisotopes

A number of long-lived radioisotopes is produced inside liquid metal coolant even under the neutron flux (considering, that the liquid metal does not see the proton beam). The example of the products of neutron activation (considering the neutron energies lower 20MeV) of the main stable isotopes of gallium ^{69}Ga , ^{71}Ga and indium ^{113}In , ^{115}In are presented in the Tables 5.4-5.7. All the sources of radioactivity are highlighted in grey colour. The produced radioisotopes with the half-life of order of hours-days are highlighted in bold, since they present the main problem for radioprotection. The data of the nuclear reactions thresholds were taken from the database of Los Alamos National Laboratory [96] and Brookhaven National Nuclear Data Center [97].

Table 5.7 Products of ^{115}I neutron irradiation ($E < 20\text{MeV}$)

Reaction Products	$T_{1/2}$	Decay mode	Decay product	Stable /radioactive
$^{116}\text{In}+\gamma$	14.1 sec	β^-	^{116}Sn	stable
$^{112}\text{Ag}+\alpha$	3.13 h	β^-	^{112}Cd	stable
$^{115}\text{In}+n$				stable
$^{115}\text{Cd}+p$	53.46 h	β^-	^{115}In	stable

$^{108}\text{Rh}+2\alpha$	16.8 sec	β -	^{108}Pd	stable
$^{111}\text{Ag}+n+\alpha$	7.45 days	β -	^{111}Cd	stable
$^{114}\text{Cd}+d$				stable
$^{111}\text{Pd}+p+\alpha$	23.4 min	β -	^{111}Ag	radioactive
$^{104}\text{Tc}+3\alpha$	18.3 min	β -	^{104}Ru	stable
$^{114}\text{Cd}+n+p$				stable
$^{113}\text{Cd}+t$				stable
$^{107}\text{Rh}+n+2\alpha$	21.7 min	β -	^{107}Pd	stable
$^{110}\text{Pd}+d+\alpha$				stable
$^{114}\text{In}+2n$	71.9 sec	β -	^{114}Sn	stable
$^{113}\text{Ag}+^3\text{He}$	5.37 h	β -	^{113}Cd	stable
$^{107}\text{Ru}+p+2\alpha$	3.75 min	β -	^{107}Rh	radioactive
$^{110}\text{Pd}+n+p+\alpha$				stable
$^{114}\text{Ag}+2p$	4.6 sec	β -	^{114}Cd	stable
$^{109}\text{Pd}+t+\alpha$	13.7 h	β -	^{109}Ag	stable
$^{100}\text{Nb}+4\alpha$	1.5 sec	β -	^{100}Mo	stable
$^{103}\text{Tc}+n+3\alpha$	54.2 sec	β -	^{103}Ru	radioactive
$^{110}\text{Ag}+2n+\alpha$	24.56 sec	β -	^{114}Sn	stable
$^{106}\text{Ru}+d+2\alpha$	371.8 days	β -	^{106}Rh	radioactive
$^{113}\text{Cd}+n+d$				stable
$^{109}\text{Rh}+^3\text{He}+\alpha$	80 sec	β -	^{109}Pd	radioactive
$^{112}\text{Cd}+n+t$				stable
$^{113}\text{Ag}+p+d$	5.37 h	β -	^{113}Cd	stable
$^{103}\text{Mo}+p+3\alpha$	67.5 sec	β -	^{103}Tc	radioactive
$^{96}\text{Y}+5\alpha$	5.34 sec	β -	^{96}Zr	stable
$^{105}\text{Ru}+t+2\alpha$	4.44 h	β -	^{105}Rh	radioactive
$^{106}\text{Ru}+n+p+2\alpha$	371.8 days	β -	^{106}Rh	radioactive
$^{110}\text{Rh}+2p+\alpha$	3.35 sec	β -	^{110}Pd	stable
$^{113}\text{Cd}+2n+p$				stable
$^{106}\text{Rh}+2n+2\alpha$	30.07 sec	β -	^{106}Pd	stable
$^{113}\text{In}+3n$				stable
$^{99}\text{Nb}+n+4\alpha$	15.0 sec	β -	^{99}Mo	radioactive
$^{113}\text{Ag}+n+2p$	5.37 h	β -	^{113}Cd	stable
$^{112}\text{Ag}+p+t$	3.13 h	β -	^{112}Cd	stable
$^{112}\text{Pd}+p+^3\text{He}$	21.04 h	β -	^{112}Ag	radioactive
$^{108}\text{Pd}+n+t+\alpha$				stable
$^{109}\text{Pd}+n+d+\alpha$	13.7 h	β -	^{109}Ag	stable
$^{112}\text{Ag}+n+^3\text{He}$	3.13 h	β -	^{112}Cd	stable
$^{102}\text{Mo}+d+3\alpha$	11.3 min	β -	^{102}Tc	radioactive
$^{105}\text{Tc}+^3\text{He}+2\alpha$	7.6 min	β -	^{105}Ru	radioactive
$^{109}\text{Rh}+p+d+\alpha$	80 sec	β -	^{109}Pd	radioactive
$^{109}\text{Ag}+3n+\alpha$				stable
$^{109}\text{Pd}+2n+p+\alpha$	13.70 h	β -	^{109}Ag	stable
$^{113}\text{Pd}+3p$	93 sec	β -	^{113}Ag	radioactive
$^{112}\text{Cd}+2n+d$				stable

5.1.2.2.2 Waste treatment problem

Cooling with low melting temperature liquid metals has another important disadvantage: liquid radioactive wastes. Another regulation is used for treatment of liquid radioactive wastes in respect to solid ones. Thus, also the costs of utilization of liquid radioactive wastes are tens of times higher than the costs for utilization of solid radioactive wastes.

Taking into account all the safety aspects and authorization problems, for the current moment the approach to use liquid metal cooling for the future cyclotron high power target for radiopharmaceutical production is not considered the most perspective. Instead, the decision to use more conventional water and gas cooling for the target was taken by LARAMED group.

5.2 Target prototype preparation

5.2.1 PVD for Mo target material deposition

For the preliminary study to define the method to deposit hundreds micron thick films by magnetron sputtering instead of Mo another refractory metal, Nb, was used.

5.2.1.1 Nb thick film deposition

A set of experiments on deposition of some tens of microns thick Nb film were realized in order to define the most critical parameters. The main deposition parameters and results are shown in the Table 5.8, Table 5.9, and Table 5.10. The stress level in thick films was controlled only qualitatively by visual inspection after deposition. Stressed films are used to buckle and delaminate from the substrate.

5.2.1.1.1 Choice of appropriate sputtering gas pressure

Theoretically, it exists a gas pressure that signs the transition from tensile to compressive stress for each combination of a sputtered material and deposition system.

From a practical point of view in order to find this transition point, a deposition onto a flexible thin substrate (for example, Kapton) can be performed. Two types of stress can be observed: tensile, in which the film is trying to contract on the substrate and compressive, in which the film is trying to expand on the substrate (see Figure 5.6). The intrinsic stress can be estimated directly from the radius of curvature of the relaxed film and substrate. Change

of a radius of curvature of the coated flexible substrate from negative to positive identifies the transition from compressive to tensile stress.

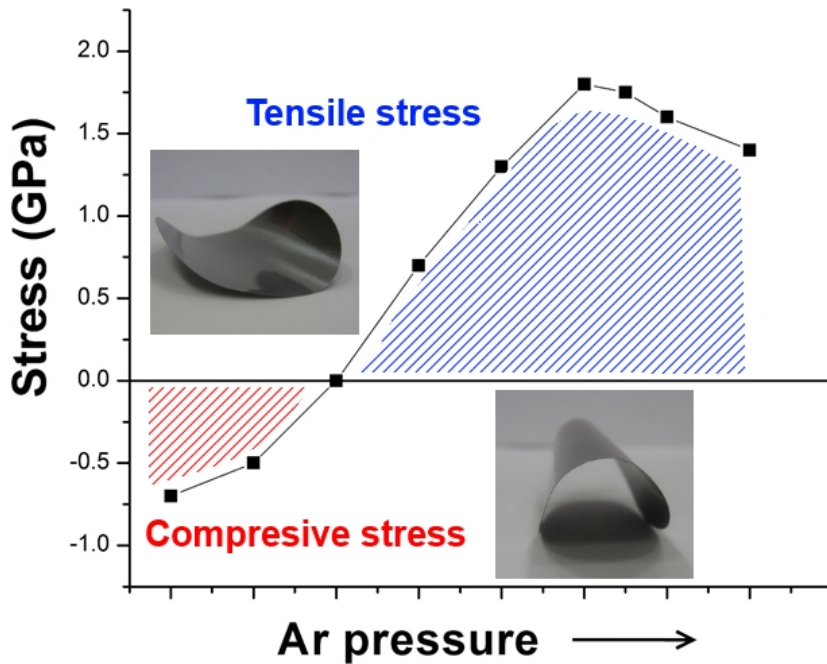


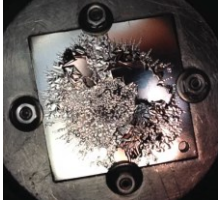



Figure 5.6: Stress vs sputtering pressure.

Table 5.8 Nb thick film deposition parameters

Sample number	TNb-8	TNb-11	TNb-12	TNb-13
Substrate-target distance, config.	5.5 cm "top-down"	5.5 cm "top-down"	5.5 cm "top-down"	5.5 cm "down-top"
Under layer	no	Al 200nm	Ag 550 nm	Ag 550 nm
Temperature:	25 °C	25 °C	25 °C	25 °C
Pwork:	8·10 ⁻³ mbar	8·10 ⁻³ mbar	8·10 ⁻³ mbar	8·10 ⁻³ mbar
P:	600 W	600 W	600 W	600 W
Time:	6h	5h	7h	8h
Duty cycle:	80% on	80% on	80% on	80% on
Thickness:	170 μm	95 μm	110 μm	120 μm
Result:	Small compressive stress, full delamination	Compressive stress, delamination from Cu in the middle	No delamination from Cu. Metallic dust:macro-defects.	No delamination from Cu
Picture				

Each material has its own pressure of the compressive-tensile stress conversion. Thus, for example, for the configuration with 2 inches standard planar magnetron cathode, 5.5 cm cathode-substrate distance the argon “transition point” pressure is $8 \cdot 10^{-3}$ mbar for Nb, for 550W sputtering power.

Table 5.9 Nb thick film deposition parameters

<i>Sample number</i>	<i>TNb-14</i>	<i>TNb-15</i>	<i>TNb-16</i>	<i>TNb-17</i>
Substrate-target distance	5.5 cm “down-top”	5.5 cm “down-top”	5.5 cm “down-top”	5.5 cm “down-top”
Under layer	Ag 550 nm	Ag 550 nm	Ag 550 nm	No
Temperature:	25 °C	25 °C	25 °C	25 °C
Pwork:	$5 \cdot 10^{-3}$ mbar	$8 \cdot 10^{-3}$ mbar	$8 \cdot 10^{-3}$ mbar	$8 \cdot 10^{-3}$ mbar
P:	600 W	600 W	600 W	600 W
Time:	5 min	12 h	3 h	6 h
Duty cycle:	80% on	80% on	No program	80% on
Thickness:	1-2 μm	160 μm	70 μm	90 μm
Result:	Delamination from Cu immediately	No delamination from Cu. Was detouched after	Partial delamination from Cu	Delamination from Cu
Picture				

It should be mentioned that this “transition point” pressure depends on other deposition parameters including substrate-target distance, sputtering voltage, vacuum system pumping regime and degassing, etc. So if any parameter of the deposition or aspect of configuration is changed, the “transition point” pressure could be modified. For example, if sputtering power is higher the “transition point” should be at higher pressure.

Nb deposition at $8 \cdot 10^{-3}$ mbar argon pressure gave not stressed film of 120 μm (TNb-13), but decrease of the argon pressure to $5 \cdot 10^{-3}$ mbar (TNb-15) after 5 min of deposition (1-2 μm) lead to immediate delamination because of strong compressive stress. Instead, increase of argon pressure to $1.2 \cdot 10^{-2}$ mbar (TNb-18) did not result to film delamination, but significantly decreased the deposition rate of sputtering.

5.2.1.1.2 Multilayers by relaxation technique

One of the approaches in sputtered film stress minimization is to separate a thick film into number of very thin (tens of nm) layers making a stop in deposition between them. This allows the re-growing of the film, minimizing the overall stress.

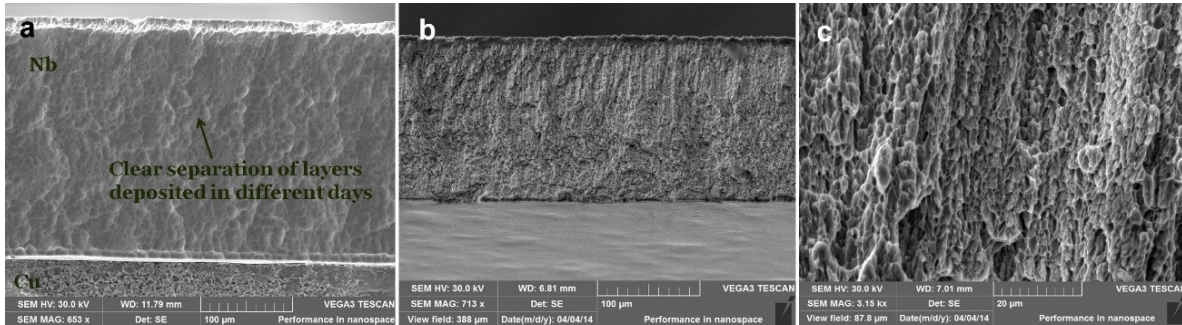


Figure 5.7: 200µm self-sustaining Nb film deposited at 25°C (TNb-15).

This approach was found very efficient for deposition onto water cooled (25°C) substrate. For comparison, samples TNb-15 and TNb-16 were deposited at all equal parameters but with multilayer approach (program) and without. The film deposited without program is strongly stressed (TNb-16).

Table 5.10 Nb thick film deposition parameters

Sample number	TNb-18	TNb-19	TNb-21
Substrate-target distance	5.5 cm	5.5 cm	5.5 cm
Multi layer Program	Yes	Yes	No
Under layer	Ag 550 nm	Ag 550 nm r.t.	Ag 550 nm r.t.
Temperature:	25 °C	450 °C	450 °C
Pwork:	$1.2 \cdot 10^{-2}$ mbar	$8 \cdot 10^{-3}$ mbar	$8 \cdot 10^{-3}$ mbar
P:	550 W	550 W	550 W
Time:	9 h	19 h	16 h
Duty cycle:	80% on	80% on	No program
Thickness:	110 µm	250 µm	250 µm
Result:	No self-delamination from Cu, film was removed after. Film is self-sustaining	No delamination from Cu, no possibility to remove film also after thermal stress	No stress, no self-delamination from Cu, not possible to delaminate. Ductile
Picture			

The XRD spectrums (see Figure 5.8) also show higher level of stress in TNb-16 sample deposited without program at 25°C, as soon as the peaks are shifted towards the lower Theta angles. TNb-16 without program has smaller crystallite size (see Table 5.11) than multilayer TNb-15 calculated from peak broadening (Scherrer formula), but this broadening could be also attributed to stress.

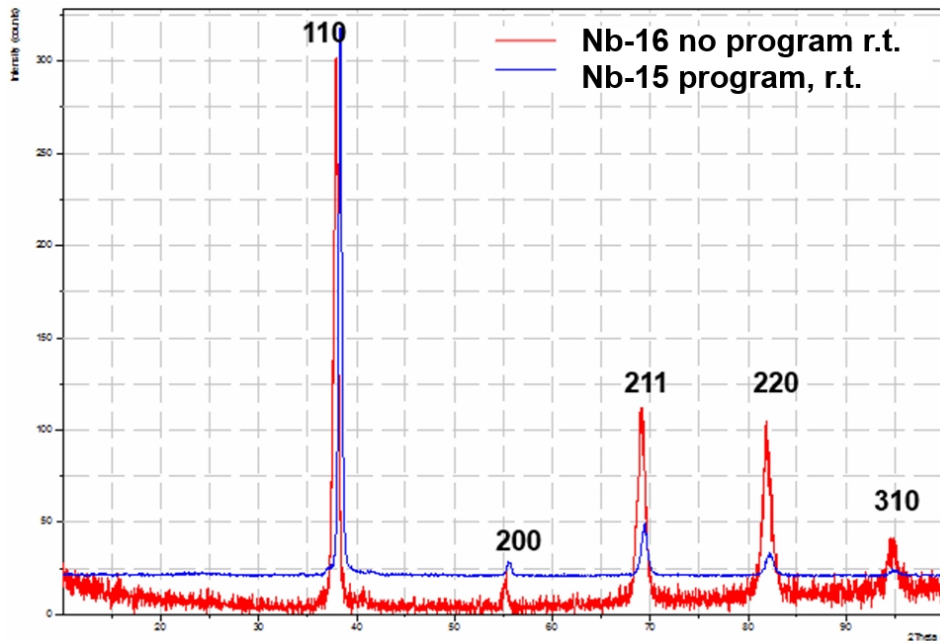


Figure 5.8: XRD patterns of TNb-15 and TNb-16 deposited at 25°C with and without program.

Table 5.11 XRD analysis of Nb sputtered thick films with and without program

<i>TNb-15, program, r.t.</i>				<i>TNb-16, no program, r.t.</i>			
Pos. [°2Th.]	d-spacing [Å]	Lattice par-r	Crystallite size [Å]	Pos. [°2Th.]	d-spacing [Å]	Lattice par-r	Crystallite size [Å]
38.29	2.349	3.322	245	37.84	2.376	3.36	161
55.54	1.653	3.306	143	55.17	1.662	3.327	171
69.34	1.354	3.317	135	69.04	1.359	3.329	116
82.13	1.173	3.316	125	81.86	1.176	3.326	108
94.84	1.046	3.308	84	94.64	1.048	3.316	96

Instead, the efficiency of multilayer deposition at elevated temperature is negated as can be observed for samples TNb-19 and TNb-21 deposited at 450°C. The microstructures of the film sputtered at different temperature with and without program is described in the next paragraph.

Comparison of deposition with or without multilayer program at r.t. and elevated temperature is presented in the Table 5.12, where “=” means similar result, “<” means

program is not preferable, “>” means program gives better result, than deposition without program.

Table 5.12 Comparison of multilayer deposition of Nb at different temperature

	<i>Deposition at 25°C</i>		<i>Deposition at 400°C</i>	
	Program	No program	Program	No program
Microstructure	Porous columnar	= Porous columnar	dense	= dense
Ductility	low	= low	high	= high
Stress	no	> high	no	= no
Time	19 h	< 16 h	19 h	< 16 h
Deposition rate	13 µm/h	< 15 µm/h	13 µm/h	< 15 µm/h

5.2.1.1.3 Deposition at different temperature

Deposition at elevated temperature allows changing a film microstructure from porous to dense, minimizing also the intrinsic stress related to grain-boundaries coalescence.

In fact, Nb-15 film prepared by deposition with a multilayer program at r.t. was detached mechanically from the substrate (see Figure 5.9). It was cracked in order to analyze the cross-section microstructure with SEM. It should be noticed that the film is not bent, means, low level of stress is present. As it can be observed from the Figure 5.7b and the Figure 5.7c, the microstructure is porous with columnar growth direction.



Figure 5.9: 200µm self-sustaining Nb-15 film deposited with program at r.t.

Interesting aspect was noticed from the SEM of cross-section of the sample cut by electro erosion and etched in a solution of H₂O₂ and NH₄OH for one minute (see Figure 5.7a). It is possible to distinguish the stop for a night between two depositions. The system was pumped during this period, but the presence of such layers proves significant oxidation of sputtered Nb layer even at 1·10⁻⁶mbar.

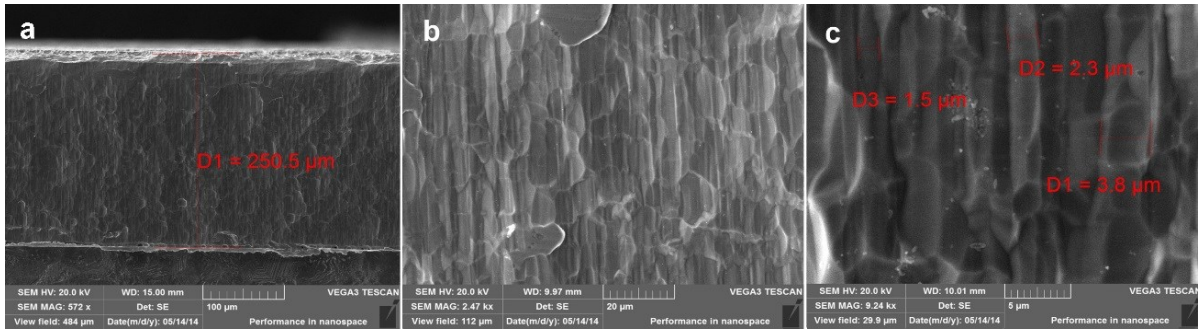


Figure 5.10: 250 μ m Nb film deposited at 450 $^{\circ}$ C with program (Nb-19).

Instead, the TNb-19 film deposited at 450 $^{\circ}$ C at all other equal parameters showed high level of adherence to copper substrate. The thermomechanical test was comprising thermal cycling by placing the sample into liquid nitrogen and then fast warming to r.t. realized for 25 times and then trial to detach mechanically. The TNb-19 film remained attached to the substrate. The sample was cut by electro erosion and chemically etched to observe the microstructure on cross-section (see Figure 5.10). The film had dense columnar microstructure with the grain size of about 2-4 μ m.

5.2.1.1.4 Magnetron position

It was shown experimentally that the position of the substrate is extremely important to avoid delamination in a case of ultra-thick film deposition. When substrate is located downside and magnetron on the top of the chamber, all metallic dust (simply the same metal we sputter) is falling down to the substrate, becoming a source of macro defect (TNb-12) that can become the starting point for film delamination. If the deposition is realized in reverse configuration (“down-top”) when magnetron is placed downside and the substrate is on the top of the chamber, metallic dust is removed from the substrate just by gravity and the amount of macro defects in film is decreased (TNb-13).

5.2.1.1.5 Buffer layer for Nb on Cu deposition

One of the hypothesis of low adherence of Nb sputtered film on copper (TNb-8) is the immiscibility of these elements. In order to improve adherence several buffer-layers were tested, like aluminum (TNb-11) and silver (TNb-12, TNb-13, etc.). Both buffer-layers were deposited by magnetron sputtering. Aluminum was not efficient, but silver buffer-layer increased the adherence of Nb to copper substrate.

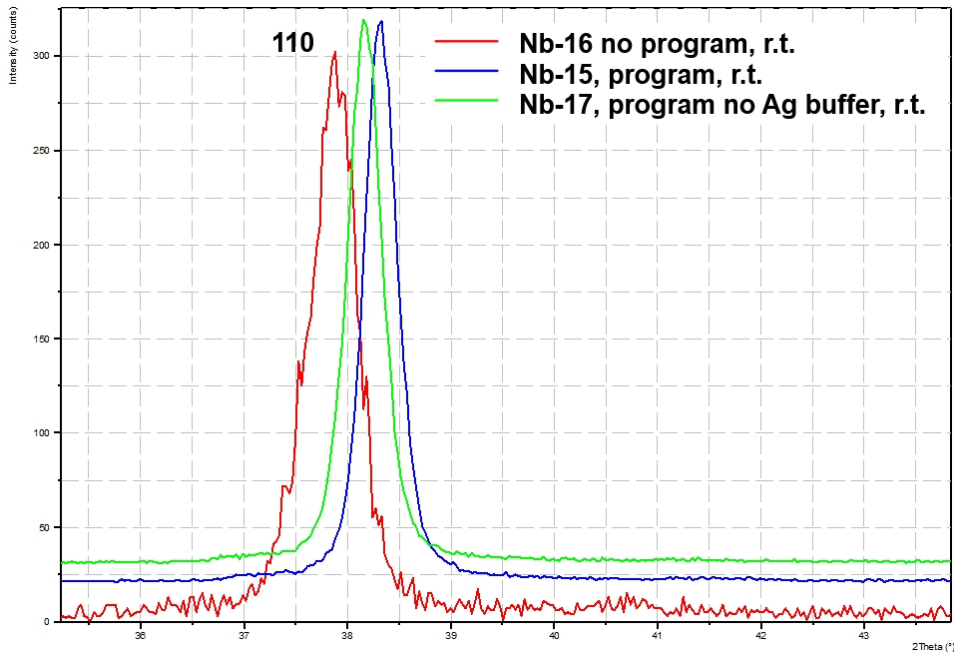


Figure 5.11: XRD patterns of 110-peak of TNb-15, TNb-16 and TNb-17 films on copper.

Main part of Nb deposition experiments were realized with Ag buffer-layer. The comparison of XRD patterns of Nb films deposited with and without Ag buffer-layer is shown in the Figure 5.11. It is clear that the 110-peak in a case of film deposited without Ag buffer-layer is shifted towards lower Theta angles, but the shift is lower than in the case of deposition without program.

The choice of deposition with or without multilayer approach can be done taking into account the summarizing Table 5.13. For example, program applied to Nb deposition at 25°C should be used to get the film as a single foil without stress not attached to the substrate. Instead, deposition at elevated temperature with program gives not stressed attached to substrate film.

Table 5.13 Efficiency of multilayer deposition of Nb sputtering at different temperature

	25 °C		450 °C
Microstructure	Porous	<	Dense
Grain size	not clear <1 μm	<	1.5-3.8 μm
Ductility	brittle	<	high
Stress	no	=	no
Time	19 h	=	19 h
Deposition rate	17 μm/h	>	15 μm/h
Adherence to Cu	low		high

The more convenient (from an economical point of view) deposition at 25⁰C with program at 8·10⁻³mbar argon pressure and 550W power was taken for the next experiment switching from copper to ceramic substrates.

5.2.1.2 Nb thick film deposition onto ceramics substrates

The parameters of first thick film deposition onto ceramics substrate are listed in the Table 5.14. The multilayer sputtering of Nb on sapphire samples of 1 mm thick was realized by using the water-cooled sample holder. The sapphire pieces were arranged on the sample holder by using silver-pain.

Table 5.14 Multilayer sputtering of Nb on thick sapphire

<i>Parameters</i>	<i>TNb-22</i>	<i>TNb-23</i>
Argon flux	9.5 sccm	9.5 sccm
Working pressure	8·10 ⁻³ mbar	8·10 ⁻³ mbar
Power	550 W	550 W
Temperature of the sample holder	25 ⁰ C	450 ⁰ C
Target-substrate distance	6 cm	6 cm
Deposition rate	11μm/h	11μm/h
Program for multilayer deposition	YES	YES
Time	14h	8h
Thickness	155μm	85μm

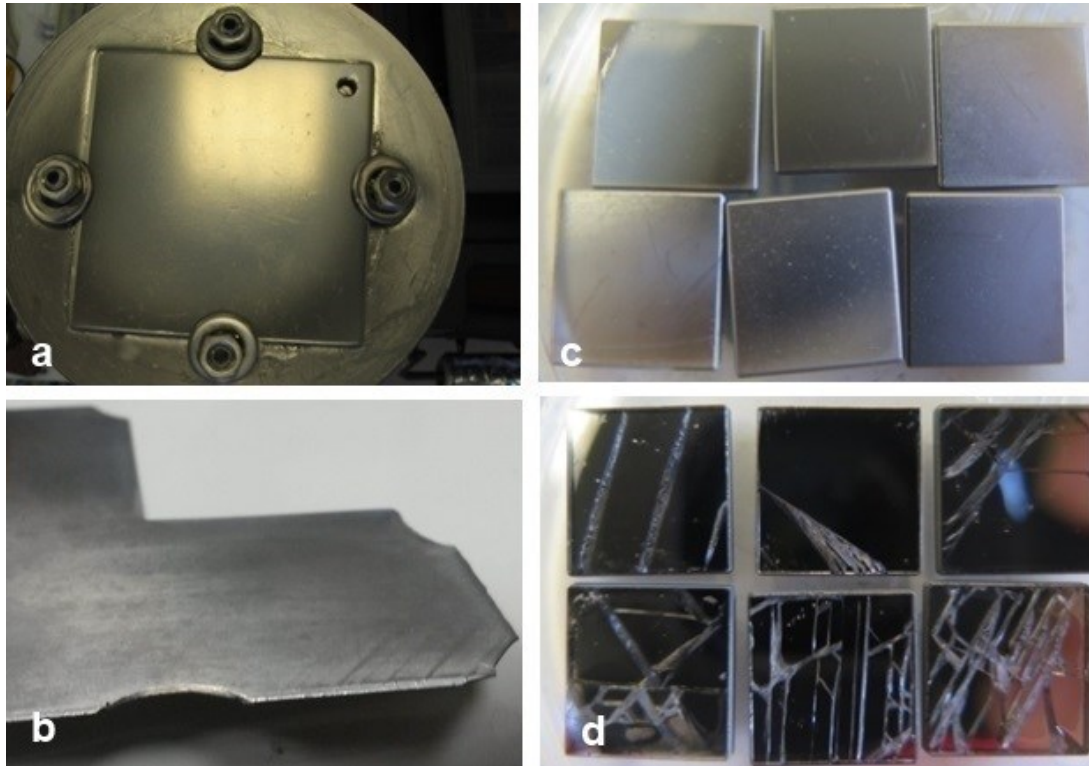


Figure 5.12: Nb films sputtered at 25⁰C on Cu TNb-15 (a, b) and sapphire TNb-22 (c, d) substrates.

Even if this method was successful, when used for deposition onto metallic substrate (see Figure 5.12a, Figure 5.12b), the ceramic substrates were cracked by the intrinsic stress in $\sim 300\mu\text{m}$ thick Nb film (see Figure 5.12c and Figure 5.12d).

One of the possible reasons, why this method did not give the same result as on copper substrate could be the lower efficiency of cooling because of lower thermal conductivity of sapphire. Otherwise, the intrinsic stress in films was not as low as was supposed, and it was enough to break brittle sapphire substrates.

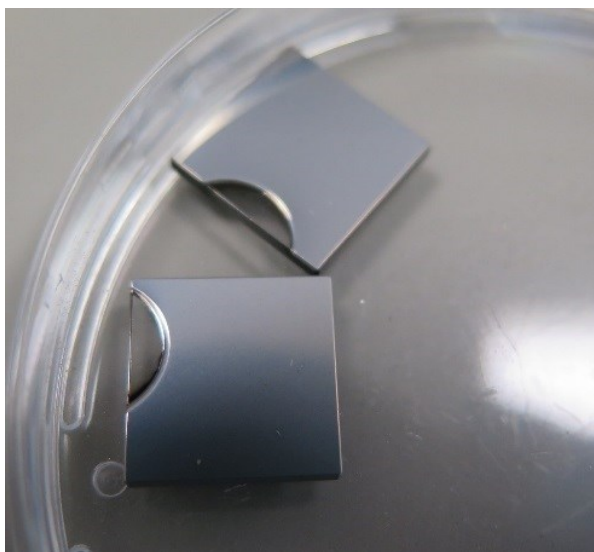


Figure 5.13: 85 μm Nb sputtered on sapphire at 400°C.

The next experiment on Nb thick films deposition onto ceramics substrates (sapphire) was realized using the second method that gave sufficient results in stress minimization – deposition at elevated temperature. The main deposition parameters are listed in the Table 5.14. As it can be seen from The Figure 5.13 the sapphire substrates were remained integer, when 85 μm Nb film was sputtered on it at 450°C.

Thus, for future experiments on Mo thick films deposition onto ceramics substrates, deposition at elevated temperature was chosen as more reliable approach.

5.2.1.3 Mo optimal sputtering pressure

The best argon flux was found by the procedure described in previous chapter using Kapton substrates. The depositions were done at 550 W sputtering power and distance between target and substrate holder 6 cm. The used parameters and the results are shown in the Figure 5.14.

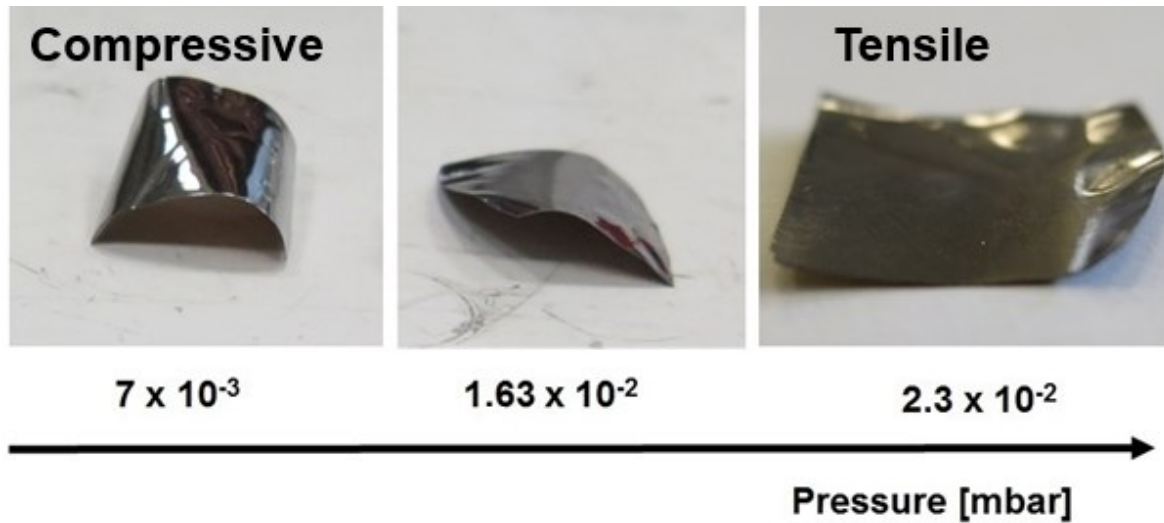


Figure 5.14: Stress in Mo sputtered vs sputtering pressure.

Thus, an argon flux of 17sccm corresponding to a working gas pressure of 1.63×10^{-2} mbar, was found to be the optimal value for Mo deposition in this system in order to minimize stress in deposited film.

5.2.1.4 Stress-free Mo deposition

Once verified that the parameters optimized for Nb film gave good results on sapphire (Figure 5.15), $5\mu\text{m}$ thick films of Mo (Mo-1) on sapphire were produced by using the program that automates the multilayer deposition. All Mo films were deposited in “down-top” configuration of the magnetron in respect to the SH. In addition to sapphire, a silicon wafer was used as a substrate, in order to obtain a film cross-section microstructure with the SEM.

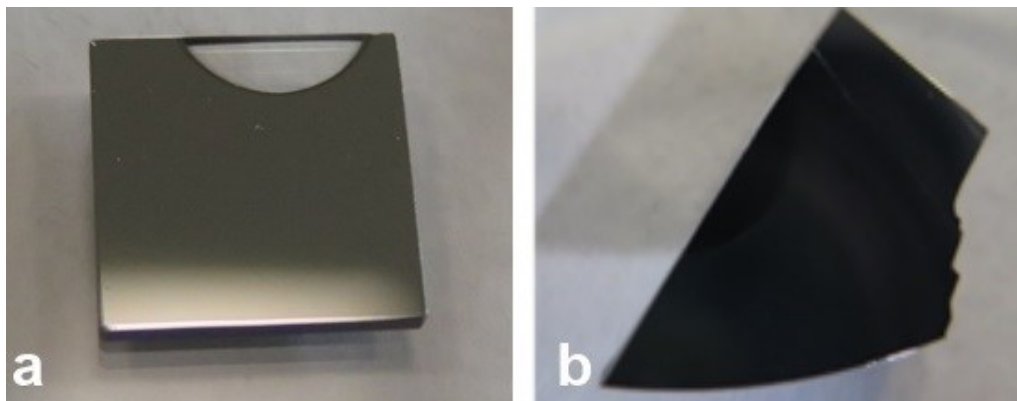


Figure 5.15: $5\mu\text{m}$ Mo sputtered at 500°C on sapphire (a) and silicon wafer (b).

From a qualitative evaluation (Figure 5.15) the coating on sapphire and Si wafer is uniform and not stressed.

Table 5.15 Multilayer sputtering of Mo onto different substrates

Parameters	Mo-1	Mo-2	Mo-3
Argon flux	17 sccm	17 sccm	17 sccm
Substrate	Sapphire 10x10, Si	Sapphire 10x10,Cu	Sapphire D13, Cu
Working pressure	$1.6 \cdot 10^{-2}$ mbar	$1.6 \cdot 10^{-2}$ mbar	$1.6 \cdot 10^{-2}$ mbar
Power	550 W	550 W	550 W
Temperature of the SH	500°C	500°C	500°C
Target-SH distance	6 cm	6 cm	6 cm
Deposition rate	11 μ m/h	11 μ m/h	11 μ m/h
Program for multilayer deposition	YES	YES	YES
Time	30min	10h	8h
Thickness	5 μ m	110 μ m	90 μ m

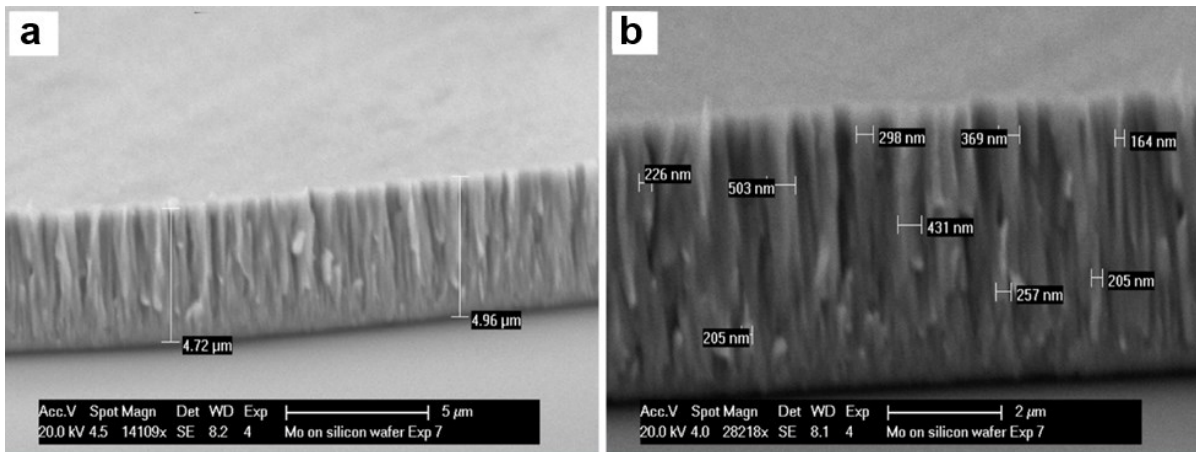


Figure 5.16: SEM of cross-section of 5 μ m Mo sputtered at 500°C on silicon wafer.

From the Figure 5.16, it can be noticed that the film microstructure is columnar and the grain size is of the order of about hundreds of nm. The elevated temperature of the substrate-holder during deposition provides denser microstructure thanks to higher ad-atom mobility.

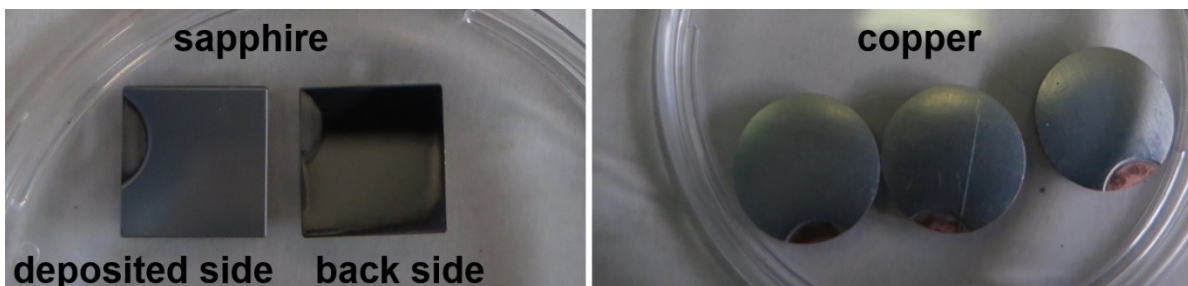


Figure 5.17: Thick molybdenum films on sapphire (a) and copper coins (b).

Since the parameters used in this experiment gave good results in terms of film density and uniformity on silicon and sapphire substrates, thicker films (Mo-2) were sputtered on sapphire and copper coins (see Figure 5.17) using the same deposition parameters (Table 5.15). After 10 hours of sputtering, films of about 110 μm thickness (Mo-2) were obtained.

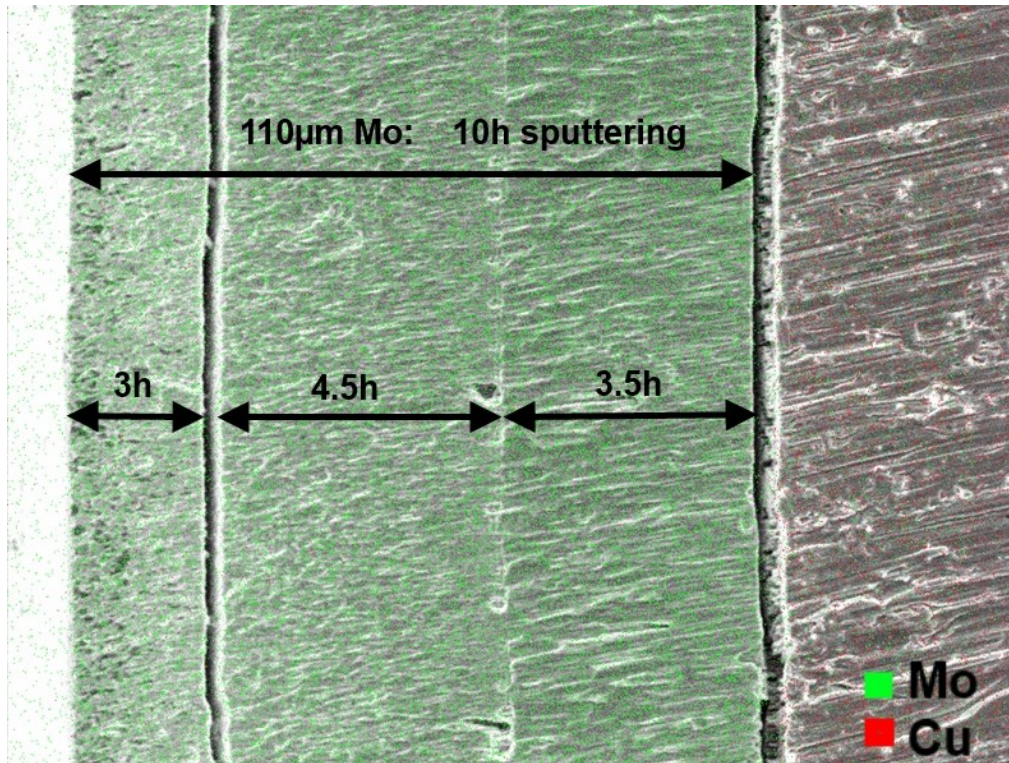


Figure 5.18: 110 μm Mo sputtered on Cu: SEM-EDS of cross-section

The films were uniform and not stressed, as illustrated in the Figure 5.17. Furthermore, the backside of the sapphire piece showed its integrity.

For the SEM cross-section analysis, the Mo-sputtered copper samples were prepared by following method:

- cut with electro erosion in the middle of the sample
- treated on the cut by abrasive papers
- chemically etched on the cut ($\text{H}_2\text{O} + \text{NaOH} + \text{H}_2\text{O}_2$ for 1 minute at 50 °C)

Chemical etching with peroxide solution allows much faster etching in the sites rich of molybdenum oxide. From the Figure 5.18 it can be observed that the film is comprised from 3-macro layers. The growth was interrupted for a night after each layer. Even if the vacuum level was kept on order of 10^{-6} mbar, there was a layer of molybdenum oxide created between depositions.

From the Figure 5.19 it can be observed that after such an oxide layer the film is re-growing starting from smaller grain size. In the Figure 5.19 the first Mo layer is on the right with average grain size $\sim 1.29 \mu\text{m}$, and second Mo layer is on the left the grain size close to the 1st layer is of order of $\sim 820 \text{ nm}$, and after is increasing with film thickness.

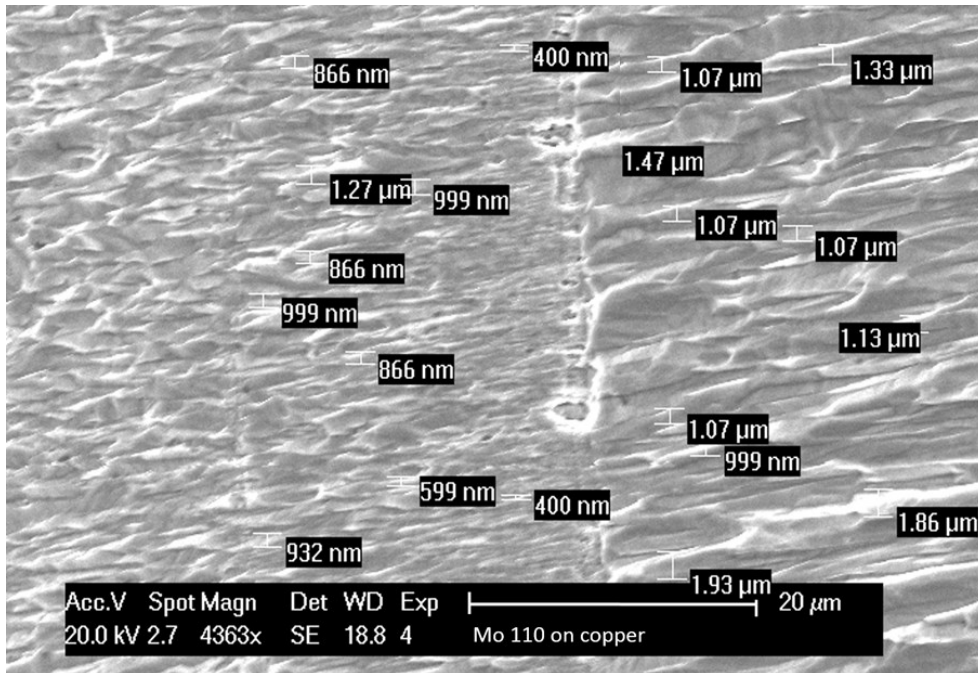


Figure 5.19: SEM of cross-section 110 μm Mo on Cu: grain size

Using the same method after 8 hours of sputtering with 550 W power and 17 sccm argon flux 90 μm of Mo film (Mo-3) was sputtered onto 13 mm diameter discs of sapphire (Figure 5.20a) and copper (Figure 5.20b). The resulted Mo films were not stressed and the sapphire samples were not cracked as it can be seen from the Figure 5.20a.

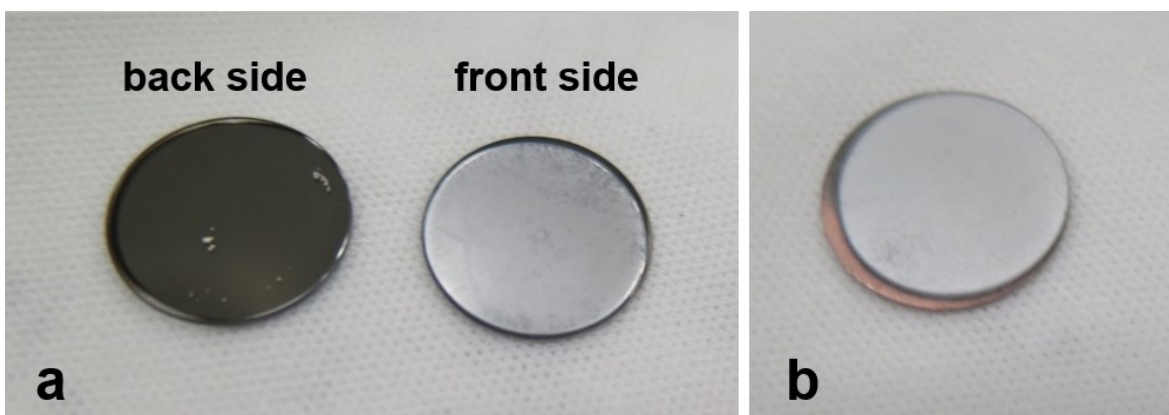


Figure 5.20: 90 μm molybdenum films on sapphire (a) and copper (b) discs.

Copper sample (Figure 5.20b) was used for cross-section SEM analysis following the same preparation procedure as it was described for Mo-2 sample. The average grain size was similar to the one obtained in Mo-2 deposition (see Figure 5.21)

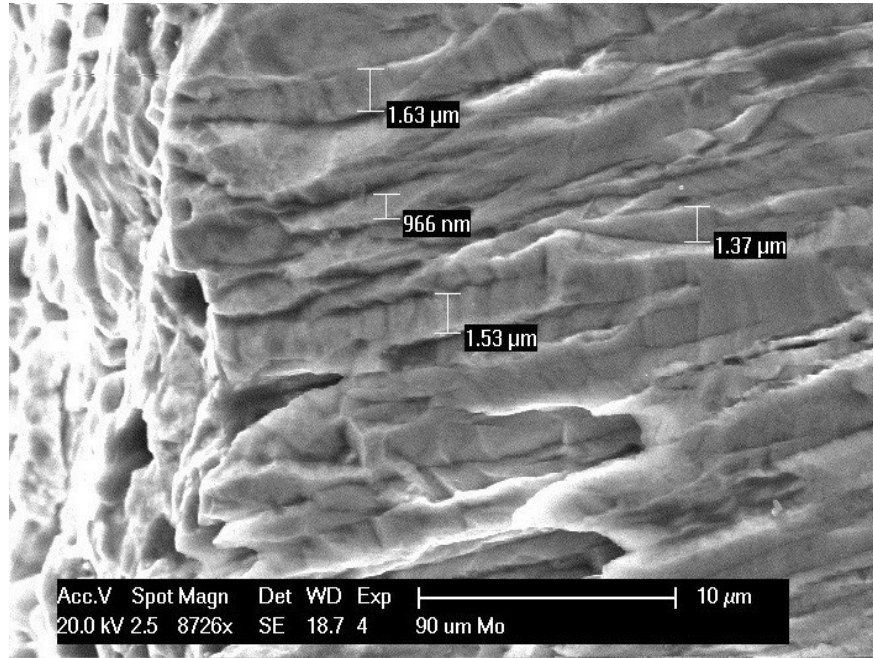


Figure 5.21: SEM of cross-section 90 μm Mo on Cu.

Mo-3 sapphire-based samples were tested under the cyclotron beam in “St. Orsola-Malpighi” Hospital of Bologna in order to evaluate the thermomechanical behavior of sputtered natural Mo thick films.

Table 5.16 Multilayer sputtering of Mo onto different substrates

Parameters	Mo-4	Mo-5	Mo-6	Mo-7
Argon flux	17 sccm	17 sccm	17 sccm	17 sccm
Substrate	Copper D32	Sapphire D13	Sapphire D19	Sapphire D25
Working pressure	$1.6 \cdot 10^{-2}$ mbar	$1.6 \cdot 10^{-2}$ mbar	$1.6 \cdot 10^{-2}$ mbar	$1.6 \cdot 10^{-2}$ mbar
Power	550 W	550 W	550 W	550 W
Temperature of the SH	500°C	500°C	500°C	500°C
Target-SH distance	6 cm	6 cm	6 cm	6 cm
Deposition rate	11 $\mu\text{m}/\text{h}$	11 $\mu\text{m}/\text{h}$	11 $\mu\text{m}/\text{h}$	11 $\mu\text{m}/\text{h}$
Program for multilayer depos.	YES	YES	YES	YES
Time	10h	10h	10h	10h
Thickness	110 μm	110 μm	110 μm	110 μm

The next experiment comprised deposition of thick Mo film on a set of different substrates: copper and sapphire discs of different dimensions (Table 5.16). Mo sputtered sapphires were used in next experiments to be brazed to copper backing to create a novel target prototype.

The substrates used in the deposition included:

- Copper of 2 mm thick, Ø 32 mm (Mo-4);
- Sapphire of 0.5 mm thick, Ø 13 mm (Mo-5);
- Sapphire of 0.5 mm thick, Ø 19 mm (Mo-6);
- Sapphire of 0.5 mm thick, Ø 25 mm (Mo-7).

In order to realize simultaneous deposition on such substrates, for thermal contact and substrates centering, a particular mask was designed (see Figure 5.22).

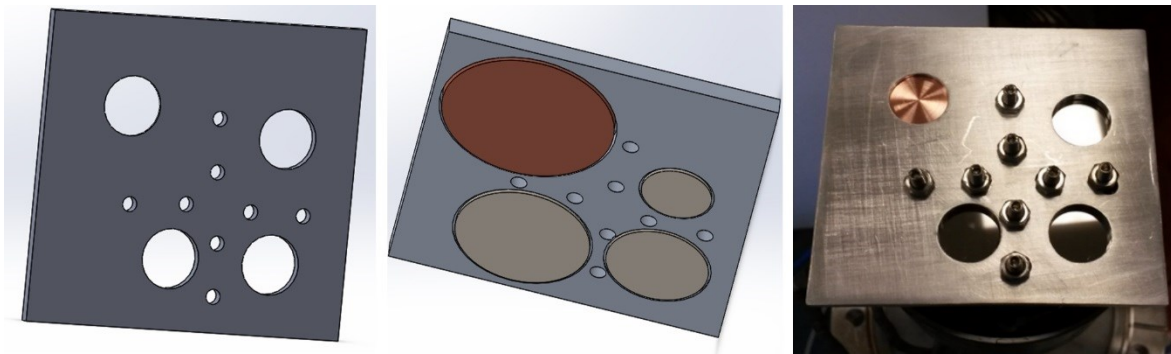


Figure 5.22: Mask for deposition onto multiple substrates.

The sapphire pieces were functionalized before Mo deposition with Ti layer on the backside to be brazed to the copper backing plate after.



Figure 5.23: Mo-4 and Mo-5 110µm thick Mo sputtered by multilayer approach at 500°C.

Thanks to the mask, Mo was deposited onto the center of each substrate as a disc of Ø12mm and about 110µm thickness.

The density of Mo material in film was estimated and it reached more than > 98% in respect to bulk Mo material.



Figure 5.24: Mo-6 and Mo-7 110µm thick Mo sputtered onto sapphire to be brazed to Cu.

The following experiment (Table 5.17) included deposition of thick Mo film on another set of different substrates: copper, sapphire and CVD synthetic diamond discs.

The substrates used in this deposition included:

- 2 copper disks of 1 mm thick, Ø 32 mm (Mo-8);
- 2 sapphire coins of 0.5 mm thick, Ø 13 mm (Mo-9);
- 4 CVD diamond coins TG 1500 of 0.3 mm thick, Ø 13 mm (Mo-10).

Table 5.17 Multilayer sputtering of Mo onto different substrates

<i>Parameters</i>	<i>Mo-8</i>	<i>Mo-9</i>	<i>Mo-10</i>
Argon flux	17 sccm	17 sccm	17 sccm
Substrate	2×Copper D32	2×Sapphire D13	4×diamond D13
Working pressure	1.6·10 ⁻² mbar	1.6·10 ⁻² mbar	1.6·10 ⁻² mbar
Power	550 W	550 W	550 W
Temperature of the SH	500°C	500°C	500°C
Target-SH distance	6 cm	6 cm	6 cm
Deposition rate	11µm/h	11µm/h	11µm/h
Program for multilayer deposition	YES	YES	YES
Time	10.5h	10.5h	10.5h
Thickness	125µm	125µm	125µm

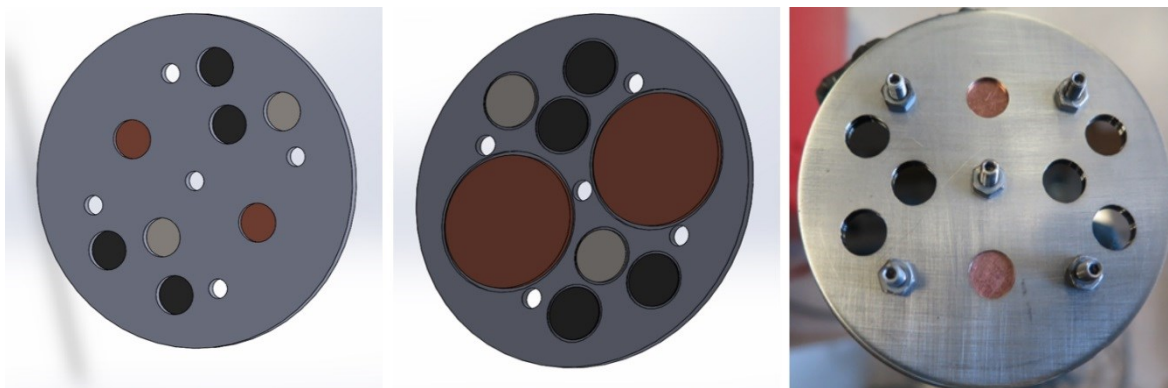


Figure 5.25: Mask for deposition onto multiple substrates.

Another heated sample holder (bigger than in previous experiment) and another mask were used correspondingly (see Figure 5.25) to host all the samples simultaneously.

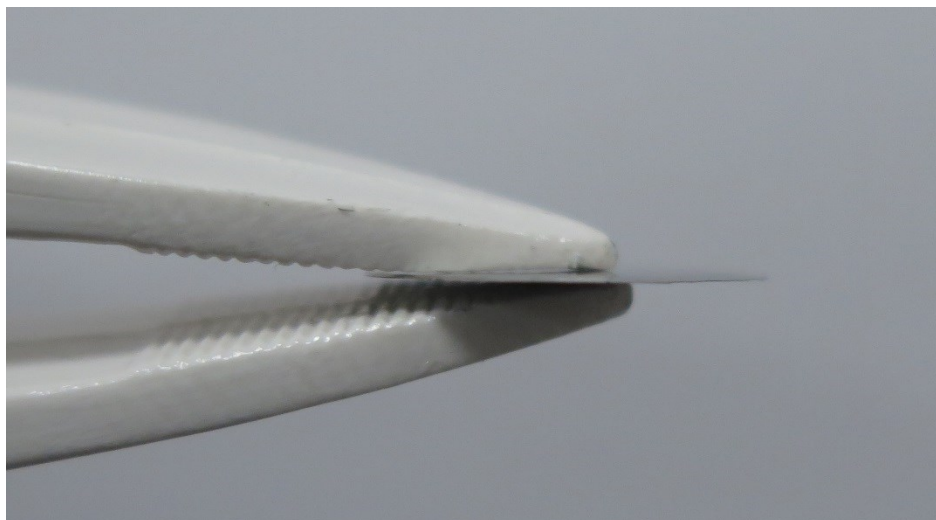


Figure 5.26: Self-sustaining 125µm Mo film delaminated from CVD synthetic diamond.

Mo film of 125µm thickness sputtered on copper and sapphire appeared to be well attached and not stressed. Mo film on one sample of CVD synthetic diamond was delaminated. Probably the reason was a not efficient cleaning, as soon as the detached from substrate film is not stressed (see Figure 5.26).

Mo-8 sputtered on 32mm diameter discs of copper (Figure 5.27) were used for cyclotron test in order to evaluate the behavior of the sputtered Mo thick film, under the proton beam with different irradiation currents.

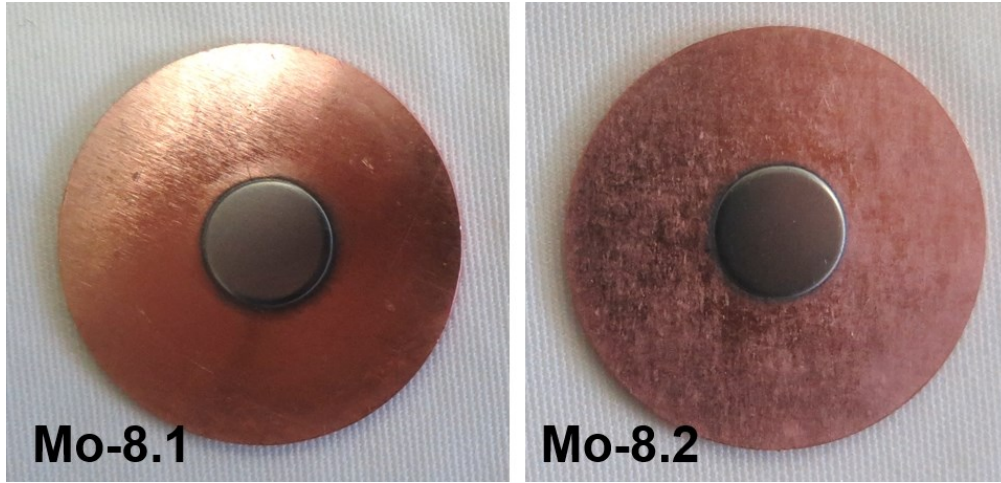


Figure 5.27: Mo-8 125 μ m Mo sputtered onto copper D32 for cyclotron test.

Two sapphire-based Mo-9 and two synthetic diamond-based Mo-10 samples were used to estimate the stress in sputtered films using curvature method.

5.2.1.5 Estimation of stress in Mo sputtered films

The estimation of an average total stress in sputtered films on thin substrates (up to 0.5mm thick) was realized by the measurement of curvature with Dektak 8 profiler and by use of modified Stoney formula already described in the Chapter 3.12.2 [64]:

$$\sigma^{(f)} = \frac{d_s^2}{6 \cdot d_f} \cdot \frac{E_s}{(1-\nu_s)} \cdot \frac{1}{R} \quad (5.1),$$

where E_s is substrate Young's modulus, d_f and d_s are the film and substrate thicknesses correspondingly, R is the radius of curvature of the coated substrate, and ν_s is Poisson's ratio of the substrate.

In order to take into account the non-planarity of the substrate (radius of curvature of the substrate R_{pre}), the next formula was used:

$$\sigma^{(f \text{ tot})} = \frac{d_s^2}{6 \cdot d_f} \cdot \frac{E_s}{(1-\nu_s)} \cdot \left(\frac{1}{R_{post}} - \frac{1}{R_{pre}} \right) \quad (5.2)$$

The Dektak 8 profiler was used to measure the curvature radius of the substrate before (R_{pre}) and after Mo film deposition (R_{post}).

The profile scans of 12mm length were taken in the central part of the disc substrate before and after deposition. The Mo film was deposited as a circular area of 10mm diameter in the middle of 13mm diameter substrate. In this case, the scan profile was covering almost the

full length of the substrate and the film on it, located in the middle of the scan. The profile scans taken by Dektak 8 (Figure 5.28) were saved and then elaborated in MS Excel.

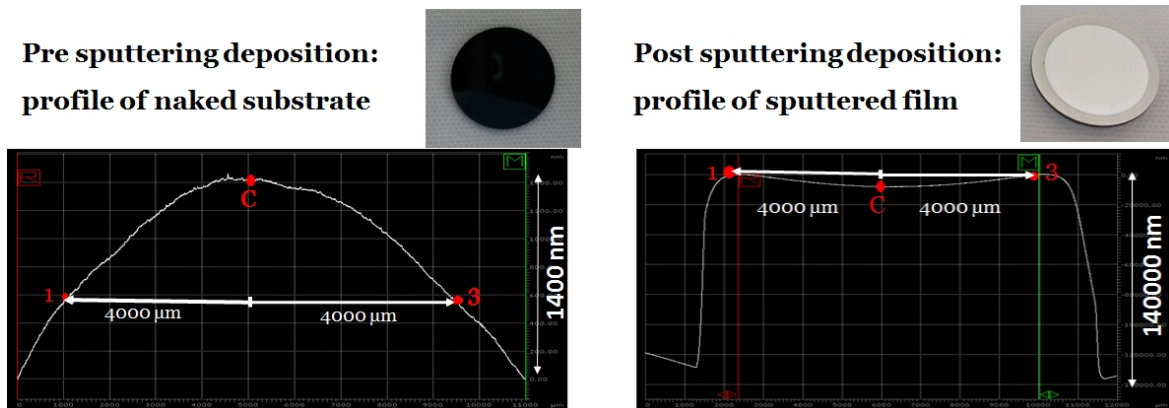


Figure 5.28: Dektak 8 profiler estimation of curvature radius.

The radius of curvature was estimated by 3 points having the next coordinates in μm (see Figure 4.8):

$$1: (x_1 = x_c - 4000; y_1)$$

$$C: (x_c; y_c)$$

$$3: (x_3 = x_c + 4000; y_3)$$

At first, the central point is defined. After the coordinates of another two points equidistant from the center were found.

Table 5.18 Properties of Mo and substrate materials

Material	E	ν	α , 25°C	α , 500°C
Molybdenum	329 GPa	0.31	$4.8 \cdot 10^{-6}$	$5.5 \cdot 10^{-6}$
Sapphire	380 GPa	0.23	$6.1 \cdot 10^{-6}$	$7.5 \cdot 10^{-6}$
Si wafer	169 GPa	0.17	$2.6 \cdot 10^{-6}$	$3.7 \cdot 10^{-6}$
CVD diamond	1220 GPa	0.1	$1 \cdot 10^{-6}$	$3.7 \cdot 10^{-6}$

The sign of the curvature radius is taken by convention as “+” for concave, and as “-” for convex profile. Having the radius of curvature R_{pre} and R_{post} the total stress was calculated by the formula (5.2).

Then the thermal mismatch stress was estimated by the formula:

$$\sigma^{(f \text{ mismatch})} = \frac{E_f}{1-\nu_s} (\alpha_f - \alpha_s) \cdot \Delta T \quad (5.3),$$

where α_s , α_f are the coefficient of thermal expansion of the substrate and film, ΔT is temperature difference (heating/cooling).

For the current calculation, a simplification was made: the properties of Mo sputtered film were considered equal to bulk. The Mo properties are shown in the Table 5.18 and the Figure 5.29 [98].

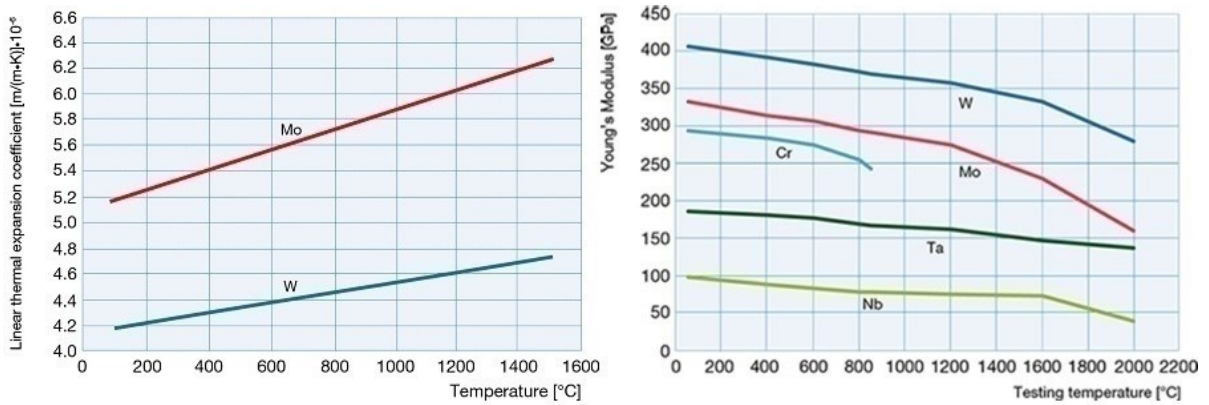


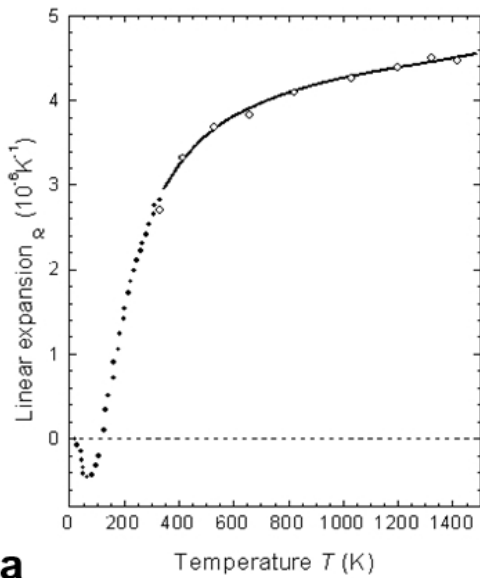
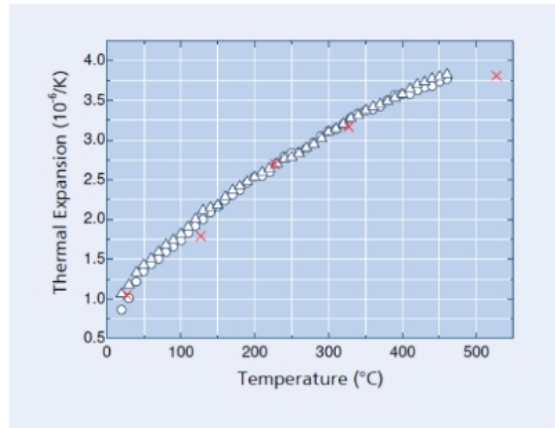
Figure 5.29: Mo properties vs temperature.

The change of the elastic properties and the thermal expansion coefficients with temperature was not available from the manufacturers of the samples used in current work. That is why several other sources were studied and the most reliable data were used for further calculations (see Table 5.18). The thermal expansion coefficients vs temperature for synthetic diamond (Figure 5.30b) were taken from the CVD diamond booklet of Advanced Diamond Technologies [99], for silicon (Figure 5.30a) from the work of Okada et al. [100] and the data on sapphire properties were extracted from NIST SR 718 polycrystalline sapphire certificate [101].

After in order to obtain the intrinsic stress of the film the stress of the thermal mismatch was subtracted:

$$\sigma^{(f \text{ intrinsic})} = \sigma^{(f \text{ tot})} - \sigma^{(f \text{ mismatch})} \quad (5.4)$$

All the results of stress estimation are presented in the Table 5.19.

Si wafer thermal expansion coefficient**a****CVD diamond thermal expansion coefficient**

Thermal expansion vs. temperature

○ High quality CVD diamond
 △ Medium quality CVD diamond
 × Values recommended by Slack⁴

b**Figure 5.30: Thermal expansion coefficient of Si wafer (a) and CVD diamond (b) vs temperature.****Table 5.19 Stress estimation in 125 μ m Mo sputtered films**

Sample	Mo-9.1	Mo-9.2	Mo-10.1	Mo-10.2
Substrate	sapphire	sapphire	CVD diamond	CVD diamond
d_s , m	0.0005	0.0005	0.0003	0.0003
R_{pre} , m	24.27	-49.87	-10.14	-10.03
R_{post} , m	-0.446	-0.396	1.0	1.08
$\sigma^{(f\ tot)}$, GPa	-0.376	-0.412	0.179	0.167
$\sigma^{(f\ mismatch)}$, GPa	-0.406	-0.406	0.313	0.313
$\sigma^{(f\ intrinsic)}$, GPa	0.030	-0.006	-0.134	-0.146

It can be seen from the profiles that sputtered sapphire is slightly convex, also the sign of the total stress is “minus”, which means compressive, instead sputtered CVD diamond has small concave curvature, and the total stress in Mo-10 samples is positive (tensile).

The intrinsic stress in Mo during this deposition (both on sapphire and CVD diamond) is enough close to zero. The small shift of intrinsic stress on CVD diamond in negative direction in respect to one on sapphire can be explained by uncertainties of the real thermal expansion coefficients of the substrate materials. It should be reminded, that they were obtained from different data-base, but not measured directly and not provided by the substrate manufacturers.

Table 5.20 Comparison of current result with literature

	<i>Current result</i>		<i>Deambrosis et al.[102]</i>	<i>Vink et al.[53]</i>
Substrate	sapphire	CVD diamond	titanium	glass
Method stress estim.	curvature	curvature	FIB-milling+HR SEM	XRD
Stress,Gpa	0.03	0.15	0.24	1
Thickness, μm	125	125	2	0.2
Argon pressure, mbar	$1.6 \cdot 10^{-2}$	$1.6 \cdot 10^{-2}$	$1 \cdot 10^{-2}$	$1 \cdot 10^{-2}$
Deposition rate, nm/min	170	170	56	30
Controlled in	Power 550 W	Power 550 W	Power 150 W	Power 800 W
Target-SH dist., cm	6	6	9	7
Bias	no	no	- 40 V	no
Substrate temperature	500 °C	500 °C	307 °C	-

The Table 5.20 shows a comparison between obtained levels of stress in 125 μm thick sputtered Mo and thin Mo films deposited by different methods in other groups. It should be noticed that the stress level obtained in current study was lower than described in previous works, even if the film thickness was hundreds times higher.

5.2.2 Novel backing plate

5.2.2.1 Study of vacuum brazing for ceramics

5.2.2.1.1 Brazing alumina to metal as the first trial

As soon as the chemical content of both sapphire and alumina is Al_2O_3 , alumina was used for preliminary study of brazing, as soon as the chemistry of the bonding is equal.

Table 5.21 Thermal expansion coefficients of brazed elements

<i>Material</i>	<i>CTE at r.t., $10^{-6} \text{ m}/(\text{m}\cdot\text{K})$</i>	<i>CTE at 900 °C, $10^{-6} \text{ m}/(\text{m}\cdot\text{K})$</i>
Alumina	8.1	8.1
Sapphire	6.1	8.1
CVD diamond	1	3.7
Stainless steel 304	17.3	17.3
Inconel	12.6	12.6
Copper	16.6	16.6
Aluminum	22.2	22.2
Titanium	8.6	8.6

The preliminary brazing tests were realized onto the system stainless steel-alumina of 5mm thick and 28 mm diameter, starting from consideration of availability of materials.

The filler metals used in current study are listed in the Table 5.22, including both active and non-active fillers. For brazing with non-active brazants preliminary metallization of ceramics was realized. It should be noticed that from a theoretical point of view, the same filler metals could be used for the systems copper-sapphire and copper-diamond.

Table 5.22 Content of brazing fillers

<i>Brazing Filler</i>	<i>Form</i>	<i>Manufacturer</i>	<i>Composition</i>			<i>Brazing temp-re</i>
Copper	Foil 0.05mm	Good fellow	Cu-100%			890°C
Pallabraz 850	Disc 0.3mm	Johnson Matthey	Ag-58.5%	Cu-31.5%	Pd-10%	860°C
TiFlo 950	Paste	Johnson Matthey	Ti-70%	Cu-15%	Ni-15%	990°C
Cusil ABA	Wire 0.8mm	WESGO metal	Ag-63%	Cu-35.3%	Ti-1.7%	900°C
Cusil ABA	Paste	Homemade	Ag-63%	Cu-35.3%	Ti-1.7%	920°C
CuTiSn ABA	Paste	Homemade	Cu-75	Sn-25	Ti-10	960°C

The set of brazing experiments with alumina discs and their results is presented in the Table 5.23 and Table 5.24. The real brazing temperatures are a bit higher than those declared by the manufacturers of filler and are listed in the Table 5.22. The brazing experiments have been realized with two preheating soaks: for 1 h at 400°C (to decompose the organic phase in paste) and at ($T_b-100^\circ\text{C}$) (T_b is brazing temperature for each filler), and a brazing soak at brazing temperature of order of 15-30min. Example of heating cycle for brazing with CuSnTi ABA paste is shown in the Figure 5.31.

Table 5.23 Brazing alumina to metal experiments






<i>Experiment</i>	<i>Filler</i>	<i>Metallic part</i>	<i>Alumina part</i>	<i>Results</i>	<i>Photo</i>
Alu-1	CuSil ABA, wire 0.8mm	Ø28, 5mm thick SS	5mm thick	Tolerance problem. The wire was too thick.	
Alu-2	CuSil ABA, wire 0.8mm	Ø28, 5mm thick SS	5mm thick	Tolerance problem. The wire was too thick.	
Alu-3	CuSil ABA, foil 0.1mm	Ø28, 5mm thick SS	5mm thick	Small foil thickness problem. Parts were not attached	
Alu-4	CuSil ABA, foil 0.1mm	Ø28, 5mm thick SS	5mm thick	Small foil thickness problem. Not good mechanical contact	
Alu-5	Cu, foil 0.05mm	Ø28, 5mm thick SS	5mm thick. Ti, Ag sputtered	Low diffusion of filler into steel, non-uniformity of distribution of filler	

Table 5.24 Brazing alumina to metal experiments

<i>Experiment</i>	<i>Filler</i>	<i>Metallic part</i>	<i>Alumina part</i>	<i>Results</i>	<i>Photo</i>
Alu-6	Cu, Ag, Ti sputtered	Ø28, 5mm thick Inconel	5mm thick. Cu, Ag, Ti sputtered	Parts were attached, Alumina was not cracked	
Alu-7	Pallabraz850, disk 0.3 mm	Ø28, 5mm thick Inconel	5mm thick. Ti sputtered	Parts were attached, alumina was cracked	
Alu-8	TiFlo, paste commercial	Ø28, 5mm thick SS	5mm thick	IR heating. Ceramics was not broken., not attached to metal	
Alu-9	TiFlo, paste commercial	Ø28, 5mm thick SS	5mm thick	IR heating. Ceramics was not broken, not attached.	
Alu-10	CuSnTi, paste homemade	Ø28, 3mm thick SS	5mm thick	Good contact between parts. Ceramics was broken	
Alu-12	CuSnTi, paste homemade	Ø28, 5mm thick SS	5mm thick	Induction heating, fast cooling. ceramics was broken	
Alu-13	CuSnTi, paste homemade	Ø28, 5mm thick SS	5mm thick	IR heating. Ceramics was broken	
Alu-14	CuSnTi, paste homemade	Ø28, 5mm thick Inconel	5mm thick	IR fast heating, slow cooling. Ceramics was not broken. Good contact between parts	
Alu-16	Pallabraz850, disk 0.3 mm	Ø28, 5mm thick Inconel	5mm thick. Ti mech. metalized	IR fast heating, slow cooling. Ceramics broken.	
Alu-17	Pallabraz850, disk 0.3 mm	Ø28, 5mm thick SS	5mm thick. Ti mech. metalized	IR fast heating, slow cooling. No attachment of alumina to metal	
Alu-18	Pallabraz850, disk 0.3 mm 3	Ø28, 5mm thick SS	5mm thick. Ti sputtered	IR fast heating, slow cooling. No attachment of alumina to metal	
Alu-19	CuSil ABA, paste homemade	Ø28, 5mm thick Inconel	5mm thick	IR fast heating, slow cooling. Ceramics was broken. Good attachment	
Alu-20	CuSil ABA, paste homemade	Ø28, 5mm thick Inconel	5mm thick	IR fast heating, slow cooling. Ceramics was broken. Good attachment	
Alu-22	CuSil ABA, paste homemade	Ø28, 5mm thick steel	5mm thick	IR fast heating, slow cooling. Ceramics was cracked, but not broken. Good contact	

As it can be seen from the Table 5.23, Table 5.24 not only different fillers, but also different filler forms were tested. Wire was found not suitable for our horizontal butt-joint (Alu-1, Alu-2). Also the commercially available fillers in foil form did not provide as good results, as expected (Alu-3, Alu-4, Alu-7, Alu-16, Alu-17, and Alu-18). Commercial paste TiFlo-950 (Alu-8, Alu-9) was not molten in our furnace at 990° (even if declared by manufacturer brazing temperature was 950°C).

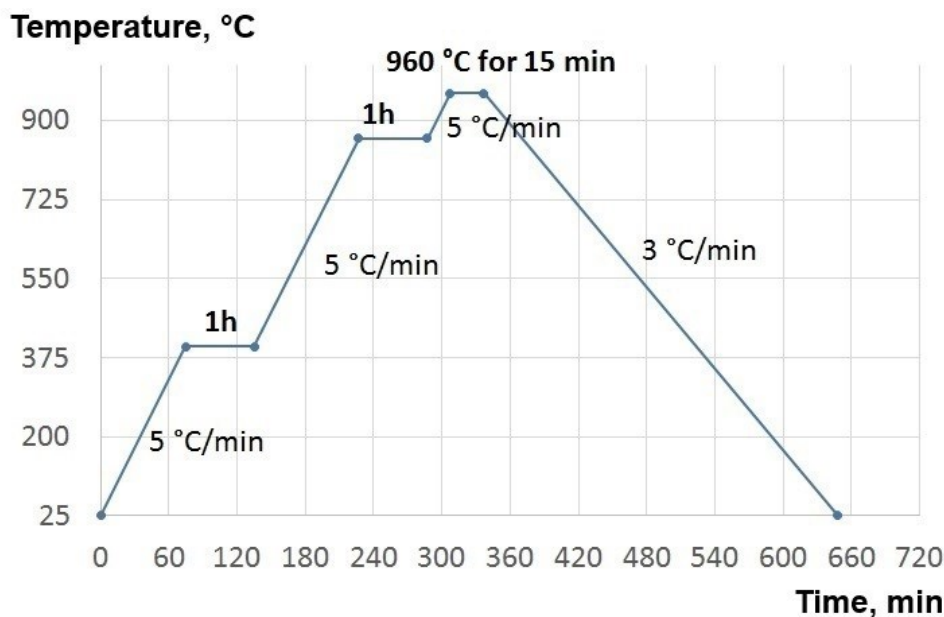


Figure 5.31: Brazing thermal cycle Alu-10, Alu-14 with CuSnTi ABA paste.

The most promising results were obtained by brazing with homemade CuSnTi and CuSiI ABA pastes. They provided reliable melting points, high uniformity of distribution, no void defects in the brazed joint. The preparation of brazing paste was described in the Chapter 4.6.4. The Figure 5.32 represents the SEM and EDS-analysis of the cross-section of the sample Alu-10 brazed with CuSnTi homemade filler.

Thus, the main candidates for future brazing of sapphire and CVD diamond to copper were CuSnTi and CuSiI ABA. The choice of the brazant was taken from the point of view of minimization of stress in ceramic-metal joint after thermal cycling due to difference of CTEs (coefficient of thermal expansion). The brazing filler with CTE value between metal and ceramics, higher ductility and lower melting point is preferable for stress minimization [103]. The ductility and CTE of CuSnTi and CuSiI ABA are similar; instead, the CuSiI ABA in our experiments was molten at a bit lower temperature. Thus, for the next experiments for brazing sapphire to copper CuSiI ABA homemade filler in paste form was used.

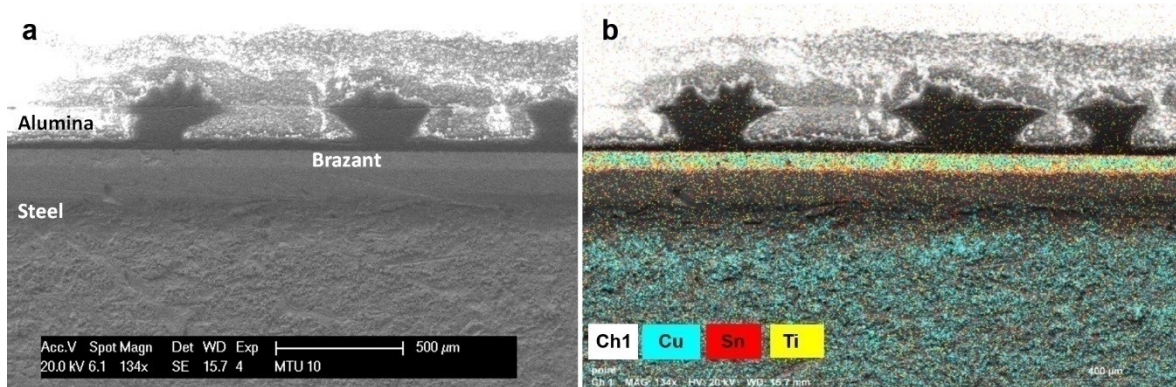


Figure 5.32: SEM (a) and EDS (b) analysis of cross section of Alu-10 brazed sample.

5.2.2.1.2 Brazing sapphire to copper

Trial of brazing sapphire to copper with a simple $10 \times 10 \times 1$ mm sapphire substrate was realized following thermal cycle presented in the Figure 5.34 using CuSil ABA as a filler. Before brazing procedure $1 \mu\text{m}$ Ti layer was pre-deposited onto half part of sapphire piece by magnetron sputtering.

The Figure 5.33 shows the sample before and after brazing procedure. It should be noted that the part of sapphire pre-sputtered with Ti layer was attached well to copper, instead, the part of sapphire not pre-coated with Ti had lower adherence to copper.

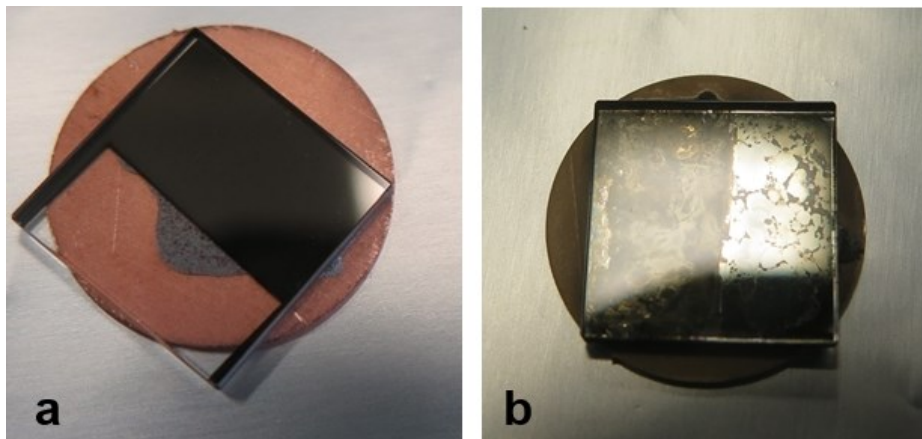


Figure 5.33: Sapphire $10 \times 10 \times 1$ mm brazing to Cu by CuSil ABA: (a) before, (b) after.

As can be seen from the Table 5.18 in previous experiments with alumina (Alu-19, Alu-20, Alu-21) the use of CuSil ABA paste filler allowed to get strong joint without pre-coating of alumina by Ti, as soon as Ti is already presented in the filler. Instead, for sapphire brazing

Ti pre-deposited is required for high adherence. It can be explained by difference of roughness of alumina and sapphire (optic quality). From the other point of view, Ti is decreasing the stress in the joint associated with the difference of thermal expansion coefficients of metal and sapphire (see Table 5.17), since Ti thermal expansion coefficient is between the values for sapphire and copper.

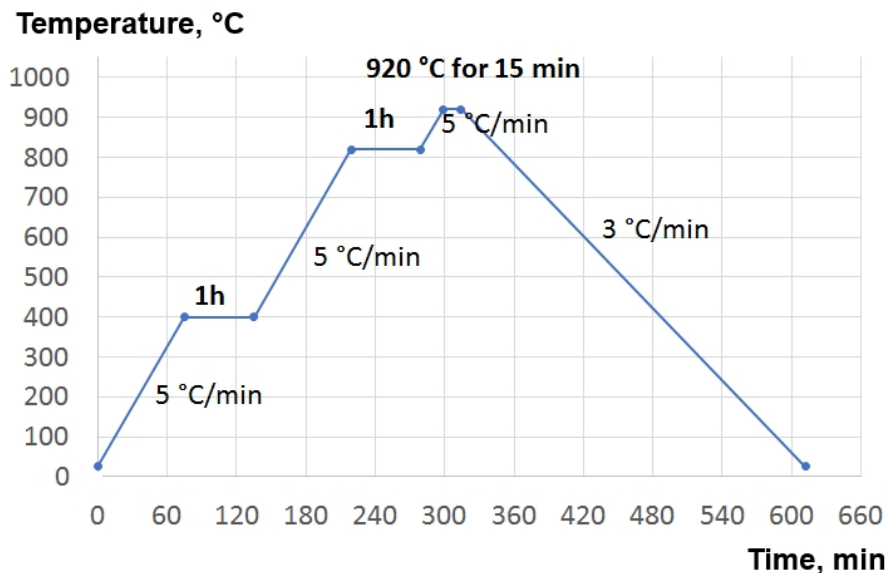


Figure 5.34: Brazing thermal cycle for brazing with CuSil ABA paste.

5.2.2.1.3 Brazing sapphire to aluminium

Copper is well-known to be used as a backing for cyclotron target, because of its high thermal conductivity. However, copper has one important disadvantage for the daily use: it is highly activated under cyclotron beam. And sometimes it is required to leave copper-based solid targets to decay after irradiation to increase the personnel safety. Aluminium and its alloys have enough high thermal conductivity and lower level of activation under the cyclotron proton beam in respect to copper.

In this thesis the approach to use aluminium-based target backing is considered not of primary interest, but, in any case, the opportunity to switch from copper to aluminium is proposed.

For the brazing experiments Al 6082 with 555 °C melting point and 10x10x1mm sapphire pieces, pre-sputtered with 1µm of Ti, were used.

Three homemade paste filler materials, having theoretical melting point of around 500°C were proposed:

- Ag–28Cu (Al-1)
- Al–9.6Si–20Cu (Al-2)
- Al–8.4Si–20Cu–10Sn (Al-3)

The contents and experimental brazing points are listed in the Table 5.25.

On each sample a pressure of about 11445 Pa (SS piece of 250g weight) was applied.

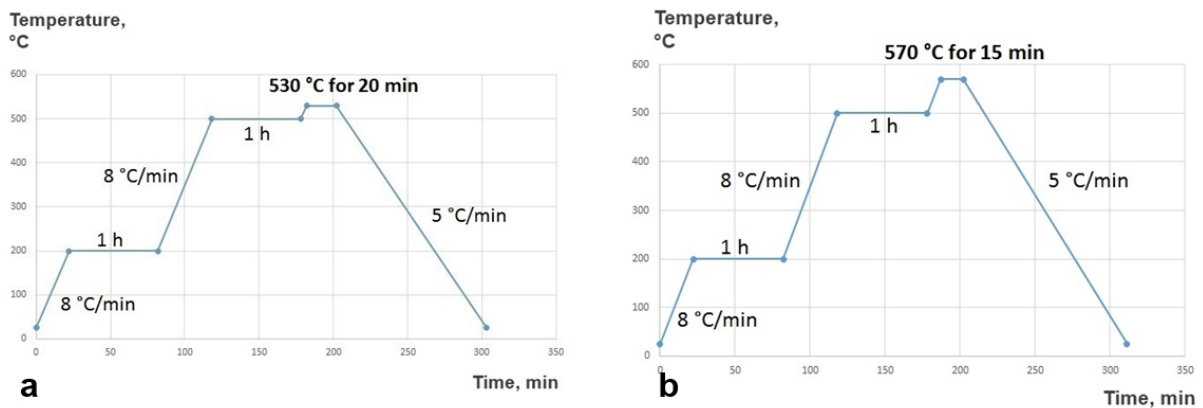


Figure 5.35: Thermal cycle for brazing sapphire to Al 6082.

The first brazing experiment was realized at 530 °C (see Figure 5.35a), and any brazing occurred, as soon as the filler melting temperature was not achieved. Probably the read-out of the thermocouple inside the brazing furnace is not equal to the real temperature of the pieces during process.

Table 5.25 Content of brazing fillers for aluminum 6082

Brazing Filler	Form	Composition				Brazing temp-re
Ag–28Cu	Paste	Ag-72%	Cu-28%			530-570°C
Al–9.6Si–20Cu	Paste	Al-70.4%	Cu-20%	Si-9.6%		530-570°C
Al–8.4Si–20Cu–10Sn	Paste	Al-61.6%	Cu-20%	Si-8.4%	Sn-10%	530-570°C

The experiment was repeated with the brazing soak at 570°C (Figure 5.32b). Two of three samples (Al-1 and Al-3) were brazed (Figure 5.36). The Al-1 and Al-2 sapphire pieces have had a good mechanical contact with aluminum alloy 6082.

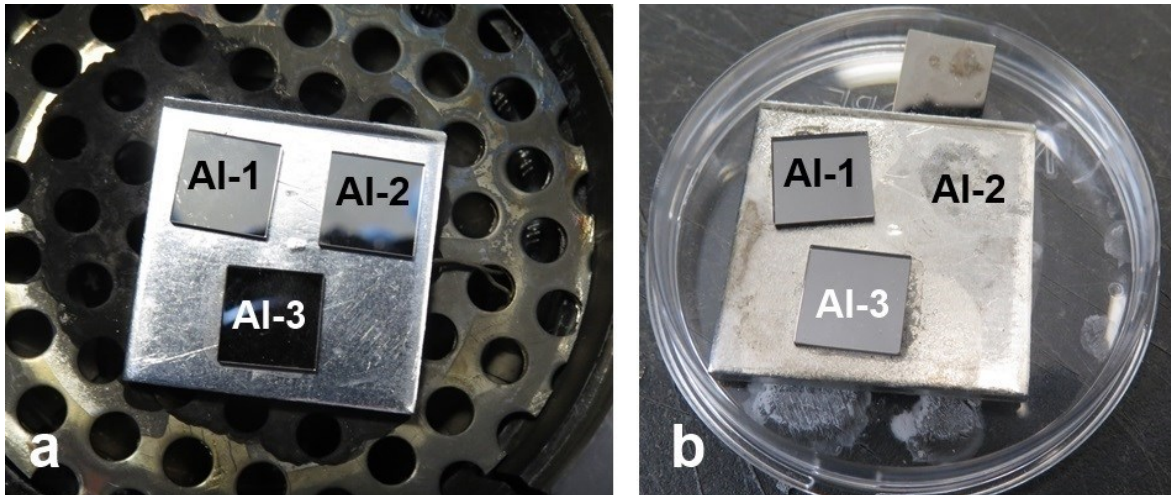


Figure 5.36: Brazing sapphire to Al 6082: (a) before and (b) after thermal cycling.

Ag – 28 Cu filler material was chosen for the next experiment with Ø19 mm, 0.5mm thick disc of sapphire with 1µm Ti and Ø32 mm disc-shaped aluminum 6082 alloy. The thermal cycling described in the Figure 5.35b was performed in vacuum.

Sapphire was brazed to Al 6082 (see Figure 5.37). The pieces were well attached mechanically. The size of Al part of this sample was chosen of Ø32 and 1.5 mm thickness in order to allow thermomechanical test under cyclotron of “St. Orsola-Malpighi” Hospital of Bologna.

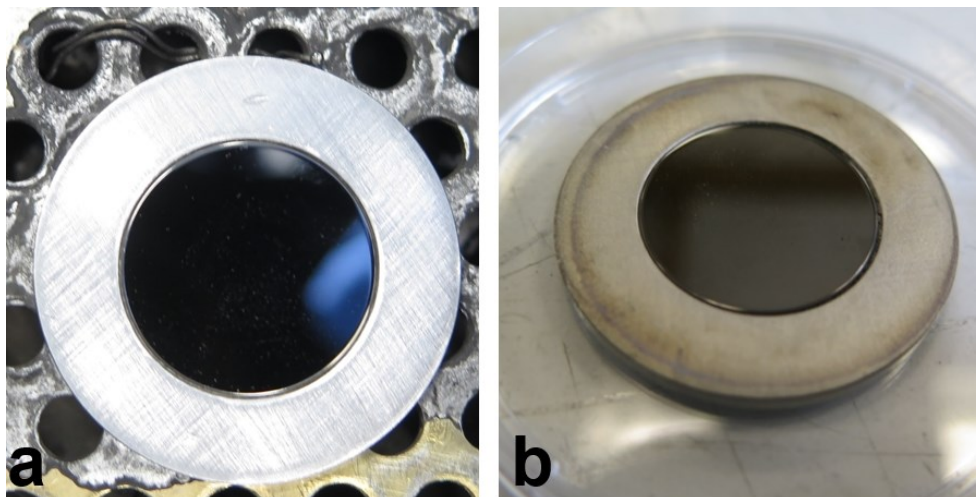


Figure 5.37: Brazing 0.5mm thick sapphire to Al 6082: (a) before and (b) after thermal cycling.

5.2.2.1.4 Preparation of sapphire-based target prototypes

The Mo sputtered sapphires were obtained by the experiments described in Chapter 5.2.1. Brazing experiments were realized for each sample separately in IR-lamp based vacuum furnace with CuSil ABA homemade paste, containing Ag-63%, Cu-35.3% and Ti-1.7%. The main process parameters are described in the Table 5.26.

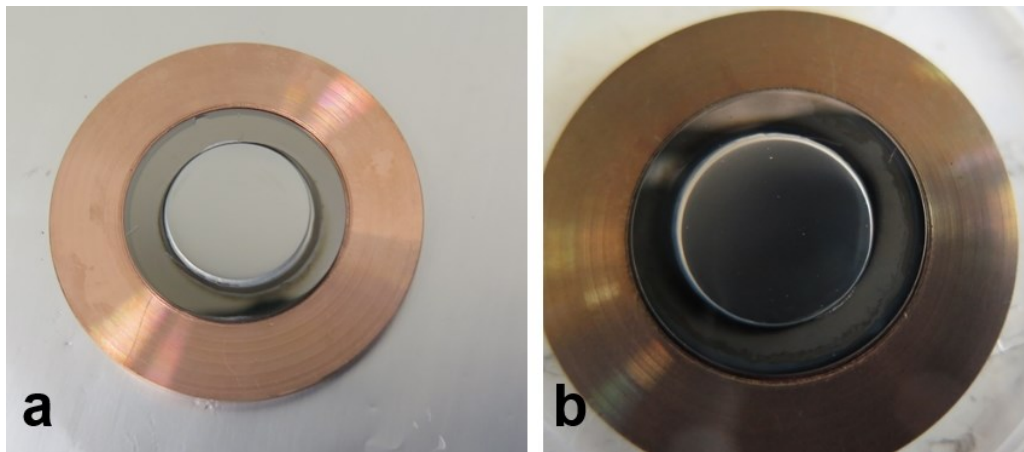


Figure 5.38: S-1. Brazing D19 sapphire to copper: (a) before and (b) after thermal cycling.

The smaller sapphire samples: $\varnothing 19.05$ (Figure 5.38) and $\varnothing 12.7$ (Figure 5.40) were brazed to copper without problem allowing good mechanical contact. Instead, the biggest sapphire disc of $\varnothing 25.4$ was cracked (Figure 5.39).

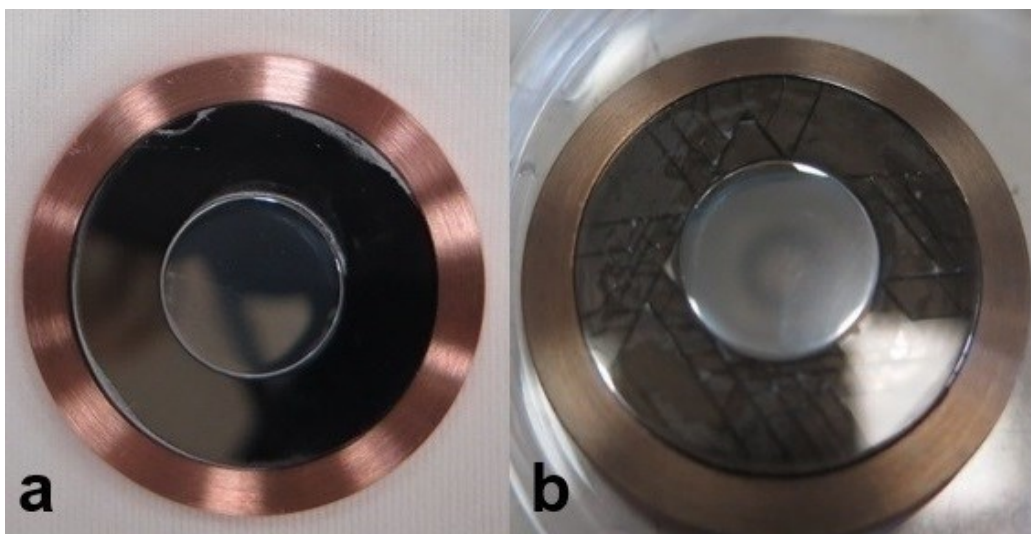


Figure 5.39: S-2. Brazing D25 sapphire to copper: (a) before and (b) after thermal cycling.

Table 5.26 Brazing discs sapphire to copper for target prototype

<i>Exp.</i>	<i>Mo film</i>	<i>Sapphire part</i>	<i>Radial clearance</i>	<i>Ti sputtered layer on sapphire</i>	<i>Brazing soak</i>	<i>Results</i>
S-1	Mo-6	Ø19.05×0.5mm	0.475mm	8·10 ⁻³ mbar, 5A, 1µm	920 ^o C, 15 min	Good mechanical attachment of sapphire to copper. Sapphire is integer
S-2	Mo-7	Ø25.4×0.5mm	0.3mm	8·10 ⁻³ mbar, 5A, 1µm	920 ^o C, 15 min	Sapphire is mechanically attached to copper, but sapphire was cracked after cooling.
S-3	Mo-5	Ø12.7×0.5mm	0.4mm	8·10 ⁻³ mbar, 5A, 1µm	920 ^o C, 15 min	Good mechanical attachment of sapphire to copper. Sapphire is integer
S-4	Mo-9.1	Ø12.7×0.5mm	0.4mm	8·10 ⁻³ mbar, 5A, 1µm	920 ^o C, 15 min	Good mechanical attachment of sapphire to copper. Sapphire is integer
S-5	Mo-9.2	Ø12.7×0.5mm	0.4mm	8·10 ⁻³ mbar, 5A, 1µm	920 ^o C, 15 min	Good mechanical attachment of sapphire to copper. Sapphire is integer

The reason is the stress, caused by difference of CTEs (coefficients of thermal expansion) of copper, brazing filler (also close to copper value) and sapphire. It is very well known problem in brazing ceramics to metal. The main approaches to solve it usually include choosing the materials with close CTEs, otherwise, minimizing the area of brazed joint[103]. In fact, the sapphire samples of smaller size were not suffering this problem. The other alternative could be to use an intermediate layer with a CTE value between sapphire and metal. In our case, the thickness of Ti layer sputtered on sapphire can be increased for this purpose, as soon as Ti has CTE value between copper and sapphire (Table 5.18).

**Figure 5.40: S-3, S-4, S-5. Brazed D13 sapphires with Mo film sputtered to copper.**

5.2.2.2 Study of synthetic diamonds vacuum brazing

5.2.2.2.1 Brazing diamond powders to metal

For the preliminary study of synthetic diamonds brazing procedure Ti-coated commercial diamond powders and $\varnothing 28 \times 5$ mm stainless steel 304 discs were used.

The filler metals used in current study are listed in the Table 5.27. All the fillers belong to active brazing alloys (ABA) and theoretically allow brazing also non-metalized ceramics. The expected brazing temperatures for fillers are listed in the Table 5.27. It should be noticed that from a theoretical point of view, the same filler metals could be used for the system copper-synthetic diamond.

Table 5.27 Content of fillers used for sunthetic diamond brazing

<i>Brazing Filler</i>	<i>Form</i>	<i>Manufacturer</i>	<i>Composition</i>			<i>Brazing temperature</i>
TiFlo 950	Paste	Johnson Matthey	Ti-70%	Cu-15%	Ni-15%	940°C
NiCuSil-3	Paste	Homemade	Ag-71%	Cu-28%	Ni-1%	840°C
TiCuSil	Paste	Homemade	Ag-68.8%	Cu-26.7%	Ti-4.5%	850-900°C
CuSil	Paste	Homemade	Ag-63%	Cu-35.3%	Ti-1.7%	780°C
CuSil ABA	Paste	Homemade	Ag-63%	Cu-35.3%	Ti-1.7%	850-950°C
CuTiSn ABA	Paste	Homemade	Cu-75	Sn-25	Ti-10	850-950°C

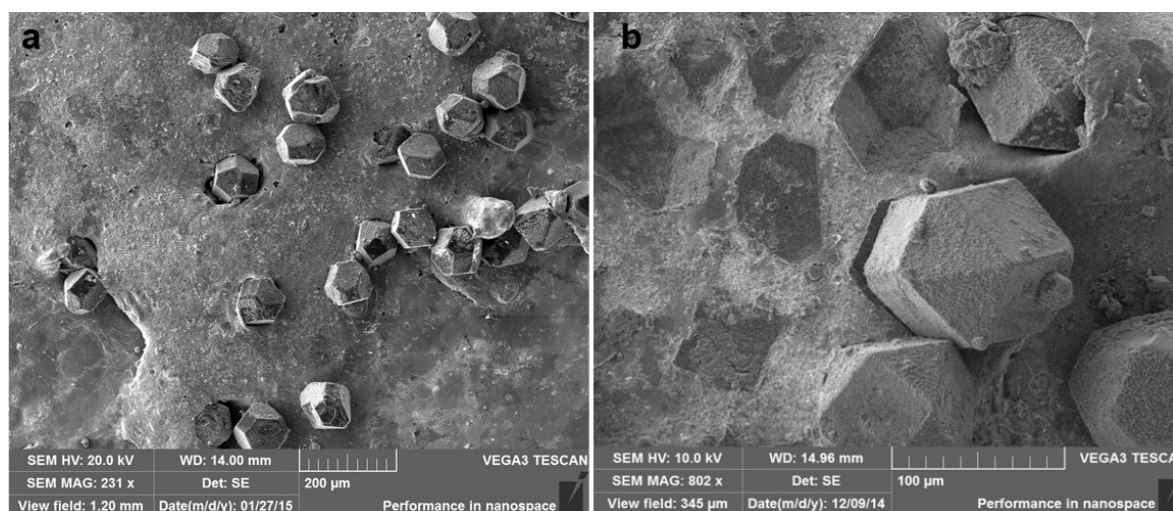
The set of brazing experiments with diamond powders and their results is presented in the Table 5.28. The experiment included the preparation of the proper composition of the brazing paste starting from commercially available metallic powders and binder material, than adding diamond powders to the mixture, application onto a metal substrate and proper thermal cycling in vacuum. Glycerine and ethanol were tested as binder materials for the paste, but ethanol did not provide the necessary viscosity and glycerine resulted some oxidation on the external boundary of the sample. The Coccoina[®] glue appeared to be the best binder.

The real brazing temperatures are listed in the Table 5.28 for each experiment. The brazing heating cycles included two preheating soaks: for 1 h at 400°C (to decompose the organic phase in paste) and second one at 750°C for 30min. The brazing soak time is also listed in the Table 5.28, as one of the parameters of the process.

Table 5.28 Experiments on brazing synthetic diamond powders to metal

<i>Experiment</i>	<i>Filler</i>	<i>Ti on diamonds</i>	<i>Brazing soak</i>	<i>Results</i>
Dp-1	TiFlo 950	yes	1140 ^o C, 30 min	The brazing temperature was too high for our purpose. High level of oxidation. Diamonds were easily detached mechanically
Dp-2	NiCuSil-3	yes	870 ^o C, 10 min	Main part of diamonds were not attached at all
Dp-3	TiCuSil	yes	980 ^o C, 10 min	The diamonds were well attached mechanically to metal substrate. Some oxidation on the boundary of the sample occurred due to glyceine.
Dp-4	TiCuSil	yes	970 ^o C, 10 min	The diamonds were well attached mechanically to metal substrate. No oxidation.
Dp-5	CuSil	yes	900 ^o C, 20 min	The diamonds were not well attached to metal substrate. It was possible to detach diamond powders.
Dp-6	CuSil ABA	yes	940 ^o C, 20 min	Diamond powders were attached well, can't be easily removed mechanically
Dp-7	CuSil ABA	yes	940 ^o C, 15 min	Diamond powders were attached well, can't be easily removed mechanically
Dp-8	CuSil ABA	no	940 ^o C, 15 min	Diamond powders were attached well, can't be easily removed mechanically
Dp-9	CuTiSn	no	980 ^o C, 17 min	Diamond powders were totally covered by brazant. Too short brazing time for such filler. No oxidation occurred.
Dp-10	CuTiSn	yes	985 ^o C, 23 min	Diamond powders were attached, patially covered by brazant. No oxidation occurred.

The only commercial paste TiFlo 950 used for the experiment did not show good results. The Ti-coated diamonds were not attached well after brazing with TiFlo (Dp-1). The reason supposed to be high level of oxidation (up to 50% atomic!), noticed from the EDS analysis.

**Figure 5.41: SEM of Ti coated diamond powders brazing by NiCuSil-3 Dp-2 (a) and CuSil Dp-6 (b)**

The use of Ni-containing NiCuSil-3 brazing filler (Dp-2) showed bed attachment of the diamonds to substrate, explained by big gaps observed with SEM (see Figure 5.41a) attributed to low wettability of the Ti-coated diamond by the molten filler.

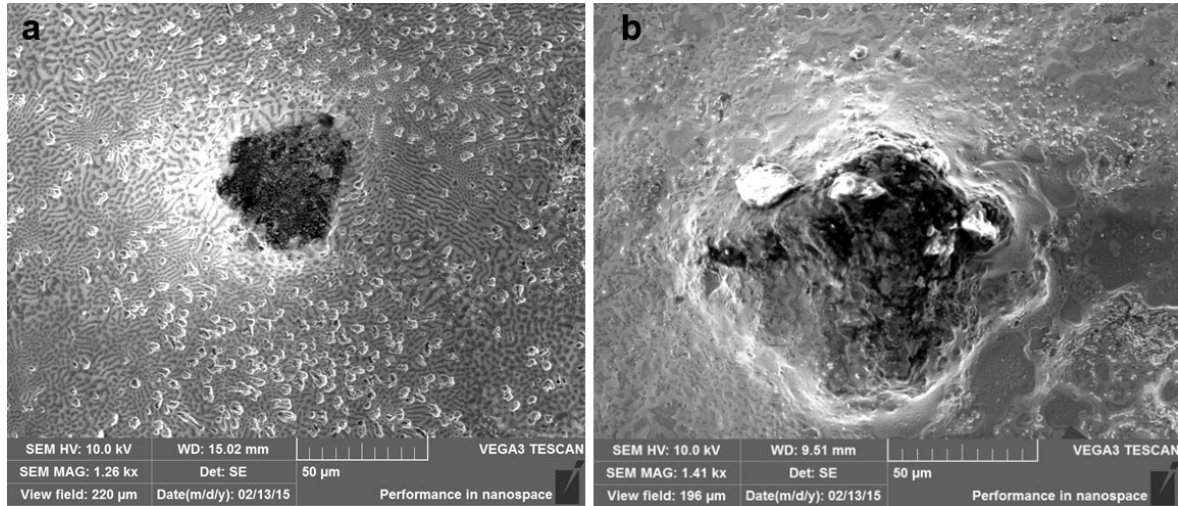


Figure 5.42: SEM of Ti coated diamond powders brazing with TiCuSil: a) Dp-3, b) Dp-4.

Instead, fillers, containing Cu, Ag, and Ti in different ratio (TiCuSil, CuSil ABA) wet well the Ti-coated diamond powders (Figure 5.42, Figure 5.43) and, as a result, provided good mechanical contact between diamonds and metallic substrate.

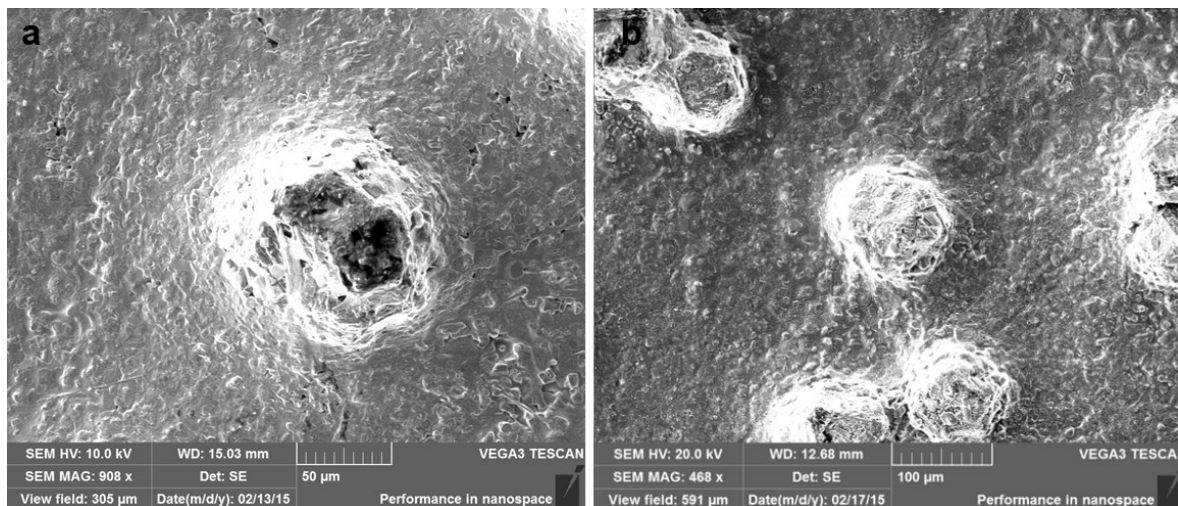


Figure 5.43: SEM of Ti coated diamond powders brazing with CuSil ABA: a) Dp-5, b) Dp-6.

It should be noticed that even for Ti-coated diamond use of an active-brazing filler, as CuSil ABA was found more effective, than non-active CuSil (see Figure 5.41b).

CuSnTi appeared to be another efficient system. The analysis of Ti-coated diamond powders brazed with homemade CuSnTi is showed in the Figure 5.44. The diamonds were wet by filler that provided good attachment of the diamond to metallic substrate.

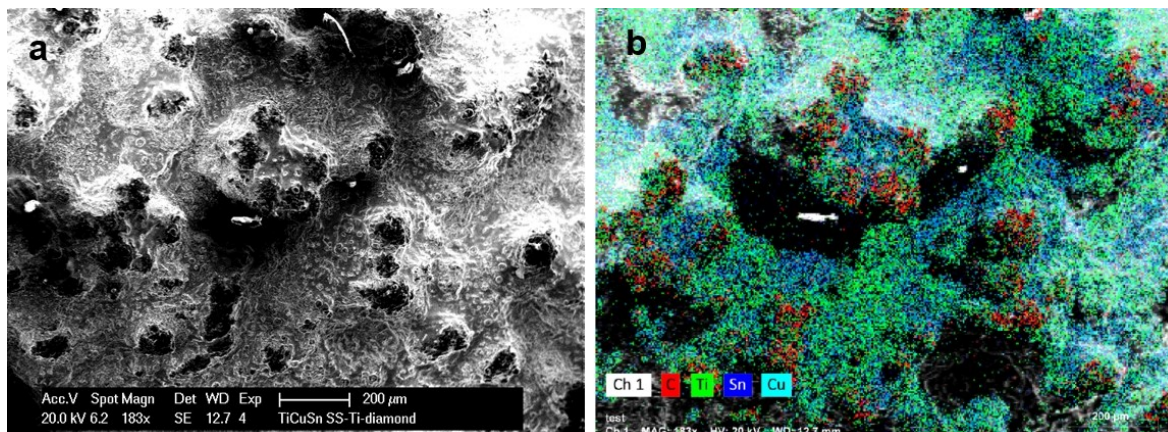


Figure 5.44: SEM (a) and EDS (b) analysis of Ti coated diamond powders brazing with CuSnTi.

Thus, the candidates for vacuum brazing diamond plate to copper for cyclotron target prototype preparation included the next filler materials: TiCuSiI, CuSiI ABA and CuSnTi ABA. All of them provided good mechanical contact and good wettability of diamond powders by molten filler. The CuSiI ABA was chosen for following experiments due to its lower brazing temperature. This aspect is important to minimize the stress induced in the joint after cooling due to the difference of CTEs of diamond and copper. Even if in preliminary experiments not coated diamonds have shown good results in brazing with CuSiI ABA (Dp-8) and CuSnTi (Dp-9), for the disc shape brazing diamond was supposed always to pre-deposit Ti, not only to improve adherence, but also in order to minimize stress.

5.2.2.2.2 Preparation of diamond-based composites

Diamond-metal composite materials are well-known of their elevated thermal conductivity. For the future prototype of high cyclotron power target for radiopharmaceuticals production the use of high thermal conductivity composite material for backing plate can be one of opportunities to increase the heat dissipation level. Following the success in vacuum brazing of diamond powders described in previous chapters, the idea to prepare a homemade diamond-based composite material arised.

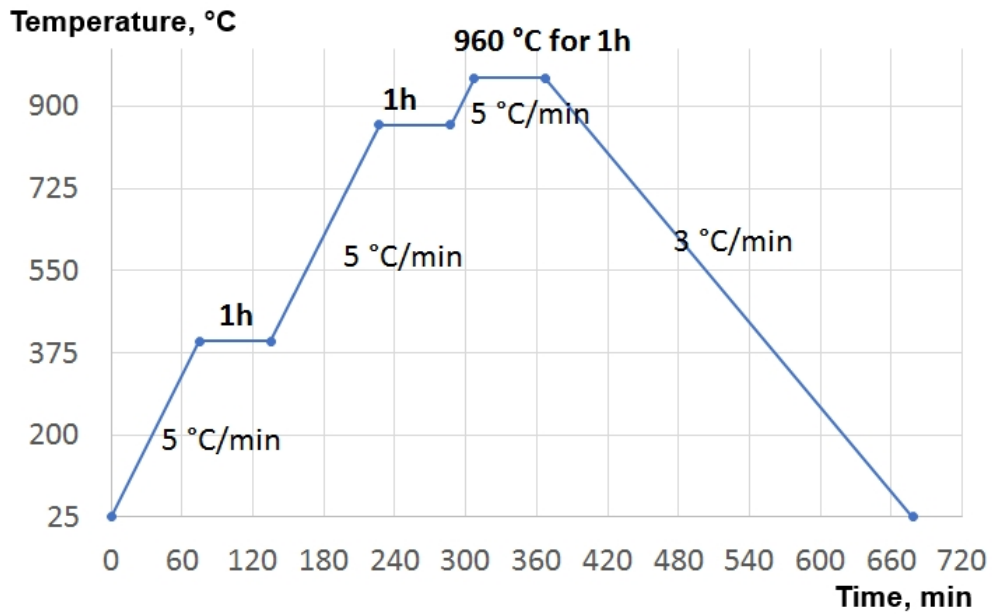


Figure 5.45: Thermal cycle for preparing diamond-metal composite material.

The experiment included the preparation of a mixture of equal masses of copper powders, silver powders and the Ti-coated diamond powders inside the Turbula mixing machine, adding a minimal amount of binder (Coccoina[®] glue), in order to remove the air stored between the powders, and make a compact material. The obtained paste was placed in the form (stamp) realized in sintered graphite and treated in vacuum with a particular thermal cycle showed in the Figure 5.45.

A piece of the obtained composite material was cut by electro erosion in order to analyse the microstructure of the material cross-section. The cross-section analysis with SEM-EDS (Figure 5.46) showed that diamonds were distributed uniformly in the metal alloy.

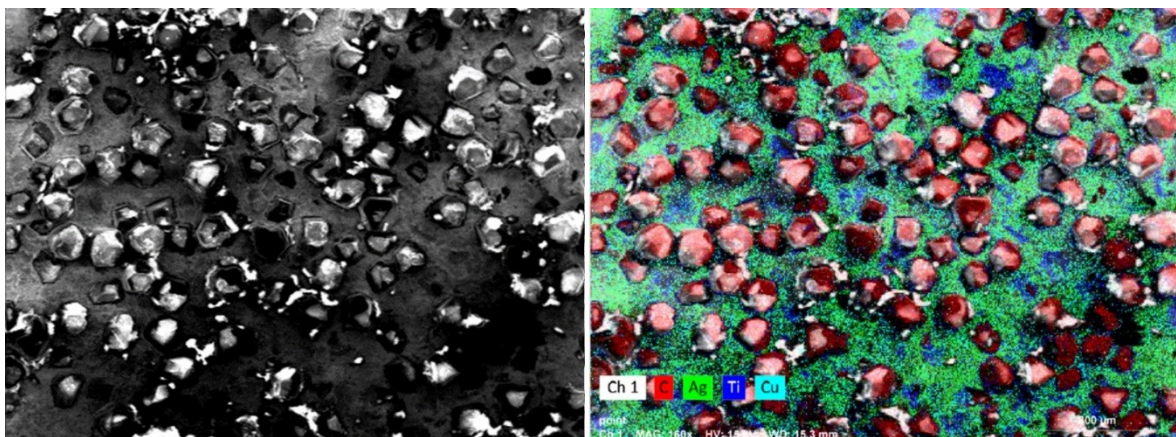


Figure 5.46: SEM (a) and EDS (b) analysis of Cu-Ag- diamond composite cross-section.

In order to roughly estimate the thermal conductivity of obtained composite material, a simple set-up was built. The experiment was realized in vacuum at $3 \cdot 10^{-5}$ mbar. IR lamp was used as a heating source. Boron nitride BN (thermal insulator) was used as a shield to minimize heat losses. The temperatures at the beginning T_1 and at the end T_2 of the bar of material with cross-section S were detected by K-type thermocouples. The distance between thermocouples was L . The experimental set-up is shown in the Figure 5.44.

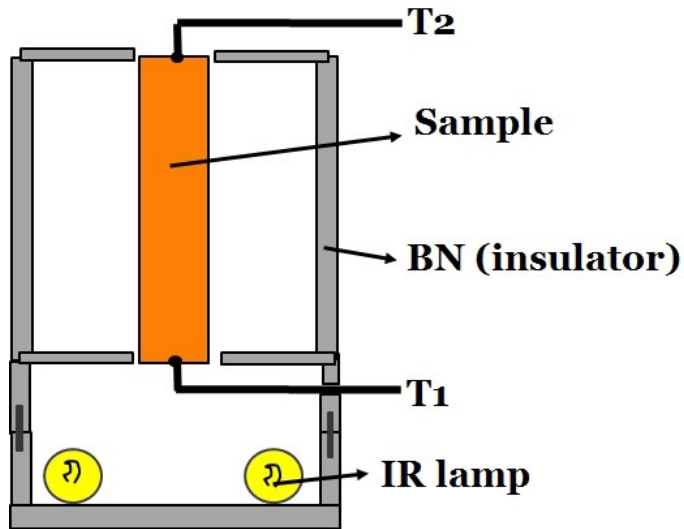


Figure 5.47: Experimental set-up for measurement of relative thermal conductivity

The amount of heat Q passing through the area S can be described as:

$$\frac{Q}{S} = K \cdot \frac{(T_1 - T_2)}{L} \quad (5.5),$$

where K is the thermal conductivity of the material.

Considering the heat Q constant (at particular voltage set up by Variac powering the lamp) and realizing two experiments with researched material and material with known thermal conductivity, the ratio (or relative thermal conductivity) can be found.

$$Q = K \cdot S \cdot \frac{(T_1 - T_2)}{L} = const \quad (5.6),$$

The geometrical measurements of the bars were realized with micrometer. The main parameters are listed in the Table 5.29.

$$K_{Cu} \cdot S_{Cu} \cdot \frac{\Delta T_{Cu}}{L_{Cu}} = K_X \cdot S_X \cdot \frac{\Delta T_X}{L_X} \quad (5.7)$$

Table 5.29 Thermal conductivity measurement.

Material	Copper	CuAgDia composite	Aluminum
S, mm ²	7.3386	7.1424	4.5216
L, mm	29	25	30
T ₁ , °C	200	200	200
T ₂ , °C	178	154	140
ΔT	22	46	60
Thermal conductivity, W·/(m·K)	386	X	249

The relative thermal conductivity of copper-silver-diamond composite material is:

$$\frac{K_X}{K_{Cu}} = \frac{\Delta T_{Cu}}{L_{Cu}} \cdot \frac{L_X}{\Delta T_X} \cdot \frac{S_{Cu}}{S_X} = \frac{22}{29} \cdot \frac{25}{46} \cdot \frac{7.3386}{7.1424} = 0.42 \quad (5.8)$$

In order to control the reliability of the system, the measurement was taken for a piece of pure aluminum. Relative thermal conductivity:

$$\frac{K_{Al}}{K_{Cu}} = \frac{\Delta T_{Cu}}{L_{Cu}} \cdot \frac{L_{Al}}{\Delta T_{Al}} \cdot \frac{S_{Cu}}{S_{Al}} = \frac{22}{29} \cdot \frac{30}{60} \cdot \frac{7.3386}{4.5216} = 0.62 \quad (5.9)$$

The ratio between thermal conductivities of copper and aluminum has been compared with theoretical (based on the literature data about thermal conductivities):

$$\frac{K_{Al}}{K_{Cu}} = \frac{249}{386} = 0.64 \quad (5.10)$$

The thermal conductivities for copper and aluminum vary a bit in different literature sources. The relative thermal conductivity estimation experiment was considered reliable.

Thus, the relative thermal conductivity of copper-silver-diamond composite is ~42% of thermal conductivity of copper. This result is not promising. The thermal conductivity of good diamond-metal composite should be at list higher than one of starting metal.

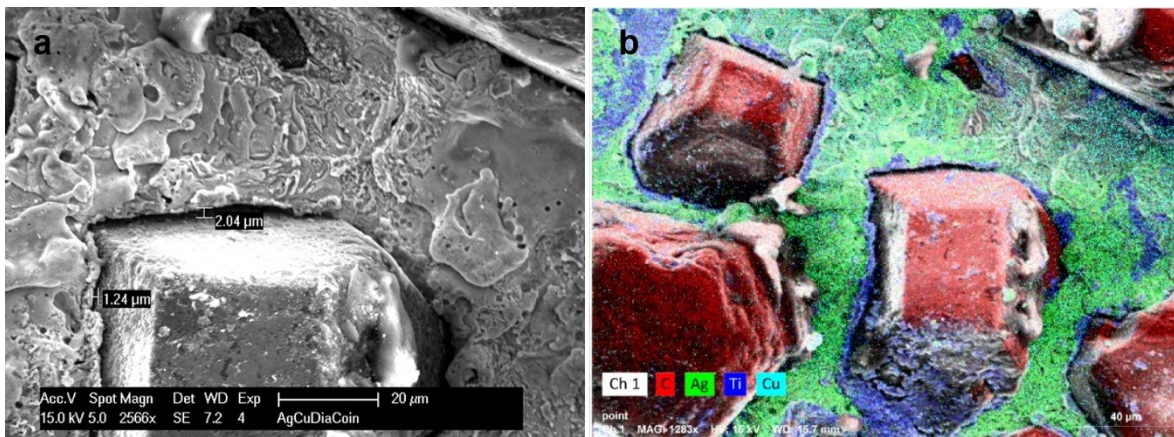


Figure 5.48: SEM (a) and EDS (b) analysis of CuAgDia composite cross-section.

The reason of such a poor result was found by SEM analysis at higher magnification (see Figure 5.48). It can be observed the presence of 1-2 μm gap between diamond and metal. From the EDS analysis (Figure 5.48b) is visible that the gap was not created between Ti and main bulk metal (copper-silver), but between diamond and titanium, that depends not only on the process performed, but mainly on the quality of Ti coating provided by diamond powders manufacturer.

It should be noted that in industry the diamond-metal composites are usually produced by hot isostatic pressing (HIP) equipment, allowing to minimize the gaps and any other kind of porosity during metal melting process.

5.2.2.2.3 Brazing diamond plate to copper (target prototypes)

Similar to sapphire-based low-energy cyclotron target prototypes, also the CVD synthetic diamond plates were used providing much higher thermal conductivity.

Diamond discs of 13 mm diameter and 0.3mm thickness were preliminary sputtered from one side with 1 μm Ti film (for brazing) and with >100 μm Mo from another side (as a target material). Then fresh homemade CuSil ABA paste, containing Cu 35.3%–Ag 63%–Ti 1.7% was prepared and placed between copper substrate and Ti coated diamond. The radial clearance between copper and diamond was increased in respect to copper-sapphire system, in order to minimize the stress related to difference of CTEs.

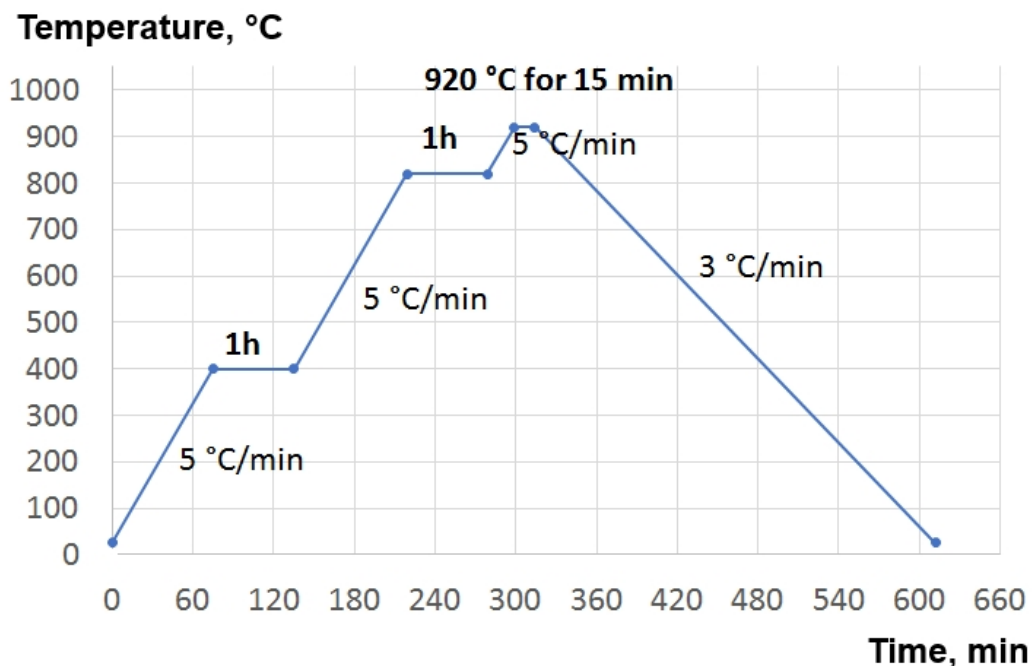


Figure 5.49: Thermal cycle for brazing diamond plate to copper with CuSil ABA paste.

The brazing thermal cycle is presented in the Figure 5.49. The main brazing process parameters and results of two experiments are shown in the Table 5.30.

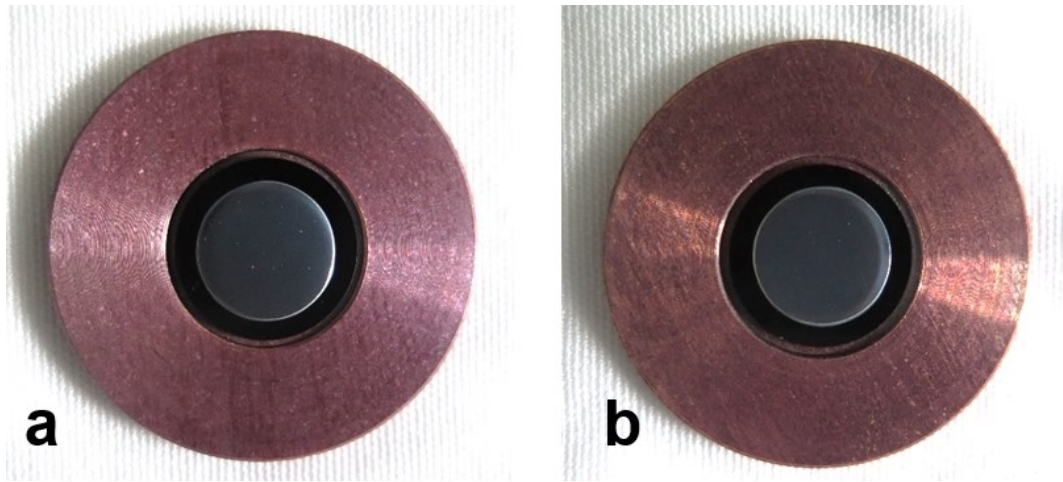


Figure 5.50: D-1(a) and D-2(b) diamond discs brazed to copper plate with CuSil ABA paste.

As it can be observed from the Figure 5.50, both 13mm diameter CVD diamond discs were integer and in a good mechanical contact with the copper.

Table 5.30 Brazing CVD diamon discs to copper for target prototype

<i>Exp.</i>	<i>Mo film</i>	<i>Sapphire part</i>	<i>Radial clearance</i>	<i>Ti sputtered layer on sapphire</i>	<i>Brazing soak</i>	<i>Results</i>
D-1	Mo-10.1	Ø13×0.3m	0.5mm	$1.6 \cdot 10^{-2}$ mbar, 5A, 1µm	920°C, 15 min	Good mechanical attachment of CVD diamond to copper. Diamond disc was integer
D-2	Mo-10.2	Ø13×0.3m	0.5mm	$1.6 \cdot 10^{-3}$ mbar, 5A, 1µm	920°C, 15 min	Good mechanical attachment of CVD diamond to copper. Diamond disc was integer

Produced target prototypes with diamond-copper composite plate were tested under the cyclotron proton beam. The results of the irradiation test are presented in the following chapter.

5.3 Irradiation tests by cyclotron

5.3.1 Mo sputtered target material

The irradiation tests were realized by the GE PET Trace cyclotron of “St. Orsola-Malpighi” Hospital, Bologna. The irradiations of the first sample: 110µm Mo-4 sputtered directly onto

the copper backing, were carried out for one minute, at 15.6 MeV and currents 30, 50, and 70 μA . The results of the irradiation were observed visually (see Figure 5.51), testing the integrity of the target and the attachment of the Mo film to the copper backing.

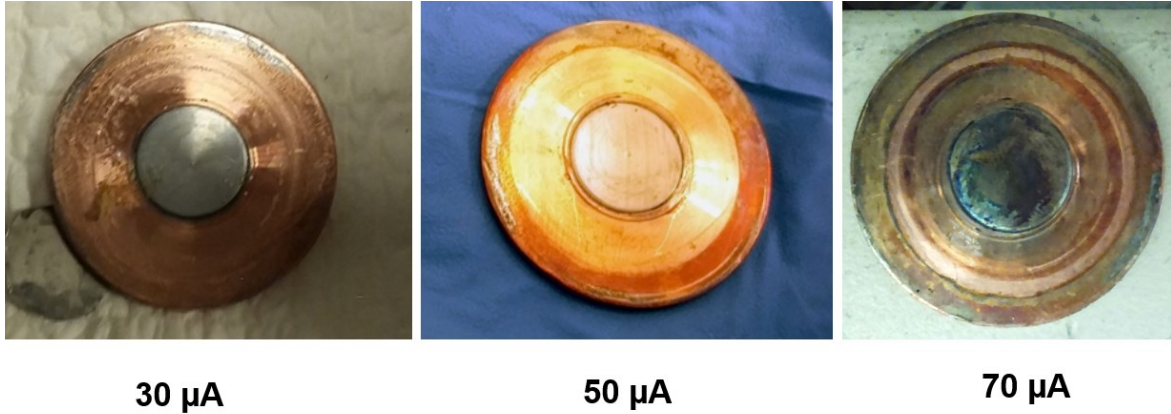


Figure 5.51: Cyclotron irradiation test of 110 μm Mo-4 sputtered onto copper.

Any sign of target damage was observed on Mo-4 sample. A surface oxidation both on Mo and Cu are evident on the photo after the 70 μA proton beam test. This is related to a previous leakage of a small amount of cooling water in the target system.

The sputtered Mo film (110 μm thick) can resist to the current up to 70 μA (15.6 MeV, >1 min), the maximum current that Sant'Orsola medical cyclotron was able to reach in the conditions set up for a medical production.

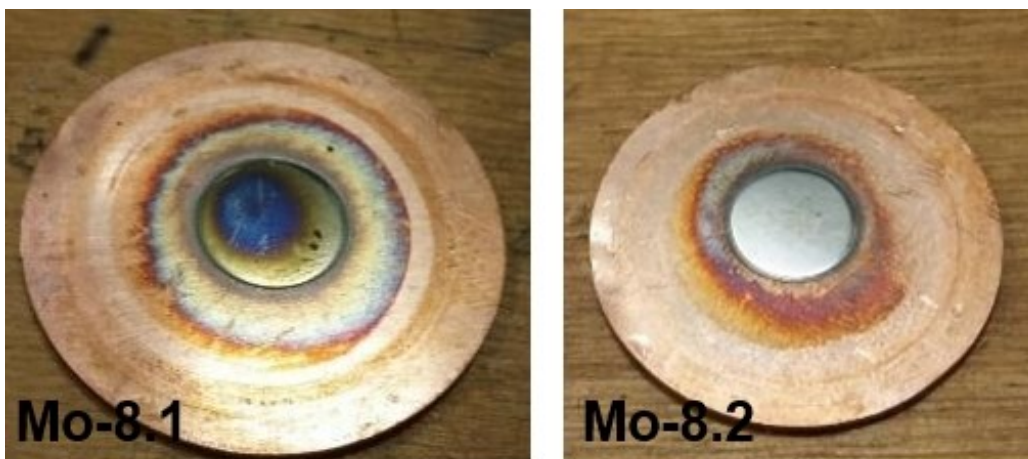


Figure 5.52: 125 μm Mo-8 samples sputtered onto copper $\varnothing 32$ after cyclotron irradiation test at 60 μA .

In order to show the reproducibility of the results another two targets 125 μm Mo sputtered on copper (sputtering experiments Mo-8.1 and Mo-8.2) were tested for 1 min under 15.6 MeV and 60 μA proton beam. Unfortunately, this was the maximum current that was possible to extract from the cyclotron. In all following experiments cyclotron was never able to provide 70 μA as in the first test. Two Mo sputtered on copper samples showed any damage, as it was expected (see Figure 5.52).

It should be noted that the maximum cyclotron current used for electrodeposited solid target (for example, 100 μm ^{64}Ni for ^{64}Cu production) is of the order of 25 μA . This proves that the performance of the sputtered target is significantly higher than that of the electrodeposited. Thus, the use of sputtering process for target preparation can improve more than twice the yields of the radiopharmaceutical production.

5.3.2 Advanced backing

5.3.2.1 Sapphire

5.3.2.1.1 Irradiation test

90 μm of natural Mo on sapphire coin (Mo-3 sputtering experiment) was placed inside the 4-pin clamping target holder for the cyclotron test. The irradiations were carried out for one minute, at 10 μA , 20 μA and 30 μA current. After each irradiation, the sample was unloaded and controlled visually.

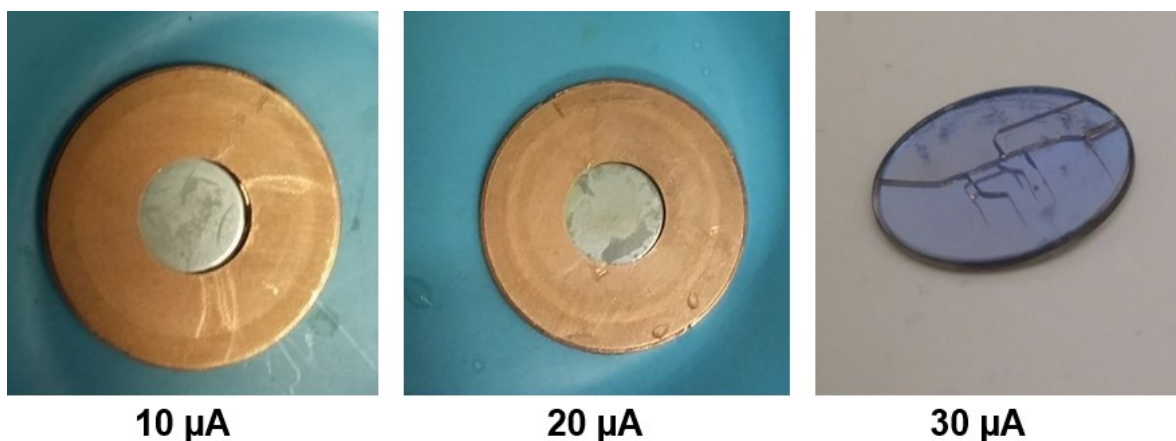


Figure 5.53: Mo-5 sputtered on sapphire after cyclotron irradiation test in 4-pin target-holder.

In the Figure 5.53 the target after each irradiation is shown: 90 μm Mo film sputtered on 0.5mm sapphire resisted under the beam current of 10 μA and 20 μA and the sapphire

remained integer (see Figure 5.53). Instead, at 30 μ A current sapphire-backing plate was cracked but the Mo film kept the pieces together, without evidence of delamination and oxidation. It is evident that the contact between sapphire and copper 4-pin holder was extremely poor.

5.3.2.1.2 Chemical inertness prove

The test of a chemical inertness of the sapphire backing, comprising dissolution followed by γ -spectroscopy analysis, was performed thanks to the Research Laboratory of “St. Orsola-Malpighi” Hospital Medical Physic Department (Bologna).

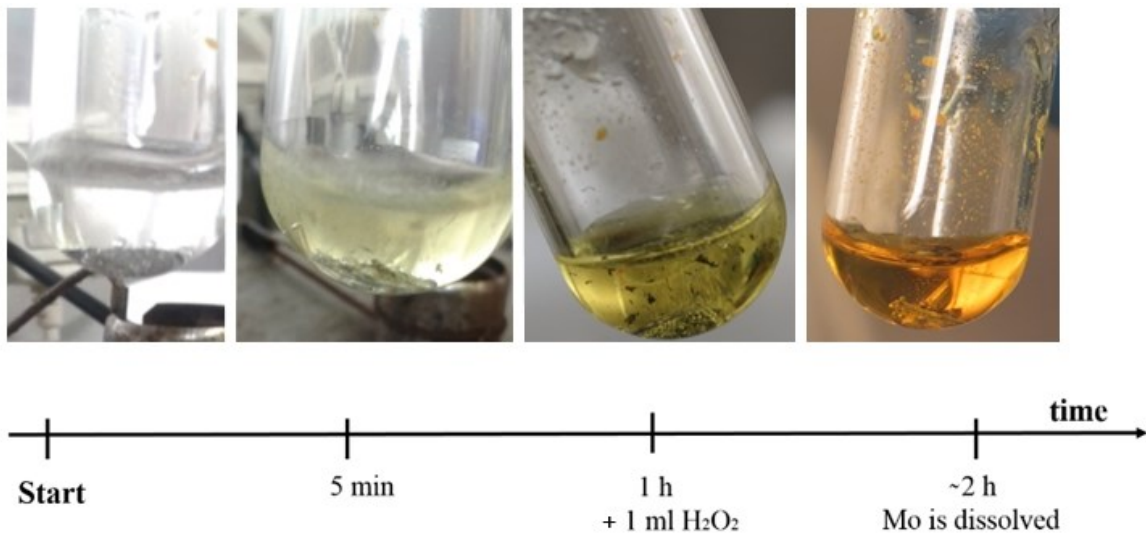


Figure 5.54: Dissolution test of irradiated Mo sputtered onto sapphire backing.

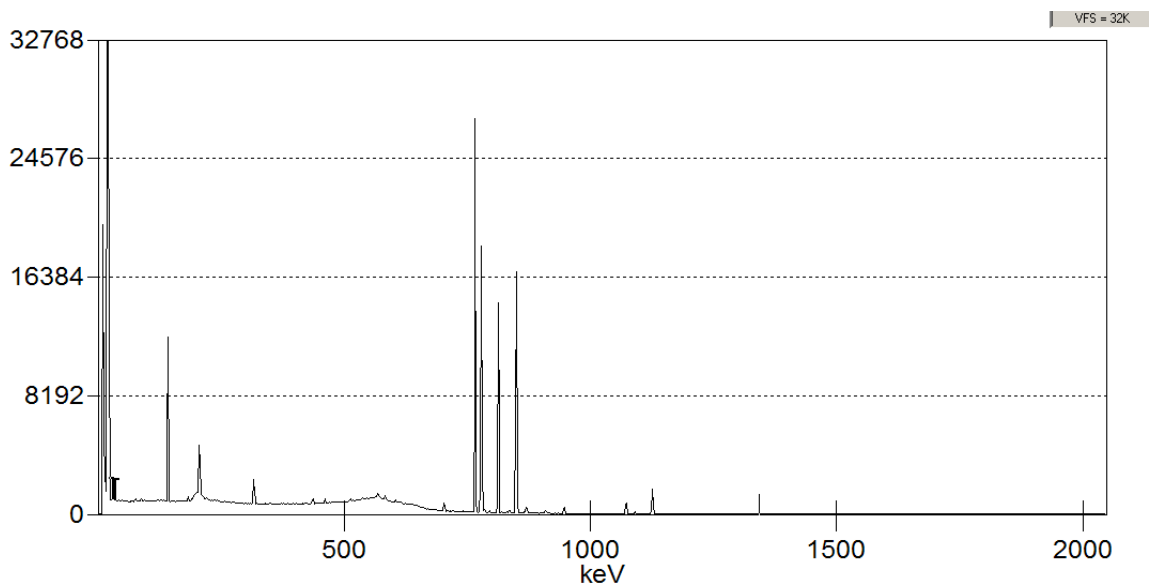


Figure 5.55: Gamma spectrum of proton irradiated ^{nat}Mo sputtered on sapphire.

A piece of irradiated target was used for a dissolution test, described in the Figure 5.54 followed by the γ -spectroscopy analysis in order to control if any impurities were released by the irradiated sapphire. 10 μ l of those solution were placed in the γ -spectrometer. The range of the γ -ray energy was 80–4096keV.

The γ -spectrum is shown in the Figure 5.55. According to the software, the peaks belonging to ^{92m}Nb , ^{94}Tc , ^{95}Tc , ^{95m}Tc , ^{96}Tc , ^{99}Mo , ^{99m}Tc were identified (see Table 5.31). All these radionuclides are the irradiation products of natural molybdenum. Indeed, ^{92m}Nb comes from the reaction $^{95}\text{Mo}(p,\alpha)$; all the other radionuclides are produced by a set of (p,xn) reactions starting from the natural molybdenum isotopes: ^{92}Mo , ^{94}Mo , ^{95}Mo , ^{96}Mo , ^{97}Mo , ^{98}Mo , ^{100}Mo [104, 105].

Table 5.31 Gamma spectrum analysis of proton-irradiated Mo sputtered sapphire

Tipo di Campione:		Campione Mo naturale			
Libreria di Nuclidi usata:		C:\GENIE2K\CAMFILES\Mo_decay_corr_no96Tc			
..... IDENTIFIED NUCLIDES					
Nuclide Name	Id Confidence	Energy (keV)	Yield (%)	Activity (Bq / .)	Activity Uncertainty
NB-92m	0.998	912.73	1.78		
		934.46*	99.00	2.841E+001	5.460E+000
TC-94	0.902	449.20	3.30		
		532.10	2.35		
		702.62*	99.60	3.680E+003	3.097E+002
		742.30	1.21		
		849.74*	95.70	1.511E+005	7.862E+003
TC-95	0.992	871.09*	100.00	4.568E+003	2.654E+002
		916.10	7.60		
		1592.10*	2.25	3.855E+004	5.607E+003
		765.79*	93.82	1.944E+004	8.073E+002
		947.67*	1.95	1.816E+004	1.224E+003
		1073.71*	3.74	2.017E+004	1.095E+003
		204.12*	63.25	2.887E+002	1.729E+001
TC-95m	0.999	582.08*	29.96	2.620E+002	5.110E+001
		616.49	1.28		
		786.20	8.66		
		820.62*	4.71	2.798E+002	1.011E+002
		835.15*	26.63	2.365E+002	1.991E+001
TC-96	0.985	1039.26	2.78		
		314.34*	2.43	1.149E+004	1.503E+003
		316.27	1.40		
		778.22*	100.00	6.895E+003	2.845E+002
		812.58*	82.00	6.923E+003	5.295E+002
		849.93*	98.00	7.121E+003	4.913E+002
		1091.35*	1.10	7.174E+003	8.664E+002
MO-99	0.981	1126.96*	15.20	6.871E+003	7.324E+002
		40.58	1.05		
		140.51*	89.43	5.822E+002	2.816E+001
		181.06*	5.99	2.552E+002	6.997E+001
		366.42	1.19		
TC-99m	0.936	739.50*	12.13	2.212E+002	6.796E+001
		777.92*	4.26	1.761E+005	7.909E+003
		140.51*	89.00	3.968E+003	5.495E+002

* = Energy line found in the spectrum.

Therefore, any contaminant radionuclides, coming from the sapphire backing, were present in the solution. This fact proves the chemical inertness of sapphire.

5.3.2.2 CVD Diamond

The thermal grade CVD diamond \varnothing 13.5mm and 0.3 mm thick with thermal conductivity 1500W/(m·K) was tested under the 15.6MeV 20 μ A cyclotron accelerated proton beam for 1 min inside the 4-pin clamping target-holder (see Figure 5.56).



Figure 5.56: CVD synthetic diamond irradiation test in 4-pin clamping target-holder.

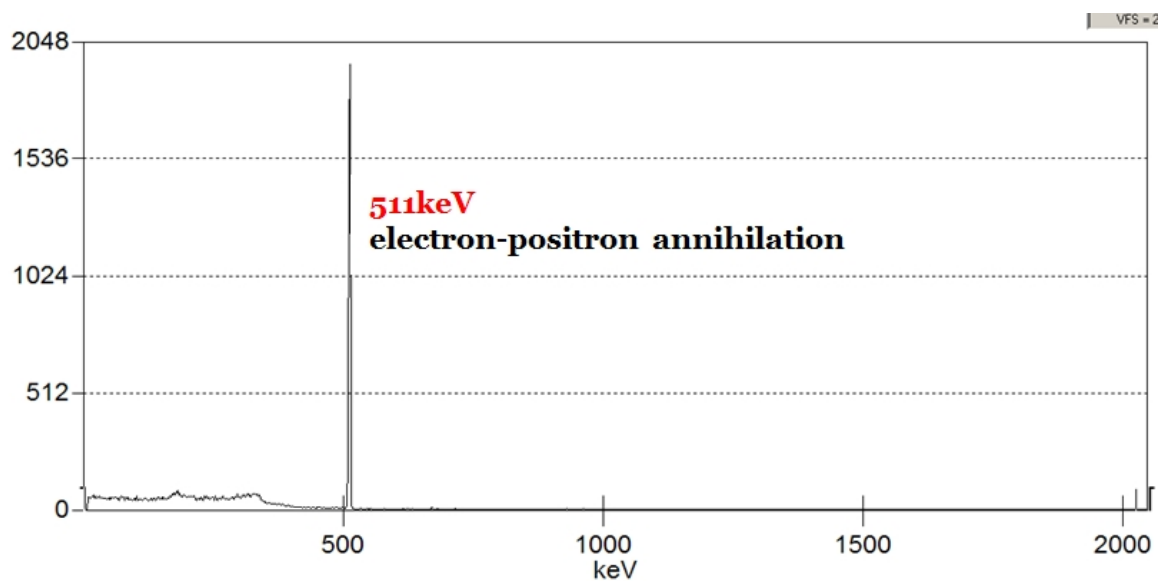


Figure 5.57: Gamma spectrum of proton irradiated CVD synthetic diamond disc.

After irradiation the synthetic diamond piece was placed into H₂O₂ concentrated. Any change of the mass was observed in respect to the mass of the diamond before dissolution. Then the piece of synthetic diamond was used for the γ -spectroscopy analysis to identify the elements created inside the diamond piece under irradiation. The γ -spectrum shown in the Figure 5.57 contains only one peak of 511keV. The 511keV is the energy of the photons coming from the electron-positron annihilation. Thus, the radioactive isotope, produced in the synthetic diamond during the proton irradiation was a positron emitter.

Table 5.32 Decay curve data of irradiated diamond obtained with dose-calibrator.

Time, min	Activity, μ Ci	% activity	Time, min	Activity, μ Ci	% activity
0.0	22.1	100	12.5	9.4	42.53
0.5	21.6	97.74	13.0	9.1	41.18
1.0	20.8	94.12	13.5	8.7	39.37
1.5	19.9	90.05	14.0	8.3	37.56
2.0	19.2	86.88	14.5	8.2	37.10
2.5	18.7	84.62	15.0	7.8	35.29
3.0	18.2	82.35	15.5	7.5	33.94
3.5	17.5	79.19	16.0	7.3	33.03
4.0	16.8	76.02	16.5	7	31.67
4.5	16.2	73.30	17.0	6.7	30.32
5.0	15.5	70.14	17.5	6.5	29.41
5.5	15.3	69.23	18.0	6.4	28.96
6.0	14.8	66.97	18.5	6.2	28.05
6.5	14.3	64.71	19.0	5.9	26.70
7.0	13.9	62.90	19.5	5.7	25.79
7.5	13.4	60.63	20.0	5.6	25.34
8.0	12.8	57.92	20.5	5.4	24.43
8.5	12.2	55.20	21.0	5.3	23.98
9.0	11.9	53.85	21.5	5	22.62
9.5	11.4	51.58	22.0	4.8	21.72
10.0	11.1	50.23	22.5	4.6	20.81
10.5	10.5	47.51	23.0	4.6	20.81
11.0	10.3	46.61	23.5	4.4	19.91
11.5	10	45.25	24.0	4.2	19.00
12.0	9.7	43.89	24.5	4.1	18.55

The only suitable radioisotope is ¹³N decaying to ¹³C, emitting a positron. In order to prove that fact, the activity from the sample was measured with the dose-calibrator versus time (Table 5.32) to build a decay curve.

The graph representing the % of starting activity versus time (Figure 5.58) shows very evident, that the time, corresponding to the moment, when 50% of activity left, is 10 min. It means that $T_{1/2}=10$ min. The radioisotope produced in CVD synthetic diamond was ¹³N.

No other products, besides ¹³N, were detected in CVD synthetic diamond plate after 15.6MeV proton beam irradiation. It can be said that synthetic diamond plate does not release any foreign radionuclides after irradiation according to γ -spectroscopy.

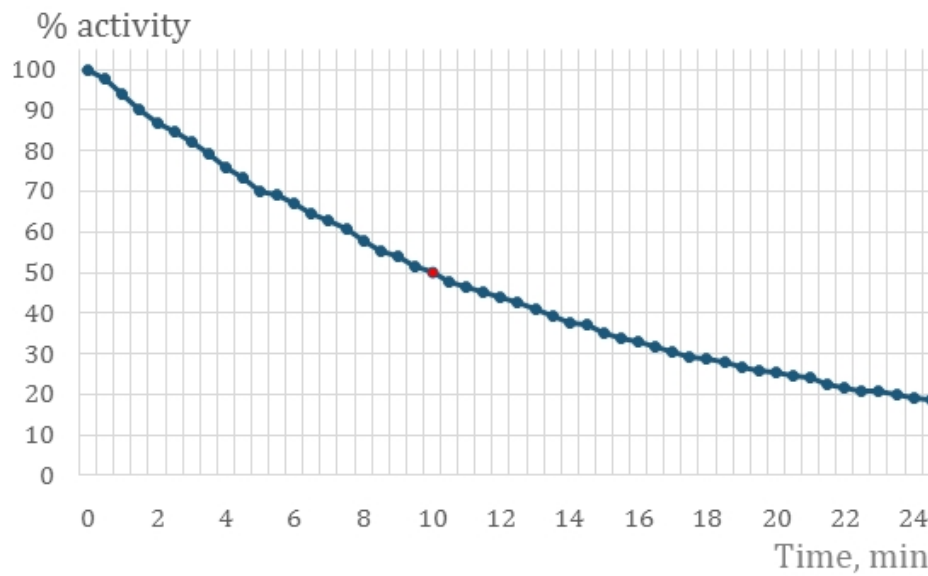


Figure 5.58: Gamma spectrum of proton irradiated CVD synthetic diamond disc.

5.3.2.3 Sapphire brazed to metal

As it was seen from the irradiation experiment of Mo sputtered sapphire inside 4-pin clamping target-holder, better contact is absolutely needed in order to perform the production at higher proton beam currents.

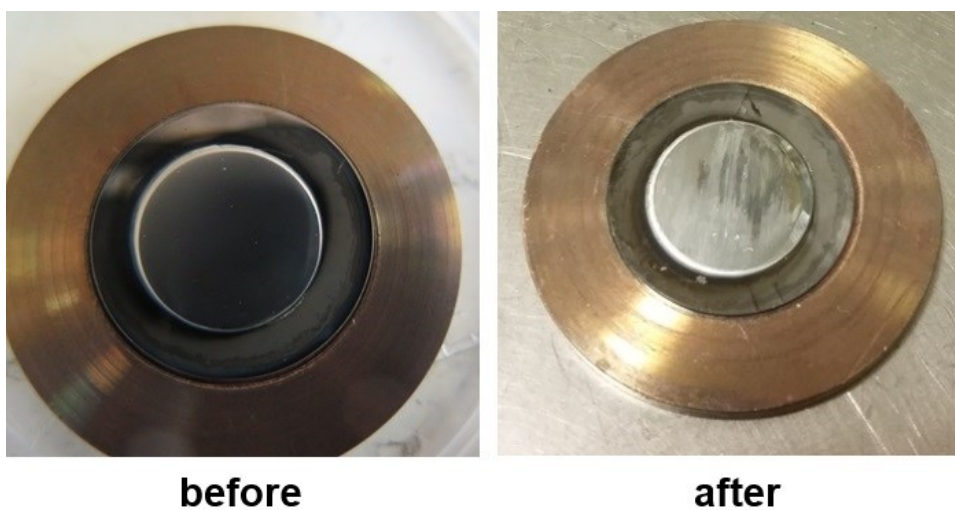


Figure 5.59: Cyclotron irradiation test of S-1 sapphire-based prototype at 40 μ A.

The S-1 prototype contained 110 μm Mo (Mo-6) sputtered onto 19mm diameter 0.5mm thick sapphire, brazed to copper with CuSil ABA filler. S-1 sample was tested directly under 40 μA at 15.6MeV for 1 min. The Figure 5.59 shows the sample S-1 after the irradiation. As can be seen, the sapphire piece was cracked.

The reason of such instability is the difference of CTEs of sapphire and copper, crucial for brazed joint. It is as more critical, as bigger is the area of joint.

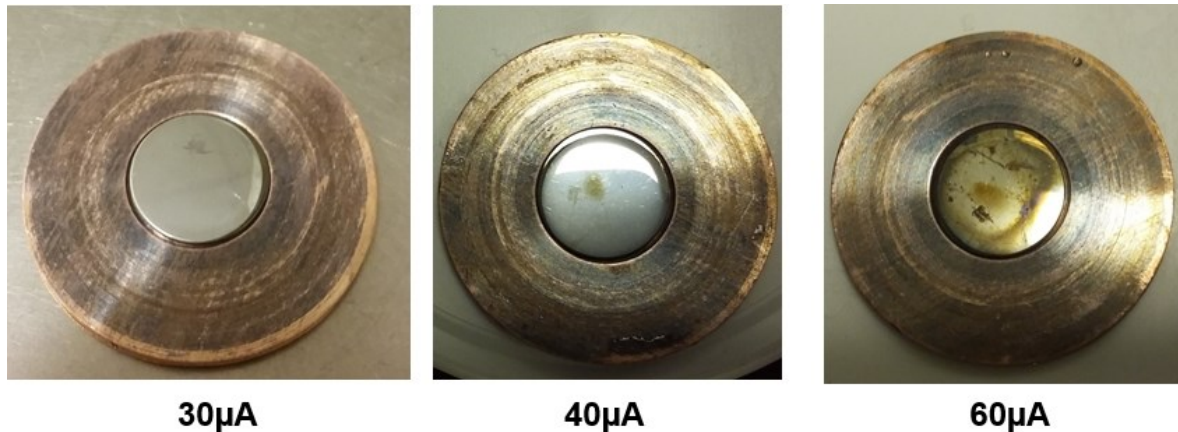


Figure 5.60: Cyclotron irradiation test of S-3 sapphire-based prototype.

The next prototype S-3 contained, instead, 12.7mm diameter sapphire, was tested in several steps by increasing the current in each following run: at 30 μA , at 40 μA and finally at maximum current of the cyclotron 60 μA , always at maximum beam energy 15.6MeV. Each irradiation test lasted for 1 min. The Figure 5.60 shows the sample after each irradiation. Any cracking of sapphire piece occurred.

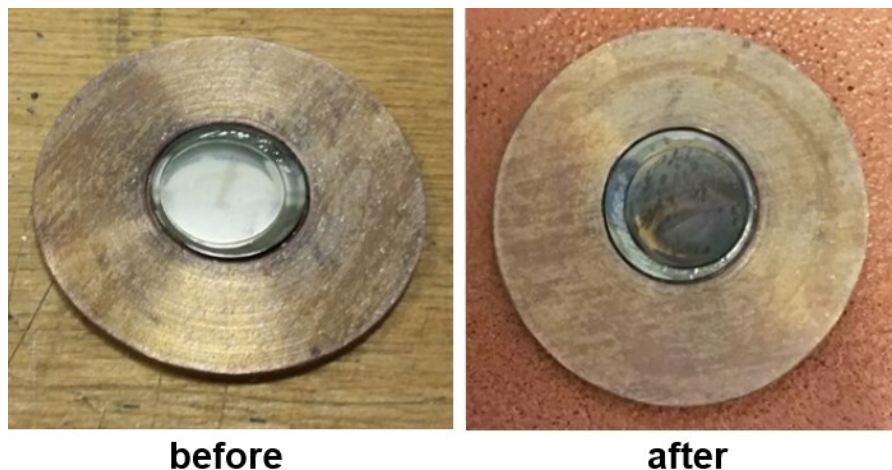


Figure 5.61: Cyclotron irradiation test of S-4 sapphire-based prototype at 60 μA .

The prototypes S-4 and S-5 based also on 12.7mm diameter sapphire were tested under the maximum current $60\mu\text{A}$, 15.6MeV for 1 minute. The Figure 5.61 and Figure 5.62 show the prototypes after the irradiation tests. The systems resisted to the proton beam irradiation. It should be noted that, when the time passed between the prototype S-4 preparation and irradiation test, a kind of defect between sapphire and brazing filler occurred (Figure 5.61). It seems to be a problem of the Ti sputtered film before the brazing process of the sapphire. For the following preparation of diamond-based prototypes the parameters of Ti sputtering were optimized and additional attention was paid to substrate cleaning procedures, in order to avoid such a problem.

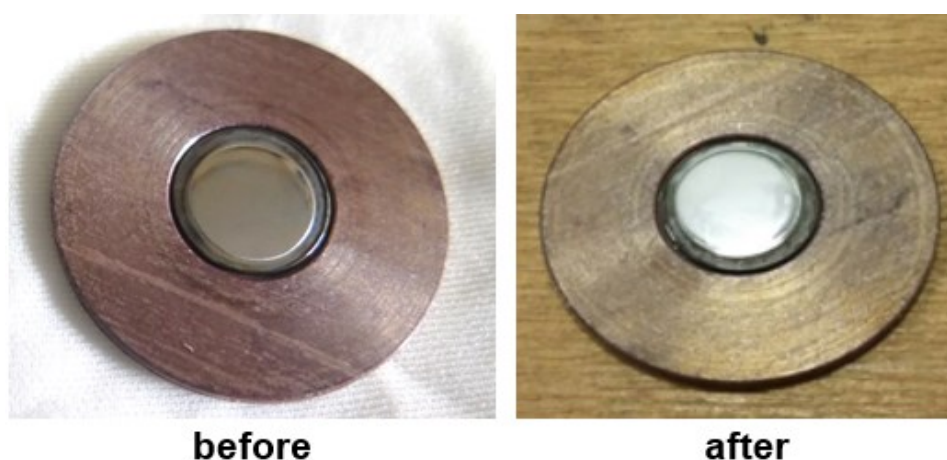


Figure 5.62: Cyclotron irradiation test of S-5 sapphire-based prototype at $60\mu\text{A}$.

All the results of the irradiation tests of the ceramics-containing target prototypes: both sapphire-based and CVD synthetic diamond-based are summarized in the Table 5.33.

Table 5.33 Tests of novel target prototype: ceramics-metal composite baseplate.

<i>Prototype name</i>	<i>Brazing exp-t</i>	<i>Ceramic (inert) part</i>	<i>Ceramics dimensions</i>	<i>Sputtering exp-t</i>	<i>Mo film thickness</i>	<i>Irradiation test results</i>
S-1	S-1	sapphire	$\varnothing 19.05 \times 0.5\text{mm}$	Mo-6	$110\mu\text{m}$	$40\mu\text{A}$, sapphire cracked
S-3	S-3	sapphire	$\varnothing 12.7 \times 0.5\text{mm}$	Mo-5	$110\mu\text{m}$	$30, 40, 60\mu\text{A}$, resisted
S-4	S-4	sapphire	$\varnothing 12.7 \times 0.5\text{mm}$	Mo-9.1	$125\mu\text{m}$	$60\mu\text{A}$, resisted
S-5	S-5	sapphire	$\varnothing 12.7 \times 0.5\text{mm}$	Mo-9.2	$125\mu\text{m}$	$60\mu\text{A}$, resisted
D-1	D-1	diamond	$\varnothing 13 \times 0.3\text{mm}$	Mo-10.1	$125\mu\text{m}$	$20, 40, 60\mu\text{A}$, resisted
D-2	D-2	diamond	$\varnothing 13 \times 0.3\text{mm}$	Mo-10.2	$125\mu\text{m}$	$60\mu\text{A}$, 30 min, resisted

5.3.2.4 CVD diamond brazed to metal

The first CVD synthetic diamond-based prototype D-1 was tested in several steps by increasing the current in each following run: at 20 μA , at 40 μA and finally at maximum current of the cyclotron 60 μA . Maximum entrance beam energy 15.6MeV was used. Each irradiation test lasted for 1 min.

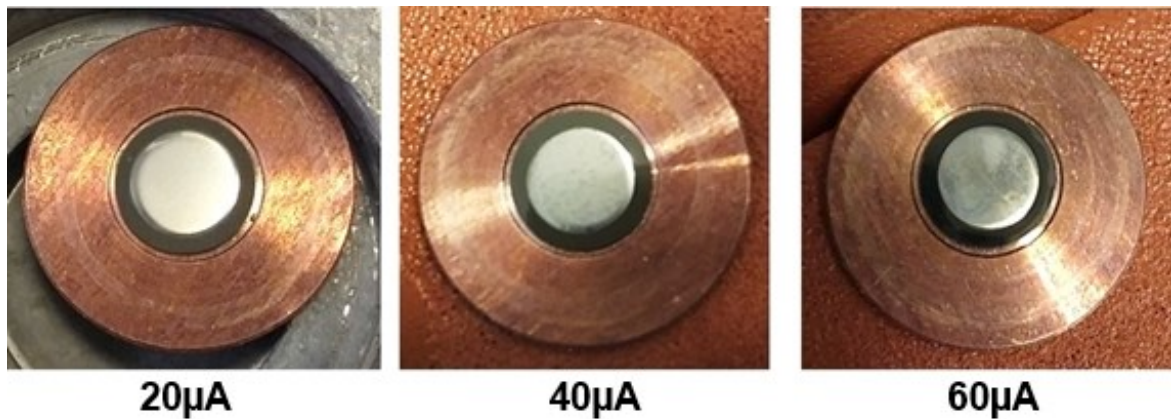


Figure 5.63: Cyclotron irradiation test of D-1 synthetic diamond-based prototype.

The Figure 5.63 shows the sample after each irradiation. Any cracking or oxidation of the target prototype occurred during irradiation.

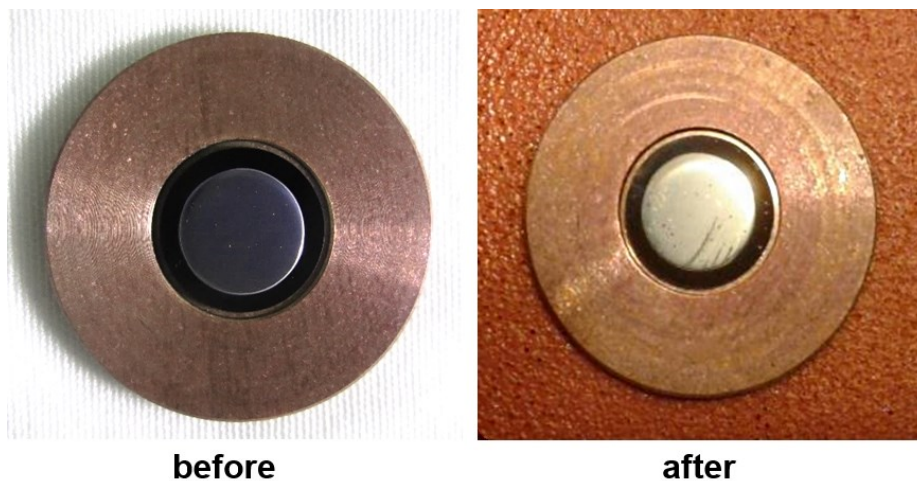


Figure 5.64: 30min cyclotron irradiation test of D-2 C synthetic diamond-based prototype at 60 μA .

One irradiation test on the D-2 CVD synthetic diamond-based prototype was performed in conditions more close to production case. The irradiation was done for 30 min at 60 μA and

15.6MeV. Similar to the first diamond-based prototype, the second one showed excellent performance during the long-irradiation test without any signs of damage (Figure 5.64).

It is possible to say that new cyclotron target prototype comprised ^{nat}Mo sputtered on synthetic diamond, brazed to Cu backing gave excellent results from the thermomechanical point of view.

5.4 Development of recovery procedure for Mo powders

The full cycle of ^{100}Mo in the cyclotron-based production of ^{99m}Tc include: preparation of a ^{100}Mo target, irradiation of the target under the proton beam, dissolution of ^{100}Mo and produced by nuclear reaction ^{99m}Tc in the concentrated H_2O_2 solution, separation of Tc and Mo by the separation module. After ^{100}Mo is coming as the waste from the separation module. In order to make the accelerator-based method to produce ^{99m}Tc economically attractive, expensive ^{100}Mo should be recovered from the waste and reused again for the target preparation. The first step of such recovery is transformation of sodium permolybdate coming from the module into MoO_3 , followed by further reduction of molybdenum oxide to metallic molybdenum.

5.4.1 MoO_3 from permolybdate

The starting material for the recovery procedure is coming from the separation module treatment of the natural molybdenum foils. The module and the dissolution procedures are described in details in the last paper of the LARAMED group [106].

According to the EDS analysis of the dried product from the module, it contained a mixture of sodium permolybdate $\text{Na}_2\text{MoO}_4 \cdot x(\text{H}_2\text{O})$ and NaOH from the separation procedure.

5.4.1.1 Literature approach and problems

The main approach for MoO_3 recovery is known as the Mo-based spent catalyst regeneration procedures. Two methods were proposed by Park [107] (Figure 6.65a) and Kar [108] (Figure 6.65b). The part of the process, interesting for current recovery study, starts from the ammonium permolybdate, dissolving in HCl at pH=2 to produce MoCl_6 , than returning back to ammonium permolybdate by adding ammonium hydroxide at controlled pH. After ammonium molybdate provide pure MoO_3 product by calcination at 450°C .

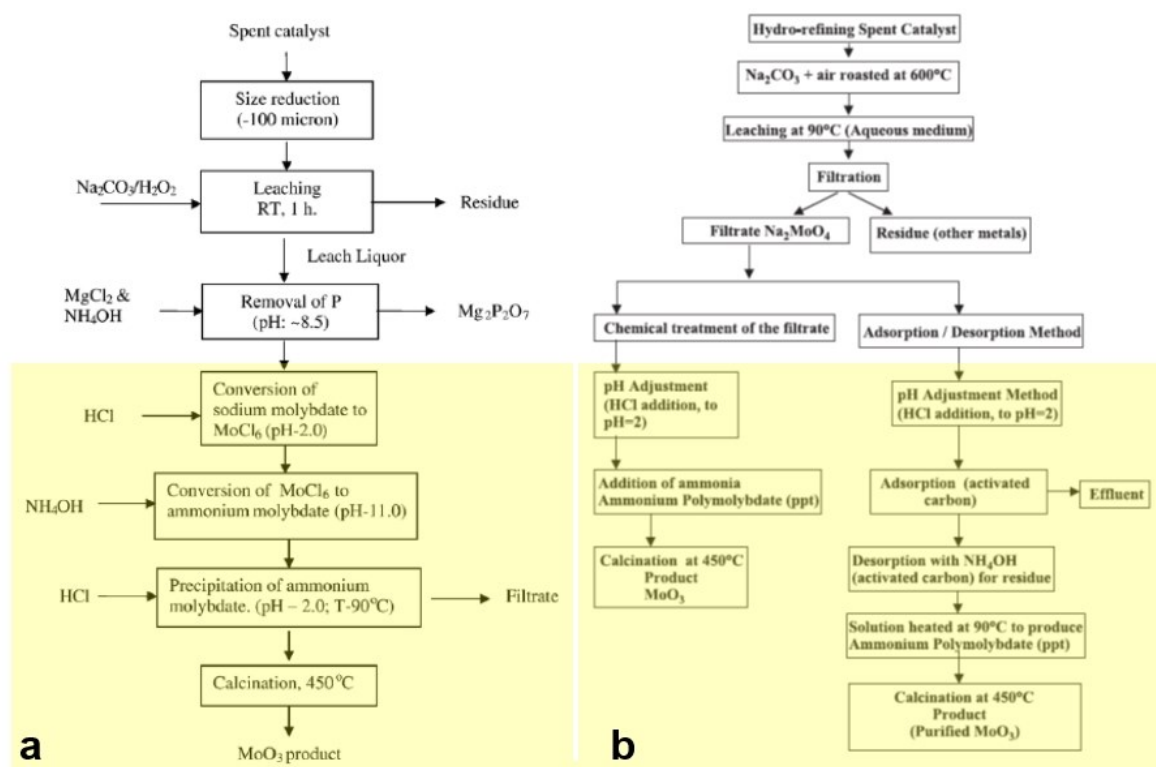


Figure 5.65: MoO_3 recovery as regeneration of spent catalyst.

Method 1: Literature approach

Experiment MoO_3 -1. To 0.5g of the product coming from separation module 15 ml 0.1M hydrochloric acid were added. The solution became yellow (MoCl_6 was produced), $\text{pH}=2$. Then 50ml 1M NH_4OH were added to the solution. The color changed from yellow to blue/transparent, $\text{pH}=10.57$. The solution was heated up to 80°C . pH decreased to 9.5. The precipitation occurred. The precipitate was centrifuged for 8 min, and mother liquor was separated. The precipitate was dried in vacuum overnight at 40°C . The product is white-yellowish powder 0.4g, containing MoCl_6 , $\text{Na}_2\text{MoO}_4(\text{H}_2\text{O})_x$, $(\text{NH}_4)_2\text{MoO}_4(\text{H}_2\text{O})_y$ (according to EDS analysis).

Anyway, the method appeared to be not efficient to transform all sodium permolybdate into ammonium permolybdate starting from the mixture coming from separation module.

In order to minimize the number of impurities (MoCl_6) the hydrochloric acid was substituted by nitric acid.

Method 2: HNO_3 instead of HCl

Experiment MoO_3 -2. To 0.495g of the product coming from the separation module 2-3 ml 5M HNO_3 and 10 ml of deionized water were added. The solution became yellow. The $\text{pH}=0$ (at the lower limit of pH -meter). Then concentrated NH_4OH was added dropwise to the

solution until pH=2. The color changed to yellow-green. The last drop of ammonium hydroxide changed pH=5.3 (desired pH=2.5-3). The solution was heated up at 80°C for 2 hours. Solution became more bluish. Precipitation of white flakes occurred. The changes of colors are showed in the Figure 5.66. The precipitate was centrifuged for 8 min, and the mother liquor was separated. The precipitate was washed twice with 10 ml of ethanol. After removing ethanol, the precipitate was dried in vacuum overnight at 40°C. The product was 0.11g white powder, containing $\text{Na}_2\text{MoO}_4(\text{H}_2\text{O})_x$, $(\text{NH}_4)_2\text{MoO}_4(\text{H}_2\text{O})_y$. According to EDS analysis the product had of about 2% Na and 11% Mo.

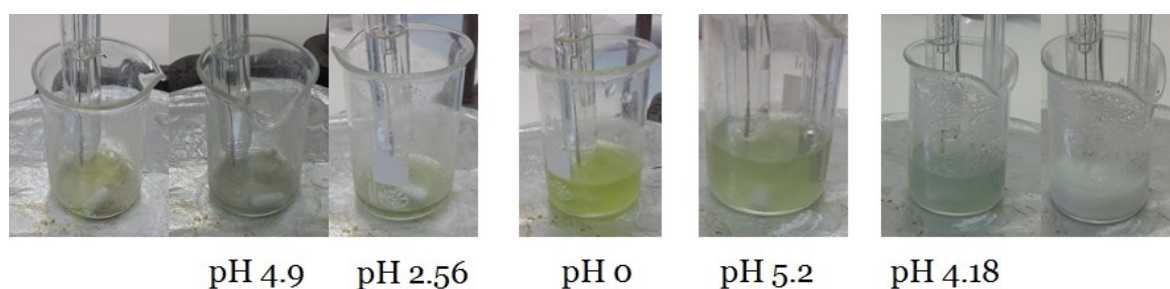


Figure 5.66: Modifications of color with pH change in MoO_3 recovery.

Experiment MoO_3 -3. The MoO_3 -2 experiment was repeated, following more precise pH control, and gave 0.112g of a product, starting from 0.222g of the sodium permolybdate, coming from module. The product contained 0.5% Na and 6% of Mo according to EDS.

Therefore, also the second method did not provide full transformation of sodium permolybdate into ammonium permolybdate.

5.4.1.2 Alternative method

The last method proposed here includes direct transformation to molybdenum oxide and molybdic acids, skipping the step of ammonium permolybdate.

Method 3: HNO_3 precipitation

Experiment MoO_3 -4. To 0.134g of the product coming from separation module were added 3-5 ml 5M HNO_3 (excess). The mixture was heated up in reflux mode at 95°C for 7 hours. The water was evaporated. The precipitate was washed twice with 15ml of the mixture of EtOH: H_2O (3:1 volumetric), then centrifuged for 8 min. The precipitate after removing mother liquor was dried in vacuum overnight at 40°C. The product was 0.082g white

powder, containing $\text{MoO}_3(\text{H}_2\text{O})_y$ with few $\text{Na}_2\text{MoO}_4(\text{H}_2\text{O})_x$. According to EDS analysis it contained of order of 0.3% Na and 15% Mo.

In all the products, coming from the separation module, Si impurity was detected. It was found that Si impurity was produced by holding the product in glass vessels. As soon as product from the module contained, besides sodium molybdate, a high concentration of sodium hydroxide, it was simply corroding glass vessels. In order to avoid the described problem the process of dissolution was reproduced starting from ^{nat}Mo foil, avoiding to keep the product in a glass vessel for a long time.

Experiment MoO₃-5. 0.14g ^{nat}Mo foil of 0.5cm² and 250μm thick was dissolved in 10ml H₂O₂ conc. at 90°C. The dissolution took about 30 min. When solution was cooled down to 50°C, 5 ml of 6M NaOH were added to the solution and it was maintained for 30 min to simulate processing in a module. 25 ml of 5M HNO₃ (excess) were added to solution. The mixture was heated up in reflux mode at 95°C overnight. The water was evaporated, giving 3.095g of precipitate. The precipitate was washed with 15 ml, after with 3×7.5 ml of distilled water. The mass of precipitate product was 0.986g. It contained MoO₃ with few NaNO₃. The theoretical yield of MoO₃ is of order of 94%. According to the EDS analysis, NaNO₃ impurity was present in about 5% weight in MoO₃ product.

Therefore, it was found that the most efficient method to recover MoO₃ from the NaOH-rich waste of the $^{100}\text{Mo}/^{99m}\text{Tc}$ -separation module is reflux heating with 5M nitric acid and after washing by minimal amounts of water the evaporated precipitate. This method allows to remove Na and provides the yield of about 94%.

5.4.2 MoO₃ recovery from sputtering of Mo

Unfortunately, two-inch planar magnetron source is not allowing focusing deposition. It means that a big amount of material is sputtered not only on the substrate-holder with the substrate, but also on the chamber walls. In a case when sputtering is done simultaneously on several substrates (batch production), there are always losses on the mask (clamping system) connecting the substrates to the substrate-holder (see Figure 5.67). This consideration does not depend on the size of magnetron.

The only way to minimize the losses on the mask is to develop the recovery method for sputtered material. For example, substrate-holder mask and chamber shield can be built of materials, more reactive than Mo, for example copper or aluminium. After a set of the depositions the mask or the shield can be dissolved in diluted HCl or HNO₃. Mo is not

dissolving in such conditions, instead, aluminium or copper will be dissolved. A non-dissolved part is the Mo film. In order to recover Mo into starting powder conditions, it should be dissolved in a solution NH_4OH and H_2O_2 1:1. This solution is dissolving Mo fast enough. After the solution can be evaporated leaving $(\text{NH}_4)_2\text{MoO}_4$. Ammonium molybdate by calcination at 450°C is giving pure MoO_3 .

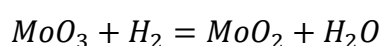
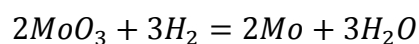


Figure 5.67: Substrate-holder with mask and six D13 substrates sputtered by Mo.

5.4.3 Mo recovery from MoO_3 by reduction

The most critical step of Mo recovery, as from the sputtering process to decrease the losses, and from the separation module Mo-rich waste, is the reduction of molybdenum oxide.

The methods for the reduction product analysis comprised XRD, EDS-SEM and quantification according to chemical reactions equations and known masses of starting and product materials. XRD can provide the analysis of crystalline forms, sometimes semi-quantitative. EDS-SEM gives the atomic and the mass compositions of elements, the quantification has a precision of not more than 5%. Moreover, the quantification due to mass change can be considered the most precise quantification method, if the set of chosen reactions and products is correct. For the reduction of MoO_3 it was considered that the products could contain Mo and MoO_2 . Thus, only two possible reactions were taken into account:



In order to know the correct mass of the precursor, MoO_3 was baked in the vacuum oven to remove the rests of water before mass measurement.

The most reliable way to identify the reduction product composition is to compare the results from several analysing techniques.

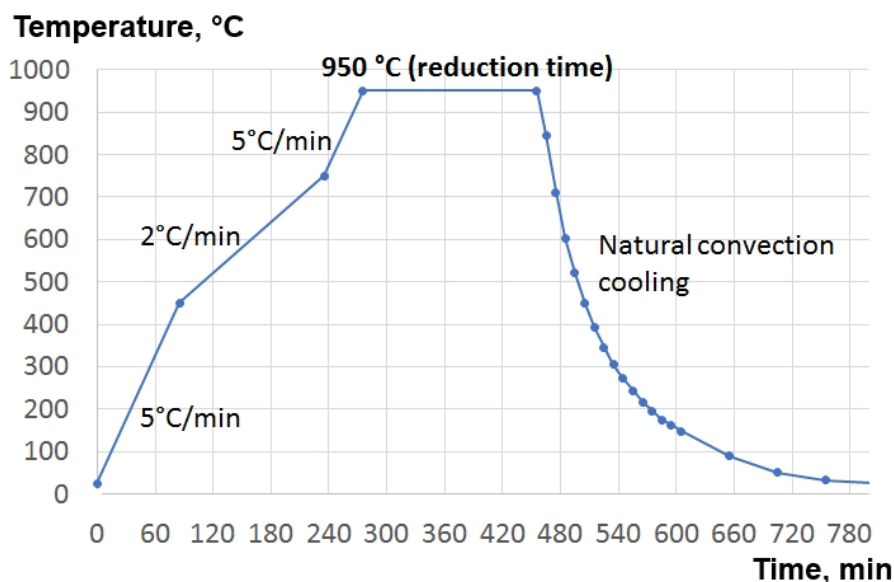


Figure 5.68: MoO_3 reduction thermal cycle.

The reduction thermal cycle is presented in the Figure 5.65. The heating velocity of $5^\circ\text{C}/\text{min}$ was used up to 450°C , then the heating velocity was decreased to $2^\circ\text{C}/\text{min}$ until the temperature 750°C was reached. In this temperature range the transformation to MoO_2 appears. A lower heating ramp was used to minimize the sublimation of MoO_3 , because of local overheating in the exothermic reaction.

Table 5.34 MoO_3 reduction experiments.

Reduction exp-t	MoO_3 origin	MoO_3 mass	Reduction time	Product mass	Product
R-1	Alfa Aesar	587mg	1 h	500 mg	MoO_2 (88%)+Mo(12%)
R-2	Alfa Aesar	389mg	6 h	261 mg	Mo(95%)+ Mo_2C (impur.)+C (impur.)
R-3.1	Alfa Aesar	1000mg	1.5 h	864 mg	MoO_2 (89%)+Mo(11%)
R-3.2	Product of R-3.1	864mg	2 h	687 mg	Mo(>90%)+ MoO_2 (>1%)+C(impur.)
R-4	Product of recovery exp. MoO_3 -2	61mg	2 h	37 mg	Mo(90%)+ SiO_2 (9%)+ Na_2SiO_3 (impur.)
R-5	Product of recovery exp. MoO_3 -4	49mg	2 h	34 mg	Mo(>90%)+ SiO_2 (impur.)

The heating from 750°C to 950°C was realized with 5°C/min ramp. Then the reduction from MoO₂ to Mo was performed at 950°C during different time intervals for each experiment, listed in the Table 5.34. Following cool-down was realized due to natural convection, just by switching off the furnace. The product was exposed to air only after the system had reached the room temperature.

5.4.3.1 Reduction of commercial MoO₃

The experimental apparatus was described in details in Chapter 4.8. To develop the method MoO₃ powders of Sigma Aldrich were used. The grain size of the powders was <5µm, as it was defined by observation with the optical microscope. The XRD spectrum of the material corresponds to MoO₃ according to the XRD-database (Ref. Code 01-076-1003).

Table 5.35 Analysis of R-1 MoO₃ reduction product.

<i>Analysis</i>	<i>XRD</i>	<i>EDS-SEM</i>	<i>Mass+quantification</i>
Mo, weight %	12	-	13.34
MoO ₂ , weight %	88	-	86.66
Mo, at %	-	29.97	37.6
O, at %	-	70.03	62.4
Mo, weight %	-	71.96	78.34
O, weight %	-	28.04	21.66

Table 5.36 Analysis of R-2 MoO₃ reduction product.

<i>Analysis</i>	<i>XRD</i>	<i>EDS-SEM</i>	<i>Mass+quantification</i>
Mo, weight %	95	-	97.79
MoO ₂ , weight %	0	-	2.21
Mo ₂ C, weight %	1	-	not considered
C, weight %	4	-	not considered
Mo, at %	-	87.91	96.77
O, at %	-	12.09	3.23
C, at %	-	was deconvoluted	not considered
Mo, weight %	-	97.76	99.45
O, weight %	-	2.24	0.55
C, weight %	-	was deconvoluted	not considered

The parameters and the results of the reduction experiments are listed in the Table 5.34. The first reduction experiment R-1, starting from ~0.6g of commercial MoO₃, was realized with just 1h reduction time at 950°C. According to the results of analysis this time was not sufficient to transform all MoO₃ to metallic Mo. Nevertheless, no MoO₃ was detected in the

final product. It means that the first step of the transition: $\text{MoO}_3 \rightarrow \text{MoO}_2 \rightarrow \text{Mo}$, was complete. The product analysis results are presented in the Table 5.35.

The following experiment R-2 with increased reduction time to 6 hours allowed to obtain more than 95% of Mo metallic starting from ~0.4g of commercial MoO_3 (Table 5.36). Some carbon-based impurities were detected in the product with XRD, probably, related to previously heating of a graphite crucible in the same furnace. In order to avoid such impurities in future the tungsten reactor was mechanically etched. According to EDS-analysis still few percent of MoO_2 remained not reduced.

Table 5.37 Analysis of R-3.1 MoO_3 reduction product.

<i>Analysis</i>	<i>XRD</i>	<i>EDS-SEM</i>	<i>Mass+quantification</i>
Mo, weight %	-	-	11.11
MoO_2 , weight %	-	-	88.89
Mo, at %	-	34.2	33.33
O, at %	-	65.8	66.67
Mo, weight %	-	75.71	77.78
O, weight %	-	24.29	22.22

The next experiment, with higher amount of MoO_3 , was realized in two steps. The R-3.1 during 1.5 hours of reduction allowed to get only about 10% of Mo metallic (see Table 5.37). In order to transform more than 90% of molybdenum oxide to Mo metallic (Table 5.38) additional 2 hours of reduction were required (R-3.2).

Table 5.38 Analysis of R-3.2 MoO_3 reduction product.

<i>Analysis</i>	<i>XRD</i>	<i>EDS-SEM</i>	<i>Mass+quantification</i>
Mo, weight %	96	-	91
MoO_2 , weight %	1	-	9
Mo_2C , weight %	-	-	not considered
C, weight %	3	-	not considered
Mo, at %	-	75.94	87.07
O, at %	-	18.66	12.93
C, at %	-	5.4	not considered
Mo, weight %	-	95.25	97.58
O, weight %	-	3.8	2.42
C, weight %	-	0.85	not considered

5.4.3.2 Reduction of recovered MoO₃

Several reduction experiments starting from MoO₃ recovered from the module Mo-rich waste were realized. It should be taken into account that the precursor (MoO₃ from the recovery procedure) was not as pure as the commercial MoO₃.

Table 5.39 Analysis of R-4 MoO₃ reduction product.

<i>Analysis</i>	<i>XRD</i>	<i>EDS-SEM</i>	<i>Mass+quantification</i>
Mo, weight %	91	-	-
MoO ₂ , weight %	0	-	-
SiO ₂ , weight %	9	-	-
Na ₂ SiO ₃ , weight %	Not detected	-	-
Mo, at %	-	73.77	-
O, at %	-	15.30	-
Si, at %	-	9.65	-
Na, at %	-	1.28	-
Mo, weight %	-	92.85	-
O, weight %	-	3.21	-
Si, weight %	-	3.56	-
Na, weight %	-	0.39	-

It was evident from the analysis of the MoO₃ precursor coming from recovery procedure, that it contained the impurities of glass SiO₂ and Na₂SiO₃. From the reduction product analysis (Table 5.39) it can be seen that the glass contaminants remained, when MoO₃ was reduced to Mo metallic. Na₂SiO₃ was not detected by XRD, because it is amorphous. The quantification due to the chemical reaction cannot be reliable, because of the glass contaminants. Nevertheless, since no MoO₂ was detected by XRD, the reduction of MoO₃ could be considered complete.

Table 5.40 Analysis of R-5 MoO₃ reduction product.

<i>Analysis</i>	<i>XRD</i>	<i>EDS-SEM</i>	<i>Mass+quantification</i>
Mo, weight %	-	-	88
MoO ₂ , weight %	-	-	-
SiO ₂ , weight %	-	-	12
Mo, at %	-	69.04	60.5
O, at %	-	20.01	13.2
Si, at %	-	10.95	26.3
Mo, weight %	-	91.36	88
O, weight %	-	4.41	6.4
Si, weight %	-	4.23	5.6

Similar to the previous experiment, the SiO₂ impurity coming from MoO₃ recovered from separation module waste was maintained in the product (Table 5.40). From the Figure 5.69 showing the EDS mapping of the reduction product, it can be clearly observed that oxygen is associated with Si to form SiO₂. Also according to EDS elemental analysis, the ratio between atomic composition of Si and O is 1:2. It means that all oxygen is associated with Si, and there is no excess oxygen to form molybdenum oxide. Therefore, complete transformation of MoO₃ was proven by absence of MoO₂ in the product. For both experiments R-4 and R-5 two hours at 950°C were sufficient to complete the reduction of about 50mg MoO₃ to Mo metallic.

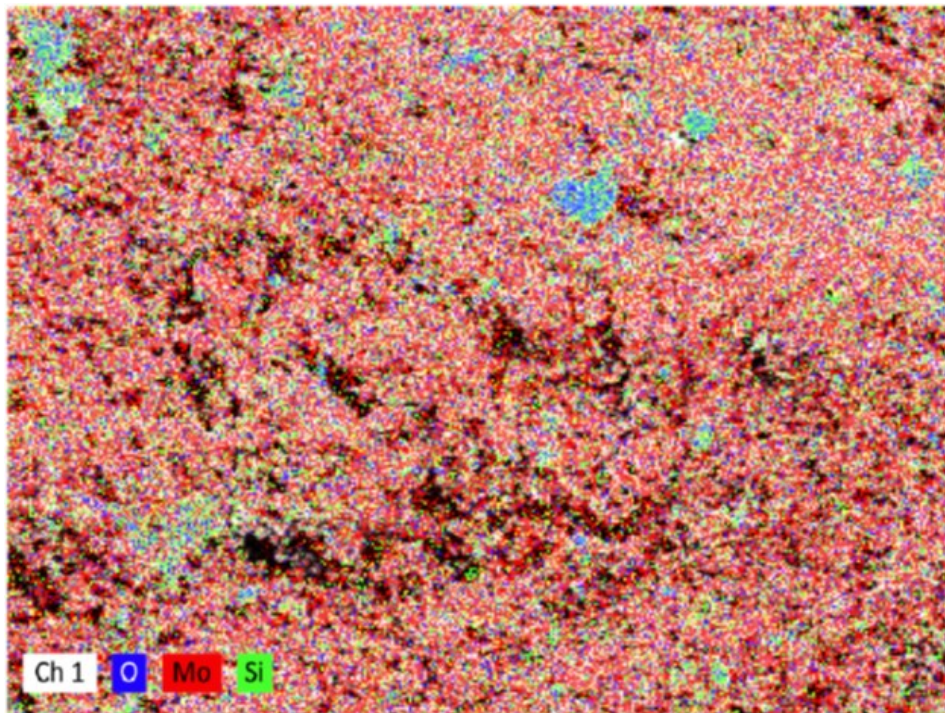


Figure 5.69: EDS-map analysis of R-5 MoO₃ reduction product.

Hereby, a reliable method providing reduction of up to 1g MoO₃ (both the commercial one, and the “working” material coming from separation module) was developed. Reduction yields of more than 95% were achieved by reduction time not longer than 4 hours (+5 hours heating). Increase of the transformation to metallic Mo, or increase of the loaded MoO₃ is also possible, but the reduction time should also be increased.

6 CONCLUSIONS

6.1 Main achievements

6.1.1 Ultra-thick films by magnetron sputtering

During the current work the method to deposit ultra-thick films (hundreds of microns) of refractory metal (Nb and Mo) by magnetron sputtering was developed. The films of such thickness, deposited by magnetron sputtering, have never been described before in literature.

The method is based on several techniques applied simultaneously:

- choice of proper sputtering pressure with minimal intrinsic stress in the film (point of transition from tensile to compressive stress)
- deposition at elevated temperature at $T_h > 0.25$ ($T_h = T_{\text{depos}}/T_m$); for Mo sputtering $T_{\text{depos}} = 500^\circ\text{C}$
- division of a thick film into a multilayer (with each layer < 100 nm), deposited by programmed DC power-supply.

The films deposited by the proposed method were dense ($> 98\%$ of bulk density) and adherent to different types of substrate (copper, sapphire, CVD diamond).

The thermal contact performance of the system $100\mu\text{m}$ thick Mo deposited onto copper backing plate was tested under 15.6MeV and $60\mu\text{A}$ proton beam (with the heat powder density of about $1\text{kW}/\text{cm}^2$).

6.1.2 Working target prototypes

In order to design the solid cyclotron target prototype, allowing minimization of impurities, ceramic materials with high thermal conductivity and chemical inertness, like sapphire and CVD synthetic diamond, were proposed. In order to minimize the costs, a composite backing plate, comprising ceramics vacuum brazed to copper, was suggested. In order to realize such prototypes, vacuum brazing of sapphire and CVD synthetic diamond to metal was studied.

Several brazing fillers were found efficient for both sapphire and synthetic diamond brazing. Among them CuSil ABA (Ag-63, Cu-35.3, Ti-1.7) and CuSnTi (Cu-75, Sn-25, Ti-10) in a form of homemade paste. CuSil ABA filler was chosen for the target prototype preparation.

In order to improve the brazed contact preliminary Ti metallization of the ceramic part by magnetron sputtering was realized.

Sputtering method was applied to deposit ~100µm thick Mo as a target material on sapphire and CVD diamond before brazing to copper.

Produced solid target prototypes were tested under the proton beam of 16MeV GE PETtrace cyclotron of different currents for 1 min (time enough to reach thermal equilibrium).

Sapphire based prototypes performed in a different way depending on the size of the sapphire plate. Thus, prototype with the 19mm diameter sapphire showed sapphire cracking because of the thermal stress during the test at 40µA; instead, three prototypes based on 13mm diameter sapphire substrates resisted to tests at the maximum current of the cyclotron (60µA).

All the CVD synthetic diamond-based prototypes resisted to maximum current and power of the cyclotron. Both short (1 min) and long test, more close to the production irradiation conditions (30 min) were realized.

Therefore, proposed cyclotron solid target prototypes were realized and tested in working conditions, proving the reliability of the concept.

6.1.3 Molybdenum recovery

In order to increase the attraction of the cyclotron-based method for production ^{99m}Tc from economical point of view, method to recover costly ^{100}Mo from the separation module waste in metallic form was developed. Thus, proposed method allowed recovery of MoO_3 with a 94% yield starting from the module Mo-rich waste. Following reduction of molybdenum oxide in a closed system in overpressure of hydrogen (without hydrogen flow) provided >95% of Mo metallic.

REFERENCES

- [1] Kowalewski J and Szczurek J 2006 Issues in vacuum brazing *Heat Treating Progress* **6** 41-5
- [2] Ruth T J 2014 The Medical Isotope Crisis: How We Got Here and Where We Are Going *Journal of Nuclear Medicine Technology* **42** 245-8
- [3] Esposito J, Vecchi G, Pupillo G, Taibi A, Uccelli L, Boschi A and Gambaccini M 2013 Evaluation of and Productions Based on a High-Performance Cyclotron *Science and Technology of Nuclear Installations* **2013** 1-14
- [4] Lagunas-Solar M C, Kiefer P M, Carvacho O F, Lagunas C A and Ya Po C 1991 Cyclotron production of NCA ^{99m}Tc and ^{99}Mo . An alternative non-reactor supply source of instant ^{99m}Tc and $^{99}\text{Mo} \rightarrow ^{99m}\text{Tc}$ generators *International Journal of Radiation Applications and Instrumentation. Part A. Applied Radiation and Isotopes* **42** 643-57
- [5] 2013 Report on the 2nd Research Coordination Meeting on “Accelerator-based Alternatives to Non-HEU Production of $^{99}\text{Mo}/^{99m}\text{Tc}$ ”, 7-11 October 2013. (Legnaro)
- [6] Froment P, Tilquin I, Cogneau M, Delbar T, Vervier J and Ryckewaert G 2002 The production of radioisotopes for medical applications by the adiabatic resonance crossing (ARC) technique *Nuclear Instruments and Methods in Physics Research Section A: Accelerators, Spectrometers, Detectors and Associated Equipment* **493** 165-75
- [7] Abbas K, Buono S, Burgio N, Cotogno G, Gibson N, Maciocco L, Mercurio G, Santagata A, Simonelli F and Tagziria H 2009 Development of an accelerator driven neutron activator for medical radioisotope production *Nuclear Instruments and Methods in Physics Research Section A: Accelerators, Spectrometers, Detectors and Associated Equipment* **601** 223-8
- [8] Nagai Y 2015 Medical Isotope Production using High Intensity Accelerator Neutrons *Physics Procedia* **66** 370-5
- [9] Clayton J E 2015 System and method for generating molybdenum-99 and metastable technetium-99, and other isotopes. (Google Patents)
- [10] 2015 Report on the 3rd Research Coordination Meeting on “Accelerator-based Alternatives to Non-HEU Production of $^{99}\text{Mo}/^{99m}\text{Tc}$ ”, June 22-26, 2015. (Vienna)
- [11] Esposito J 2011 Feasibility Study Report on Alternative $^{99}\text{Mo}/^{99m}\text{Tc}$ Production Routes using Particle Accelerators at LNL. In: *INFN Report*, (Legnaro: LNL-INFN) p 48
- [12] Kandil F A, Lord J D, Fry A T and Grant P V 2001 A review of residual stress measurement methods - a guide to technique selection. In: *NPL Report National Physical Laboratory*, Teddington, Middlesex, UK pp 1-42
- [13] Nishikata K, Kimura A, Ishida T, Kitagishi S, Tsuchiya K, Akiyama H, Nagakura M and Suzuki K 2013 Method of producing radioactive molybdenum
- [14] Avetisyan A, Dallakyan R, Sargsyan R, Melkonyan A, Mkrtchyan M, Harutyunyan G and Dobrovolsky N 2015 The powdered molybdenum target preparation technology for ^{99m}Tc production on C18 cyclotron *International Journal of engineering and Innovative Technology* **4** 37-44

- [15] Barbosa L A M M 2014 System and method for producing radiomedical-grade Tc-99m
- [16] Gagnon K, Wilson J S, Holt C M B, Abrams D N, McEwan A J B, Mitlin D and McQuarrie S A 2012 Cyclotron production of ^{99m}Tc : Recycling of enriched 100Mo metal targets *Appl. Radiat. Isot.* **70** 1685-90
- [17] Gagnon K, McQuarrie S and Wilson J 2012 Production of technetium from a molybdenum metal target. Patent WO 2012139220 A1. (United States: The Governors Of The University Of Alberta)
- [18] Wilson J, Gagnon K and McQuarrie S 2014 Production of technetium from a molybdenum metal target. (United States: The governors of University of Alberta)
- [19] Zeisler S K, Hanemaayer V and Buckley K R 2015 Target system for irradiation of molybdenum with particle beams. Patent WO2015161385 A1. (United States: Triumph)
- [20] Schaffer P, Bénard F, Bernstein A, Buckley K, Celler A, Cockburn N, Corsaut J, Dodd M, Economou C and Eriksson T 2015 Direct Production of ^{99m}Tc via 100 Mo (p, 2n) on Small Medical Cyclotrons *Physics Procedia* **66** 383-95
- [21] Manenti S, Holzwarth U, Loriggiola M, Gini L, Esposito J, Groppi F and Simonelli F 2014 The excitation functions of 100 Mo (p, x) ^{99}Mo and 100 Mo (p, 2n) ^{99m}Tc *Appl. Radiat. Isot.* **94** 344-8
- [22] Zyuzin A, Guérin B, van Lier E, Tremblay S, Rodrigue S, Rousseau J A, Dumulon-Perreault V, Lecomte R and van Lier J E 2012 Cyclotron Production of ^{99m}Tc . In: *WTTC*,
- [23] Fink C G 1932 Electroplating and process of producing same. Patent 1,885,700.
- [24] Morley T J, Penner L, Schaffer P, Ruth T J, Bénard F and Asselin E 2012 The deposition of smooth metallic molybdenum from aqueous electrolytes containing molybdate ions *Electrochem. Commun.* **15** 78-80
- [25] Kazimierczak H, Ozga P and Socha R P 2013 Investigation of electrochemical co-deposition of zinc and molybdenum from citrate solutions *Electrochim. Acta* **104** 378-90
- [26] Kipouros G J and Sadoway D R 1988 The electrodeposition of improved molybdenum coatings from molten salts by the use of electrolyte additives *J. Appl. Electrochem.* **18** 823-30
- [27] Ene N and Donath C 2006 Texture of electrolytic Mo deposition from molten alkali halide *Journal of Optoelectronics and Advanced Materials* **8** 708
- [28] Schaffer P, Benard F, Buckley K R, Hanemaayer V, Manuela C H, Klug J A, Kovacs M S, Morley T J, Ruth T J and Valliant J 2013 Processes, systems, and apparatus for cyclotron production of technetium-99m. Patent US 2013/0301769 A1. (United States: TRIUMF)
- [29] Jalilian A R, Targholizadeh H, Raisali G R, Zandi H and Dehgan M K 2011 Direct Technetium radiopharmaceuticals production using a 30MeV Cyclotron *DARU: Journal of Faculty of Pharmacy, Tehran University of Medical Sciences* **19** 187
- [30] Folger H, Klemm J and Muller M 1983 Preparation of Nuclear Accelerator Targets by Focused Ion Beam Sputter Deposition *Nuclear Science, IEEE Transactions on* **30** 1568-72

- [31] Morrall P S 2008 The Target Preparation Laboratory at Daresbury *Nuclear Instruments and Methods in Physics Research Section A: Accelerators, Spectrometers, Detectors and Associated Equipment* **590** 118-21
- [32] Maier H J, Friebel H U, Frischke D and Grossmann R 1993 State of the art of high vacuum sputter deposition of nuclear accelerator targets *Nuclear Instruments and Methods in Physics Research Section A: Accelerators, Spectrometers, Detectors and Associated Equipment* **334** 137-41
- [33] Johnson R R, Gelbart W Z, Abeysekera B, Matei L and McRae G 2016 Target, apparatus and process for the manufacture of molybdenum-100 targets. Google Patents)
- [34] Stolarz A, Kowalska J A, Jasiński P, Janiak T and Samorajczyk J 2015 Molybdenum targets produced by mechanical reshaping *J. Radioanal. Nucl. Chem.* **305** 947-52
- [35] Lebeda O, Jiran R, Ráliš J and Stursa J 2005 A new internal target system for production of (211)At on the cyclotron U-120M *Applied radiation and isotopes : including data, instrumentation and methods for use in agriculture, industry and medicine* **63** 49-53
- [36] NuPECC 2014 *Nuclear Physics for Medicine: Nuclear Physics European Collaboration Committee*
- [37] L. Tang D E R, D.W. McCarthy and M.J. Welch 2002 Remote and Automated Solvent Extraction of Gallium-66. In: *Proceedings of the Ninth International Workshop on Targetry and Target Chemistry*, ed Sven-Johan Heselius, et al. (Turku, Finland: Gillot Oy Painotalo-Turku, Finland) pp 74-7
- [38] Hur M G, Yang S D, Kim S W, Kim I J and Choi S M 2014 High current solid target for radioisotope production at cyclotron using metal foam. (Google Patents)
- [39] Bakhtiari S, Gelbart W Z, Ho W and Stevenson N R 1997 Encapsulated Target for Isotope Production Cyclotrons. In: *Particle Accelerator Conference*, Vancouver, B.C., Canada pp 3842-4
- [40] Chattopadhyay S and Das M K 2008 A novel technique for the effective concentration of ^{99m}Tc from a large alumina column loaded with low specific-activity (n, γ)-produced ^{99}Mo *Appl. Radiat. Isot.* **66** 1295-9
- [41] Morley T J, Dodd M, Gagnon K, Hanemaayer V, Wilson J, McQuarrie S A, English W, Ruth T J, Bénard F and Schaffer P 2012 An automated module for the separation and purification of cyclotron-produced $^{99m}\text{TcO}_4^-$ *Nucl. Med. Biol.* **39** 551-9
- [42] Chattopadhyay S, Das S S and Barua L 2010 A simple and rapid technique for recovery of ^{99m}Tc from low specific activity (n, γ) ^{99}Mo based on solvent extraction and column chromatography *Appl. Radiat. Isot.* **68** 1-4
- [43] Hoffman D W and Thornton J A 1977 Internal stresses in sputtered chromium *Thin Solid Films* **40** 355-63
- [44] Hoffman R W 1976 Stresses in thin films: The relevance of grain boundaries and impurities *Thin Solid Films* **34** 185-90
- [45] Thornton J A 1974 Influence of apparatus geometry and deposition conditions on the structure and topography of thick sputtered coatings *Journal of Vacuum Science and Technology* **11** 666-70
- [46] Abermann R 1990 Measurements of the intrinsic stress in thin metal films *Vacuum* **41** 1279-82

- [47] Floro J, Hearne S, Hunter J, Kotula P, Chason E, Seel S and Thompson C 2001 The dynamic competition between stress generation and relaxation mechanisms during coalescence of Volmer–Weber thin films *J. Appl. Phys.* **89** 4886-97
- [48] Spaepen F 2000 Interfaces and stresses in thin films *Acta Mater.* **48** 31-42
- [49] Chason E, Sheldon B W, Freund L B, Floro J A and Hearne S J 2002 Origin of Compressive Residual Stress in Polycrystalline Thin Films *Phys. Rev. Lett.* **88** 156103
- [50] Movchan B A and Demchishin A V 1969 Structure and properties of thick condensates of nickel, titanium, tungsten, aluminum oxides, and zirconium dioxide in vacuum *Fiz. Metal. Metalloved.* **28**: 653-60 (Oct 1969).
- [51] Schneeweiß H J and Abermann R 1993 On the influence of the substrate properties on the internal growth stress of titanium films at 250 °C *Thin Solid Films* **228** 40-3
- [52] Stelmakh V, Rinnerbauer V, Joannopoulos J D, Soljačić M, Celanovic I, Senkevich J J, Tucker C, Ives T and Shrader R 2013 Evolution of sputtered tungsten coatings at high temperature *Journal of Vacuum Science & Technology A* **31** 061505
- [53] Vink T J, Somers M A J, Daams J L C and Dirks A G 1991 Stress, strain, and microstructure of sputter - deposited Mo thin films *J. Appl. Phys.* **70** 4301-8
- [54] Hoffman D W and Thornton J A 1977 The compressive stress transition in Al, V, Zr, Nb and W metal films sputtered at low working pressures *Thin Solid Films* **45** 387-96
- [55] Lin J, Moore J J, Sproul W D, Lee S L and Wang J 2010 Effect of Negative Substrate Bias on the Structure and Properties of Ta Coatings Deposited Using Modulated Pulse Power Magnetron Sputtering *IEEE Transactions on Plasma Science* **38** 3071-8
- [56] Al-masha'al A a, Bunting A and Cheung R 2016 Evaluation of residual stress in sputtered tantalum thin-film *Appl. Surf. Sci.* **371** 571-5
- [57] Davis C A 1993 A simple model for the formation of compressive stress in thin films by ion bombardment *Thin Solid Films* **226** 30-4
- [58] Teixeira V and Andritschky M 1993 *Multicomponent and Multilayered Thin Films for Advanced Microtechnologies: Techniques, Fundamentals and Devices*, ed O Auciello and J Engemann (Dordrecht: Springer Netherlands) pp 121-7
- [59] Bemporad E, Sebastiani M, Casadei F and Carassiti F 2007 Modelling, production and characterisation of duplex coatings (HVOF and PVD) on Ti–6Al–4V substrate for specific mechanical applications *Surf. Coat. Technol.* **201** 7652-62
- [60] Karabacak T, Senkevich J J, Wang G-C and Lu T-M 2005 Stress reduction in sputter deposited films using nanostructured compliant layers by high working-gas pressures *Journal of Vacuum Science & Technology A: Vacuum, Surfaces, and Films* **23** 986
- [61] Karabacak T, Picu C R, Senkevich J J, Wang G-C and Lu T-M 2004 Stress reduction in tungsten films using nanostructured compliant layers *J. Appl. Phys.* **96** 5740-6
- [62] Alagoz A S, Kamminga J-D, Grachev S Y, Lu T-M and Karabacak T 2009 Residual Stress Reduction in Sputter Deposited Thin Films by Density Modulation *MRS Proceedings* **1224**
- [63] Daniel R, Keckes J, Matko I, Burghammer M and Mitterer C 2013 Origins of microstructure and stress gradients in nanocrystalline thin films: The role of growth parameters and self-organization *Acta Mater.* **61** 6255-66

- [64] Feng X, Huang Y and Rosakis A J 2007 On the Stoney Formula for a Thin Film/Substrate System With Nonuniform Substrate Thickness *Journal of Applied Mechanics* **74** 1276-81
- [65] Song X, Yeap K B, Zhu J, Belnoue J, Sebastiani M, Bemporad E, Zeng K Y and Korsunsky A M 2011 Residual stress measurement in thin films using the semi-destructive ring-core drilling method using Focused Ion Beam *Procedia Engineering* **10** 2190-5
- [66] Korsunsky A M, Sebastiani M and Bemporad E 2009 Focused ion beam ring drilling for residual stress evaluation *Mater. Lett.* **63** 1961-3
- [67] Sebastiani M, Eberl C, Bemporad E and Pharr G M 2011 Depth-resolved residual stress analysis of thin coatings by a new FIB–DIC method *Materials Science and Engineering: A* **528** 7901-8
- [68] Nicolet M-A 1978 *Thin Solid Films*, (Lausanne: Elsevier Sequoia S.A.) pp 415-43
- [69] Zolotuhin I V and Kalinin Y E 1990 Amorphous metallic materials *Progress of Physical Sciences* **160** 75-110
- [70] Mehmood M, Akiyama E, Habazaki H, Kawashima A, Asami K and Hashimoto K 2000 Effects of nanocrystalline heterogeneity on the corrosion behavior of sputter-deposited chromium–niobium alloys *Corros. Sci.* **42** 361-82
- [71] Antonetc I V, Kotov L N, Nekipelov S V and Golubev E A 2004 Features of nanostructure and conductivity of thin films of various metals *Journal of Technical Physics* **74** 24-7
- [72] Chambers D L, Wan C T, Susi G T and Taylor K A 1989 Sputter deposition of aluminum and other alloys at cryogenic temperatures *Journal of Vacuum Science and Technology A* **7** 1305-9
- [73] El-moneim A A, Akiyama E, Habazaki H, Kawashima A, Asami K and Hashimoto K 1998 XPS and electrochemical studies on the corrosion behaviour of sputter-deposited amorphous Mn-Nb alloys in a neutral chloride solution *Corros. Sci.* **40** 1513-31
- [74] Hauser J J, Schutz R J and Augustyniak W M 1978 Amorphous metal films by getter sputtering at 25 K *Phys. Rev. B: Condens. Matter* **18** 3890-6
- [75] Kuzmenko V M and N. V A 1999 Hydrogen in amorphous and crystalline films of ytterbium *Solid State Physics* **41** 177-82
- [76] Radić N, Tonejc A, Ivkov J, Dubček P, Bernstorff S and Medunić Z 2004 Sputter-deposited amorphous-like tungsten *Surf. Coat. Technol.* **180–181** 66-70
- [77] Roberts A D, Daniel L C and Nickles R J 1995 A high power target for the production of [¹⁸F] fluoride. *Nuclear Instruments and Methods in Physics Research Section B: Beam Interactions with Materials and Atoms* **99** 797-9
- [78] Green J E, Barnett S A, Sundgren J E and Rocket A 1989 ed T Itoh (Amsterdam: Elsevier)
- [79] Schwartz M M 2003 *Brazing* (Ohio: ASM international)
- [80] S. K. Gupta M S N, and A. Kak. 2007 A study on the effect of brazing time on element diffusion *Welding Journal* 47-50
- [81] Hodges C A W a V C 2008 Comparing metal-ceramics brazing methods *Welding Journal* 43-50

- [82] Moret F and Eustathopoulos N 1993 Ceramic to metal direct brazing *J. Phys. IV France* **03** C7-1043-C7-52
- [83] Jacobson D M and Humpston G H 2005 *Principles of Brazing*, (Ohio: ASM international)
- [84] Savvides N and Window B 1986 Unbalanced magnetron ion-assisted deposition and property modification of thin films *J. Vac. Sci. Technol., A* **4** 504-8
- [85] Skliarova H, Azzolini O, Cherenkova-Dousset O, Johnson R R and Palmieri V 2014 Niobium-based sputtered thin films for corrosion protection of proton-irradiated liquid water targets for [¹⁸F] production *J. Phys. D: Appl. Phys.* **47** 045306
- [86] Skliarova H, Azzolini O, Johnson R R and Palmieri V 2015 Co-sputtered amorphous Nb-Ta, Nb-Zr and Ta-Zr coatings for corrosion protection of cyclotron targets for [18F] production *J. Alloys Compd.* **639** 488-95
- [87] Skliarova H, Renzelli M, Azzolini O, de Felicis D, Bemporad E, Johnson R R and Palmieri V 2015 Niobium-niobium oxide multilayered coatings for corrosion protection of proton-irradiated liquid water targets for [18F] production *Thin Solid Films*
- [88] Schulmeyer W V and Ortner H M 2002 Mechanisms of the hydrogen reduction of molybdenum oxides *International Journal of Refractory Metals and Hard Materials* **20** 261-9
- [89] Pak J-J, Jo J-O, Park C-H, Kang J-G and Shin D-H 2008 Recovery of Molybdenum from Spent Acid by Ammonia Gas Neutralization *Mater. Trans.* **49** 202-7
- [90] Kim B-S, Kim E-y, Jeon H-S, Lee H-I and Lee J-C 2008 Study on the Reduction of Molybdenum Dioxide by Hydrogen *Mater. Trans.* **49** 2147-52
- [91] Gupta C K 1992 *Extractive metallurgy of molybdenum* (Boca Raton: CRC Press)
- [92] Grosskreutz J C 1969 Mechanical Properties of Metal Oxide Films *J. Electrochem. Soc.* **116** 1232-7
- [93] Chen Z and Mecholsky J J 1993 Control of strength and toughness of ceramic/metal laminates using interface design *J. Mater. Res.* **8** 2362-9
- [94] Marulanda D M, Olaya J J, Piratoba U, Mariño A and Camps E 2011 The effect of bilayer period and degree of unbalancing on magnetron sputtered Cr/CrN nano-multilayer wear and corrosion *Thin Solid Films* **519** 1886-93
- [95] Major L, Lackner J M, Kot M, Janusz M and Major B 2014 Contribution of TiN/Ti/a-C:H multilayers architecture to biological and mechanical properties *Bulletin of the Polish Academy of Sciences Technical Sciences* **62** 565-70
- [96] <http://t2.lanl.gov/nis/> Los Alamos National Laboratory database.
- [97] <http://www.nndc.bnl.gov/> Brookhaven National Laboratory Database.
- [98] www.plansee.com/en/materials/molybdenum.html
- [99] http://www.diamond-materials.com/downloads/cvd_diamond_booklet.pdf
- [100] Okada Y and Tokumaru Y 1984 Precise determination of lattice parameter and thermal expansion coefficient of silicon between 300 and 1500 K *J. Appl. Phys.* **56** 314-20
- [101] <https://www-s.nist.gov/srmors/certArchive.cfm>

- [102] Deambrosis S M, Miorin E, Montagner F, Zin V, Fabrizio M, Sebastiani M, Massimi F and Bemporad E 2015 Structural, morphological and mechanical characterization of Mo sputtered coatings *Surf. Coat. Technol.* **266** 14-21
- [103] Osmanda A M, Battenbough A J and A.M. S 2012 Effects of Dissimilar Materials on Joint Properties. In: *Nicrobraze News*: American Institute of Physics)
- [104] Targholizadeh H, Raisali G, Jalilian A R, Rostampour N, Ensaf M and Dehghan M K 2010 Cyclotron production of technetium radionuclides using a natural metallic molybdenum thick target and consequent preparation of [Tc]-BRIDA as a radio-labelled kit sample *Nukleonika* **55** 113-8
- [105] Celler A, Hou X, Bénard F and Ruth T 2011 Theoretical modeling of yields for proton-induced reactions on natural and enriched molybdenum targets *Physics in medicine and biology* **56** 5469
- [106] Martini P, Boschi A, Cicoria G, Uccelli L, Pasquali M, Duatti A, Pupillo G, Marengo M, Loriggiola M and Esposito J 2016 A solvent-extraction module for cyclotron production of high-purity technetium-99m *Appl. Radiat. Isot.* **118** 302-7
- [107] Park K H, Reddy B R, Mohapatra D and Nam C-W 2006 Hydrometallurgical processing and recovery of molybdenum trioxide from spent catalyst *Int. J. Miner. Process.* **80** 261-5
- [108] Kar B B, Datta P and Misra V N 2004 Spent catalyst: secondary source for molybdenum recovery *Hydrometallurgy* **72** 87-92